Stagnation-point Flows

A thesis submitted to the School of Mathematics of the University of East Anglia in partial fulfilment of the requirements for the degree of Doctor of Philosophy

By Rachel Tooke

August 2010

Abstract

The aim of this thesis is to consider an unsteady two-dimensional oblique stagnation-point flow travelling towards a wall. The far-field comprises an unsteady orthogonal stagnation-point flow, consisting of a mean component and an oscillatory component characterised by a relative amplitude and a dimensionless frequency parameter. Superimposed onto this, is a shear flow with constant vorticity and a time-dependent uniform stream. A similarity solution is sought, which is an exact solution of the Navier-Stokes equations.

The flow is discussed in two limiting cases. At high frequency, the asymptotic structure is dependent upon the relative sizes of the mean and oscillatory components. When the mean flow is large, with a relatively small oscillatory component, the flow can be described with a Stokes layer at the wall matching an outer layer. However, when the oscillatory component dominates, a steady streaming layer is introduced to match to the far-field, which is considerably larger than that of the outer layer in the previous case. It is shown numerically in this case that the flow structure described breaks down when the relative amplitude of the oscillatory component is increased above a certain threshold, dependent upon the frequency. In the low frequency limit, at leading order, the problem is quasi-steady.

Two special cases are considered, the first where the vorticity is zero in the far-field and the streamlines approach the wall orthogonally. In this case the flow is chosen to approach an oscillating wall. The second case is when the flow is steady.

In certain time intervals over a single period, the flow structure becomes multi-layered. The behaviour of the flow within these intervals is investigated. Additionally, in the high frequency case, the streamline pattern is discussed in both the Stokes and steady streaming layers and the particle paths are analysed in the steady streaming layer.

Acknowledgements

Firstly, I thank Mark Blyth and Paul Hammerton for all their guidance and support throughout the production of this thesis. Thanks also go to the entire maths department for their friendship over the years, particularly Simon Kirby, without whom, life in the postgrad room would have been a lot less interesting.

A special thank you goes to Melissa Hindley for her friendship throughout my undergraduate and PhD studies.

Lastly, thank you to my parents and Jen for their love and support throughout my time at UEA.

Contents

Abstract **iii**

Acknowledgements **iv**

1 Introduction **1**

2 Unsteady orthogonal stagnation-point flow **10**

2.1 Introduction 10

2.2 Problem formulation 11

2.3 Large frequency analysis 17

2.4 The primary flow 18

2.4.1 The Stokes layer 18

2.4.2 The steady streaming layer 20

2.4.3 Numerical Scheme: Runge-Kutta technique 23

2.4.4 Asymptotic solution of $f_0(\zeta)$ about $a_0 \approx 0.75$ 24

2.4.5 Numerical scheme: Finite-Difference technique 30

2.4.6 The first order correction, $f_1(\zeta)$ 33

2.5 Summary of primary flow 34

2.6 The subsidiary flow 35

2.6.1 The Stokes layer 35

2.6.2 The steady streaming layer 37

2.6.3 Numerics 40

2.7 Summary of subsidiary flow 44

2.8 Wall shear stress 44

2.9 Summary 47

3 Steady oblique stagnation-point flow **49**

3.1 Introduction 49

3.2 Steady oblique stagnation-point flow 50

3.3 General form of the oblique stagnation-point flow 55

3.4 Summary 60

4 Unsteady oblique stagnation-point flow **62**

4.1 Introduction 62

4.2 Problem formulation 63

4.2.1 The initial velocity profile for the primary flow 69

4.2.2 Initial profile for the oblique flow 71

4.3 Numerics 73

4.3.1 The behaviour of the velocity profiles close to the finite-time singularity 81

4.4 Small frequency 86

4.5 The structure of the near-wall flow 95

4.6 Summary 113

5 Unsteady oblique stagnation-point flow in the large frequency limit **116**

5.1 Introduction 116

5.2 Problem formulation 117

5.3 Summary of primary flow 119

5.4 The oblique equation 120

5.4.1 Stokes layer 120

5.4.2 Steady streaming layer 123

5.5 The structure of the near-wall flow 129

5.6 Summary 147

6 Conclusion **149**

6.1 Concluding remarks 149

6.2 Further work 152

A Asymptotic solution of $F_0(\zeta)$ about $a_0 \approx 0.75$ **154**

B Change of frame of reference **159**

References **161**

List of tables

4.1 Computing the gradient and the intercept of $\psi^{-1}_{q_{min}}$, where τ_R is the range over which the least squares analysis is conducted. 89

List of figures

1.1 An illustration of an arterial end-to-side anastomosis. 5

2.1 An illustration of the unsteady oscillating stagnation-point flow approaching an oscillating wall, where the stagnation point is represented by the solid dot and is fixed at the origin. 14

2.2 (a) The asymptotic structure valid for high frequency, σ, and the oscillation amplitude, $\Delta < 1$. (b) The asymptotic structure valid for high frequency, σ, and large oscillation amplitude, Δ. 15

2.3 The primary leading order velocity profiles for the two solutions of $f_0'(\zeta)$ for $a_0 = 0.6017$ (solid line), $a_0 = 0.65$ (dotted lines) and $a_0 = 0.7$ (dashed lines). 24

2.4 Using the results from the Runge-Kutta method close to $a_0 \approx 0.7$, a relationship develops between the shear component $\widehat{f}_0''(0)$ and ϵ, given by $\widehat{f}_0''(0) \sim \epsilon^{1/2}$ as $\epsilon \to 0$. 26

2.5 The leading order asymptotic solution for $\epsilon \to 0$, where $\epsilon = 0.05$ (solid line), $\epsilon = 0.025$ (dotted lines) and $\epsilon = 0.01$ (dashed lines). The vertical lines represent $\widehat{\zeta}_0$, the point at which the solution no longer satisfies the far-field boundary condition. . . 28

2.6 The leading order asymptotic solution to equation (2.60) for selected values of ϵ. Due to the scalings on the axes, the region 1 solution is unaffected by the choice of ϵ. As $\epsilon \to 0$, the region 2 solution matches to the region 1 solution. 30

2.7 The velocity profile for the finite-difference method, represented by the crosses and the Runge-Kutta method, represented by the solid line, for $\lambda = 1.0714$ i.e. $a_0 = 0.7$, showing excellent agreement. 32

2.8 The asymptotic leading order solution for $\epsilon = 0.001$, illustrated by the crosses, showing excellent agreement with the numerical solution for the same value of ϵ, represented by the solid line. 32

2.9 The possible values of λ for which solutions of equation (2.51) exist, where $\lambda = \frac{3}{4a_0}$. The solid line represents the numerics calculated from the Runge-Kutta technique, while the dotted line corresponds to the results from the finite difference scheme. 33

2.10 The primary shear component $f_1''(0)$ for $a_0 = 0.6017$ and $a_1 = -0.56$ (dashed lines), $a_1 = -0.55$ (dotted lines) and $a_1 = -0.55237$ (solid line). This illustrate that for $a_1 = -0.55237$, a unique value of $f_1''(0)$ exists. 34

2.11 (a) The first primary velocity profile for $a_0 = 0.6017, 0.65, 0.7$ with its corresponding subsidiary velocity profile. (b) The second primary velocity profile for $a_0 = 0.6017, 0.65, 0.7$ with its corresponding subsidiary velocity profile. We note that this solution is unable to be calculated by the Runge-Kutta method when $a_0 \gtrsim 0.7$. In each case, the solid line represents $a_0 = 0.6017$, the dotted line, $a_0 = 0.65$ and the dashed line, $a_0 = 0.7$. 41

2.12 The subsidiary solution for the finite-difference method, represented by the crosses and the Runge-Kutta method, represented by solid line for $a_0 = 0.7$, showing excellent agreement. 43

2.13 The possible values of λ for which solutions to equation (2.132) exist. The solid line represents the numerics calculated from the Runge-Kutta method and the dotted line represents the finite difference method results. 43

3.1 An illustration of the dividing streamline meeting the wall obliquely at an angle of $\theta = \tan^{-1}(-2k/\zeta)$. 51
3.2 (a) Profiles of the shear flow component for $\beta = 5, \alpha, 0, -\alpha, -5$, reading from left to right. (b) Streamlines for the case $k/\zeta = 0.5$ and $\beta = \alpha$, where $\xi = (k/\nu)^{1/2}x$. 52
4.1 An illustration of the unsteady oblique stagnation-point flow at an instant in time. Away from the wall, the gradient of the dividing streamline, $\psi = 0$, is given by $M = -2ak/\widehat{\zeta}$. As discussed in chapter 3, the viscosity in the region close to the wall affects the gradient of the dividing streamline. 64
4.2 The range of the far-field dividing streamline when (a) $\Delta < 1$ and (b) $\Delta > 1$. Both cases are for $\widehat{\beta} = 0$. 66
4.3 The function $a(t) = 1 + \Delta\cos\omega t$ for $\omega = 1$ and $\Delta = 0.85$ (solid line), $\Delta = 1.2$ (dotted lines) and $\Delta = 1.5$ (dashed lines), illustrating when $\Delta > 1$, the function $a(t)$ develops zeros. . . . 67
4.4 The streamlines in the far-field plotted for $\Delta = 1.5$, and $\widehat{\beta} = 1$, with $\nu = k = \omega = \widehat{\zeta} = 1$ for (a) $t = 2$, (b) $t = 2.25$, (c) $t = 2.35$, (d) $t = 2.8$. This illustrates the gradient of the dividing streamline changing sign from negative in (a) and (b) to positive in (c) and (d), which corresponds to t increasing through the zero at $\tau \approx 2.3$. 68
4.5 The initial velocity profile $\psi_{P\eta}(\eta, \tau)$, given in (4.48), for $\sigma = 0.5$ and $\Delta = 0.5$, initiated at different starting times, from left to right, $\tau = 0.0001$, $\tau = 0.001$ and $\tau = 0.01$. 76
4.6 The initial velocity profile for $\psi_O(\eta, \tau)$ for $\widehat{\beta} = 1$ and $\sigma = 0.5$, initiated at different starting times, from top to bottom, $\tau = 0.01$, $\tau = 0.001$ and $\tau = 0.0001$. 78

4.7 (a) The primary velocity profile for $\sigma = 0.5$ and $\Delta = 0.1, 0.5, 0.8$ at $\tau = 1$. (b) The oblique velocity profile for $\widehat{\beta} = 0$, $\sigma = 0.5$ and $\Delta = 0.1, 0.5, 0.8$ at $\tau = 1$. (c) A close up of the oblique velocity profile for the same parameters at $\tau = 1$. In each case $\Delta = 0.1$ is represented by the solid line, $\Delta = 0.5$, the dotted lines and $\Delta = 0.1$, the dashed lines. 79

4.8 (a) The oblique velocity profile for $\sigma = 0.5$, $\Delta = 0.5$ at $\tau = 1$, where $b_O = 0$ and, from left to right, $b_M = 1.5, 1.02, 0$. (b) The oblique velocity profile for $\sigma = 0.5$, $\Delta = 0.5$ at $\tau = 1$, where $b_M = 0$ and, from left to right, $b_O = 3, 2.28, 0$. 80

4.9 (a) The primary wall shear component $\psi_{P_{\eta\eta}}(0, \tau)$ for $\sigma = 0.5$ and $\Delta < \Delta_c$ over a single time period, for $\Delta = 0.5$ (solid line), $\Delta = 0.8$ (dotted lines) and $\Delta = 1$ (dashed lines). (b) The primary wall shear component $\psi_{P_{\eta\eta}}(0, \tau)$ for $\sigma = 0.5$ and $\Delta > \Delta_c$, where $\Delta = 2$ (solid line), $\Delta = 4$ (dotted lines) and $\Delta = 6$ (dashed lines). The dots represent where the numerics break down. 82

4.10 (a) The oblique wall shear component $\psi_{O_\eta}(0, \tau)$ illustrated for $\widehat{\beta} = 0$, $\sigma = 0.5$ and $\Delta < \Delta_c$ over a single time period, for $\Delta = 0.5$ (solid line), $\Delta = 0.8$ (dotted lines) and $\Delta = 1$ (dashed lines). (b) The oblique wall shear component $\psi_{O_\eta}(0, \tau)$ for $\widehat{\beta} = 0$, $\sigma = 0.5$ and $\Delta > \Delta_c$, where $\Delta = 2$ (the solid line), $\Delta = 4$ (dotted lines) and $\Delta = 6$ (dashed lines). 83

4.11 (a) The primary velocity profile, illustrating a minimum as $\tau \to \tau_s$ for $\sigma = 0.5$ and $\Delta = 2$ at $\tau = 3.37$. (b) The oblique velocity profile showing a maximum as $\tau \to \tau_s$, where $\sigma = 0.5$ and $\Delta = 2$ at $\tau = 3.37$. For these given parameters, the finite-time singularity is numerically calculated and given by $\tau_s = 3.396$. 84

4.12 (a) The primary function, $\psi^{-1}_{q_{min}}(\eta_{min}, \tau)$ plotted against τ as $\tau \to \tau_s^-$ for $\Delta = 2$ and $\sigma = 0.5$. (b) A close-up of the primary function, $\psi^{-1}_{q_{min}}(\eta_{min}, \tau)$ plotted against τ as $\tau \to \tau_s^-$ for $\Delta = 2$ and $\sigma = 0.5$. (c) The oblique function, $\psi^{-1}_{O_{max}}(\eta_{max}, \tau)$ plotted against τ as $\tau \to \tau_s^-$ for $\widehat{\beta} = 0$, $\Delta = 2$ and $\sigma = 0.5$. 87

4.13 The time singularities calculated for fixed values of Δ. Lines of constant Δ are plotted, from left to right, $\Delta = 1.5, 2, 3, 4, 5, 6, 7$. 88

4.14 The leading order asymptotic primary wall shear component $\psi_{P_{\eta\eta}}(0, \tau)$ plotted against τ for $\Delta = 0.5$ (solid line), $\Delta = 1$ (dotted lines) and $\Delta = 2$ (dashed lines). When $\Delta > 1$, it is observed that the primary wall shear component breaks down. 90

4.15 (a) The primary function $Q^{-1}_{min}(Y_{min}, T)$ plotted against T as $T \to T_s^+$ for $\Delta = 2$. (b) The oblique function $O^{-1}_{max}(Y_{max}, T)$ plotted against T as $T \to T_s^+$, for $\widehat{\beta} = 0$. Both of these figures illustrate a linear relationship as $T \to T_s^+$. 93

4.16 The primary function $Q^{-1}_{min}(Y_{min}, T)$ plotted against T as $T \to T_s^+$, confirming the accuracy of the finite-time singularity $T_s = -1.557$. The solid line represents a spacial and temporal step size of 0.001. The crosses represent a spacial step size of $h = 0.001$ and a temporal step size of $dt = 0.0005$. The circles represent a spacial step size of $h = 0.0005$ and a temporal step size of $dt = 0.001$. 94

4.17 The finite-time singularity approximation (4.81), represented by the solid line, plotted alongside some numerical results from section 4.3 for $\Delta = 2$, represented by the crosses. Good agreement can be seen between the numerical results and the asymptotic solution for $\sigma \sim 1$. 95

4.18 (a) The primary wall shear component $\psi_{P_{\eta\eta}}(0, \tau)$ and (b) the oblique wall shear component $\psi_{O_\eta}(0, \tau)$, both for $\widehat{\beta}(\tau) = 0$, $\sigma = 1$ and $\Delta = 0.5$ (solid line), $\Delta = 0.85$ (dashed lines) and $\Delta = 1.2$ (dotted lines). 98

4.19 (a) The attachment point x_0 over a single time period for $\sigma = 1$ and $\Delta = 0.5$. (b) The attachment point x_0 for $\sigma = 1$ and $\Delta = 1.2$. (c) The gradient of the dividing streamline at the wall over a single time period for $\sigma = 1$ and $\Delta = 0.5$. (d) The gradient of the dividing streamline at the wall for $\sigma = 1$ and $\Delta = 1.2$. In each case, $\widehat{\zeta} = \nu = k = 1$. 99

4.20 The instantaneous streamlines for $\widehat{\zeta} = \nu = k = 1$, $\widehat{\beta} = 0$, $\sigma = 1$ and $\Delta = 0.5$ over a period of 2π in equally spaced intervals of $\pi/4$, beginning at 2π. 100

4.21 (a) The primary function $\psi_P(\eta, \tau)$ for $\sigma = 1$, $\Delta = 1.2$ at $\tau = 11\pi/4$, illustrating the two stagnation points at $\eta = 0$ and $\eta = \eta_1^*$, which are represented by the solid dots. (b) The corresponding dividing streamline x_d. At $\tau = 11\pi/4$, the vertical distance of the horizontal streamline from the wall is $\eta_1^* = 2.475$, the horizontal position of the stagnation point is $X_1 = -21.776$ and the attachment point is $x_0 = 4.04$ where $\widehat{\zeta} = k = 1$. 102

4.22 The instantaneous streamlines for $\widehat{\zeta} = \nu = k = 1$, $\widehat{\beta} = 0$, $\sigma = 1$ and $\Delta = 1.2$ over a period of 2π in equally spaced intervals of $\pi/4$, beginning at 2π. 103

4.23 (a) The vertical location of the horizontal streamline for $\sigma = 1$ and $\Delta = 0.8$ (bottom curve), $\Delta = 0.85$ (middle curve) and $\Delta = 0.95$ (top curve). (b) The vertical location of the horizontal streamline for $\sigma = 1$ and $\Delta = 1.2$ 104

4.24 The instantaneous streamlines for $\Delta = 0.95$ and $\sigma = 1$ at $\tau = 9.66$, illustrating a triple-layered structure, where $\nu = k = \widehat{\zeta} = 1$.105

4.25 The instantaneous streamlines as $\tau \to \tau_s$ at intervals of $\tau = \pi/2$, for $\widehat{\beta} = 0$, $\Delta = 20$ and $\sigma = 40$, beginning at $\tau = \pi/2$, where $\widehat{\zeta} = \nu = k = 1$. 107

4.26 The streamlines as $\tau \to \tau_s$ at intervals of $\tau = \pi/2$ beginning at $\tau = 9\pi/2$ for $\widehat{\beta} = 0$, $\Delta = 20$ and $\sigma = 40$, where $\widehat{\zeta} = \nu = k = 1$. This figure is a continuation of figure 4.25. 108

4.27 The streamlines as $\tau \to \tau_s^-$, for $\sigma = 40$ and $\Delta = 20$ at (a) $\tau = 18.0$, (b) $\tau = 18.1$, (c) $\tau = 18.2$, (d) $\tau = 18.3$, where $\tau_s = 18.443$ and $\widehat{\zeta} = \nu = k = 1$. This figure is a continuation of figure 4.26. 108

4.28 The vertical location of the horizontal streamlines for $\sigma = 40$ and $\Delta = 20$. 109

4.29 (a) The primary velocity profile as $\tau \to \tau_s$ for $\sigma = 40$ and $\Delta = 20$, working from right to left at $\tau = 18.0, 18.1, 18.2, 18.3$. (b) The oblique velocity profile for $\widehat{\beta} = 0$ at the same times approaching the finite-time singularity $\tau_s = 18.443$. 110

4.30 (a) The oblique wall shear stress component $\psi_{O_\eta}(0, \tau)$ for $\sigma = 1$, $\Delta = 0.5$, $b_O = 0$ and $b_M = 0$ (solid line), $b_M = 0.94$ (dotted lines) and $b_M = 1.54$ (dashed lines). (b) The oblique wall shear stress component $\psi_{O_\eta}(0, \tau)$ for $\sigma = 1$, $\Delta = 0.5$, $b_M = 0$ and $b_O = 0$ (solid line), $b_O = 0.9$ (dotted lines) and $b_O = 1.5$ (dashed lines). 111

4.31 (a) The oblique wall shear stress component $\psi_{O_\eta}(0, \tau)$ for $\sigma = 1$, $\Delta = 1.2$, $b_O = 0$ and $b_M = 0$ (solid line), $b_M = 0.78$, (dotted lines) and $b_M = 1.5$ (dashed lines). (b) The oblique wall shear stress component $\psi_{O_\eta}(0, \tau)$ for $\sigma = 1$, $\Delta = 1.2$, $b_M = 0$ and $b_O = 0$ (solid line), $b_O = 0.77$ (dotted lines) and $b_O = 1.5$ (dashed lines). 111

4.32 (a) The attachment point x_0 for $\sigma = 1$, $\Delta = 0.5$, $b_O = 0$ and, from bottom to top, $b_M = 0, 0.94, 1.54$, where $\widehat{\zeta} = \nu = k = 1$. (b) The attachment point for $\sigma = 1$, $\Delta = 0.5$, $b_M = 0$ and $b_O = 0$ (solid line), $b_O = 0.9$ (dotted line) and $b_O = 1.5$ (dashed lines). (c) A point in the far-field x_N for $\sigma = 1$, $\Delta = 0.5$, $b_O = 0$ and from bottom to top $b_M = 0, 0.94, 1.54$. (d) A point in the far-field x_N for $\sigma = 1$, $\Delta = 0.5$, $b_M = 0$ and $b_O = 0$ (solid line), $b_O = 0.9$ (dotted line) and $b_O = 1.5$ (dashed lines). 112

5.1 (a) The oblique function $h_1(\zeta)$ for, working from left to right, $\beta_0^M = 4, 2, 0, -2, -4$ and $a_0 = 1$. (b) The oblique function $h_2(\zeta)$ for, working from left to right, $\beta_0^M = 4, 2, 0, -2, -4$, $a_0 = 1$ and $a_1 = -0.5$. 128

5.2 The numerically calculated non-trivial zero ξ_0, in the Stokes layer, which is represented by the solid line, alongside the asymptotic predictions of the behaviour of the zeros ξ_0, close to $\pi/4$ and $\pi/2$, which are represented by the dotted lines. . . 132

5.3 The asymptotic prediction of the behaviour of the zeros ζ_0, alongside the numerically calculated zeros, which are represented by the crosses, showing excellent agreement. 135

5.4 The constant d given in (5.84) plotted against a_0, illustrating for all values of a_0, d is positive. The upper branch of the curve asymptotes to $a_0 = 0.75$. 136

5.5 The orthogonal steady streamlines in the steady streaming layer for (a) $a_0 = 0.6017$ and (b) $a_0 = 1$. In both cases $\nu = k = 1$ and the solid dots represent the stagnation points. . . . 138

5.6 The mean components of the steady streaming layer illustrated for $a_0 = 1$ and (a) $\beta_0^M = 1.2$, (b) $\beta_0^M = 1.4442$, (c) $\beta_0^M = 1.5$, (d) $\beta_0^M = 1.582$, (e) $\beta_0^M = 1.8$. In each case $\widehat{\zeta} = \nu = k = 1$. . . 139

5.7 The leading order mean component of the time-dependent function, β_0^M plotted against x^*, the horizontal position of the stagnation-point for $\widehat{\zeta} = \nu = k = a_0 = 1$. 140

5.8 (a) The streamlines that correspond to the streamlines of steady components in the steady streaming layer for $a_0 = 1$ and $\beta_0^M = 1.2$ with $\widehat{\zeta} = \nu = k = 1$. (b) The particle paths for the same parameters where the oscillation amplitude is $\Omega = 100$. . 143

5.9 The constant $\frac{c}{\beta_0^M}$, given in (5.123), plotted against a_0. The lower branch of the curve asymptotes to $a_0 = 0.75$. 147

A.1 The numerical results for the subsidiary problem illustrating a linear relationship between $\widehat{F}_0''(0)$ and ϵ. 155

A.2 The region 1, 2 and 3 asymptotic solutions, represented by the solid line, the dotted lines and the dashed lines for $\epsilon = 0.001$, where $\delta = (2\epsilon)^{1/2}$, alongside the numerical solution for the same parameter, represented by the crosses. 158

A.3 An illustration of the primary and subsidiary regions. 158

Chapter 1

Introduction

Stagnation-point flows occur when a fluid approaches the impermeable boundary of a body, for example, on an aircraft wing or on an oscillating cylinder immersed in fluid. These flows have a stagnation-point present in the fluid, about which the streamlines locally resemble those about a saddle point. Another example of particular interest, is blood flow at a junction within an artery. In this thesis, we will be exploring stagnation points, focussing on two-dimensional flows, in which the flow approaches a body either obliquely or orthogonally.

An exact solution of the Navier-Stokes equations, which describes the two-dimensional stagnation-point flow towards a fixed plane wall, was first examined by Hiemenz (1911). As the flow approaches a rigid wall, it divides in two and creates a stagnation point at the origin. Due to the no-slip condition not being satisfied at the wall, a similarity solution is introduced, which enables the solution to be obtained everywhere in the fluid, matching the velocity on the wall to that of the far-field.

Riley (1965) and Stuart (1966) were among many to consider a time dependent stagnation-point flow travelling orthogonally towards a fixed wall. The far-field streamfunction was considered to be purely oscillatory and dependent upon a relative amplitude parameter and a dimensionless frequency parameter. Similar to that of the Hiemenz problem, the far-field flow does not satisfy the no-slip condition on the wall, so it is necessary to seek a

solution in the form of a similarity solution close to the wall. In the large frequency limit, the solution exhibits a double layer structure. A Stokes layer is present close to the wall, where the unsteady time-dependent components are balanced by the viscous terms in the Navier-Stokes equations. Due to a mean velocity component persisting to the top of this layer, the Stokes layer is unable to match to the far-field flow. To allow for the necessary matching to occur, the introduction of a steady streaming layer between the Stokes layer and far-field flow is required. The thickness of the steady streaming layer is on the order of the dimensionless frequency parameter, times the thickness of the Stokes layer.

Riley and Vasantha (1989) considered this problem, where the free stream in the far-field is purely oscillatory and solved it numerically to find that for any value of the dimensionless frequency parameter, the equations break down at a finite-time singularity. They attributed this to a horizontal velocity moving towards the origin, causing the fluid to erupt from the boundary layer, which in turn causes the flow equations to break down.

The inclusion of a mean flow component at infinity was considered by Pedley (1972) and Grosch and Salwen (1982), where the oscillatory component is small compared to the mean component and the frequency of the oscillations is large. As above, there exists a Stokes layer nearest the wall, which matches to a layer whose thickness is on the order of the square root of the dimensionless frequency parameter, times the thickness of the Stokes layer. The size of this layer is considerably smaller than the problem discussed by Riley (1965) discussed above, where a mean flow is absent at infinity.

Merchant and Davis (1989) summarised the work of Pedley (1972) and Grosch and Salwen (1982), extending it to consider the case where the dimensionless frequency parameter is large and the oscillatory component is much larger than the mean component. If the relative amplitude parameter is large enough, the flow will be allowed to reverse over some portion of the time period. This case is comparable to the problem discussed by Riley (1965), where the far-field flow is purely oscillatory, thus, the flow structure

is similar. Merchant and Davis investigated the case where the two outer layers coincided and found that for a fixed dimensionless frequency, there exists a critical amplitude, above which, no solutions occur.

Blyth and Hall (2003) considered this problem for a large dimensionless frequency and when the relative amplitude parameter is at the critical value. They concluded that for a fixed frequency, when the critical amplitude is exceeded, the solutions break down at a finite-time singularity. Additionally, they examined the behaviour of the solutions close to the break-down time. Blyth and Hall also discussed this problem in the small frequency limit and found that the leading order solution is quasi-steady. When the relative amplitude parameter is large enough, solutions again break down at a finite-time singularity.

All of the studies mentioned above have been stagnation-point flows travelling towards fixed walls. Next, we consider problems in which stagnation-point flows approach oscillatory walls. By simply changing the frame of reference, this problem can be considered equivalent to the case where the far-field flow oscillates horizontally and travels towards a fixed wall, where only the pressure term is affected.

Rott (1956) examined the case where the plate performed periodic oscillations in its own plane, with a steady orthogonal flow far from the plate. As before, a similarity solution is introduced comprising two components: a steady orthogonal function and an oscillatory function. The problem was discussed in terms of the two limiting cases of small and large frequency. Glauert (1956) also considered this problem using series methods for solving the large and small frequency cases. An application of this is a cylinder which performs horizontal oscillations in a fluid. Watson (1959) generalised Rott's and Glauert's work by allowing the periodic oscillations to be replaced by an arbitrary horizontal motion. Watson also discussed the problem when the fluid is instantly started from rest.

Hazel and Pedley (1998), considered an unsteady orthogonal oscillating two-dimensional stagnation-point flow approaching an oscillating wall. In

comparison to the earlier work on oscillatory walls described above, they considered the problem in a frame of reference where the stagnation point is fixed at the origin. In the far-field, the flow is made up of an unsteady stagnation-point flow containing both a mean and an oscillatory component, which has been discussed above. Added to this is a periodic horizontal oscillation, with the same dimensionless frequency as the orthogonal stagnation-point flow. This flow approaches a wall, which oscillates with the same dimensionless frequency as the far-field. They considered the problem where the mean component is dominant over the oscillatory component and in the large frequency limit, the solution exhibited a double layer structure at the wall which was previously addressed by Pedley (1972), among others. Hazel and Pedley considered this problem, when the relative amplitude parameter was chosen such that the flow cannot reverse. The wall shear stress was obtained and the mean wall shear stress was discussed for all the limiting cases. For the large frequency case, the oscillating wall was found to have no effect on the mean wall shear stress and is only reliant upon the orthogonal flow. They attributed this to the viscous forces within the Stokes layer counteracting any effect from the oscillating wall.

This configuration can represent a model of the reattachment flow at an end-to-side anastomosis. These are often used to bypass a blockage within an artery, where the graft artery bypasses the blockage and rejoins the main artery beyond the blockage. At the point of reattachment, the end of the graft artery joins to the side of the main artery. This creates a highly complex three-dimensional stagnation-point flow opposite the point of reattachment, which is illustrated in figure 1.1

A full study of the flow in the region of the graft is found in the review article by Loth et al. (2008), with further references included and here we provide a brief overview. There are three different formations of anastomoses, end-to-side, end-to-end and side-to-side. Within the end-to-side configuration, there are two different types of grafts. The first is an arterial bypass graft, which is a bypass of a blockage in an artery; in this case the flow is

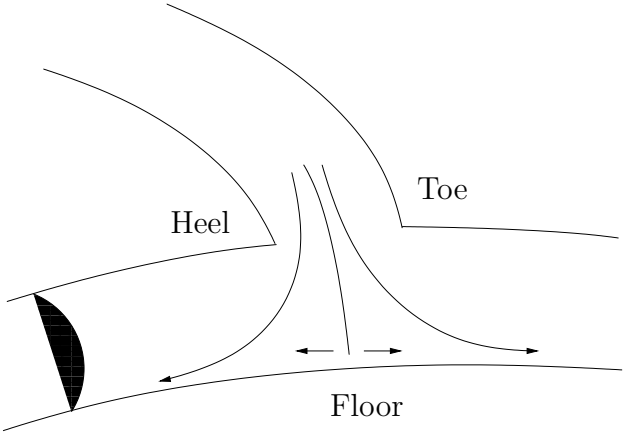

Figure 1.1: An illustration of an arterial end-to-side anastomosis.

laminar. The second is an arteriovenous graft, which is the join between an artery and a vein with the flow being turbulent. In this thesis we consider only the first configuration.

The flow in the region of the arterial end-to-side anastomosis is of interest as the local haemodynamics are significant to the longevity of the graft. A common cause of graft failure is intimal hyperplasia, which is the thickening of the tunica intima, the inner layer of the artery. Intimal hyperplasia occurs at three areas: the heel, toe and floor of the graft. At the heal and toe, thickening is attributed to the healing process around the graft join. However, the thickening of the artery on the floor opposite the graft is associated with low wall shear stress. Hence, in our analysis presented in later chapters, attention is drawn to the effect of the flow parameters on the wall shear stress.

In order to model this problem as an arterial end-to-side anastomosis, certain assumptions were made by Hazel and Pedley (1998). Near the stagnation point, the wall is considered to be flat and the blood is modelled as a Newtonian fluid. Also, the pulsatile nature of the blood is taken to be sinusoidal and the authors consider this problem in both two and three dimensions. However, in the subsequent sections we focus our attention purely on the two-dimensional problem.

Having discussed the two-dimensional steady and unsteady orthogonal stagnation-point flows, we turn our attention to considering the case where

the dividing streamline meets the wall obliquely. This was first discussed by Stuart (1959), where the flow comprises a steady orthogonal stagnation-point flow, a shear flow with constant vorticity and a uniform stream. Like that of the orthogonal problems, the flow can be represented in terms of a streamfunction. As this streamfunction in the far-field does not match to the velocity on the wall, a similarity solution is established, comprising a Hiemenz function and an integral of the shear flow function. Later, Tamada (1979) discussed this problem with reference to jets impinging a wall obliquely. Dorrepaal (1986) also considered the oblique stagnation-point flow with a different uniform stream at infinity, but he still reported comparable results. The behaviour of the dividing streamline close to the wall was also investigated by considering the series expansions of the Hiemenz and shear functions in the normal variable. It was observed that, due to the viscous forces close to the wall, the dividing streamline bends and meets the wall at an angle closer to the normal.

Much later, Drazin and Riley (2006) generalised the previous work, to include a free parameter at infinity, which corresponds to the strength of the uniform stream in the far-field. Upon increasing the free parameter, the shear velocity profile exhibits a region of flow reversal close to the wall. They concluded their analysis with a discussion of the gradient of the dividing streamline close to the wall, with similar conclusions to that of Dorrepaal (1986). In particular, it was shown that the ratio of the dividing streamline gradient close to the wall, to that of the gradient in the far-field is independent of the vorticity. Tooke and Blyth (2008) extended the work of Drazin and Riley by considering what effect the uniform stream has on the streamlines.

Having summarised the previous work in this field, we outline the analysis which will follow in the subsequent chapters. We begin our analysis on stagnation-point flows in chapter 2, by considering the two-dimensional stagnation-point flow travelling towards an oscillating wall, as previously discussed by Hazel and Pedley (1998) above. They considered solutions for a

large dimensionless frequency parameter and chose a relative amplitude parameter which does not allow for flow reversal. We extend their analysis by allowing for flow reversal, while still considering the large frequency limit. By expressing the problem in the form of a similarity solution, it can be represented by two coupled equations. The first represents the unsteady orthogonal flow travelling towards a flat wall and the seconds represents the oscillatory components of the flow. For solely the orthogonal problem, the solution breaks down when, for a fixed dimensionless frequency, the critical relative amplitude is exceeded. Therefore, we consider the same parameter range and solve the oscillatory problem. Initially, we consider the orthogonal problem, which exhibits a double layer structure at the wall, with a Stokes layer close to the wall matching to a steady streaming layer, which in turn matches to the far-field flow. As the oscillatory equation is coupled with that of the orthogonal, it has the same structure. Although the orthogonal equation has been solved previously, a detailed account is included as the methods and results will form a basis for the subsequent chapters. The oscillatory equation is then solved using similar techniques. The wall shear stress is obtained and the effect of the oscillatory components on the mean wall shear stress is discussed for large frequency.

In chapter 3, a steady oblique stagnation-point flow is considered, where the problem comprises an orthogonal stagnation-point flow, an oblique shear flow with constant vorticity and a uniform stream. Previous analyses of oblique stagnation-point flow at a plane wall are discussed and unified with reference to a free parameter, which can be thought of as altering the strength of the uniform stream in the far-field. As the strength of the uniform stream is increased, the oblique component exhibits a region of flow reversal close to the wall. We consider the effect of increasing the strength of the uniform stream on the streamline pattern. We note that these results were given in Tooke and Blyth (2008).

In the latter half of the chapter, a general form of the oblique stagnation-point flow is obtained, where the flow consists of a Hiemenz flow and an

oblique component. A solution is sought, using a typical boundary layer approach. In the far-field, an inviscid solution is obtained, which satisfies the vorticity-transport equation. Close to the wall, viscosity is no longer negligible and a similarity solution is used. Matching these together, it is observed that no matching region is necessary and the solutions in the far-field and close to the wall match directly together.

Having explored the steady oblique stagnation-point flow, in chapter 4 we discuss the effect of the time-dependent terms. We choose the orthogonal stagnation-point flow component to be time-dependent, with a mean and an oscillatory component dependent upon a relative amplitude and a dimensionless frequency parameter, approaching a fixed wall. To consider an unsteady oblique flow, we add to this a shear flow with constant vorticity and time-dependent horizontal velocity component. We note that the shear flow is unable to be time-dependent, as the vorticity-transport equation is not satisfied. A similarity solution is obtained, which is simply a time dependent version of one previously stated by Stuart (1959) in chapter 3. Using this approach, two coupled equations (denoted the orthogonal and oblique equations) are obtained and solved using a Crank-Nicolson finite-difference technique. For certain values of the relative amplitude and the dimensionless frequency parameter, a horizontal streamline appears in the flow over some period of the cycle, creating a double-layered flow. In some cases, two horizontal streamlines are present and the flow becomes triple-layered. The instantaneous streamlines are considered numerically with specific attention given to those time intervals in which the flow is multi-layered.

As discussed in chapter 2, for a fixed value of the frequency, there exists a critical amplitude, above which solutions break down at a finite-time singularity. The behaviour of both the orthogonal equation, previously solved by Blyth and Hall (2003) and the oblique equation close to the finite-time singularity are discussed. Additionally, the orthogonal and oblique equations are considered in the small frequency limit.

Chapter 5 continues directly on from chapter 4, by performing a large

frequency analysis in the parameter range discussed in chapter 2. In this parameter range, the orthogonal problem exhibits a double layer structure at the wall. As the oblique equation is coupled with the orthogonal equation, the structure of the oblique solution is expected to be the same and the results from the orthogonal problem are utilised. The instantaneous streamlines are considered in both the Stokes and steady streaming layers, with comparisons being drawn with the analysis of chapter 4, where the flow structure becomes multi-layered in some time intervals over the cycle. A particle path analysis is performed in the steady streaming layer using the method of multiple scales. Concluding the chapter, is a discussion on the mean wall shear stress and the magnitude of the time-dependent horizontal velocity component.

Finally, chapter 6 presents the main conclusions from each chapter.

Chapter 2

Unsteady orthogonal stagnation-point flow

2.1 Introduction

In this chapter, a two-dimensional unsteady stagnation-point flow travelling towards an oscillating wall is discussed. This problem has previously been considered by Hazel and Pedley (1998), as a simplied model of an end-to-side anastomosis located at a bypass graft in an artery, which is seen in figure 1.1. The problem in the far-field comprises of an unsteady Hiemenz flow containing both a mean component and an oscillatory component dependent upon a relative amplitude parameter and a dimensionless frequency parameter. Added to this is a horizontal oscillatory velocity. This flow approaches a wall that is oscillating with the same frequency as that of the horizontal velocity in the far-field. The problem is discussed in the frame of reference where the stagnation-point is located at the origin. As the no-slip condition is not satisfied on the wall, a similarity solution is introduced. This is made up of two components: an unsteady orthogonal stagnation-point flow component and an oscillatory component, which is an exact solution of the Navier-Stokes equations. Using this similarity solution, the problem can be described in terms of two coupled equations, an orthogonal stagnation-point equation and an oscillatory equation.

Hazel and Pedley (1998) considered this problem for large frequency, but restricted the amplitude of oscillations to prevent flow reversal occurring. As discussed in the introduction, the orthogonal equation has been addressed previously. Merchant and Davis (1989) found that for large frequency, there exists a critical amplitude dependent upon the frequency, above which solutions do not exist. Therefore, in this chapter, we will seek solutions to the problem described by Hazel and Pedley, but consider solutions close to the critical amplitude found by Merchant and Davis, for large frequency.

We begin by considering the orthogonal equation, which exhibits a double layer structure with a Stokes layer at the wall and a steady streaming layer matching the Stokes layer to the far-field flow. As the oscillatory equation is coupled with the orthogonal equation, we expect there to be a similar structure present. One of the motivations of Hazel and Pedley's analysis was to consider what effect the oscillatory components have on the mean wall shear stress. We will also consider the wall shear stress and consider what effect the oscillatory components have on the mean wall shear stress when the relative amplitude parameter is larger and allows for flow reversal to occur.

2.2 Problem formulation

In this section, a two-dimensional unsteady stagnation-point flow with a horizontal velocity in the far-field travelling towards an oscillating wall is described. We begin by mentioning the well-documented Hiemenz stagnation-point flow travelling towards a flat fixed plate at $y = 0$, which can be found, for example, in Batchelor (2000). The flow in the far-field can be expressed in terms of the velocity components $u = kx$ and $v = -ky$, where x and y are the coordinates parallel and normal to the wall. The velocity components (u, v) are in the (x, y) directions respectively and k is the strength of the flow. As the flow is two-dimensional and incompressible, it can be expressed in terms of the streamfunction $\psi = kxy$, where $u = \psi_y$ and $v = -\psi_x$.

Pedley (1972) and Grosch and Salwen (1982) were some of those to address an unsteady version of the Hiemenz flow. The streamfunction is expressed as $\psi = a(t)kxy$, where $a(t)$ consists of a mean component and an oscillatory component. Riley and Vasantha (1989) ascertained that when $a(t)$ is purely oscillatory, solutions break down at a finite-time singularity for any given frequency. Hazel and Pedley (1998) extended this analysis by considering an oscillating unsteady stagnation-point flow, which travels towards an oscillating wall.

We begin by describing the oscillating unsteady stagnation-point flow travelling towards a fixed wall, as this is the approach we take in latter chapters. However, we show that by a simple change of frame of reference, this problem is equivalent to the flow travelling towards an oscillating wall, as discussed by Hazel and Pedley (1998). We then proceed by solving the problem in this frame.

The velocity components are expressed as

$$u^*(x^*, y^*, t^*) = a(t)k\left(x^* + \frac{U_S \sin(\omega t^* - \phi)}{\omega}\right), \tag{2.1}$$

$$v^*(x^*, y^*, t^*) = -a(t)ky^*, \tag{2.2}$$

as $y^* \to \infty$, where k is the strength of the flow at infinity, ω is the frequency of the oscillations, U_S is the speed of the wall and ϕ is an arbitrary phase difference. At the wall, the velocity components are given by

$$u^* = 0, \quad v^* = 0 \quad \text{on} \quad y^* = 0, \tag{2.3}$$

where the stagnation point is located at $x^* = -U_S \sin(\omega t^* - \phi)/\omega$. The two-dimensional Navier-Stokes equations in this frame are given by

$$u^*_{t^*} + u^* u^*_{x^*} + v^* u^*_{y^*} = -\frac{p^*_{x^*}}{\rho} + \nu(u^*_{x^*x^*} + u^*_{y^*y^*}), \tag{2.4}$$

$$v^*_{t^*} + u^* v^*_{x^*} + v^* v^*_{y^*} = -\frac{p^*_{y^*}}{\rho} + \nu(v^*_{x^*x^*} + v^*_{y^*y^*}), \tag{2.5}$$

$$u^*_{x^*} + v^*_{y^*} = 0, \tag{2.6}$$

with the parameters, kinematic viscosity: ν, pressure: p and density: ρ. To perform this change of frame of reference to one where the wall is oscillating,

we write $x = x^* + U_S \sin(\omega t^* - \phi)/\omega$ and $u = u^* + U_S \cos(\omega t^* - \phi)$ with $t^* = t$. We note there is no change to the vertical length and velocity scale, $y^* = y$ and $v^* = v$. Therefore, we write

$$\frac{\partial}{\partial x^*} = \frac{\partial}{\partial x}, \qquad \frac{\partial}{\partial y^*} = \frac{\partial}{\partial y}, \qquad \frac{\partial}{\partial t^*} = \frac{\partial}{\partial t} + U_S \cos(\omega t^* - \phi)\frac{\partial}{\partial x}, \tag{2.7}$$

and (2.4) is rewritten as

$$u_t + uu_x + vu_y = -\frac{p_x}{\rho} + \nu(u_{xx} + u_{yy}), \tag{2.8}$$

where $p = p^* - x\rho\omega U_s \sin(\omega t - \phi)$. We note that the y-momentum equation and the continuity equation are unaffected by this change of frame of reference. The velocity profiles are now given by

$$u = a(t)kx + U_S \cos(\omega t - \phi), \tag{2.9}$$

$$v = -a(t)ky, \tag{2.10}$$

as $y \to \infty$ and the velocity on the wall is given by

$$u = U_S \cos(\omega t - \phi), \quad v = 0 \quad \text{on} \quad y = 0. \tag{2.11}$$

Therefore, these velocity components now describe an unsteady stagnation-point flow with a horizontal velocity component in the far-field travelling towards an oscillating wall and is illustrated in figure 2.1. We note that the wall is oscillating with the same frequency, ω, as that of the horizontal component in far-field and the time-dependent function $a(t) = 1 + \Delta \cos \omega t$, where Δ is the amplitude and ω is the frequency of the oscillations at infinity.

As the velocity components (2.9) - (2.11) are two-dimensional and incompressible, they can be expressed in terms of the streamfunction $\psi(x, y, t)$, to give

$$\psi = k(1 + \Delta \cos \tau)xy + U_S \cos(\omega t - \phi)y \quad \text{as} \quad y \to \infty, \tag{2.12}$$

with the boundary conditions on the wall

$$\psi_y(x, y, t) = U_s \cos(\omega t - \phi), \quad \psi_x(x, y, t) = 0 \quad \text{on} \quad y = 0. \tag{2.13}$$

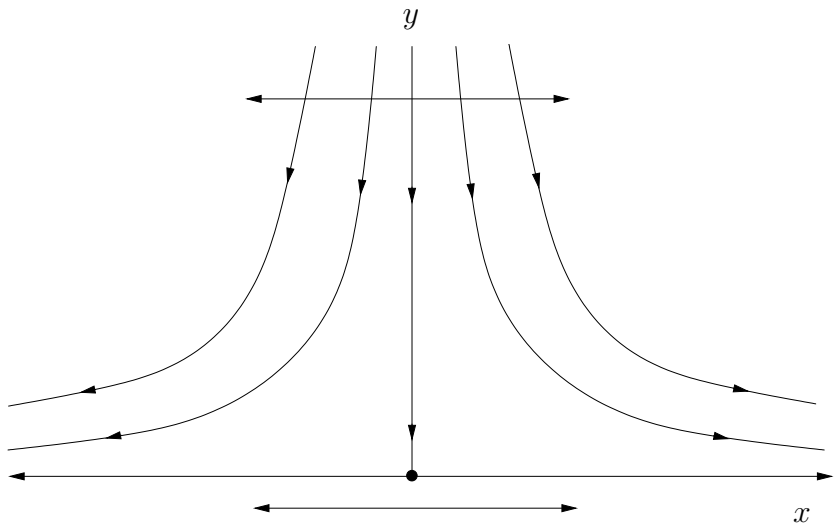

Figure 2.1: An illustration of the unsteady oscillating stagnation-point flow approaching an oscillating wall, where the stagnation point is represented by the solid dot and is fixed at the origin.

The Navier-Stokes equations are also rewritten in terms of the streamfunction, to give

$$\psi_{yt} + \psi_y\psi_{xy} - \psi_x\psi_{yy} = -\frac{p_x}{\rho} + \nu(\psi_{xxy} + \psi_{yyy}), \tag{2.14}$$

$$-\psi_{xt} - \psi_y\psi_{xx} + \psi_x\psi_{xy} = -\frac{p_y}{\rho} - \nu(\psi_{xxx} + \psi_{xyy}), \tag{2.15}$$

where $u = \psi_y$ and $v = -\psi_x$, with the incompressibility condition automatically satisfied.

As the far-field streamfunction (2.12) does not satisfy the no-slip condition, a similarity solution is sought close to the wall, which matches the flow at the wall to that of the far-field. Due to the form of (2.12), the streamfunction is expressed as

$$\psi(x, y, t) = (\nu k)^{1/2} x\psi_P(\eta, \tau) + U_S \left(\frac{\nu}{k}\right)^{1/2} \psi_S(\eta, \tau), \tag{2.16}$$

with $\eta = (k/\nu)^{1/2}\, y$ and $\tau = \omega t$. The first term in (2.16) represents the orthogonal stagnation-point flow and is denoted $\psi_P(\eta, \tau)$, the primary flow. The second term corresponds to the oscillating wall, denoted $\psi_S(\eta, \tau)$, the subsidiary flow. Matching the far-field streamfunction (2.12) to the similarity solution (2.16), we find $\psi_{P\eta}(\eta, \tau) \to 1 + \Delta\cos\tau$ and $\psi_{S\eta}(\eta, \tau) \to \cos(\tau - \phi)$ as $\eta \to \infty$. Therefore, upon substituting streamfunction (2.16) into the x-momentum equation (2.14) and matching to the far-field, to eliminate the

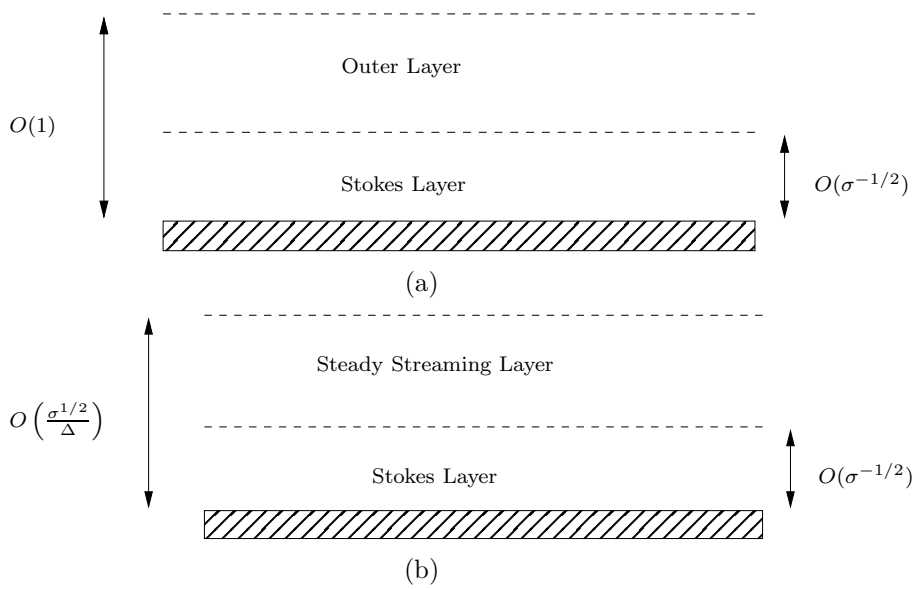

Figure 2.2: (a) The asymptotic structure valid for high frequency, σ, and the oscillation amplitude, $\Delta < 1$. (b) The asymptotic structure valid for high frequency, σ, and large oscillation amplitude, Δ.

pressure term p_x, we obtain

$$\sigma\psi_{P\eta\tau} + \left(\psi_{P\eta}\right)^2 - \psi_P\psi_{P\eta\eta} = -\sigma\Delta\sin\tau + (1+\Delta\cos\tau)^2 + \psi_{P\eta\eta\eta}, \quad (2.17)$$

$$\sigma\psi_{S\eta\tau} + \psi_{S\eta}\psi_{P\eta} - \psi_P\psi_{S\eta\eta} = \quad (2.18)$$
$$-\sigma\sin(\tau-\phi) + \cos(\tau-\phi)(1+\Delta\cos\tau) + \psi_{S\eta\eta\eta},$$

with boundary conditions for the primary flow

$$\psi_P(0,\tau) = 0, \quad \psi_{P\eta}(0,\tau) = 0 \quad \text{on} \quad \eta = 0, \quad (2.19)$$

$$\psi_{P\eta}(\eta,\tau) \to 1+\Delta\cos\tau \quad \text{as} \quad \eta\to\infty, \quad (2.20)$$

and subsidiary flow boundary conditions

$$\psi_S(0,\tau) = 0, \quad \psi_{S\eta}(0,\tau) = \cos(\tau-\phi) \quad \text{on} \quad \eta = 0, \quad (2.21)$$

$$\psi_{S\eta}(\eta,\tau) \to \cos(\tau-\phi) \quad \text{as} \quad \eta\to\infty. \quad (2.22)$$

Here $\sigma = \omega/k$ is the Strouhal number, a dimensionless frequency parameter, which is a measure of the time-dependent terms. It should be emphasised that (2.17) and (2.18) are an exact reduction of the Navier Stokes equations and it has not been assumed that the Reynolds number is large.

Following the earlier work of Pedley (1972) and Grosch and Salwen (1982), Merchant and Davis (1989) considered solutions to the primary equation (2.17) in the large frequency limit and the mean component of $a(\tau)$ is much larger than the oscillatory component. In this case, the asymptotic structure consists of a Stokes layer of thickness $O(\sigma^{-1/2})$ at the wall, which occurs in oscillatory problems and is a balance between the unsteady and the viscous terms. This layer matches to an outer layer of $O(1)$ thickness, as illustrated in figure 2.3(a). Consequently, the thickness of the outer layer is of the order $\sigma^{1/2}$ multiplied by that of the Stokes layer. Work by Riley (1965) and Stuart (1966) showed that in the absence of a mean flow at infinity, the asymptotic structure requires a Stokes layer at the wall, of thickness $O(\sigma^{-1/2})$ and a steady streaming layer of thickness $O(\sigma^{1/2})$, as illustrated in figure 2.3(b). In this case, the thickness of the steady streaming layer is of the order σ, multiplied by that of the Stokes layer. The implication for the present work is that the asymptotic structure required to describe the flow at a high frequency changes, when the amplitude of the oscillatory flow at infinity also becomes large. Merchant and Davis (1989) and subsequently Blyth and Hall (2003) considered the latter limit, where both the frequency and the oscillation amplitude were large. The former authors found a critical amplitude dependent upon the frequency, above which solutions do not exist. This amplitude arises when the thickness of the outer layer coincides with the thickness of the steady streaming layer. Blyth and Hall showed that when the oscillation amplitude exceeds the critical threshold

$$\Delta \sim O(\sigma^{1/2}), \tag{2.23}$$

the primary solution terminates at a finite-time singularity. The behaviour of the primary solution close to the finite-time singularity is discussed in chapter 5. We expand the relation (2.23) as

$$\Delta = A_0\sigma^{1/2} + A_1 + O(\sigma^{-1/2}), \tag{2.24}$$

where the constant A_0 corresponds to the boundary between solutions existing and breaking down. The second term in the expansion is the correction

term and only has relevance when solutions are discussed close to the boundary. Through solving the primary problem, both A_0 and A_1 are obtained and compared later with the results of Blyth and Hall (2003).

Hazel and Pedley (1998) considered solutions for large σ, but confined their attention to the case where the amplitude was restricted, to prevent flow reversal, i.e. $\Delta < 1$. To proceed with our investigation, we use the relation (2.23) and consider the solutions to the primary and subsidiary problems in the asymptotic limit $\sigma \to \infty$. The amplitude parameter is also large, which allows the flow to reverse. As the subsidiary equation is coupled with that of the primary equation, it is expected that the subsidiary equation will also break down when this relation is exceeded.

2.3 Large frequency analysis

In this section, we consider the asymptotic solution to equations (2.17) and (2.18) for large frequency and in the parameter range $\Delta \sim O(\sigma^{1/2})$. For convenience, the scalings $\psi_S = \Delta^{-1/2}\widehat{\psi_S}$, $\psi_P = \Delta^{1/2}\widehat{\psi_P}$ and $\widehat{\eta} = \Delta^{1/2}\eta$ are introduced so that the amplitude Δ is no longer coupled with the oscillatory component of $a(\tau)$. Furthermore, we introduce new parameters, $\widehat{\epsilon} = 1/\Delta$ and $\Omega = \sigma/\Delta$. Subsequently, the rescaled equations become

$$\Omega\widehat{\psi}_{P\widehat{\eta}\tau} + \left(\widehat{\psi}_{P\widehat{\eta}}\right)^2 - \widehat{\psi}_P\widehat{\psi}_{P\widehat{\eta}\widehat{\eta}} = -\Omega\sin\tau + (\widehat{\epsilon} + \cos\tau)^2 + \widehat{\psi}_{P\widehat{\eta}\widehat{\eta}\widehat{\eta}}, \tag{2.25}$$

$$\Omega\widehat{\psi}_{S\widehat{\eta}\tau} + \widehat{\psi}_{S\widehat{\eta}}\widehat{\psi}_{P\widehat{\eta}} - \widehat{\psi}_P\widehat{\psi}_{S\widehat{\eta}\widehat{\eta}} = \tag{2.26}$$
$$-\Omega\sin(\tau-\phi) + (\cos\tau + \widehat{\epsilon}\,)\cos(\tau-\phi) + \widehat{\psi}_{S\widehat{\eta}\widehat{\eta}\widehat{\eta}},$$

with primary boundary conditions

$$\widehat{\psi}_P(0,\tau) = 0, \quad \widehat{\psi}_{P\widehat{\eta}}(0,\tau) = 0 \quad \text{on} \quad \widehat{\eta} = 0, \tag{2.27}$$

$$\widehat{\psi}_{P\widehat{\eta}}(\widehat{\eta},\tau) \to \cos\tau + \widehat{\epsilon} \quad \text{as} \quad \widehat{\eta} \to \infty, \tag{2.28}$$

and subsidiary boundary conditions

$$\widehat{\psi}_S(0,\tau) = 0, \quad \widehat{\psi}_{S\widehat{\eta}}(0,\tau) = \cos(\tau-\phi) \quad \text{on} \quad \widehat{\eta} = 0, \tag{2.29}$$

$$\widehat{\psi}_{S\widehat{\eta}}(\widehat{\eta},\tau) \to \cos(\tau-\phi) \quad \text{as} \quad \widehat{\eta} \to \infty. \tag{2.30}$$

The relation (2.23) is rewritten in terms of the new parameters $\widehat{\epsilon}$ and Ω to obtain an equivalent relation $\widehat{\epsilon} \sim O(\Omega^{-1})$ and we express this as the asymptotic expansion

$$\widehat{\epsilon} = a_0\Omega^{-1} + a_1\Omega^{-2} + O(\Omega^{-3}). \tag{2.31}$$

The constants a_0 and a_1 can be rewritten in terms of the constants A_0 and A_1, given in (2.23) and are expressed as $a_0 = \frac{1}{A_0^2}$ and $a_1 = -2A_1a_0^2$. The constants a_0 and a_1 are obtained numerically when solving the primary equation (2.25).

We note that (2.25) and its corresponding boundary conditions are independent of $\widehat{\psi}_S$, while (2.26) and its boundary conditions involve a coupling of $\widehat{\psi}_S$ and $\widehat{\psi}_P$. Consequently, we first need to seek a solution to $\widehat{\psi}_P$, by duplicating the work of Blyth and Hall (2003), before we obtain a solution for $\widehat{\psi}_S$, in which results and methods from the primary problem are used.

2.4 The primary flow

To solve the primary equation (2.25) in the limit $\Omega \to \infty$ with $\widehat{\epsilon} \sim O(\Omega^{-1})$, we seek solutions in the Stokes and the steady streaming layers. We begin by solving the primary equation in the Stokes layer.

2.4.1 The Stokes layer

Initially, we seek a solution to the primary equation (2.25) close to the wall. The dominating terms in equation (2.25) are $\Omega\widehat{\psi}_{P\widehat{\eta}\tau} \sim \widehat{\psi}_{P\widehat{\eta}\widehat{\eta}\widehat{\eta}}$, which suggests the scaling $\widehat{\eta} \sim \Omega^{-1/2}$. Therefore, a Stokes layer is present of thickness $O(\Omega^{-1/2})$. Subsequently, we introduce the variable $\xi = \Omega^{1/2}\widehat{\eta}$, where $\xi = O(1)$ and equation (2.25) becomes

$$\begin{aligned}\Omega^{3/2}\widehat{\psi}_{P\xi\tau} + \Omega\left(\left(\widehat{\psi}_{P\xi}\right)^2 - \widehat{\psi}_P\widehat{\psi}_{P\xi\xi}\right) = \\ -\Omega\sin\tau + (\cos\tau + a_0\Omega^{-1})^2 + \Omega^{3/2}\widehat{\psi}_{P\xi\xi\xi} + O(\Omega^{-2}),\end{aligned} \tag{2.32}$$

with boundary conditions on the wall

$$\widehat{\psi}_P(0,\tau) = 0, \quad \widehat{\psi}_{P\xi}(0,\tau) = 0 \quad \text{on} \quad \xi = 0, \tag{2.33}$$

and the matching condition to the far-field

$$\widehat{\psi}_{P\xi} \to \Omega^{-1/2}\cos\tau + a_0\Omega^{-3/2} + a_1\Omega^{-5/2} + O(\Omega^{-7/2}) \quad \text{as} \quad \xi \to \infty. \tag{2.34}$$

To solve (2.32), we pose the asymptotic expansion

$$\widehat{\psi}_P = \Omega^{-1/2}\Psi_{P_0}(\xi,\tau) + \Omega^{-3/2}\Psi_{P_1}(\xi,\tau) + O(\Omega^{-2}). \tag{2.35}$$

Substituting the expansion (2.35) into (2.32), gives at leading and first order

$$\Psi_{P_0\xi\tau} - \Psi_{P_0\xi\xi\xi} = -\sin\tau, \tag{2.36}$$

$$\Psi_{P_1\xi\tau} - \Psi_{P_1\xi\xi\xi} = \cos^2\tau + \Psi_{P_0}\Psi_{P_0\xi\xi} - \left(\Psi_{P_0\xi}\right)^2, \tag{2.37}$$

with the leading and first order boundary conditions on the wall

$$\Psi_{P_0}(0,\tau) = 0, \quad \Psi_{P_0\xi}(0,\tau) = 0, \quad \Psi_{P_1}(0,\tau) = 0, \quad \Psi_{P_1\xi}(0,\tau) = 0. \tag{2.38}$$

Upon integrating (2.36) and (2.37), we find the leading and first order solutions in the Stokes layer are

$$\Psi_{P_0}(\xi,\tau) = \xi\cos\tau - \cos\left(\tau - \frac{\pi}{4}\right) + e^{-\xi/\sqrt{2}}\cos\left(\tau - \frac{\xi}{\sqrt{2}} - \frac{\pi}{4}\right), \tag{2.39}$$

$$\begin{aligned}\Psi_{P_1}(\xi,\tau) = {} & \frac{13}{4\sqrt{2}} - \frac{3}{4}\xi - \frac{1}{2\sqrt{2}}\cos\left(2\tau + \frac{\pi}{4}\right) \\ & -\frac{1}{4\sqrt{2}}e^{-\xi\sqrt{2}} + \frac{1}{2\sqrt{2}}e^{-\xi}\cos\left(\xi - 2\tau - \frac{\pi}{4}\right) \\ & +\frac{\xi}{2}e^{-\xi/\sqrt{2}}\left[\sin\left(\frac{\xi}{\sqrt{2}} - 2\tau\right) - \sin\left(\frac{\xi}{\sqrt{2}}\right)\right] \\ & -e^{-\xi/\sqrt{2}}\left[\frac{3\sqrt{2}}{2}\cos\left(\frac{\xi}{\sqrt{2}}\right) + \sqrt{2}\sin\left(\frac{\xi}{\sqrt{2}}\right)\right].\end{aligned} \tag{2.40}$$

We note that the term proportional to $e^{-\xi}$ in the first order solution (2.40) arises due to the non-linear terms in equation (2.37). In solving equations (2.36) and (2.37), we have used the boundary conditions on the wall and the fact that the functions $\Psi_{P_0}(\xi,\tau)$ and $\Psi_{P_1}(\xi,\tau)$ are periodic and bounded. In the limit $\xi \to \infty$,

$$\widehat{\psi}_{P\xi} \to \Omega^{-1/2}\cos\tau - \frac{3}{4}\Omega^{-3/2} + O(\Omega^{-5/2}) \quad \text{as} \quad \xi \to \infty. \tag{2.41}$$

Matching the solution (2.41) to the boundary condition (2.34), it can be seen that the leading order solution matches to the far-field boundary condition. However, the first order solution (2.40) does not satisfy the condition

$\Psi_{P_1\xi}(\xi,\tau) \to a_0$ as $\xi \to \infty$. Instead, $\Psi_{P_1\xi}(\xi,\tau) \to -3/4$ as $\xi \to \infty$. This term can be interpreted as a horizontal velocity at the top of the Stokes layer moving towards the origin, which arises due to the non-linear terms in equation (2.37). To enable this velocity to match with the far-field flow, it is necessary to introduce a steady streaming layer to match between the Stokes layer and the far-field.

2.4.2 The steady streaming layer

In this section, we solve equation (2.25) in the steady streaming layer. To enable this layer to match with the Stokes layer, we introduce the new variable $\zeta = \Omega^{-1/2}\widehat{\eta}$, where $\zeta = O(1)$ and the steady streaming layer has thickness $O(\Omega^{1/2})$. Rewriting equation (2.25) in terms of ζ, we obtain

$$\Omega^{1/2}\widehat{\psi}_{P\zeta\tau} + \Omega^{-1}\left(\left(\widehat{\psi}_{P\zeta}\right)^2 - \widehat{\psi}_P\widehat{\psi}_{P\zeta\zeta}\right) = \tag{2.42}$$
$$-\Omega\sin\tau + (\cos\tau + a_0\Omega^{-1})^2 + \Omega^{-3/2}\widehat{\psi}_{P\zeta\zeta\zeta} + O(\Omega^{-2}),$$

with far-field boundary condition

$$\widehat{\psi}_{P\zeta} \to \Omega^{1/2}\cos\tau + a_0\Omega^{-1/2} + a_1\Omega^{-3/2} + O(\Omega^{-5/2}) \quad \text{as} \quad \zeta \to \infty. \tag{2.43}$$

To determine the form of the asymptotic expansion, we rewrite the Stokes layer solution as $\xi \to \infty$, in terms of the steady streaming layer variable ζ. The dominate terms are given by $\widehat{\psi}_P \sim \Omega^{1/2}\zeta\cos\tau - \Omega^{-1/2}\cos\left(\tau - \frac{\pi}{4}\right) + \cdots$. This suggests the expansion

$$\widehat{\psi}_P = \Omega^{1/2}\zeta\cos\tau + \Omega^{-1/2}\left(-\cos\left(\tau - \frac{\pi}{4}\right) + G_P(\zeta,\tau)\right), \tag{2.44}$$

with $G_P(\zeta,\tau)$ given by

$$\begin{aligned} G_P(\zeta,\tau) \;=\; & \Big(\Phi_{P_0}(\zeta,\tau) + f_0(\zeta)\Big) + \Omega^{-1}\Big(\Phi_{P_1}(\zeta,\tau) + f_1(\zeta)\Big) + \\ & \Omega^{-2}\Big(\Phi_{P_2}(\zeta,\tau) + f_2(\zeta)\Big) + O(\Omega^{-3}). \end{aligned} \tag{2.45}$$

The functions $f_i(\zeta)$ are the mean components and $\Phi_{P_i}(\zeta,\tau)$ are the oscillatory components with a zero time-average, for $i \geq 0$. The last component of (2.45) is included as $\Phi_{P_2}(\zeta,\tau)$ is required to obtain the equation for $f_0(\zeta)$.

By substituting the steady streaming layer expansions, (2.44) and (2.45), into the equation (2.42), the leading and first order equations are

$$\Phi_{P_0\zeta\tau} = 0, \tag{2.46}$$

$$\Phi_{P_1\zeta\tau} = 2a_0\cos\tau + (\Phi_{P_0\zeta\zeta} + f_{0\zeta\zeta})\zeta\cos\tau - 2(\Phi_{P_0\zeta} + f_{0\zeta})\cos\tau. \tag{2.47}$$

To proceed, we integrate equation (2.46) once with respect to τ and take a time-average to obtain the function of integration. Secondly, we integrate with respect to ζ to give $\Phi_{P_0} = g_0(\tau)$. Repeating this process for (2.47), we find $\Phi_{P_1} = (2a_0\zeta + f_0'\zeta - 3f_0)\sin\tau + g_1(\tau)$, where the prime denotes differentiation with respect to ζ. The functions $g_0(\tau)$ and $g_1(\tau)$, are found via matching to the Stokes layer solution. In the matching region, between the Stokes and the steady streaming layer, the Stokes layer solution is written in terms of the steady streaming layer variable ζ, to give

$$\begin{aligned}\widehat{\psi}_P \sim\ & \Omega^{1/2}\zeta\cos\tau - \Omega^{-1/2}\left[\cos\left(\tau - \frac{\pi}{4}\right) + \frac{3\zeta}{4}\right] \\ & + \Omega^{-3/2}\left[\frac{13}{4\sqrt{2}} - \frac{1}{2\sqrt{2}}\cos\left(2\tau + \frac{\pi}{4}\right)\right] + O(\Omega^{-5/2}).\end{aligned} \tag{2.48}$$

From this, it can be seen that $g_0(\tau) = 0$ and $g_1(\tau) = -\frac{1}{2\sqrt{2}}\cos\left(2\tau + \frac{\pi}{4}\right)$. To obtain the steady stream layer solution, we substitute the values for $\Phi_{P_0}(\zeta,\tau)$ and $\Phi_{P_1}(\zeta,\tau)$ into (2.44) and (2.45) and find

$$\begin{aligned}\widehat{\psi}_P =\ & \Omega^{1/2}\zeta\cos\tau + \Omega^{-1/2}\left[f_0(\zeta) - \cos\left(\tau - \frac{\pi}{4}\right)\right] \\ & + \Omega^{-3/2}\left[\left(\zeta f_0'(\zeta) - 3f_0(\zeta)\right)\sin\tau + 2a_0\zeta\sin\tau\right. \\ & \left. - \frac{1}{2\sqrt{2}}\cos\left(2\tau + \frac{\pi}{4}\right) + f_1(\zeta)\right] + O(\Omega^{-5/2}).\end{aligned} \tag{2.49}$$

To obtain the equation for $f_0(\zeta)$, we collect terms of size $O(\Omega^{-2})$ in (2.42) to obtain

$$\begin{aligned}\Psi_{P_2\zeta\tau} =\ & -f_0'^2 - 2\cos\tau\left[(2a_0 + \zeta f_0'' - 2f_0')\sin\tau + f_1'\right] \\ & + \zeta\cos\tau\left[(\zeta f_0''' - f_0'')\sin\tau + f_1''\right] - \cos\left(\tau - \frac{\pi}{4}\right)f_0'' \\ & + f_0 f_0'' + a_0^2 + 2a_1\cos\tau + f_0'''.\end{aligned} \tag{2.50}$$

Averaging over a single time period, we find

$$f_0''' - f_0'^2 + f_0 f_0'' + a_0^2 = 0. \tag{2.51}$$

To find the boundary condition on $\zeta = 0$, we match the Stokes layer solution (2.48) to the steady streaming layer solution (2.49), to obtain $f_0(\zeta) \to -3\zeta/4$ as $\zeta \to 0$. The boundary condition as $\zeta \to \infty$ is found by matching the steady streaming layer solution to the far-field boundary condition (2.43). Therefore, the boundary conditions for equation (2.51) are given by

$$f_0(0) = 0, \qquad f_0'(0) = -\frac{3}{4}, \qquad f_0'(\zeta) \to a_0 \quad \text{as} \quad \zeta \to \infty. \tag{2.52}$$

Similarly, to calculate the equation for $f_1(\zeta)$, we collect terms of size $O(\Omega^{-3})$ in (2.42) and find

$$\begin{aligned} \Psi_{P_3\zeta\tau} \;=\; & -2\cos\tau(\Psi_{P_2\zeta} + f_2') - 2f_0'\Big[(2a_0 + \zeta f_0'' - 2f_0')\sin\tau + f_1'\Big] \\ & + \;\; \zeta\cos\tau(\Psi_{P_2\zeta\zeta} + f_2'') - \cos\left(\tau - \frac{\pi}{4}\right)\Big[(\zeta f_0''' - f_0'')\sin\tau + f_1''\Big] \\ & + f_0 f_1'' + f_0''\left[(2a_0 + \zeta f_0' - 3f_0)\sin\tau - \frac{1}{2\sqrt{2}}\cos\left(2\tau + \frac{\pi}{4}\right) + f_1\right] \\ & + 2a_0 a_1 + \zeta f_0''''\sin\tau + f_1'''. \end{aligned} \tag{2.53}$$

Before taking a time-average of (2.53), we note that $\Psi_{P_2\zeta}$ and $\Psi_{P_2\zeta\zeta}$ are needed. For convenience, we note that the only term which gives a non-zero time-average when the integral of (2.50) is multiplied by the terms in (2.53), is $\Psi_{P_2\zeta\tau} \sim -\cos(\tau - \pi/4) f_0''$. Therefore, upon taking a time-average of (2.53), we obtain

$$f_1''' + f_1 f_0'' + f_0 f_1'' - 2f_0' f_1' = \frac{f_0''}{2\sqrt{2}} - 2a_0 a_1. \tag{2.54}$$

We note that Merchant and Davis (1989) do not have the term on the right-hand side proportional to $f_0''(\zeta)$, but we agree with Blyth and Hall (2003) that this term should be included. The boundary conditions for equation (2.54) are obtained using a similar method to that described for equation (2.51) and are given by

$$f_1(0) = \frac{13}{4\sqrt{2}}, \qquad f_1'(0) = 0, \qquad f_1'(\zeta) \to a_1 \quad \text{as} \quad \zeta \to \infty. \tag{2.55}$$

In the next section, we solve equation (2.51) with boundary conditions (2.52), which has previously been addressed by Merchant and Davis (1989) and Blyth and Hall (2003). Additionally, these results are used to solve the subsidiary equation (2.26).

2.4.3 Numerical Scheme: Runge-Kutta technique

To solve the equation for $f_0(\zeta)$, given in (2.51) with boundary conditions (2.52), we use a fourth order Runge-Kutta technique. Both Merchant and Davis (1989) and Blyth and Hall (2003), found that there are no solutions when $a_0 < a_{0c}$, two solutions when $a_{0c} < a_0 < 0.75$ and a unique solution when $a_0 > 0.75$, where the critical value $a_{0c} = 0.602$. We proceed by solving equation (2.51), not only to verify these results, but also to use these to solve the subsidiary equation, which is considered in section 2.6.3. We convert the third order equation into three first order equations by letting $f_0 = y_1$ and it follows that

$$y_1' = y_2, \tag{2.56}$$

$$y_2' = y_3, \tag{2.57}$$

$$y_3' = y_2^2 - y_1 y_3 - a_0^2, \tag{2.58}$$

with boundary conditions

$$y_1(0) = 0, \quad y_2(0) = -\frac{3}{4}, \quad y_2(\infty) = a_0. \tag{2.59}$$

This system is solved using a fourth-order Runge-Kutta technique, which can be found in Cheney and Kincaid (1994), for example. This is an iterative numerical method, evaluating the function at the initial point, two trial midpoints and at the end of the interval, where a spatial step size of $h = 0.001$ is chosen. Since (2.51) is a third order equation, the second order boundary condition $f_0''(0)$ is needed. To calculate this, we use a shooting technique by means of Newton's method and iterate until the condition at infinity, $y_2(\infty) \to a_0$ is satisfied.

Upon solving equation (2.51), we have been able to improve the critical value calculated by Merchant and Davis (1989), to $a_{0c} = 0.6017$. Upon increasing a_0, we find two solutions for $0.6017 < a_0 < 0.7$. In figure 2.3, the velocity profiles are illustrated for $a_0 = 0.6017, 0.65, 0.7$. However, using this method and increasing the value of a_0 beyond 0.7, one of the solutions becomes more sensitive to the initial conditions and is difficult to compute.

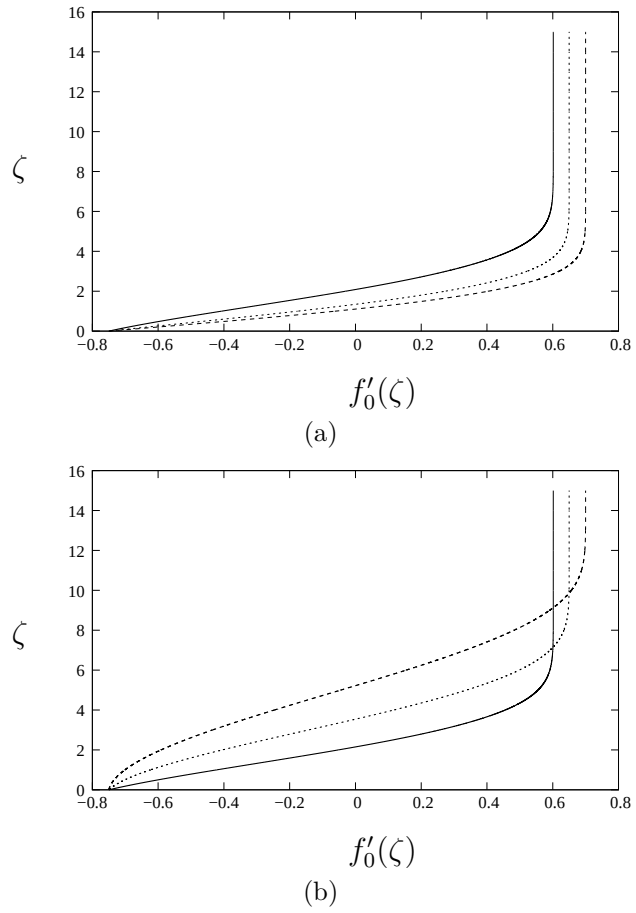

Figure 2.3: The primary leading order velocity profiles for the two solutions of $f_0'(\zeta)$ for $a_0 = 0.6017$ (solid line), $a_0 = 0.65$ (dotted lines) and $a_0 = 0.7$ (dashed lines).

This breakdown corresponds to the velocity profiles in figure 2.3(b). We note that Merchant and Davis (1989) also had this problem. Attempting to rectify this, we increase the accuracy of the numerical method, however, this becomes time-consuming and impractical.

To calculate the remaining solution of $f_0(\zeta)$ for $0.7 < a_0 < 0.75$, we use a finite-difference numerical technique, which was used by Riley and Weidman (1989). Initially, an asymptotic solution at $a_0 \approx 0.75$ is obtained and used as an approximation to begin the numerics.

2.4.4 Asymptotic solution of $f_0(\zeta)$ about $a_0 \approx 0.75$

In the previous section, two solutions to equation (2.51) have only been found for $0.6017 < a_0 < 0.7$, but as a_0 increases, one of the solutions is unable to

be calculated using the Runge-Kutta technique. To obtain the remaining solution of $f_0(\zeta)$ for $0.7 < a_0 < 0.75$, we follow Riley and Weidman (1989) by seeking the solution using a finite-difference technique. Firstly, an asymptotic solution to equation (2.51) is required for $a_0 \approx 0.75$, which is used as an initial guess to begin the numerics. The numerics are then marched backwards from $a_0 \approx 0.75$ to match with the Runge-Kutta results for $a_0 \approx 0.7$.

To begin, we rewrite the equation (2.51), using the scalings $f_0(\zeta) = a_0^{1/2}\widehat{f}_0(\widehat{\zeta})$ and $\widehat{\zeta} = a_0^{1/2}\zeta$, which expresses the equation in the form that was discussed by Riley and Weidman (1989) and is given by

$$\widehat{f}_0''' - \widehat{f}_0'^2 + \widehat{f}_0\widehat{f}_0'' + 1 = 0, \tag{2.60}$$

with boundary conditions

$$\widehat{f}_0(0) = 0, \qquad \widehat{f}_0'(0) = -\lambda, \qquad \widehat{f}_0'(\widehat{\zeta}) \to 1 \quad \text{as} \quad \widehat{\zeta} \to \infty, \tag{2.61}$$

where $\lambda = \frac{3}{4a_0}$. We note that equation (2.60) is a special case of the Falkner-Skan equation. To begin, we duplicate the work of Riley and Weidman (1989), not only to find an asymptotic solution to begin the numerics, but also, the details of this asymptotic solution are required for the subsidiary asymptotic solution, which is discussed in Appendix A.

To find an asymptotic solution to equation (2.60), we write $\lambda = 1 + \epsilon$ where $0 < \epsilon \ll 1$. When $\lambda = 1$, this corresponds to the case when $a_0 = 0.75$ and as ϵ increases, a_0 decreases. From our numerical results in section 2.4.3, it appears that $\widehat{f}_0''(0) \sim \epsilon^{1/2}$ as $\epsilon \to 0$, with this relationship illustrated in figure 2.4. This relation, along with the boundary conditions at $\widehat{\zeta} = 0$, given in (2.61), indicates the scaling $\widehat{f}_0 = \frac{1}{\delta(\epsilon)}\bar{f}_0(\chi)$ with new variable $\chi = \delta\widehat{\zeta}$, where $\delta = a\epsilon^{1/2}$. The constant a is obtained when finding the first order asymptotic solution. We write equation (2.60) in terms of the new variables, to obtain

$$a^2\epsilon\bar{f}_0''' - \bar{f}_0'^2 + \bar{f}_0\bar{f}_0'' + 1 = 0, \tag{2.62}$$

with boundary conditions

$$\bar{f}_0(0) = 0, \quad \bar{f}_0'(0) = -\lambda, \quad \text{on} \quad \chi = 0, \tag{2.63}$$

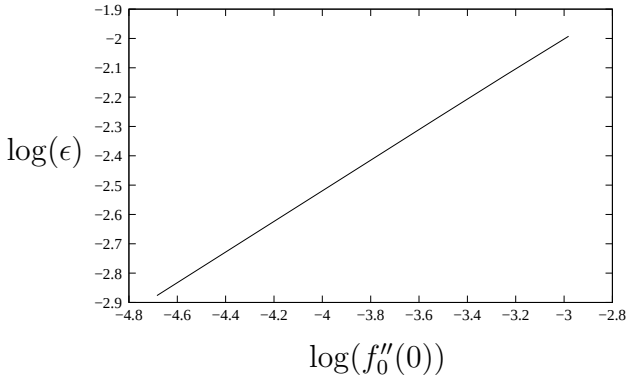

Figure 2.4: Using the results from the Runge-Kutta method close to $a_0 \approx 0.7$, a relationship develops between the shear component $\widehat{f}_0''(0)$ and ϵ, given by $\widehat{f}_0''(0) \sim \epsilon^{1/2}$ as $\epsilon \to 0$.

and the matching condition to the far-field is given by $\bar{f}_0'(\chi) \to 1$ as $\chi \to \infty$.

The form of equation (2.62) suggests that we pose the asymptotic expansion $\bar{f}_0(\chi) = \bar{f}_A(\chi) + \epsilon \bar{f}_B(\chi) + O(\epsilon^2)$. Substituting this expansion into (2.62), we find at leading order

$$\bar{f}_A(\chi)\bar{f}_A''(\chi) - \bar{f}_A'^2(\chi) + 1 = 0, \tag{2.64}$$

with boundary conditions $\bar{f}_A(0) = 0, \bar{f}_A'(0) = -1$. A solution to equation (2.64) satisfying the boundary condition at $\zeta = 0$, is given by

$$\bar{f}_A(\chi) = -\sin(\chi). \tag{2.65}$$

This is denoted the region 1 solution. As the far-field boundary condition is not satisfied, we seek a solution to match between the region 1 solution and the far-field condition. Before obtaining this solution, we find the first order solution $\bar{f}_B$, to obtain the constant a, where $\delta = a\epsilon^{1/2}$. At this stage, it is not known whether the first order solution is required to begin the finite-difference numerics. This is discussed in section 2.4.5, where the leading order approximation is plotted against the numerical solution for $f_0(\widehat{\zeta})$ to assess its accuracy.

The first order asymptotic expansion of equation (2.62) is given by

$$\bar{f}_B'' - 2\cot(\chi)\bar{f}_B' - \bar{f}_B = a\cot(\chi), \tag{2.66}$$

with the boundary conditions on $\chi = 0$ given by $\bar{f}_B(0) = 0$ and $\bar{f}_B'(0) = -1$. To find the homogeneous solution to (2.66), we notice that by using the

simplification $\bar{f}_B = \sin(\chi)u(\chi)$, it reduces to

$$\sin^2\chi u''(\chi) - 2u(\chi) = 0. \tag{2.67}$$

Upon solving equation (2.67), we obtain $u(\chi) = A\cot\chi + B(1 - \chi\cot\chi)$. Hence, the homogeneous solution to equation (2.66) is given by

$$\bar{f}_B(\chi) = A\cos(\chi) + B(\sin(\chi) - \chi\cos(\chi)), \tag{2.68}$$

where A and B are constants. To seek the particular solution of (2.66), we use the method of variation of parameters and write $\bar{f}_B(\chi) = u_1(\chi)v_1(\chi) + u_2(\chi)v_2(\chi)$, where the functions $u_1(\chi)$ and $u_2(\chi)$ are the solutions from the homogeneous case, $u_1(\chi) = \cos\chi$ and $u_2(\chi) = \sin(\chi) - \chi\cos(\chi)$. The functions $v_1(\chi)$ and $v_2(\chi)$ are obtained using this method and equation (2.66) becomes

$$\begin{aligned} v_1'\cos(\chi) + v_2'(\sin(\chi) - \chi\cos(\chi)) &= 0, & (2.69)\\ -v_1'\sin(\chi) + v_2'\chi\sin(\chi) &= a^2\cot(\chi). & (2.70) \end{aligned}$$

Solving these, we find

$$\begin{aligned} v_1(\chi) &= \frac{a^2}{2}\left[\frac{1}{\sin(\chi)} + \int_0^\chi \ln\left(\tan\left(\frac{\widehat{\chi}}{2}\right)\right)\mathrm{d}\widehat{\chi} - \frac{\chi\cos(\chi)}{\sin^2(\chi)}\right. & (2.71)\\ &\quad \left. -\chi\ln\left(\tan\left(\frac{\widehat{\chi}}{2}\right)\right)\right],\\ v_2(\chi) &= -\frac{a^2}{2}\left[\frac{\cos(\chi)}{\sin^2\chi} + \ln\left(\tan\left(\frac{\widehat{\chi}}{2}\right)\right)\right]. & (2.72) \end{aligned}$$

Therefore, combining the homogeneous and particular solution, the general solution of $\bar{f}_B(\chi)$ is given by

$$\begin{aligned} \bar{f}_B(\chi) &= A\cos(\chi) + B(\sin(\chi) - \chi\cos(\chi)) & (2.73)\\ &\quad + \frac{a^2}{2}\cos(\chi)\int_0^\chi \ln\left(\tan\left(\frac{\widehat{\chi}}{2}\right)\right)\mathrm{d}\widehat{\chi} - \frac{a^2}{2}\sin(\chi)\ln\left(\tan\left(\frac{\widehat{\chi}}{2}\right)\right). \end{aligned}$$

Applying the boundary conditions $\bar{f}_B(0) = 0$ and $\bar{f}_B'(0) = -1$, we find $A = 0$ and $a^2 = 2$. However, the constant B is undetermined at this order. This value for a implies that $\delta = (2\epsilon)^{1/2}$ and the first order solution is given by

$$\begin{aligned} \bar{f}_B(\chi) &= B(\sin(\chi) - \chi\cos(\chi)) + \cos(\chi)\int_0^\chi \ln\left(\tan\left(\frac{\widehat{\chi}}{2}\right)\right)\mathrm{d}\widehat{\chi} & (2.74)\\ &\quad - \sin(\chi)\ln\left(\tan\left(\frac{\widehat{\chi}}{2}\right)\right). \end{aligned}$$

Combining the leading order solution (2.65), with the first order solution (2.74), we obtain the primary asymptotic solution

$$\begin{aligned}\bar{f}_0(\chi) &= -\frac{\sin(\chi)}{\delta} + \frac{\delta}{2}\Bigg[B(\sin(\chi) - \chi\cos(\chi)) \\ &\quad + \cos(\chi)\int_0^{\chi} \ln\left(\tan\left(\frac{\widehat{\chi}}{2}\right)\right) \mathrm{d}\widehat{\chi} - \sin(\chi)\ln\left(\tan\left(\frac{\widehat{\chi}}{2}\right)\right)\Bigg] + \cdots .\end{aligned} \tag{2.75}$$

As discussed previously, this solution is unable to satisfy the far-field boundary condition, $\bar{f}_0'(\chi) \to 1$ as $\chi \to \infty$. It can be seen that the leading order solution

$$\widehat{f}_0' = -\cos(\chi), \tag{2.76}$$

is only valid until $\chi_0 = \pi$ i.e. $\widehat{\zeta}_0 = \pi/\delta$. Consequently, another region is required to match this solution to that of the far-field. Figure 2.5 illustrates the leading order solution (2.76) for selected values of ϵ along with $\widehat{\zeta}_0$ for each value of ϵ and it can be seen that as $\epsilon \to 0$, $\widehat{\zeta}_0$ increases.

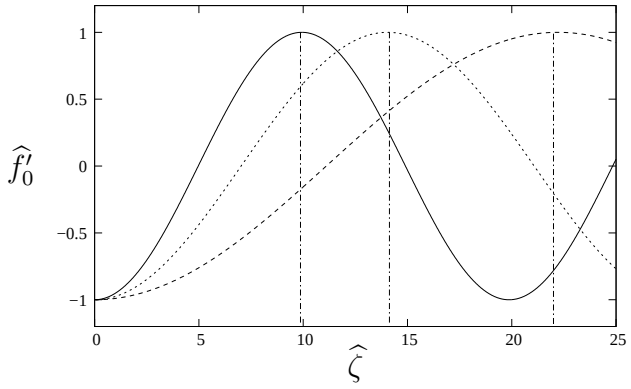

Figure 2.5: The leading order asymptotic solution for $\epsilon \to 0$, where $\epsilon = 0.05$ (solid line), $\epsilon = 0.025$ (dotted lines) and $\epsilon = 0.01$ (dashed lines). The vertical lines represent $\widehat{\zeta}_0$, the point at which the solution no longer satisfies the far-field boundary condition.

We introduce a new region centered on $\widehat{\zeta} = \pi/\delta$, which is denoted region 2. Upon writing $\widehat{f}_0 = Z + N(Z)$ with new variable $Z = \widehat{\zeta} - \frac{\pi}{\delta}$, where $|N'(\widehat{\zeta})| \ll 1$, equation (2.60) is rewritten, after neglecting the quadratic terms, as

$$N'''(Z) + ZN''(Z) - 2N'(Z) = 0. \tag{2.77}$$

Writing $N' = Ae^{-Z^2/4}u(Z)$, equation (2.77) reduces to

$$u'' - u\Big(\frac{Z^2}{4} + \frac{5}{2}\Big) = 0, \tag{2.78}$$

where A is a constant, which is found through matching to the region 1 solution. The solution for $u(Z)$ has a solution in the form of a parabolic cylinder function, which can be found in Abramowitz and Stegun (1964). Therefore, the solution to (2.77) is given by

$$N'(Z) = Ae^{-Z^2/4}D_{-3}(Z), \tag{2.79}$$

where $D_{-3}(Z)$ is a parabolic cylinder function. Subsequently, the leading order region 2 solution is given by

$$\widehat{f}_0' = 1 + Ae^{-Z^2/4}D_{-3}(Z). \tag{2.80}$$

To obtain the constant A, we match the region 1 and 2 solutions together. In the matching region, the region 1 leading order solution (2.76) is expressed as $\widehat{f}_0' = \cos(\delta Z)$. In the limit $\delta \to 0$, this can be expanded as

$$\widehat{f}_0' = 1 - \frac{\delta^2 Z^2}{2} + O(Z^4). \tag{2.81}$$

For the region 2 solution, an expansion for $D_{-3}(Z)$ as $Z \to -\infty$ is required. From Whittaker and Watson (1963), $D_{-3}(Z) \sim \frac{\sqrt{2\pi}}{2}e^{Z^2/4}Z^2$ as $Z \to -\infty$. Substituting this expansion into the region 2 solution (2.80), gives

$$\widehat{f}_0' = 1 + A\frac{\sqrt{2\pi}}{2}Z^2 + O(Z^4). \tag{2.82}$$

Upon matching the region 1 and region 2 solutions, (2.81) and (2.82), we find $A = -\frac{\delta^2}{\sqrt{2\pi}}$. Riley and Weidman (1989) obtained the same formula for A but without the δ^2 factor. We think the δ^2 is necessary in order for the correct matching to take place. Therefore, the region 2 leading order expansion is given by

$$\widehat{f}_0' = 1 - \frac{2\delta^2}{2\sqrt{2\pi}}e^{-Z^2/4}D_{-3}(Z). \tag{2.83}$$

In figure 2.6, the leading order region 1 solution is plotted alongside the region 2 solution for selected values of ϵ. It can be seen as $\epsilon \to 0$, the region 1 and 2 solutions match together.

In this section, we have obtained the asymptotic solution of $f_0(\zeta)$ close to $a_0 \approx 0.75$. We proceed by using this as an initial guess to begin the finite-difference numerics for $a_0 \approx 0.75$. The numerics are then marched backwards in a_0 to match with the Runge-Kutta results obtained in section 2.4.3.

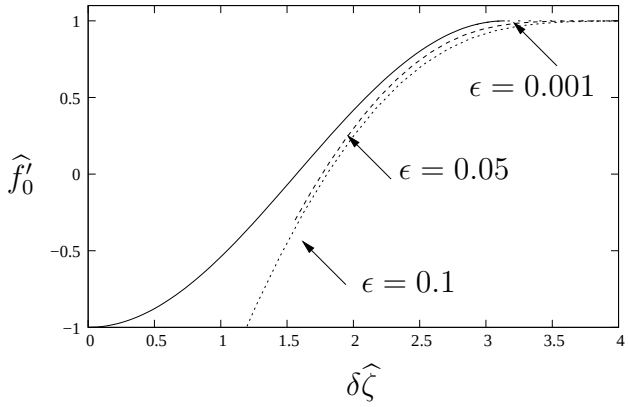

Figure 2.6: The leading order asymptotic solution to equation (2.60) for selected values of ϵ. Due to the scalings on the axes, the region 1 solution is unaffected by the choice of ϵ. As $\epsilon \to 0$, the region 2 solution matches to the region 1 solution.

2.4.5 Numerical scheme: Finite-Difference technique

To obtain the remaining solutions to $f_0(\zeta)$ for $0.7 < a_0 < 0.75$, which were unable to be calculated using the Runge-Kutta technique, we follow Riley and Weidman (1989) and use a finite-difference technique. This method involves an initial guess with an iteration. In section 2.4.4, an asymptotic solution was obtained close to $a_0 \approx 0.75$, which is used in this section as an initial guess to begin the finite-difference numerics.

By introducing a new variable $g_0 = \widehat{f_0'}$, equation (2.60) is rewritten as the second order equation

$$g_0'' + \widehat{f}_0 g_0' - g_0^2 + 1 = 0. \tag{2.84}$$

The non-linear term g_0^2, is rewritten as $g_0^2 = 2g_0\tilde{g}_0 - \tilde{g}_0^2$, where $\widetilde{g}_0$ and g_0 are successive iterates. When $\widetilde{g}_0$ and g_0 are within a small tolerance of each other, this relation is satisfied and the solution for g_0 is captured. We centrally discretise equation (2.84) to give

$$\frac{1}{h^2}\Big(g_{0_{i+1}} - 2g_{0_i} + g_{0_{i-1}}\Big) + \frac{\widehat{f}_{0_i}}{2h}\Big(g_{0_{i+1}} - g_{0_{i-1}}\Big) - 2g_{0_{i-1}}\tilde{g}_{0_i} = -1 - \tilde{g}_{0_i}^2, \tag{2.85}$$

with boundary conditions

$$\widehat{f}_{0_1} = 0, \quad g_{0_1} = -\lambda, \quad g_{0_N} = 1, \tag{2.86}$$

where $\lambda = 1 + \epsilon$ with $0 < \epsilon \ll 1$. The functions $\widehat{f}_{0_i}$ and g_{0_i} are unknown at each grid point $\widehat{\zeta}_i = ih$, where h is the spatial step size and $i = 1...N$.

Equation (2.85) is rewritten in terms of the tridiagonal system

$$a_i g_{0_{i+1}} + b_i g_{0_i} + c_i g_{0_{i-1}} = d_i, \tag{2.87}$$

where the constants $a_i \ldots d_i$ are given by

$$a_i = \frac{1}{h^2} + \frac{\widehat{f}_{0_i}}{2h}, \tag{2.88}$$

$$b_i = \frac{-2}{h^2} - 2\tilde{g}_{0_i}, \tag{2.89}$$

$$c_i = \frac{1}{h^2} - \frac{\widehat{f}_{0_i}}{2h}, \tag{2.90}$$

$$d_i = -1 - \tilde{g}^2_{0_i}. \tag{2.91}$$

We begin by solving equation (2.87), by using the leading order asymptotic solution obtained in section 2.4.4 as the initial guess to the solution. This is expressed as

$$\widehat{f}_0(\widehat{\zeta}) = \begin{cases} -\frac{\sin(\delta\widehat{\zeta})}{\delta} & \text{if } 0 < \delta\widehat{\zeta} < \pi \\ \delta\widehat{\zeta} - \pi & \delta\widehat{\zeta} > \pi \end{cases} \tag{2.92}$$

$$\tilde{g}_0(\widehat{\zeta}) = \begin{cases} -\cos(\delta\widehat{\zeta}) & \text{if } 0 < \delta\widehat{\zeta} < \pi \\ 1 & \delta\widehat{\zeta} > \pi \end{cases} \tag{2.93}$$

where $\delta = (2\epsilon)^{1/2}$ and we choose $\epsilon = 0.001$. The spatial step size $h = 0.001$ to agree with that used in the Runge-Kutta method.

The numerics begin when $\lambda \approx 1$ with (2.92) and (2.93) being used as the initial guess to the system (2.87), which is solved using the Thomas algorithm, which can be found in Hoffman (2001), for example. Once the solution for g_0 is computed, $\widehat{f}_0$ can easily be calculated by using the trapezium rule. At the next value of λ, the previous solution is used as the initial guess and the iterative procedure is repeated.

The numerics continue until $\lambda \approx 1.0714$ i.e. $a_0 \approx 0.7$, where $\lambda = \frac{3}{4a_0}$ and the solutions match to those obtained using the Runge-Kutta technique. In figure 2.7, we compare the velocity profiles from both numerical methods for $\lambda = 1.0714$, showing excellent agreement.

We note that only the leading order asymptotic solution is required to obtain an accurate solution for g_0, with figure 2.8 showing excellent agreement between the numerical and the asymptotic solutions for $\epsilon = 0.001$.

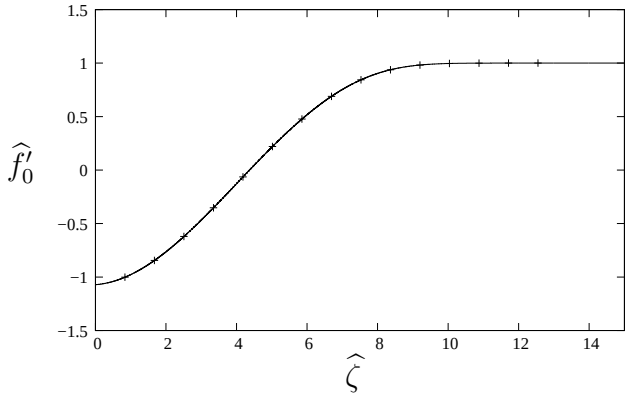

Figure 2.7: The velocity profile for the finite-difference method, represented by the crosses and the Runge-Kutta method, represented by the solid line, for $\lambda = 1.0714$ i.e. $a_0 = 0.7$, showing excellent agreement.

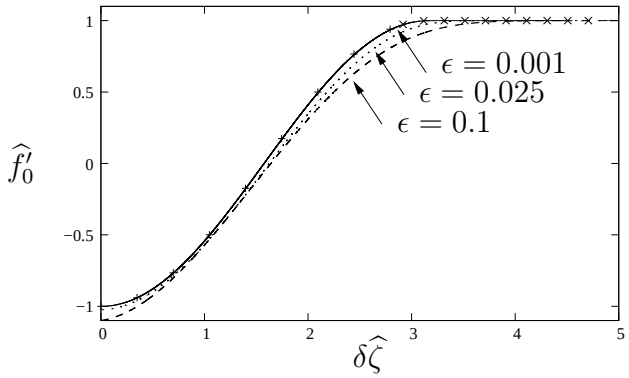

Figure 2.8: The asymptotic leading order solution for $\epsilon = 0.001$, illustrated by the crosses, showing excellent agreement with the numerical solution for the same value of ϵ, represented by the solid line.

Combining the numerical results from the Runge-Kutta and the finite-difference methods, we construct a curve of the possible values of a_0, illustrated in figure 2.9. The results show that there is a unique solution when $\lambda < 1$, two solutions when $1 < \lambda < 1.246$ and no solutions when $\lambda > 1.246$. These are equivalent to a unique solution when $a_0 > 0.75$, two solutions when $0.6017 < a_0 < 0.75$ and no solutions when $a_0 < 0.6017$.

The previous three sections have been dedicated to solving the equation for $f_0(\zeta)$, given in (2.51). In the next section, we consider the solution to $f_1(\zeta)$ whose equation is given by (2.54). This solution is not important in the context of the steady streaming layer solution (2.49), but the constant a_1 is discussed.

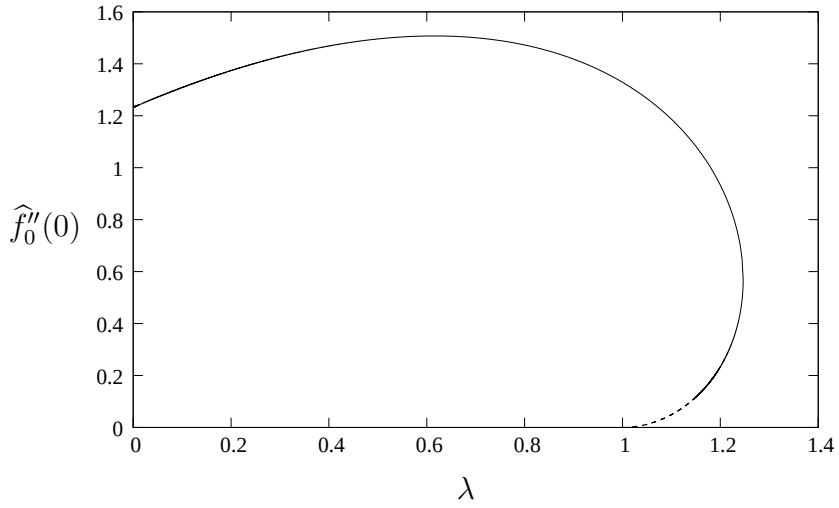

Figure 2.9: The possible values of λ for which solutions of equation (2.51) exist, where $\lambda = \frac{3}{4a_0}$. The solid line represents the numerics calculated from the Runge-Kutta technique, while the dotted line corresponds to the results from the finite difference scheme.

2.4.6 The first order correction, $f_1(\zeta)$

In this section, solutions are obtained for $f_1(\zeta)$, whose equation is given by (2.54). In solving this, we obtain the value of a_1 which corresponds to the critical value of a_{0c}, i.e. the correction term in the boundary between the solutions existing and breaking down at a finite-time singularity.

The first order equation, previously defined in equation (2.54), is given by

$$f_1''' + f_1 f_0'' + f_0 f_1'' - 2f_0' f_1' = \frac{f_0''}{2\sqrt{2}} - 2a_0 a_1, \tag{2.94}$$

with boundary conditions

$$f_1(0) = \frac{13}{4\sqrt{2}}, \qquad f_1'(0) = 0, \qquad f_1'(\zeta) \to a_1 \quad \text{as} \quad \zeta \to \infty, \tag{2.95}$$

where $a_0 > 0.6017$. Equation (2.94) is solved using a fourth-order Runge-Kutta technique, which is the same method that was used in solving the equation for $f_0(\zeta)$. In solving equation (2.94), the solutions to $f_0(\zeta)$ at each value of a_0 are used. As $f_1(\zeta)$ is reliant upon $f_0(\zeta)$, we find for each value of a_1, there are no solutions when $a_0 < 0.6017$, two solutions when $0.6017 < a_0 < 0.75$ and a unique solution when $a_0 > 0.75$. Figure 2.10 illustrates the primary shear component $f_1''(0)$ against a_0. At the critical value $a_{0c} = 0.6017$,

we find a unique value of $f_1''(0)$ for $a_1 = -0.55237$. For all other values of a_1, $f_1''(0)$ tends to either positive or negative infinity. This value agrees with Blyth and Hall (2003).

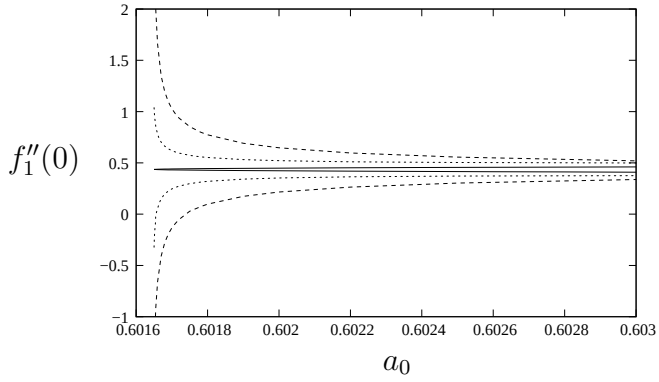

Figure 2.10: The primary shear component $f_1''(0)$ for $a_0 = 0.6017$ and $a_1 = -0.56$ (dashed lines), $a_1 = -0.55$ (dotted lines) and $a_1 = -0.55237$ (solid line). This illustrate that for $a_1 = -0.55237$, a unique value of $f_1''(0)$ exists.

2.5 Summary of primary flow

In section 2.4, we have solved the primary equation (2.25) in the parameter range $\Delta \sim O(\sigma^{1/2})$, where Δ and σ are large. This problem represents an unsteady stagnation-point flow travelling towards a fixed wall. The primary solution exhibits a double layer structure, with a Stokes layer next to the wall. Due to a horizontal velocity persisting to the top of the Stokes layer, a steady streaming layer is included to match between the Stokes layer and the far-field flow.

In solving the primary equation (2.17), we find the critical value given in (2.24) can be written as

$$\Delta = 1.289\sigma^{1/2} + 0.763 + O(\sigma^{-1/2}), \tag{2.96}$$

which is in excellent agreement with that of Blyth and Hall (2003). Above this critical value, solutions break down at a finite-time singularity and the behaviour of the solutions close to the time-singularity are discussed in chapter 4. In the next section, the subsidiary equation (2.26) is solved using methods and results from the primary problem.

2.6 The subsidiary flow

In this section, the subsidiary equation (2.26) is solved in the limit $\Omega \to \infty$ with $\widehat{\epsilon} \sim O(\Omega^{-1})$. Due to the coupling between the primary and subsidiary functions in equation (2.26), the structure of the subsidiary solution is similar to that of the primary solution. A Stokes layer is present at the wall with a steady streaming layer matching between the Stokes layer and the far-field flow.

We recall the subsidiary equation, which was initially stated in equation (2.26), is given by

$$\Omega\widehat{\psi}_{S\widehat{\eta}\tau} + \widehat{\psi}_{S\widehat{\eta}}\widehat{\psi}_{P\widehat{\eta}} - \widehat{\psi}_P\widehat{\psi}_{S\widehat{\eta}\widehat{\eta}} = \tag{2.97}$$
$$-\Omega\sin(\tau-\phi) + (\cos\tau + \widehat{\epsilon}\,)\cos(\tau-\phi) + \widehat{\psi}_{S\widehat{\eta}\widehat{\eta}\widehat{\eta}},$$

with boundary conditions

$$\widehat{\psi}_S(0,\tau) = 0, \quad \widehat{\psi}_{S\widehat{\eta}}(0,\tau) = \cos(\tau-\phi) \quad \text{on} \quad \widehat{\eta} = 0, \tag{2.98}$$
$$\widehat{\psi}_{S\widehat{\eta}}(\widehat{\eta},\tau) \to \cos(\tau-\phi) \quad \text{as} \quad \widehat{\eta} \to \infty, \tag{2.99}$$

where $\widehat{\epsilon} = a_0\Omega^{-1} + a_1\Omega^{-2} + O(\Omega^{-3})$. We begin by seeking a solution in the Stokes layer.

2.6.1 The Stokes layer

A Stokes layer is a small layer close to a boundary, occurring in oscillatory flow problems, where the unsteady and viscous components balance. The dominating terms in equation (2.97) are $\Omega\widehat{\psi}_{S\widehat{\eta}\tau} \sim \widehat{\psi}_{S\widehat{\eta}\widehat{\eta}\widehat{\eta}}$, which implies the scaling $\widehat{\eta} \sim \Omega^{-1/2}$. Therefore, the Stokes layer is of thickness $O(\Omega^{-1/2})$ with variable $\xi = \Omega^{1/2}\widehat{\eta}$, where $\xi = O(1)$. We note that this is the same thickness as that of the primary Stokes layer. Rewriting equation (2.97) in terms of ξ, we obtain

$$\Omega^{3/2}\widehat{\psi}_{S\xi\tau} + \Omega\left(\widehat{\psi}_{P\xi}\widehat{\psi}_{S\xi} - \widehat{\psi}_P\widehat{\psi}_{S\xi\xi}\right) = \tag{2.100}$$
$$-\Omega\sin(\tau-\phi) + (\cos\tau + \widehat{\epsilon}\,)\cos(\tau-\phi) + \Omega\widehat{\psi}_{S\xi\xi\xi},$$

with boundary conditions on the wall

$$\widehat{\psi}_S(0,\tau) = 0, \quad \widehat{\psi}_{S\eta}(0,\tau) = \Omega^{-1/2}\cos(\tau-\phi) \quad \text{on} \quad \xi = 0, \tag{2.101}$$

and the matching boundary condition to the far-field flow

$$\widehat{\psi}_{S\xi}(\xi,\tau) \to \Omega^{-1/2}\cos(\tau-\phi) \quad \text{as} \quad \xi \to \infty. \tag{2.102}$$

We seek a solution to (2.100), by posing the asymptotic expansion

$$\bar{\psi}_S = \Omega^{-1/2}\Psi_{S_0}(\xi,\tau) + \Omega^{-3/2}\Psi_{S_1}(\xi,\tau) + O(\Omega^{-5/2}). \tag{2.103}$$

Substituting the asymptotic expansion (2.103) into the subsidiary equation (2.100), we find at leading and first order

$$\Psi_{S_0\xi\tau} - \Psi_{S_0\xi\xi\xi} = -\sin(\tau-\phi), \tag{2.104}$$

$$\Psi_{S_1\xi\tau} - \Psi_{S_1\xi\xi\xi} = \cos\tau\cos(\tau-\phi) + \Psi_{P_0}\Psi_{S_0\xi\xi} - \Psi_{P_0\xi}\Psi_{S_0\xi}, \tag{2.105}$$

with boundary conditions on the wall

$$\Psi_{S_0}(0,\tau) = 0, \quad \Psi_{S_0\xi}(0,\tau) = \cos(\tau-\phi), \tag{2.106}$$

$$\Psi_{S_1}(0,\tau) = 0, \quad \Psi_{S_1\xi}(0,\tau) = 0. \tag{2.107}$$

Integrating (2.104) and (2.105), we obtain

$$\Psi_{S_0}(\xi,\tau) = \xi\cos(\tau-\phi), \tag{2.108}$$

$$\begin{aligned}\Psi_{S_1}(\xi,\tau) = {} & \frac{1}{2}\xi\sin\phi + \frac{1}{2}\Big(1-\frac{1}{\sqrt{2}}\Big)\sin\Big(2\tau-\phi-\frac{\pi}{4}\Big) \\ & + \frac{1}{2}\cos\Big(\phi+\frac{\pi}{4}\Big) + \frac{1}{2\sqrt{2}}e^{-\xi}\sin\Big(2\tau-\phi-\xi-\frac{\pi}{4}\Big) \\ & - \frac{1}{2}e^{-\xi/\sqrt{2}}\left[\cos\Big(\frac{\xi}{\sqrt{2}}-\phi-\frac{\pi}{4}\Big) + \sin\Big(2\tau-\frac{\xi}{\sqrt{2}}-\phi-\frac{\pi}{4}\Big)\right].\end{aligned} \tag{2.109}$$

When solving the leading and first order equations, (2.104) and (2.105), we have used the boundary conditions on the wall and the condition that $\Psi_{S_0}(\xi,\tau)$ and $\Psi_{S_1}(\xi,\tau)$ are periodic and bounded. As $\xi \to \infty$, the Stokes layer solution is given by

$$\widehat{\psi}_{S_\xi} \to \Omega^{-1/2}\cos(\tau-\phi) + \Omega^{-3/2}\frac{1}{2}\sin\phi + O(\Omega^{-5/2}) \quad \text{as} \quad \xi \to \infty. \tag{2.110}$$

This is unable to satisfy the far-field boundary condition (2.102), due to the first order component in (2.110), which can be interpreted as a horizontal velocity at the top of the Stokes layer. We proceed by introducing a steady streaming layer to match the velocity at the top of the Stokes layer to that of the far-field flow.

2.6.2 The steady streaming layer

In the previous section, it was found that at first order, the solution (2.109) in the Stokes layer is unable to satisfy the boundary condition in the far-field. As a result, like that of the primary problem, it is necessary to introduce a steady streaming layer of thickness $O(\Omega^{1/2})$ between the Stokes layer and the far-field flow. Therefore, we introduce the variable $\zeta = \Omega^{-1/2}\widehat{\eta}$, where $\zeta = O(1)$. Rewriting equation (2.97) in terms of the steady streaming layer variable, we obtain

$$\begin{aligned}\Omega^{1/2}\widehat{\psi}_{S\zeta\tau} + \Omega^{-1}\left(\widehat{\psi}_{P\zeta}\widehat{\psi}_{S\zeta} - \widehat{\psi}_{P}\widehat{\psi}_{S\zeta\zeta}\right) = \\ -\Omega\sin(\tau-\phi) + (\cos\tau + \widehat{\epsilon}\,)\cos(\tau-\phi) + \Omega^{-3/2}\widehat{\psi}_{S\zeta\zeta\zeta},\end{aligned} \tag{2.111}$$

with the far-field boundary condition

$$\widehat{\psi}_{S\zeta} \to \Omega^{1/2}\cos(\tau-\phi) \quad \text{as} \quad \zeta \to \infty. \tag{2.112}$$

To obtain the form of the asymptotic expansion in the steady streaming layer, we rewrite the Stokes layer solution as $\xi \to \infty$ in terms of the steady streaming layer variable ζ. The dominating terms are given by $\widehat{\psi}_S \sim \Omega^{1/2}\zeta\cos(\tau-\phi) + \Omega^{-1/2}\frac{1}{2}\zeta\sin\phi + \cdots$. This suggests the steady streaming layer expansion takes the form

$$\widehat{\psi}_S = \Omega^{1/2}\zeta\cos(\tau-\phi) + \Omega^{-1/2}G_S(\zeta,\tau), \tag{2.113}$$

where $G_S(\zeta,\tau)$ is given by

$$\begin{aligned}G_S(\zeta,\tau) = &\left(\Phi_{S_0}(\zeta,\tau) + F_0(\zeta)\right) + \Omega^{-1}\left(\Phi_{S_1}(\zeta,\tau) + F_1(\zeta)\right) \\ &+\Omega^{-2}\left(\Phi_{S_2}(\zeta,\tau) + F_2(\zeta)\right)\cdots.\end{aligned} \tag{2.114}$$

The functions $\Phi_{S_i}(\zeta,\tau)$ have a zero time-average and F_i are mean components, for $i \geq 0$. The last term in (2.114) is included because $\Phi_{S_2}(\zeta,\tau)$ is required to obtain the equation for $F_0(\zeta)$. Substituting the primary steady streaming layer solution, (2.49) and the subsidiary expansion given by (2.113) and (2.114) into the subsidiary equation (2.111), the leading and first order equations are given by

$$\Phi_{S_0\zeta\tau} = 0, \tag{2.115}$$

$$\begin{aligned}\Phi_{S_1\zeta\tau} &= a_0\cos(\tau-\phi) - \cos(\tau-\phi)\Big(\Phi_{P_0\zeta} + f_{0\zeta}\Big) \\ &\quad - \cos\tau\Big(\Phi_{S_0\zeta} + F_{0\zeta}\Big) + \zeta\cos\tau\Big(\Phi_{S_0\zeta\zeta} + F_{0\zeta\zeta}\Big).\end{aligned} \tag{2.116}$$

Integrating (2.115) and (2.116) with respect to τ and taking a time-average to obtain the function of integration, we obtain $\Phi_{S_0\zeta} = 0$, and $\Phi_{S_1\zeta} = (a_0\zeta - f_0)\sin(\tau-\phi) + (\zeta F_0' - 2F_0)\sin\tau$, where the prime denotes differentiation with respect to ζ. Upon integrating these equations with respect to ζ, we obtain $\Phi_{S_0}(\zeta,\tau) = g_0(\tau)$ and $\Phi_{S_1}(\zeta,\tau) = (a_0\zeta - f_0)\sin(\tau-\phi) + (\zeta F_0' - 2F_0)\sin\tau + g_1(\tau)$, where $g_0(\tau)$ and $g_1(\tau)$ are found by matching to the Stokes layer solution. In the matching region, the Stokes layer solution is written in terms of the steady streaming layer variable ζ and is given by

$$\begin{aligned}\widehat{\psi}_S &\sim \Omega^{1/2}\zeta\cos(\tau-\phi) + \Omega^{-1/2}\frac{1}{2}\zeta\sin\phi \\ &\quad + \Omega^{-3/2}\frac{1}{2}\Bigg[\left(1-\frac{1}{\sqrt{2}}\right)\sin\left(2\tau-\phi-\frac{\pi}{4}\right) \\ &\quad + \cos\left(\phi+\frac{\pi}{4}\right)\Bigg] + O(\Omega^{-5/2}).\end{aligned} \tag{2.117}$$

Therefore, matching (2.117) and (2.113), we find $g_0(\tau) = 0$ and $g_1(\tau) = \frac{1}{2}\left(1-\frac{1}{\sqrt{2}}\right)\sin\left(2\tau-\phi-\frac{\pi}{4}\right)$ and the subsidiary steady streaming layer solution is given by

$$\begin{aligned}\widehat{\psi}_S &= \Omega^{1/2}\zeta\cos(\tau-\phi) + \Omega^{-1/2}F_0(\zeta) \\ &\quad + \Omega^{-3/2}\Bigg[\Big(a_0\zeta - f_0(\zeta)\Big)\sin(\tau-\phi) + \Big(\zeta F_0'(\zeta) - 2F_0(\zeta)\Big)\sin\tau \\ &\quad + \frac{1}{2}\left(1-\frac{1}{\sqrt{2}}\right)\sin\left(2\tau-\phi-\frac{\pi}{4}\right) + F_1(\zeta)\Bigg] + O(\Omega^{-5/2}).\end{aligned} \tag{2.118}$$

To obtain a relationship for the unknown functions $F_0(\zeta)$, we collect terms of size $O(\Omega^{-2})$ in equation (2.111), to find

$$\begin{aligned}\Psi_{S_2\zeta\tau} &= -\cos(\tau-\phi)\Big[(2a_0+\zeta f_0''-2f_0')\sin\tau+f_1'\Big]-F_0'f_0' \\ &\quad -\cos\tau\Big[(a_0-f_0')\sin(\tau-\phi)+(\zeta F_0''-F_0')\sin\tau+F_1'\Big] \\ &\quad +\zeta\cos\tau\Big[\zeta F_0'''\sin\tau-f_0''\sin(\tau-\phi)+F_1''\Big] \\ &\quad -\cos\left(\tau-\frac{\pi}{4}\right)F_0''+f_0F_0''+a_1\cos(\tau-\phi)+F_0'''.\end{aligned} \tag{2.119}$$

Averaging over a single time period, we find

$$F_0'''-f_0'F_0'+f_0F_0''=\left(\frac{a_0-f_0'}{2}\right)\sin\phi. \tag{2.120}$$

The boundary conditions at $\zeta=0$ are obtained by matching the steady streaming layer solution (2.118) to the Stokes layer solution (2.117). In doing so, we find $F_0(\zeta)\to\zeta\sin\phi/2$ as $\zeta\to 0$. The far-field boundary condition is obtained by matching the steady streaming layer solution (2.118) to the far-field condition (2.112). Therefore, the boundary conditions for equation (2.120) are given by

$$F_0(0)=0,\qquad F_0'(0)=\frac{1}{2}\sin\phi,\qquad F_0'(\zeta)\to 0\quad\text{as}\quad\zeta\to\infty. \tag{2.121}$$

If the phase difference is such that $\sin\phi=0$ i.e. $\phi=0,\pi$, the problem reduces to

$$F_0'''-f_0'F_0'+f_0F_0''=0, \tag{2.122}$$

$$F_0(0)=0,\qquad F_0'(0)=0,\qquad F_0'(\zeta)\to 0\quad\text{as}\quad\zeta\to\infty, \tag{2.123}$$

and the only solution is the trivial one, $\widehat{F}_0(\widehat{\zeta})=0$. For other values of ϕ, it is convenient to allow equation (2.120) to be independent of the phase difference, ϕ. We let $F_0(\zeta)=\sin\phi\bar{F}_0(\zeta)$ and the first order equation (2.120) becomes

$$\bar{F}_0'''-f_0'\bar{F}_0'+f_0\bar{F}_0''=\frac{a_0-f_0'}{2}, \tag{2.124}$$

with boundary conditions

$$\bar{F}_0(0)=0,\qquad \bar{F}_0'(0)=\frac{1}{2},\qquad \bar{F}_0'(\zeta)\to 0\quad\text{as}\quad\zeta\to\infty. \tag{2.125}$$

For completeness, we include the equation for $F_1(\zeta)$, however, it is not be solved as it would have little effect on the steady streaming layer solution (2.118). To obtain the equation for $F_1(\zeta)$, we collect the terms of size $O(\Omega^{-3})$ in equation (2.111) and average over a single time period, to find

$$F_1''' + f_1 F_0'' + f_0 F_1'' - f_0' F_1' - f_1' F_0' = \frac{F_0''}{2\sqrt{2}} + \left(\frac{a_1 - f_1'}{2}\right) \sin\phi, \quad (2.126)$$

with boundary conditions

$$F_1(0) = \frac{1}{2}\cos\left(\phi + \frac{\pi}{4}\right), \quad F_1'(0) = 0, \qquad F_1'(\zeta) \to 0 \quad \text{as} \quad \zeta \to \infty, \quad (2.127)$$

which are obtained in a similar way to that described for $F_0(\zeta)$.

In the next section, we solve equation (2.124) with boundary conditions (2.125) using similar techniques to those used to solve the primary equation (2.51).

2.6.3 Numerics

In this section, we solve equation (2.124) by initially using a fourth order Runge-Kutta technique. We write (2.124) in terms of three first order equations by letting $\bar{F}_0 = z_1$ and $f_0 = y_1$. It follows that

$$z_1' = z_2, \quad (2.128)$$

$$z_2' = z_3, \quad (2.129)$$

$$z_3' = y_2 z_2 - y_1 z_3 + \frac{(a_0 - y_2)}{2}, \quad (2.130)$$

with boundary conditions

$$z_1(0) = 0, \qquad z_2(0) = \frac{1}{2}, \qquad z_2(\infty) = 0. \quad (2.131)$$

In section 2.4.3, we found that by using a Runge-Kutta technique, $f_0(\zeta)$ has no solutions when $a_0 < 0.6017$. As a_0 increases, we find two solutions when $0.6017 < a_0 < 0.7$. When $a_0 \approx 0.7$, one of the solutions breaks down due to the primary equation becoming sensitive to the initial conditions. Therefore, due to the subsidiary equation (2.124) being coupled with the primary equation, we find there are no solutions for $\bar{F}_0(\zeta)$ when $a_0 < 0.6017$ and two

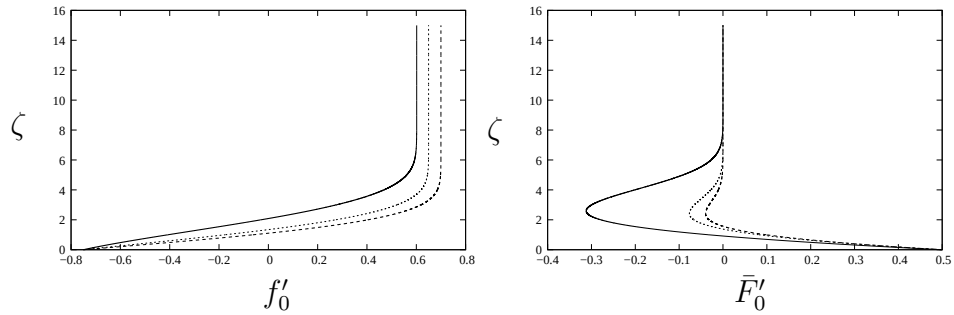

(a)

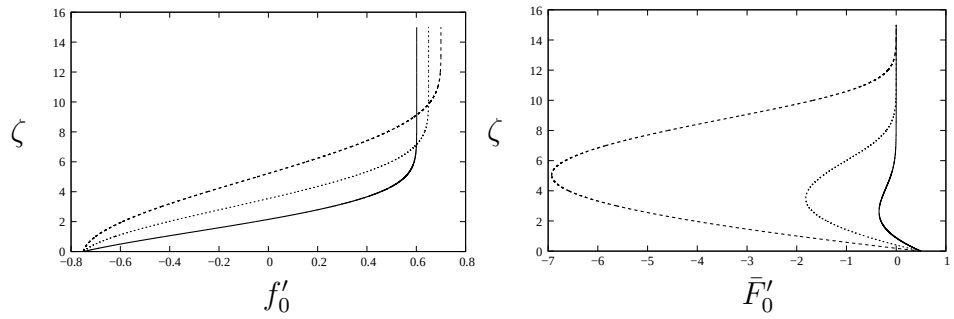

(b)

Figure 2.11: (a) The first primary velocity profile for $a_0 = 0.6017, 0.65, 0.7$ with its corresponding subsidiary velocity profile. (b) The second primary velocity profile for $a_0 = 0.6017, 0.65, 0.7$ with its corresponding subsidiary velocity profile. We note that this solution is unable to be calculated by the Runge-Kutta method when $a_0 \gtrsim 0.7$. In each case, the solid line represents $a_0 = 0.6017$, the dotted line, $a_0 = 0.65$ and the dashed line, $a_0 = 0.7$.

solutions when $0.6017 < a_0 < 0.7$. In figure 2.11, the subsidiary velocity profiles are plotted for $a_0 = 0.6017, 0.65, 0.7$, along with the corresponding primary velocity profiles. As is shown in figure 2.11(b), as a_0 increases, the disturbance close to $\zeta = 0$ increases and exhibits a larger region of flow reversal than the velocity profiles in figure 2.11(a). This behaviour is confirmed in Appendix A, where the asymptotic solution for $F_0(\zeta)$ is found close to $a_0 \approx 0.75$.

To obtain the remaining solutions to $\bar{F}_0(\zeta)$ when $0.7 < a_0 < 0.75$, we use a finite-difference technique. We rewrite equation (2.124) without the a_0 dependence, by letting $\bar{F}_0 = a_0^{-1/2}\widehat{F}_0$ and as before, $f_0 = a^{1/2}\widehat{f}_0$ with $\widehat{\zeta} = a_0^{1/2}\zeta$, to obtain

$$\widehat{F}_0''' - \widehat{f}_0'\widehat{F}_0' - \widehat{f}_0\widehat{F}_0'' = \frac{1 - \widehat{f}_0'}{2}. \tag{2.132}$$

Like that of the primary problem discussed in section 2.4.5, we let $\widehat{F}_0' = G_0$ and $\widehat{f}_0' = g_0$, which enables equation (2.132) to be rewritten as the second order equation

$$G_0'' - g_0 G_0 + \widehat{f}_0 G_0' = \frac{1 - g_0}{2}. \tag{2.133}$$

Centrally discretising equation (2.133), gives

$$\frac{1}{h^2}\Big(G_{0_{i+1}} - 2G_{0_i} + G_{0_{i-1}}\Big) - g_{0_i} G_{0_i} + \frac{\widehat{f}_{0_i}}{2h}\Big(G_{0_{i+1}} - G_{0_{i-1}}\Big) = \frac{1 - g_{0_i}}{2}, \tag{2.134}$$

with boundary conditions

$$\widehat{F}_{0_1} = 0, \quad G_{0_1} = \frac{1}{2}, \quad G_{0_N} = 0. \tag{2.135}$$

The functions $\widehat{f}_{0_i}$ and g_{0_i} represent the primary solution and $\widehat{F}_{0_i}$ and G_{0_i} represent the unknown subsidiary functions at each grid point $\widehat{\zeta}_i = ih$, where h is the spatial step size and $i = 1...N$. Equation (2.134) can be rewritten in the form of the tridiagonal system

$$A_i G_{0_{i+1}} + B_i G_{0_i} + C_i G_{0_{i-1}} = D_i, \tag{2.136}$$

where the constants $A_i \ldots D_i$ are given by

$$A_i = \frac{1}{h^2} + \frac{\widehat{f}_{0_i}}{2h}, \tag{2.137}$$

$$B_i = \frac{-2}{h^2} - g_{0_i}, \tag{2.138}$$

$$C_i = \frac{1}{h^2} - \frac{\widehat{f}_{0_i}}{2h}, \tag{2.139}$$

$$D_i = \frac{1 - g_{0_i}}{2}. \tag{2.140}$$

As before, we solve the discretised equation using the Thomas algorithm, where the spatial step size $h = 0.001$. This corresponds to the spatial step size chosen in the primary finite-difference method. The numerics are initiated at $\lambda \approx 1$, which corresponds to $a_0 \approx 0.75$, where $\lambda = 1 + \epsilon$ and $0 < \epsilon \ll 1$, which was initially defined when solving the primary equation using the finite-difference technique. The numerics are marched backwards until $\lambda \approx 1.0714$, which corresponds to $a_0 \approx 0.7$. In figure 2.12, we illustrate the subsidiary

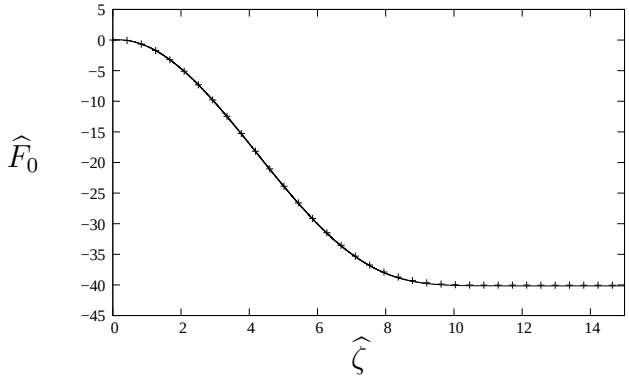

Figure 2.12: The subsidiary solution for the finite-difference method, represented by the crosses and the Runge-Kutta method, represented by solid line for $a_0 = 0.7$, showing excellent agreement.

solution for both the Runge-Kutta and finite-difference methods for $a_0 = 0.7$, showing excellent agreement between these methods.

In figure 2.13, we illustrate the numerical results from the Runge-Kutta and the finite-difference schemes. This illustrates that there is a unique solution when $\lambda < 1$, two solutions when $1 < \lambda < 1.246$ and no solutions when $\lambda > 1.246$, where $\lambda = \frac{3}{4a_0}$. These correspond to a unique solution when $a_0 > 0.75$, two solutions when $0.6017 < a_0 < 0.75$ and no solutions when $a_0 < 0.6017$. Contrary to the primary problem, where the solutions were well behaved close to $a_0 \approx 0.75$, figure 2.13 illustrates as $\lambda \to 1$, $\widehat{F}_0''(0) \to -\infty$.

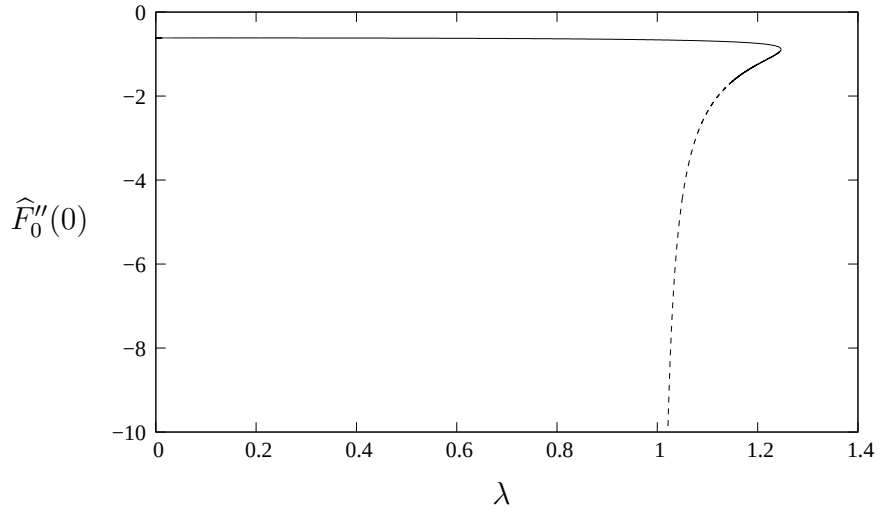

Figure 2.13: The possible values of λ for which solutions to equation (2.132) exist. The solid line represents the numerics calculated from the Runge-Kutta method and the dotted line represents the finite difference method results.

2.7 Summary of subsidiary flow

In section 2.6, the subsidiary equation (2.26) has been solved in the large frequency limit, in the parameter range $\Delta \sim O(\sigma^{1/2})$. As the subsidiary equation is coupled with the primary equation (2.25), the structure of the subsidiary problem near the wall is the same. At the wall, there exists a Stokes layer with a steady streaming layer matching between the Stokes layer and the far-field flow. In solving the primary equation, the critical value between solutions existing and breaking down at a finite-time singularity is found and given in (2.96). Due to the dependence on the primary equation, we have found that no solutions for the subsidiary equation occur above this limit.

Having obtained solutions to both the primary and subsidiary equations, in the next section, we consider the wall shear stress and the effect the oscillating components have on the mean wall shear stress.

2.8 Wall shear stress

In this section, we obtain the wall shear stress in the large frequency limit and discuss the effect of the horizontal oscillating components. In section 2.2, the oscillating stagnation-point flow was discussed in two frames of reference. Firstly, where the oscillatory stagnation-point flow travels towards a fixed wall and the stagnation point oscillates along the fixed wall. The second frame was where the oscillating stagnation-point flow travels towards an oscillating wall and the stagnation point is fixed at the origin. Solutions were found in the latter frame of reference. However, to obtain the wall shear stress, we revert back to the original frame and consider a moving stagnation point.

The wall shear stress is defined as

$$S = \mu u_y\big|_{y=0} = \mu \psi_{yy}\big|_{y=0}, \tag{2.141}$$

where μ is the viscosity. The streamfunction ψ, initially stated in (2.16), is

written in terms of the scalings, $\psi_S = \Delta^{-1/2}\widehat{\psi_S}$, $\psi_P = \Delta^{1/2}\widehat{\psi_P}$ and $\widehat{\eta} = \Delta^{1/2}\eta$ with $\eta = (k/\nu)^{1/2}y$, which were introduced in section 2.3, to give

$$\psi(x,y,t) = (\nu k)^{1/2}x\Delta^{1/2}\widehat{\psi}_P(\widehat{\eta},\tau) + U_S\left(\frac{\nu}{k}\right)^{1/2}\Delta^{-1/2}\widehat{\psi}_S(\widehat{\eta},\tau). \quad (2.142)$$

We write $x = x_0^* + \frac{U_S}{\omega}\sin(\tau-\phi)$, where x_0^* is the coordinate in the first frame of reference. Upon substituting this and the streamfunction (2.142) into (2.141), the wall shear stress is given by $S = \mu k S^*$. In this, S^* is non-dimensional and given by

$$S^* = \left[\Delta^{3/2}\left[X_0 + \frac{\kappa}{\sigma}\sin(\tau-\phi)\right]\widehat{\psi}_{P_{\widehat{\eta}\widehat{\eta}}} + \Delta^{1/2}\kappa\widehat{\psi}_{S_{\widehat{\eta}\widehat{\eta}}}\right]\Bigg|_{\widehat{\eta}=0}, \quad (2.143)$$

where $X_0 = \left(\frac{k}{\nu}\right)^{1/2}x_0^*$ and $\kappa = \frac{U_S}{(k\nu)^{1/2}}$, which is a measure of the effect of the oscillatory components.

Solutions to the primary and subsidiary problems have been obtained in the parameter range $\widehat{\epsilon} \sim O(\Omega^{-1})$, where $\Omega = \sigma\widehat{\epsilon}$ and $\widehat{\epsilon} = 1/\Delta$. We recall that $\widehat{\epsilon} = a_0\Omega^{-1} + a_1\Omega^{-2} + O(\Omega^{-3})$, as was initially stated in (2.31). Using this expansion, relations for Ω and σ in terms of Δ are given by

$$\Omega = a_0\Delta + \frac{a_1}{a_0} + O(\Delta^{-1}), \qquad \sigma = a_0\Delta^2 + \frac{a_1\Delta}{a_0} + O(1). \quad (2.144)$$

Equation (2.143) is rewritten in terms of the Stokes layer variable $\xi = \Omega^{1/2}\widehat{\eta}$, where the Stokes layer expansions were previously defined in (2.35) and (2.103). Using the relations given in (2.144), we find

$$\begin{aligned} S^* \;=\; & \Delta^2 a_0^{1/2}X_0\Psi_{P_0\xi\xi} + \frac{\Delta X_0}{a_0^{1/2}}\left(\frac{a_1}{2a_0}\Psi_{P_0\xi\xi} + \Psi_{P_1\xi\xi}\right) \\ & + \frac{\kappa}{a_0^{1/2}}\left(\Psi_{S_1\xi\xi} + \sin(\tau-\phi)\Psi_{P_0\xi\xi}\right) \\ & + \frac{X_0}{a_0^{3/2}}\left(\frac{a_1^2}{8a_0^2}\Psi_{P_0\xi\xi} - \frac{a_1}{2a_0}\Psi_{P_1\xi\xi} + \Psi_{P_2\xi\xi}\right)\Bigg|_{\xi=0} + O(\Delta^{-1}). \end{aligned} \quad (2.145)$$

We note that $\Psi_{S_0\xi\xi}(0,\tau) = 0$ and $\Psi_{P_2\xi\xi}(\xi,\tau)$ has not previously been found, but is required when calculating the mean wall shear stress and is discussed later in this section. Evaluating the primary and subsidiary functions at

$\xi = 0$, the wall shear stress is given by

$$\begin{aligned} S^* &= \Delta^2 a_0^{1/2} X_0 \cos\Big(\tau + \frac{\pi}{4}\Big) + \frac{\Delta X_0}{a_0^{1/2}}\Bigg[\frac{a_1}{2a_0}\cos\Big(\tau + \frac{\pi}{4}\Big) + \frac{1}{2\sqrt{2}} \\ &\quad + \Big(\frac{1}{\sqrt{2}} - \frac{1}{2}\Big)\Big(\cos 2\tau + \sin 2\tau\Big)\Bigg] \\ &\quad + \frac{\kappa}{a_0^{1/2}}\Bigg[\frac{1}{2}\sin\Big(\phi + \frac{\pi}{4}\Big) + \Big(\frac{1}{\sqrt{2}} - \frac{1}{2}\Big)\sin\Big(2\tau - \phi + \frac{\pi}{4}\Big) \\ &\quad + \sin(\tau - \phi)\cos\Big(\tau + \frac{\pi}{4}\Big)\Bigg] \\ &\quad + \frac{X_0}{a_0^{3/2}}\Bigg[\frac{a_1^2}{8a_0^2}\cos\Big(\tau + \frac{\pi}{4}\Big) - \frac{a_1}{2a_0}\Bigg(\frac{1}{2\sqrt{2}} \\ &\quad + \Big(\frac{1}{\sqrt{2}} - \frac{1}{2}\Big)\Big(\cos 2\tau + \sin 2\tau\Big)\Bigg) + \Psi_{P_2\xi\xi}\Big|_{\xi=0}\Bigg] + O(\Delta^{-1}). \end{aligned} \tag{2.146}$$

The wall shear stress (2.146) is a linear function of X_0 and at the stagnation point the wall shear stress is at its lowest. Although it appears in (2.146) that the wall shear stress tends to infinity as $X_0 \to \infty$, this model is only valid local to the stagnation point.

To calculate the mean wall shear stress a time-average of (2.146) is taken. Before doing so, $\Psi_{P_2}(\xi, \tau)$ is needed. By using the same method used in section 2.4, the equation for $\Psi_{P_2}(\xi, \tau)$ is given by

$$\psi_{P_2\xi\tau} - \psi_{P_2\xi\xi\xi} = 2a_0\cos\tau - 2\psi_{P_0\xi}\psi_{P_1\xi} + \psi_{P_0}\psi_{P_1\xi\xi} + \psi_{P_0\xi\xi}\psi_{P_1}, \tag{2.147}$$

with wall boundary conditions $\psi_{P_2}(0, \tau) = 0$ and $\psi_{P_2\xi}(0, \tau) = 0$. From equations (2.36) and (2.37), the functions $\psi_{P_0}(\xi, \tau)$ and $\psi_{P_1}(\xi, \tau)$ can be written in the form $\psi_{P_0}(\xi, \tau) = e^{i\tau}g(\xi) + e^{-i\tau}g^*(\xi)$ and $\psi_{P_1}(\xi, \tau) = e^{2i\tau}h_0(\xi) + e^{-2i\tau}h_0^*(\xi) + h_1(\xi)$ where $g^*(\xi)$ and $h_0^*(\xi)$ are the complex conjugates of $g(\xi)$ and $h_0(\xi)$ respectively. Therefore, on substituting the expansions for $\psi_{P_0}(\xi, \tau)$ and $\psi_{P_1}(\xi, \tau)$ into equation (2.147), we find $\psi_{P_2}(\xi, \tau)$ has the form $\psi_{P_2}(\xi, \tau) = e^{3i\tau}P_1(\xi) + e^{i\tau}P_2(\xi) + e^{-3i\tau}P_1^*(\xi) + e^{-i\tau}P_2^*(\xi)$, where $P_1^*(\xi)$ and $P_2^*(\xi)$ are the complex conjugates of $P_1(\xi)$ and $P_2(\xi)$ respectively. Hence, once a time-average has been taken, there is no contribution from $\psi_{P_2}(\xi, \tau)$ and it is not necessary to calculate it. Therefore, upon taking a time-average of the wall

shear stress (2.146), we obtain the mean wall shear stress

$$\bar{S}^* = \Delta^{3/2}\Big(a_0\Delta + \frac{a_1}{a_0}\Big)^{-1/2}\frac{1}{2\sqrt{2}}X_0, \tag{2.148}$$

where $\bar{S}^*$ indicates the averaged value. The mean wall shear stress (2.148) is a linear function of X_0, where X_0 is the distance from the stagnation point. Consequently, the mean wall shear stress is equal to zero when $X_0 = 0$, at the stagnation point. As X_0 increases, the mean wall shear stress also increases. It can be seen that the mean wall shear stress has no contribution from the oscillatory components and is solely dependent upon the primary problem.

Hazel and Pedley (1998) considered the problem described by (2.17) - (2.22) in the limit of large frequency, but restricted the amplitude to less than one, to prevent flow reversal from occurring. They ascertained that for large frequency, the oscillatory component had no effect on the mean wall shear stress. Therefore, having extended this analysis to allow for flow reversal to occur, in the parameter range $\Delta \sim O(\sigma^{1/2})$, the effect of the oscillatory component on the mean wall shear stress is unchanged, even though the asymptotic structure has changed.

2.9 Summary

In this chapter, a two-dimensional orthogonal unsteady stagnation-point flow travelling towards an oscillating wall has been discussed. The flow in the far-field comprises an unsteady orthogonal stagnation-point flow, consisting of a mean component and an oscillatory component, dependent upon a relative amplitude parameter: Δ and dimensionless frequency parameter: σ. Added to this is a horizontal oscillating component, with the same frequency as the oscillatory wall. Close to the wall, a similarity solution was sought, which is an exact solution of the Navier-Stokes equations. The similarity solution is made up of two terms: an unsteady orthogonal stagnation-point flow component and an oscillatory component. The problem is described in terms of two equations, the orthogonal equation, which was denoted the primary equation and has previously been addressed by Merchant and Davis (1989),

among others, and an oscillatory equation, denoted the subsidiary equation, which had a coupling with the primary. This problem has previously been addressed by Hazel and Pedley (1998), who chose a relative amplitude that does not allow the flow to reverse. In this chapter, we have considered solutions to the subsidiary equation, where relative amplitude is chosen to allow for flow reversal.

For a fixed dimensionless frequency, when the relative amplitude parameter exceeds a critical amplitude, the primary and subsidiary equations break down at a finite-time singularity. Later in this thesis, in chapter 4, the primary equation is solved numerically and the behaviour of the solutions, as the finite-time singularity is approached, are discussed. In the present chapter, an asymptotic analysis has been performed for large frequency close to this critical amplitude, i.e. $\Delta \sim O(\sigma^{1/2})$. At the wall, a Stokes layer of thickness $O\left(\sigma^{-1/2}\right)$ is present. In this regime, where the oscillatory component of the unsteady orthogonal flow is much larger than the mean component, the steady streaming layer, which matches the Stokes layer to the far-field flow, has thickness on the order of σ/Δ times that of the Stokes layer. This structure is unlike that of the one considered by Hazel and Pedley (1998), who solved this problem where the mean component dominates in the unsteady orthogonal component and the steady streaming layer thickness is on the order of $\sigma^{1/2}/\Delta$ times that of the Stokes layer.

Hazel and Pedley (1998), who restricted the relative amplitude parameter to prevent flow reversal occurring, found that the oscillatory components did not effect the mean wall shear stress, which was only dependent upon the orthogonal stagnation-point flow. Having extended this analysis to allow for flow reversal to occur, we found that even though the asymptotic structure has changed, the oscillatory components did not effect the mean wall shear stress.

Chapter 3

Steady oblique stagnation-point flow

3.1 Introduction

Continuing our investigation into stagnation-point flows, we consider a problem, which is a generalisation of the Hiemenz stagnation-point flow, where the streamlines meet the wall obliquely. This problem comprises of a Hiemenz stagnation-point flow and, superimposed onto this, a shear flow with constant vorticity and a uniform stream, whose strength is represented by a free parameter. We denote these two latter terms as the oblique component. Due to the no-slip condition not being satisfied at the wall, a similarity solution is introduced consisting of two components: a Hiemenz function and the integral of the oblique component.

A special case of the above problem was first considered by Stuart (1959) with Tamada (1979) and Dorrepaal (1986) later revisiting this problem with slightly different conditions on the far-field flow. These different cases can be thought of as changing the uniform stream in the far-field, but ultimately they obtained similar results. Drazin and Riley (2006) generalised the work of the previous authors to include a free parameter, which altered the strength of the uniform stream. They found the free parameter changes the magnitude of the pressure gradient, which in turn alters the structure of the oblique

component. If the free parameter is large enough, the oblique velocity component has a region of flow reversal near the wall.

In this chapter, we extend the work of Drazin and Riley (2006) to find what effect this parameter has on the streamlines, even if the oblique component has a region of flow reversal close to the wall. Having considered the form of the oblique stagnation-point flow discussed initially by Stuart (1959), we then obtain the general form of the far-field solution where a Hiemenz flow and a general horizontal function is present.

We note that section 3.2 has already been published in the Physics of Fluids.

3.2 Steady oblique stagnation-point flow

We consider the two-dimensional oblique stagnation-point flow of a viscous fluid of kinematic viscosity ν towards a plane wall. In Cartesian (x, y) coordinates, the wall is located at $y = 0$ and the fluid occupies the region $y > 0$. It is convenient to represent the flow with a streamfunction, $\psi(x, y)$, defined in the usual way so that $u = \psi_y$ and $v = -\psi_x$, where u and v are the velocity components in the x and y directions respectively. A long way from the wall, the flow is given by

$$\psi = kxy + \frac{1}{2}\zeta y^2 - \beta\zeta \left(\frac{\nu}{k}\right)^{1/2} y, \tag{3.1}$$

comprising an irrotational straining flow of strength k, and a rotational shear flow in the x direction with vorticity $-\zeta < 0$. The dividing streamline, $\psi = 0$, meets the horizontal boundary at the angle $\tan^{-1}(-2k/\zeta)$ and is illustrated in figure 3.1.

Close to the wall, we seek a solution in the more general form, given by Stuart (1959)

$$\psi = (\nu k)^{1/2} x f(\eta) + \zeta \left(\frac{\nu}{k}\right) \int_0^\eta g(t)\,\mathrm{d}t, \tag{3.2}$$

where $\eta = (k/\nu)^{1/2} y$. Consistency with the outer flow (3.1) requires both that $f \sim \eta - \alpha$ and $g \sim \eta - \beta$ as $\eta \to \infty$, where α and β are constants.

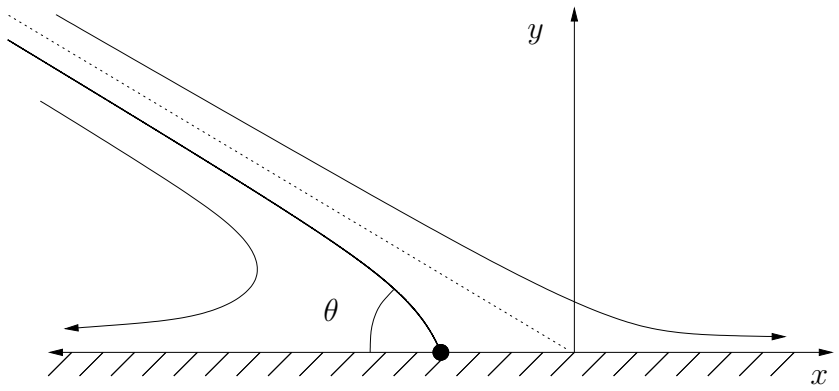

Figure 3.1: An illustration of the dividing streamline meeting the wall obliquely at an angle of $\theta = \tan^{-1}(-2k/\zeta)$.

Substituting (3.2) into the Navier-Stokes equation, demanding no-slip and no-penetration at the wall, and requiring a match with the outer flow, we find that f satisfies

$$f''' + ff'' - f'^2 + 1 = 0, \tag{3.3}$$

with

$$f(0) = 0, \quad f'(0) = 0, \quad f'(\infty) = 1, \tag{3.4}$$

and that g satisfies

$$g'' + fg' - f'g = \beta - \alpha, \tag{3.5}$$

with

$$g(0) = 0, \quad g'(\infty) = 1. \tag{3.6}$$

The primes denote differentiation with respect to η. The pressure at any point in the fluid is given by

$$p = p_0 - \frac{1}{2}\rho k^2 x^2 - \frac{1}{2}\rho\nu k f^2 - \rho\nu k f' + \zeta\rho(\nu k)^{1/2}\,(\beta - \alpha)\,x, \tag{3.7}$$

where p_0 is a constant reference value and ρ is the density of the fluid. When $\beta = \alpha$ the pressure field is independent of the shear flow.

When $\zeta = 0$ and the shear flow is removed, we recover the orthogonal stagnation-point flow studied by Hiemenz (1911) and discussed by Batchelor

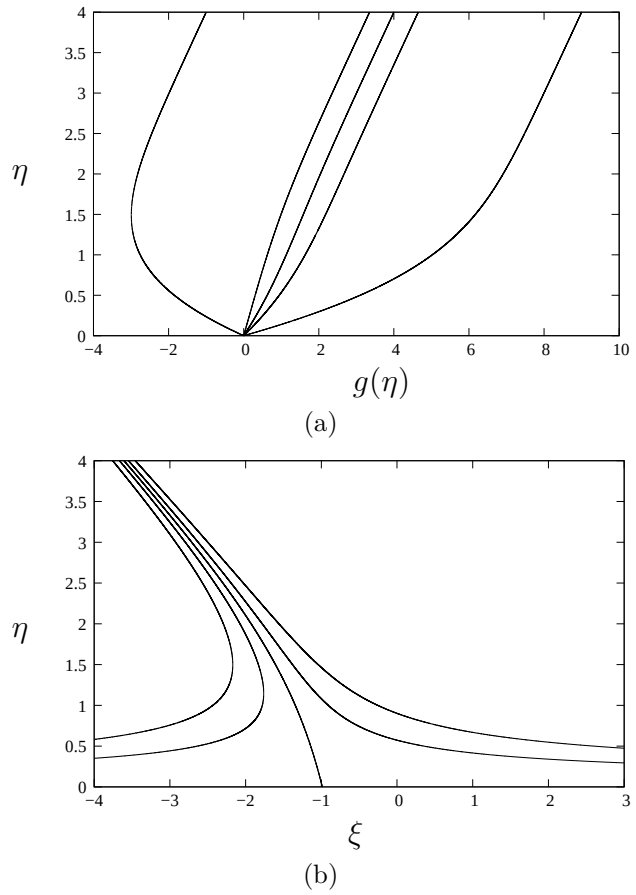

Figure 3.2: (a) Profiles of the shear flow component for $\beta = 5, \alpha, 0, -\alpha, -5$, reading from left to right. (b) Streamlines for the case $k/\zeta = 0.5$ and $\beta = \alpha$, where $\xi = (k/\nu)^{1/2}x$.

(2000), for example. Accordingly, the whole flow may be viewed as being composed of orthogonal stagnation-point flow, represented by the first term in (3.2), combined with a horizontal shear flow represented by the second term in (3.2). The solution for the shear flow, $g(\eta)$, is contingent on the solution for the orthogonal flow, $f(\eta)$, but not vice versa.

The constant α in (3.5) is determined as part of the solution for the orthogonal flow, f. However, β is a free parameter. The analyses of Stuart (1959) and Tamada (1979) correspond to $\beta = \alpha$ and the analysis of Dorrepaal (1986) corresponds to $\beta = 0$. Referring to (3.7), varying β may be interpreted physically as varying the horizontal pressure gradient linked to the shear flow. The horizontal velocity u, is given by

$$u = kxf'(\eta) + \zeta \left(\frac{\nu}{k}\right)^{1/2} g(\eta), \tag{3.8}$$

and in figure 3.2(a), we show profiles of the shear flow component, g, for a number of different values of β. When $\beta > 1.141$, there is a distinct region of reversed flow corresponding to negative values of g. When combined with the orthogonal flow, we would expect such a feature to have a significant effect on the structure of the complete flow. In particular, we would expect it to shift the stagnation-point of attachment along the wall.

The solution of (3.3) and (3.4) has been obtained numerically (e.g., Goldstein (1965)) to find $\gamma \equiv f''(0) = 1.233$ and $\alpha = 0.648$. Introducing $\delta \equiv g'(0)$, the general solution to (3.5) and (3.6), previously given by Stuart (1959), is

$$g(\eta) = (\alpha - \beta) f'(\eta) + \gamma\lambda\, h(\eta), \tag{3.9}$$

where

$$h(\eta) = f''(\eta) \int_0^\eta [f''(t)]^{-2}\, e^{-\int_0^t f(s)\, ds}\, \mathrm{d}t, \tag{3.10}$$

and $\lambda = \delta + (\beta - \alpha)\gamma$. The value of δ depends on the choice of β. Taking the limit $\eta \to \infty$ in (3.9), and using the fact that

$$f''(\eta) \int_0^\eta [f''(t)]^{-2}\, e^{-\int_0^t f(s)\, ds}\, \mathrm{d}t \sim 1.335\,(\eta - \alpha) + \cdots \tag{3.11}$$

as $\eta \to \infty$, which was used by Glauert (1956), we confirm that (3.9) fulfills the condition at infinity in (3.6), provided that

$$\lambda = 0.608, \tag{3.12}$$

regardless of the value of β. It follows from (3.9) and (3.10) that

$$g(\eta) = w(\eta) - \beta f'(\eta) \tag{3.13}$$

where $w(\eta) = \alpha f'(\eta) + \gamma\lambda\, h(\eta)$ satisfies the same system as $g(\eta)$, namely (3.5) and (3.6), with β set to zero. Substituting (3.13) into (3.2), we find

$$\psi = (\nu k)^{1/2} \chi f(\eta) + \zeta \left(\frac{\nu}{k}\right) \int_0^\eta w(t)\, \mathrm{d}t, \tag{3.14}$$

where $\chi = x - \zeta(\nu/k^3)^{1/2}\beta$.

Since neither $f(\eta)$ nor $w(\eta)$ depend upon β, we see that the effect of increasing β is to shift the streamlines to the right in the positive x direction,

without changing the overall flow structure. From a mathematical standpoint, this simply reflects the freedom to shift the origin of the axes noted by Stuart (1959). So Dorrepaal's solution, with $\beta = 0$, is identical to Stuart's and Tamada's solution, both with $\beta = \alpha$, to within a simple horizontal translation. However, from a physical standpoint, this seems a remarkable result. Adding shear flows of quite different character, even with possible flow reversal, to an orthogonal stagnation-point flow produces an oblique flow which appears identical to an observer at the stagnation-point, now shifted a prescribed distance, $\zeta(\nu/k^3)^{1/2}\beta$. Contrary to intuition, which suggests the flow associated with an increasing pressure gradient would move the point of attachment from right to left, increasing the adverse pressure gradient, by increasing the value of β, shifts the stagnation-point of attachment further to the right in the positive x direction. To provide an explanation, we note that when the flow pattern shifts, the dividing streamline does not change its shape but is displaced from the boundary an amount proportional to β. When $\beta > 0$, this shifts the stagnation-point of attachment to the right.

To illustrate the flow in a sample case, figure 3.2(b) displays the streamlines when $k/\zeta = 0.5$ and $\beta = \alpha$, corresponding to the value chosen by Stuart (1959) and Tamada (1979). Applying the analysis of Drazin and Riley (2006) we find that the dividing streamline meets the wall at the point $x = x_s$, where

$$x_s = -\zeta(\nu/k^3)^{1/2}\,\delta/\gamma = -\zeta(\nu/k^3)^{1/2}\,(1.141 - \beta), \tag{3.15}$$

which in the present case is equal to $-0.99(\nu/k)^{1/2}$. The instantaneous slope of the dividing streamline at the stagnation point is given by

$$-3(\gamma^2/\lambda)\frac{k}{\zeta} = -7.5\,\frac{k}{\zeta}. \tag{3.16}$$

So in figure 3.2(b) the dividing streamline meets the wall at 75° to the horizontal. When $\beta = 1.141$, corresponding to the critical value for reversal in the shear flow component discussed above, the dividing streamline meets the wall at the origin.

3.3 General form of the oblique stagnation-point flow

In the previous section, we considered an oblique stagnation-point flow travelling towards a fixed wall, where the flow in the far-field is made up of a Hiemenz stagnation-point flow, a shear flow with constant vorticity $-\zeta < 0$ and a uniform stream, which was previously given by (3.1). In this section, we wish to find the general form of the oblique stagnation-point flow, which comprises of a Hiemenz flow and an additional horizontal velocity component. In the far-field, we write $\psi = xF(y)+G(y)$, where $F(y)$ is the Hiemenz function and $G(y)$ is a horizontal component, which does not affect the flow in the normal direction.

To begin, we define the dimensional Vorticity Streamfunction Equation as

$$\psi_y^* \left(\nabla^2\psi^*\right)_x - \psi_x^* \left(\nabla^2\psi^*\right)_y = \nu\nabla^4\psi^*. \tag{3.17}$$

By writing $\psi^* = k\psi$, where ψ is non-dimensional, equation (3.17) is rewritten as

$$\psi_y \left(\nabla^2\psi\right)_x - \psi_x \left(\nabla^2\psi\right)_y = \frac{\nu}{k}\nabla^4\psi. \tag{3.18}$$

We introduce the new parameter $\epsilon^2 = \nu/k$, where ϵ has the dimensions of length. It follows that the variable $y = (\nu/k)^{1/2}\eta = \epsilon\eta$, which was introduced in section 3.2 and is used later in this section. We proceed by looking for a solution to (3.18), where $(\nu/k) \ll 1$. Later in this section, we seek a solution close to the wall, when the viscous term in (3.18) is significant.

Substituting the streamfunction $\psi(x, y) = xF(y) + G(y)$ into equation (3.18) we obtain, after one integration and letting $G(y) = \int_0^y g(\widehat{y})\mathrm{d}\widehat{y}$

$$\epsilon^2 F''' + FF'' - F'^2 + C = 0, \tag{3.19}$$

$$\epsilon^2 g'' + Fg' - F'g + D = 0, \tag{3.20}$$

where C and D are constants of integration. The corresponding boundary conditions on the wall are given by

$$F(0) = 0, \quad F'(0) = 0, \quad g(0) = 0 \quad \text{on} \quad y = 0, \tag{3.21}$$

satisfying the no-penetration and no-slip conditions. We begin by considering the solution to (3.19) far from the wall, with the boundary condition $F'(y) \to 1$ as $y \to \infty$, as $F(y)$ is the Hiemenz function. Due to the form of equation (3.19), we pose the asymptotic expansion $F(y) = F_0(y) + \epsilon^2 F_1(y) + O(\epsilon^4)$ and find the leading order equation is given by

$$F_0 F_0'' - F_0'^2 + C = 0. \tag{3.22}$$

The solution to (3.22) is given by $F_0 = C^{1/2} y - A$, where A and C are constants. To find C, we use the far-field boundary condition $F_0'(y) \to 1$ as $y \to \infty$ and obtain $C = 1$, where C is assumed to be positive. Therefore, the leading order solution is given by $F_0(y) = y - A$ as $y \to \infty$. However, this solution does not satisfy the boundary condition at the wall. Subsequently, a region is introduced at the wall to match the velocity on the wall to that in the far-field, which is discussed later in this section.

We proceed by considering the higher order equations to equation (3.19). The first order equation is given by

$$(y - A)F_1'' - 2F_1' = 0, \tag{3.23}$$

and after one integration we find, $F_1'(y) = K_1(y - A)^2$. This only satisfies the far-field boundary condition $F_1'(y) \to 0$ as $y \to \infty$ if the constant $K_1 = 0$. So the first order solution is given by $F_1(y) = 0$. For higher order terms, we obtain

$$(y - A)F_n'' - 2F_n' = 0, \tag{3.24}$$

for $n > 1$, which has the same structure as that of the first order equation (3.23). After one integration, equation (3.24) becomes $F_n'(y) = K_n(y - A)^2$. To enable the far-field boundary conditions $F_n'(y) \to 0$ as $y \to \infty$ to be satisfied, the constants $K_n = 0$, which gives the trivial solutions $F_n(y) = 0$. Therefore, combining these results, the far-field Hiemenz solution is given by

$$F = y - A. \tag{3.25}$$

We now consider solutions to $g(y)$, the horizontal velocity component satisfying equation (3.20). Due to the form of (3.20), we expand $g(y)$ similarly

to $F(y)$ and write $g(y) = g_0(y) + \epsilon^2 g_1(y) + O(\epsilon^4)$. At leading order, we obtain

$$(y - A)g_0' - g_0 + D = 0. \tag{3.26}$$

Upon solving (3.26), we obtain $g_0(y) = D + E(y - A)$, where D and E are arbitrary constants. Unlike the equation for $F(y)$, we make no assumptions on the far-field boundary condition for $g(y)$. At first order, we find

$$(y - A)g_1' - g_1 = 0. \tag{3.27}$$

Upon solving this, we find $g_1(y) = k_1(y - A)$, where k_1 is a constant. As this solution is very similar to that at leading order, we can rewrite the leading order solution as $g_0 = D + \widehat{E}(y - A)$, where $\widehat{E} = E + \epsilon^2 k_1$. The form of the higher order equations are the same as that at first order and are given by

$$(y - A)g_n' - g_n = 0, \tag{3.28}$$

for $n > 1$. Solving equation (3.28), we find $g_n = k_n(y - A)$, which can, similar to that of the first order equation, be incorporated into the previous solution. Therefore, the far-field solution is given by $g(y) = D + \widehat{E}(y - A)$ and after one integration we find

$$G(y) = \frac{\widehat{E}y^2}{2} - By. \tag{3.29}$$

A constant of integration has not been included, as adding a constant to the streamfunction does not affect the velocity components. Combining the solutions for $F(y)$ and $G(y)$, we obtain the general form of the streamfunction

$$\psi = x(y - A) + \frac{\widehat{E}y^2}{2} - By, \quad \text{as} \quad y \to \infty, \tag{3.30}$$

satisfying the far-field boundary condition $F'(y) \to 1$ as $y \to \infty$. The first term corresponds to an orthogonal stagnation-point flow, with the constant A representing the displacement from the wall in the normal direction. We find $\nabla^2\psi = \widehat{E}$, therefore, the second component is a shear flow with constant vorticity $-\widehat{E}$. We let $\widehat{E} = \widehat{\zeta}$, as this is a known constant to represent the vorticity. The third term is a uniform stream with strength $-B$, where the

minus is included to allow for comparison to the streamfunction discussed in section 3.2.

To obtain the streamfunction (3.30), we have assumed that the viscous term is small compared to the convective terms in the Vorticity Streamfunction Equation (3.18). Hence, (3.30) is no longer valid when these terms become comparable. This occurs when $y = \epsilon\eta$ and $\psi = \epsilon\widehat{\psi}$, where $\epsilon = (\nu/k)^{1/2}$, which has previously been defined. Expressing equation (3.18) in terms of these variables, we find

$$\widehat{\psi}_\eta \widehat{\psi}_{\eta x} - \widehat{\psi}_x \widehat{\psi}_{\eta\eta} = \widehat{\psi}_{\eta\eta\eta}, \tag{3.31}$$

with boundary conditions on the wall

$$\widehat{\psi}_x(x,0) = 0, \qquad \widehat{\psi}_\eta(x,0) = 0 \quad \text{on} \quad \eta = 0. \tag{3.32}$$

To calculate the form of the streamfunction to substitute into (3.31), we express the solution (3.30) in terms of the scalings above, to obtain

$$\widehat{\psi} = x\left(\eta - \widehat{A}\right) + \widehat{\zeta}\epsilon\left(\frac{\eta^2}{2} - \widehat{B}\eta\right), \tag{3.33}$$

where $A = \epsilon\widehat{A}$ and $B = \widehat{\zeta}\epsilon\widehat{B}$. Therefore, the streamfunction (3.33) suggests the similarity solution

$$\widehat{\psi} = xH_1(\eta) + \widehat{\zeta}\epsilon H_2(\eta), \tag{3.34}$$

where $H_1(\eta)$ and $H_2(\eta)$ are functions of η. Substituting the streamfunction (3.34) into equation (3.31), we obtain after one integration and letting $H_2(\eta) = \int_0^\eta h_2(\widehat{\eta})\mathrm{d}\widehat{\eta}$

$$H_1''' + H_1H_1'' - H_1'^2 + \widehat{C} = 0, \tag{3.35}$$

$$h_2'' + H_1h_2' - H_1'h_2 + \widehat{D} = 0. \tag{3.36}$$

The corresponding boundary conditions on the wall are

$$H_1(0) = 0, \quad H_1'(0) = 0, \quad h_2(0) = 0, \quad \text{on} \quad \eta = 0, \tag{3.37}$$

with matching conditions to the far-field

$$H_1(\eta) \to \eta - \widehat{A}, \quad h_2(\eta) \to \eta - \widehat{B} \quad \text{as} \quad \eta \to \infty. \tag{3.38}$$

Upon substituting the far-field flow boundary conditions (3.38) into equations (3.35) and (3.36), we find the constants $\widehat{C} = 1$ and $\widehat{D} = \widehat{A} - \widehat{B}$. We note that these equations are the same as equations (3.3) and (3.5) and have been solved in section 3.2.

To allow for a direct comparison between the streamfunctions (3.30) and (3.34), we express them in terms of ψ^*. The streamfunction in the far-field is given by

$$\psi^* = k\left[x\left(y - \left(\frac{\nu}{k}\right)^{1/2}\widehat{A}\right) + \frac{\widehat{\zeta}y^2}{2} - \widehat{B}\widehat{\zeta}\left(\frac{\nu}{k}\right)^{1/2} y\right] \quad \text{as} \quad y \to \infty. \tag{3.39}$$

The first term corresponds to the orthogonal stagnation-point flow, where $\widehat{A}$ acts as a displacement effect in the normal direction and as we get further away from the wall, this constant becomes negligible in comparison to the other terms in (3.39). The second term relates to a shear flow of constant vorticity $-\widehat{\zeta}$ and the third term is a uniform stream with strength $-\widehat{B}$. These two latter terms are denoted the oblique components. As we approach the wall, this solution is no longer valid and close to the wall the streamfunction takes the form

$$\psi^* = (\nu k)^{1/2}\left[xH_1(\eta) + \widehat{\zeta}\left(\frac{\nu}{k}\right)^{1/2}\int_0^{\eta} h_2(\widehat{\eta})\mathrm{d}\widehat{\eta}\right]. \tag{3.40}$$

Again, the first term relates to the orthogonal stagnation-point flow and the second term represents the oblique components. When $(\nu/k) \ll 1$, the orthogonal component is dominant. Unlike many boundary layer problems, where a matching region is required between the inner and outer solutions, the streamfunction close to the wall matches directly onto the far-field streamfunction as $y \to \infty$.

In order to compare this streamfunction with the streamfunction (3.2), we write $\zeta = k\widehat{\zeta}$, $H_1(\eta) = f(\eta)$ and $h_2(\eta) = g(\eta)$ and the streamfunction (3.40) becomes

$$\psi^* = (\nu k)^{1/2} xH_1(\eta) + \zeta\left(\frac{\nu}{k}\right)\int_0^{\eta} h_2(\widehat{\eta})\mathrm{d}\widehat{\eta}. \tag{3.41}$$

Therefore, in this section we have determined the general form of the oblique stagnation-point flow, containing an orthogonal stagnation-point flow and a

general horizontal velocity. It is found that the general form of the oblique stagnation-point flow is that discussed in section 3.2, where the horizontal component comprises of a shear flow with constant vorticity and a uniform stream.

3.4 Summary

In this chapter, we have investigated a two-dimensional stagnation-point flow, where the streamlines in the far-field meet the wall obliquely. In the far-field, the flow comprises a Hiemenz stagnation-point flow and superimposed onto this, a shear flow of a constant vorticity and a uniform stream. These two terms we denote the oblique component. At the wall, a similarity solution is found, which was first used by Stuart (1959), incorporating two components. This is an exact solution of the Navier-Stokes equations. The first component is a Hiemenz function and the second is the integral of the oblique component. The problem can be described in terms of two coupled ordinary differential equations. The first equation describes the orthogonal stagnation-point flow, previously addressed by Hiemenz. The second equation, which is coupled with the first, describes the oblique component of the flow. These equations are solved numerically and it is found that upon increasing the uniform stream, the oblique velocity component exhibits a region of flow reversal at the wall.

The streamlines were considered and due to the viscosity, as the flow approaches the wall, the dividing streamline bends towards the wall and meets the wall at an angle close to the normal. Increasing the strength of the uniform stream increases the pressure gradient and, contrary to intuition, increasing the strength of the uniform stream in the far-field, simply shifts the streamlines and the attachment point with the wall to the right, without altering its structure.

A general form of the oblique stagnation-point flow was then considered, consisting of a Hiemenz flow and an arbitrary horizontal component. It was

demonstrated that the problem initially discussed by Stuart (1959) is the most general form of oblique stagnation-point flow possible.

In the next chapter, a time-dependent version of the oblique stagnation-point flow discussed in this chapter is considered, with results and analysis being used.

Chapter 4

Unsteady oblique stagnation-point flow

4.1 Introduction

Continuing the investigation into oblique stagnation-point flows, we extend the problem discussed in chapter 3, where a steady oblique stagnation-point flow travelling towards a fixed wall was discussed. We now consider a time-dependent version of this problem. In the far-field, the structure of the flow incorporates an unsteady orthogonal stagnation-point flow, which is dependent upon a dimensionless frequency parameter σ and a relative amplitude parameter Δ. Added to this is a shear flow with constant vorticity and a horizontal time-dependent velocity component. The latter term was steady in chapter 3 and represented a shift of the streamlines along the wall.

Close to the wall, due to the no-slip condition not being satisfied, a similarity solution is introduced comprising of two components. The first component describes the unsteady orthogonal stagnation-point flow and is the same as that discussed in chapter 2. The second describes the shear and the horizontal velocity components, which in future are denoted as the oblique components.

In chapter 2, when considering purely the orthogonal problem, Merchant

and Davis (1989) obtained, for large frequency, a critical amplitude dependent upon the frequency given by $\Delta_c = 1.289\sigma^{1/2} + 0.763 + O(\sigma^{-1/2})$. When this critical amplitude is exceeded, Blyth and Hall (2003) found that the orthogonal solutions break down at a finite-time singularity. Due to the oblique equation being coupled with the primary, we expect the oblique solution to also break down at a finite-time singularity, when the amplitude is above the critical amplitude.

A discussion on the flow structure near the wall over one time period concludes this chapter, with the effect of the time-dependent horizontal velocity component also being considered.

4.2 Problem formulation

In chapter 3, the general form of the steady oblique stagnation-point flow was obtained, which comprised in the far-field of a Hiemenz stagnation-point flow, a shear flow and a uniform stream, given in (3.1). To consider the unsteady version of this problem, we write

$$\psi = a(t)kxy + \frac{1}{2}\widehat{\zeta}(t)y^2 - \widehat{\beta}(t)\widehat{\zeta}(t)\left(\frac{\nu}{k}\right)^{1/2} y, \tag{4.1}$$

as $y \to \infty$, where the problem is described in Cartesian (x, y) coordinates and the velocity components (u, v) are in the (x, y) directions respectively with $u = \psi_y$ and $v = -\psi_x$. Also, $a(t)$ and $\widehat{\beta}(t)$ are arbitrary time-dependent functions, $\widehat{\zeta}(t)$ is the vorticity, k is the strength of the orthogonal stagnation-point flow and ν is the viscosity. To confirm the validity of (4.1), we use the unsteady Vorticity Streamfunction Equation

$$\left(\nabla^2\psi\right)_t + \psi_y\left(\nabla^2\psi\right)_x - \psi_x\left(\nabla^2\psi\right)_y = \nu\nabla^4\psi. \tag{4.2}$$

Substituting the streamfunction (4.1) into (4.2) reduces the Vorticity Streamfunction Equation to $\widehat{\zeta}_t = 0$, which implies that flows of this form are only possible if the vorticity is constant. Therefore, the streamfunction (4.1) is rewritten as

$$\psi = a(t)kxy + \frac{1}{2}\widehat{\zeta}y^2 - \widehat{\beta}(t)\widehat{\zeta}\left(\frac{\nu}{k}\right)^{1/2} y. \tag{4.3}$$

The first term corresponds to an unsteady orthogonal stagnation-point flow, where $a(t) = 1+\Delta\cos\omega t$ with amplitude Δ and frequency ω. The form of $a(t)$ has been chosen to be the same as that used in chapter 2, when considering a purely orthogonal stagnation-point flow. The second term is a shear flow with constant vorticity $-\widehat{\zeta} < 0$ and the third component is a time-dependent horizontal velocity, whose strength is dependent upon $\widehat{\beta}(t)$. We note the functions $a(t)$ and $\widehat{\beta}(t)$ are dimensionless. We choose $\widehat{\beta}(\tau) = b_M + b_O\cos\tau$ to reflect the oscillatory nature of the problem, where the oscillations are at the same frequency as $a(\tau)$, but b_M and b_O, the mean and oscillatory components, have arbitrary amplitudes.

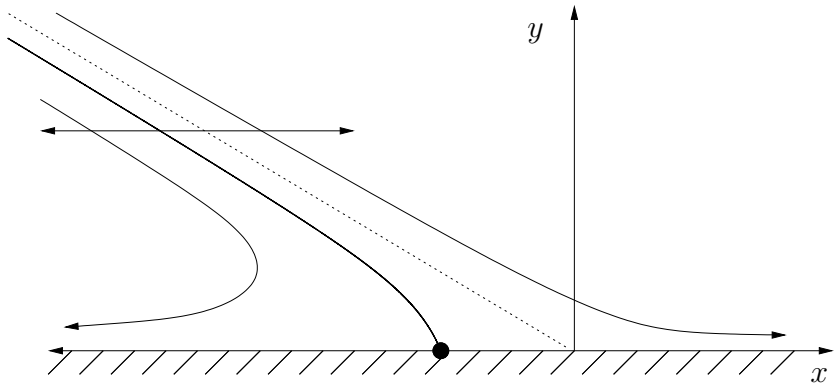

Figure 4.1: An illustration of the unsteady oblique stagnation-point flow at an instant in time. Away from the wall, the gradient of the dividing streamline, $\psi = 0$, is given by $M = -2ak/\widehat{\zeta}$. As discussed in chapter 3, the viscosity in the region close to the wall affects the gradient of the dividing streamline.

Problems of this nature can be considered either travelling towards a fixed wall or an oscillating wall by a simple change of frame of reference. In chapter 2, we followed the work of Hazel and Pedley (1998) and considered the orthogonal flow travelling towards an oscillating wall. In the present chapter, we consider the problem described by the streamfunction (4.3) travelling towards a fixed wall at $y = 0$, illustrated in figure 4.1. However, details of the change of frame of reference to one where the oblique stagnation-point flow is travelling towards an oscillating wall can be found in Appendix B.

In chapter 3, when considering the steady version of this problem, the gradient of the dividing streamline in the far-field was only dependent upon

the vorticity and the strength of the orthogonal component. We now consider the streamfunction (4.3) and find the equation of the dividing streamline, $\psi = 0$, is given by

$$y = -\frac{2akx}{\widehat{\zeta}} + 2\widehat{\beta}\left(\frac{\nu}{k}\right)^{1/2}. \tag{4.4}$$

Therefore, the gradient of the dividing streamline far from the wall is given by $M = -2ak/\widehat{\zeta}$. Also, similar to that of the steady problem, the unknown function $\widehat{\beta}(t)$ only affects the horizontal displacement of the dividing streamline.

To consider the streamlines in the far-field, we examine the gradient of the dividing streamline over a single time period. To obtain the dividing streamline, we note that $a(t)$ has a maximum at $a_{max} = 1+\Delta$ and a minimum at $a_{min} = 1-\Delta$. Therefore, the gradient has a maximum at $M_{max} = -2(1+\Delta)/\widehat{\zeta}$ and a minimum at $M_{min} = -2(1-\Delta)/\widehat{\zeta}$. When $\Delta < 1$, both M_{max} and M_{min} are negative and over a single time period, the dividing streamline oscillates between two bounding values, which can be seen in figure 4.2(a) for $\widehat{\beta} = 0$.

When $\Delta > 1$, M_{max} is negative, similar to the previous case, but M_{min} is positive. This configuration is illustrated in figure 4.2(b). To consider how the dividing streamline oscillates between M_{min} and M_{max}, we note that when $\Delta > 1$, $a(t)$ has a zero at some point in the time period, which is illustrated in figure 4.3, for selected values of Δ. This corresponds to the point at which the flow reverses in the cycle. When $a(t) > 0$, the gradient of the dividing streamline M, is negative. Using the property that $v = -\psi_x$, we find the vertical velocity component of (4.3) is given by $v = -a(t)y$. Therefore, when $a(t)$ is positive, the vertical velocity v is negative and the flow approaches the wall. As we progress through the time period, $a(t)$ decreases, causing the gradient of the dividing streamline to decrease within $x < 0$. When $a(t) < 0$, the gradient of the dividing streamline is positive and lies within $x > 0$. As $a(t)$ decreases, the gradient of the dividing streamline increases in $x > 0$. Also the vertical velocity is positive which corresponds to the flow travelling away from the wall. In figure 4.4, we illustrate the far-field streamlines for

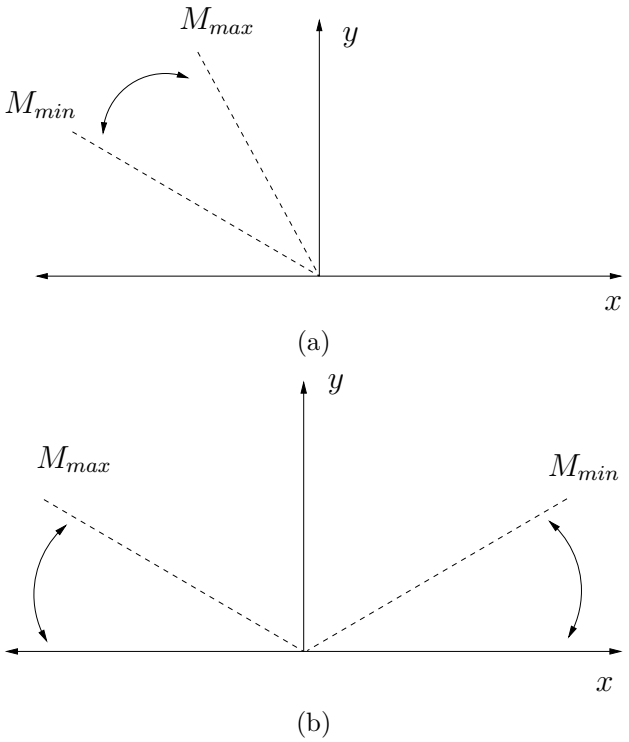

Figure 4.2: The range of the far-field dividing streamline when (a) $\Delta < 1$ and (b) $\Delta > 1$. Both cases are for $\widehat{\beta} = 0$.

$\Delta = 1.5$ and $\widehat{\beta} = 1$ over a single time period. The time interval considered in this figure corresponds to the time interval in which a zero is present in $a(t)$.

Having considered the behaviour of the dividing streamline far from the wall, we now find the exact equation of the dividing streamline to observe the behaviour close to the wall. As the streamfunction (4.3) is unable to be satisfy the no-slip condition on the wall, we write

$$\psi(x, \eta, \tau) = (\nu k)^{1/2} x \psi_P(\eta, \tau) + \widehat{\zeta}\Big(\frac{\nu}{k}\Big) \int_0^{\eta} \psi_O(z, \tau) \mathrm{d}z, \tag{4.5}$$

with non-dimensional variable $\eta = (k/\nu)^{1/2} y$ and time component $\tau = \omega t$. We note that the form of (4.5) was initially used by Stuart (1959) when considering the steady problem discussed in chapter 3.

The first term in (4.5) represents the unsteady orthogonal stagnation-point flow, which is the same as that in chapter 2 and denoted $\psi_P(\eta, \tau)$, the primary component. The second term represents the shear flow and the time-dependent horizontal velocity components and is denoted $\psi_O(\eta, \tau)$,

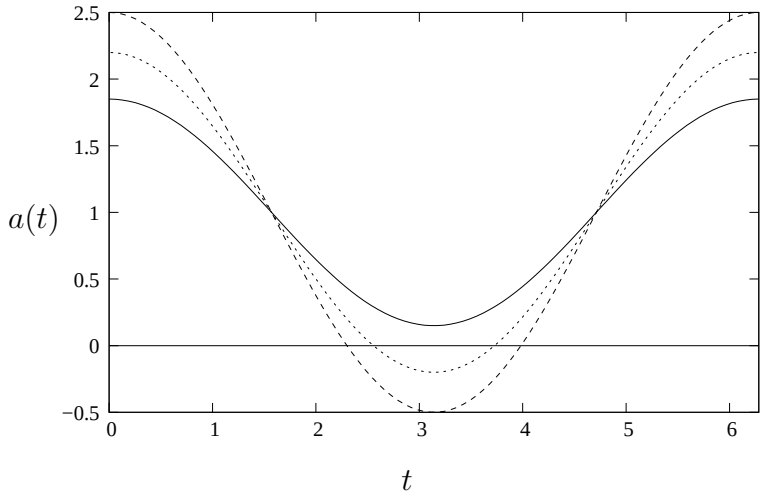

Figure 4.3: The function $a(t) = 1 + \Delta \cos \omega t$ for $\omega = 1$ and $\Delta = 0.85$ (solid line), $\Delta = 1.2$ (dotted lines) and $\Delta = 1.5$ (dashed lines), illustrating when $\Delta > 1$, the function $a(t)$ develops zeros.

the oblique component. Matching (4.5) with the far-field flow (4.3), requires $\psi_P(\eta, \tau) \to a(\tau)\eta - \widehat{\alpha}(\tau)$ and $\psi_O(\eta, \tau) \to \eta - \widehat{\beta}(\tau)$ as $\eta \to \infty$, where $a(\tau) = 1 + \Delta \cos \tau$, $\widehat{\beta}(\tau)$ is an arbitrary function and $\widehat{\alpha}(\tau)$ acts similarly to the constant α in chapter 3, which was a displacement in the vertical direction. Upon substituting the far-field streamfunction (4.3) into the horizontal momentum equation (2.8) and matching to the far-field to eliminate the pressure term p_x, we obtain

$$\sigma\psi_{P\eta\tau} + \left(\psi_{P\eta}\right)^2 - \psi_P\psi_{P\eta\eta} = \sigma a_\tau + a^2 + \psi_{P\eta\eta\eta}, \tag{4.6}$$

$$\sigma\psi_{O\tau} + \psi_{P\eta}\psi_O - \psi_P\psi_{O\eta} = -\sigma\widehat{\beta}_\tau + \widehat{\alpha} - a\widehat{\beta} + \psi_{O\eta\eta}, \tag{4.7}$$

with primary boundary conditions

$$\psi_P(0, \tau) = 0, \quad \psi_{P\eta}(0, \tau) = 0 \quad \text{on} \quad \eta = 0 \tag{4.8}$$

$$\psi_P(\eta, \tau) \to a(\tau)\eta - \widehat{\alpha} \quad \text{as} \quad \eta \to \infty, \tag{4.9}$$

and oblique boundary conditions

$$\psi_O(0, \tau) = 0 \quad \text{on} \quad \eta = 0 \tag{4.10}$$

$$\psi_O(\eta, \tau) \to \eta - \widehat{\beta} \quad \text{as} \quad \eta \to \infty, \tag{4.11}$$

where $\sigma = \omega/k$ is the Strouhal number, a dimensionless parameter, which is a measure of the unsteadiness.

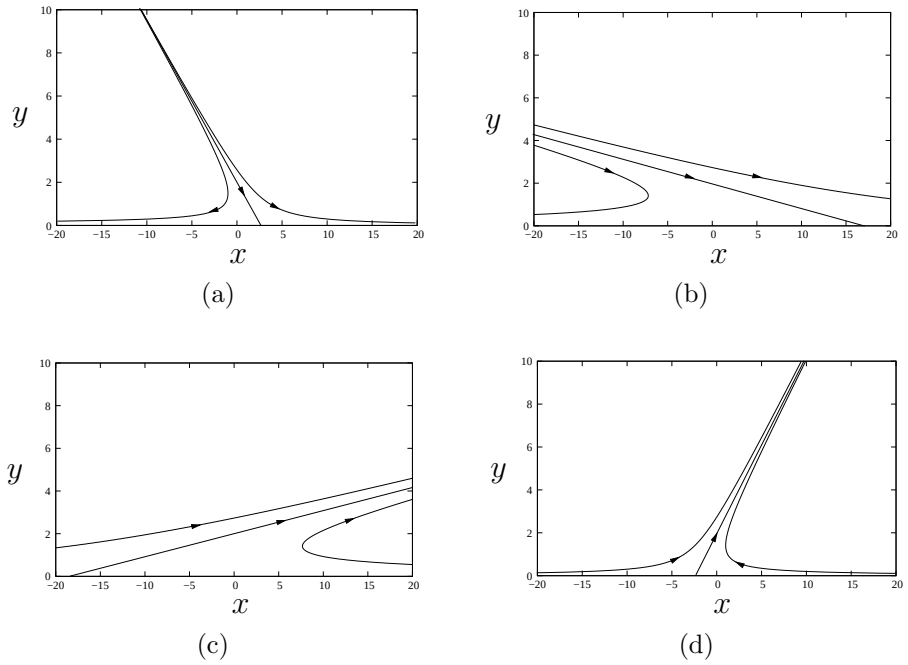

Figure 4.4: The streamlines in the far-field plotted for $\Delta = 1.5$, and $\widehat{\beta} = 1$, with $\nu = k = \omega = \widehat{\zeta} = 1$ for (a) $t = 2$, (b) $t = 2.25$, (c) $t = 2.35$, (d) $t = 2.8$. This illustrates the gradient of the dividing streamline changing sign from negative in (a) and (b) to positive in (c) and (d), which corresponds to t increasing through the zero at $\tau \approx 2.3$.

To find the dividing streamline, we set the streamfunction (4.5) equal to zero, which corresponds to the dividing line that intersects the wall, to obtain

$$x_d = -\widehat{\zeta}\left(\frac{\nu}{k^3}\right)^{1/2} \frac{\int_0^\eta \psi_O(z,\tau)\mathrm{d}z}{\psi_P(\eta,\tau)}. \tag{4.12}$$

As $\psi_P(0,\tau) = \psi_{P_\eta}(0,\tau) = 0$, the denominator equals zero at the wall. Therefore, we need to approximate the solutions close to $\eta = 0$ by expanding $\psi_O(0,\tau) = \psi_{O_\eta}(0,\tau)\eta + \psi_{O_{\eta\eta}}(0,\tau)\eta^2/2 + O(\eta^3)$ and $\psi_P(0,\tau) = \psi_{P_{\eta\eta}}(0,\tau)\eta^2/2 + \psi_{P_{\eta\eta\eta}}(0,\tau)\eta^3/6 + O(\eta^4)$. Upon substituting these expansions into (4.12), we obtain $x_d = x_0 + G\eta$, where x_0 is the point at which the dividing streamline meets the wall and is given by

$$x_0 = -\widehat{\zeta}\left(\frac{\nu}{k^3}\right)^{1/2} \frac{\psi_{O_\eta}(0,\tau)}{\psi_{P_{\eta\eta}}(0,\tau)}, \tag{4.13}$$

and $1/G$ is the gradient of the dividing streamline at the wall, which is given later in (4.85).

To proceed, we seek numerical solutions to the primary and subsidiary equations, given in (4.6) and (4.7) respectively, by marching forward in time using a Crank-Nicolson finite-difference method. To begin these numerics, initial profiles for $\tau \ll 1$ are required, which are obtained in the next section.

4.2.1 The initial velocity profile for the primary flow

To numerically integrate the primary problem (4.6), an initial profile for small τ is required to begin the numerics, which are then marched forwards in τ. Riley and Vasantha (1989) solved the primary problem where $a(\tau)$ was purely oscillatory, i.e. $\psi_{P\eta}(\eta,\tau) \to \cos\tau$ as $\eta \to \infty$. We duplicate their analysis to find the initial profile for the primary equation (4.6), where $a(\tau)$ includes a mean component. To allow for comparisons to be made with Riley and Vasantha, we write $a(\tau) = K_1 + K_2\cos\tau$, with constants K_1 and K_2 and note in their case $K_1 = 0$ and $K_2 = 1$. Therefore, the primary equation, which was previously defined in equation (4.6), is rewritten as

$$\begin{aligned} \sigma\psi_{P\eta\tau} + \left(\psi_{P\eta}\right)^2 - \psi_P\psi_{P\eta\eta} &= -\sigma K_2 \sin\tau \\ &\quad +(K_1 + K_2\cos\tau)^2 + \psi_{P\eta\eta\eta}, \end{aligned} \tag{4.14}$$

with boundary conditions

$$\psi_P(0,\tau) = 0, \quad \psi_{P\eta}(0,\tau) = 0, \tag{4.15}$$

$$\psi_P(\eta,\tau) \to (K_1 + K_2\cos\tau)\eta - \widehat{\alpha} \quad \text{as} \quad \eta \to \infty. \tag{4.16}$$

At $\tau = 0$, the flow is impulsively started with the velocity component $\psi_{P\eta}(\eta,\tau) = K_1 + K_2$ for all $\eta > 0$. Therefore, there must be a small transition layer to match the flow at the wall, $\psi_{P\eta}(0,\tau) = 0$, to the impulsively started flow for $\eta > 0$, $\psi_{P\eta}(\eta,\tau) = K_1 + K_2$. When $\tau \ll 1$, close to the wall the dominating terms in equation (4.14) are $\sigma\psi_{P\eta\tau} \sim \psi_{P\eta\eta\eta}$, which suggests the scaling $\eta \sim (\tau/\sigma)^{1/2}$. Hence, the layer has thickness $O\left((\tau/\sigma)^{1/2}\right)$ with new variable $\widehat{\eta} = (\sigma/\tau)^{1/2}\eta$ where $\widehat{\eta} \sim O(1)$. Also, the far-field boundary condition (4.16), suggests the rescaling $\psi_P(\eta,\tau) = (\tau/\sigma)^{1/2}F(\widehat{\eta},\tau)$ with $\widehat{\alpha} = (\tau/\sigma)^{1/2}\bar{\alpha}$, where $\bar{\alpha} \sim O(1)$. Rewriting equation (4.14) in terms of these

scalings with $\tau \ll 1$, we obtain

$$\frac{\sigma}{\tau}\left(F_{\widehat{\eta}\widehat{\eta}\widehat{\eta}} + \frac{\widehat{\eta}}{2}F_{\widehat{\eta}\widehat{\eta}}\right) - F_{\widehat{\eta}}^2 + FF_{\widehat{\eta}\widehat{\eta}} + (K_1 + K_2)^2 - \sigma F_{\widehat{\eta}\tau} + O(\tau) = 0, \quad (4.17)$$

with boundary conditions

$$F(0,\tau) = 0, \quad F_{\widehat{\eta}}(0,\tau) = 0, \quad (4.18)$$

$$F(\widehat{\eta},\tau) \to \left[K_1 + K_2\left(1 - \tfrac{\tau^2}{2} + O(\tau^4)\right)\right]\widehat{\eta} - \bar{\alpha} \quad \text{as} \quad \widehat{\eta} \to \infty, \quad (4.19)$$

where small τ expansions for $\sin\tau$ and $\cos\tau$ have been used. From now on, as the constants K_1 and K_2 always appear together, we write $K = K_1 + K_2$. To seek a solution to (4.17), we express $F(\widehat{\eta},\tau)$ as the asymptotic expansion, $F(\widehat{\eta},\tau) = F_0(\widehat{\eta}) + \tau F_1(\widehat{\eta}) + O(\tau^2)$. Upon substituting this expansion into (4.17), we obtain

$$\frac{\sigma}{\tau}\left(F_0''' + \frac{\widehat{\eta}}{2}F_0''\right) + \sigma\left(F_1''' + \frac{\widehat{\eta}}{2}F_1'' - F_1'\right) - F_0^2 + F_0F_0'' + K^2 + O(\tau) = 0, \quad (4.20)$$

where the prime denotes differentiation with respect to $\widehat{\eta}$. At leading order in τ, we find

$$F_0''' + \frac{\widehat{\eta}}{2}F_0'' = 0, \quad (4.21)$$

with boundary conditions $F_0'(0) = 0$, $F_0'(0) = 0$ and $F_0'(\widehat{\eta}) \to K$ as $\widehat{\eta} \to \infty$. Solving (4.21) and after applying the boundary conditions, the leading order solution takes the form

$$F_0 = K\left[\widehat{\eta}\,\mathrm{erf}\left(\frac{\widehat{\eta}}{2}\right) + \frac{2}{\sqrt{\pi}}\left(e^{-\widehat{\eta}^2/4} - 1\right)\right], \quad (4.22)$$

where $\bar{\alpha} = \frac{2(1+\Delta)}{\sqrt{\pi}}$ and $\widehat{\alpha} \to (\tau/\sigma)^{1/2}\frac{2(1+\Delta)}{\sqrt{\pi}}$ as $\tau \to 0$. Upon differentiating (4.22), we obtain the leading order velocity profile

$$F_0' = K\,\mathrm{erf}\left(\frac{\widehat{\eta}}{2}\right), \quad (4.23)$$

where $K = K_1 + K_2$.

The first order equation is given by

$$\sigma\left(F_1''' + \frac{\widehat{\eta}}{2}F_1'' - F_1'\right) = F_0^2 - F_0F_0'' - K^2, \quad (4.24)$$

with boundary conditions $F_1(0) = 0$, $F_1'(0) = 0$ and $F_1'(\widehat{\eta}) \to 0$ as $\widehat{\eta} \to \infty$, where the leading order solution $F_0(\widehat{\eta})$ is given by (4.22). At this stage, it is not known whether the first order solution is required to give accurate numerical solutions, as the leading order solution may be sufficient. This will be discussed in section 4.3.

Having obtained an initial velocity profile for $a(\tau) = K_1 + K_2 \cos\tau$, we let $K_1 = 1$ and $K_2 = \Delta$. Therefore, the primary leading order initial profile, in terms of the original variable η, is given by

$$\psi_P(\eta,\tau) = (1+\Delta)\left[\eta \mathrm{erf}\left(\left(\frac{\sigma}{\tau}\right)^{1/2}\frac{\eta}{2}\right) + \left(\frac{\tau}{\sigma}\right)^{1/2}\left(e^{-\frac{\sigma\eta^2}{4\tau}} - 1\right)\right], \quad (4.25)$$

$$\psi_{P\eta}(\eta,\tau) = (1+\Delta)\mathrm{erf}\left[\left(\frac{\sigma}{\tau}\right)^{1/2}\frac{\eta}{2}\right]. \quad (4.26)$$

In section 4.3, the solutions (4.25) and (4.26) are used as the initial profile to begin the primary finite-difference numerics, as well as a check on the validity of the numerical method for small τ. Before solving the primary equation, an initial velocity profile is needed for the oblique problem.

4.2.2 Initial profile for the oblique flow

In section 4.2.1, an initial profile for the primary equation was obtained for small τ. However, in this section, we only consider the case when $K_1 = 1$ and $K_2 = \Delta$. To obtain an initial profile for the oblique problem when $\tau \ll 1$, we use a similar analysis to that used for the primary equation. We recall the oblique equation, which was previously defined in equation (4.7), is given by

$$\sigma\psi_{O\tau} + \psi_{P\eta}\psi_O - \psi_P\psi_{O\eta} = -\sigma\widehat{\beta}_\tau + \widehat{\alpha} - a\widehat{\beta} + \psi_{O\eta\eta}, \quad (4.27)$$

with boundary conditions

$$\psi_O(0,\tau) = 0, \quad \psi_O(\eta,\tau) \to \eta - \widehat{\beta}, \quad (4.28)$$

where $a(\tau) = 1 + \Delta\cos\tau$ and $\widehat{\beta}(\tau)$ is an arbitrary function. As the oblique equation is reliant upon the primary, which is impulsively started at $\tau = 0$ with velocity $\psi_{P\eta}(\eta, 0) = 1 + \Delta$, a layer close to the wall is required to match the velocity on the wall to that of the impulsively started flow for $\eta > 0$. Close

to the wall when $\tau \ll 1$, the dominant terms in equation (4.27) are given by $\sigma\psi_{O\tau} \sim \psi_{O\eta\eta}$. Therefore, the layer has the same thickness as the primary flow and we write $\widehat{\eta} = (\sigma/\tau)^{1/2}\eta$. Also, the far-field boundary condition (4.28) requires $\psi_O(\eta,\tau) = (\tau/\sigma)^{1/2}G(\widehat{\eta},\tau)$ with $\widehat{\beta}(\tau) = (\tau/\sigma)^{1/2}\bar{\beta}(\tau)$, where $\bar{\beta} \sim O(1)$ as $\tau \to 0$. In addition, from section 4.2.1, we recall the scalings $\psi_P(\eta,\tau) = (\tau/\sigma)^{1/2}F(\widehat{\eta},\tau)$ with $\widehat{\alpha} = (\tau/\sigma)^{1/2}\bar{\alpha}$, where $\bar{\alpha} \sim O(1)$ as $\tau \to 0$. Hence, equation (4.27) written in terms of these scalings, is given by

$$\begin{aligned}\left(\frac{\sigma}{\tau}\right)^{1/2}\left(G_{\widehat{\eta}\widehat{\eta}} + \frac{\widehat{\eta}}{2}G_{\widehat{\eta}} - \frac{1}{2}G - \frac{1}{2}\bar{\beta}\right) = \\ + (\sigma\tau)^{1/2}\left(G_\tau + \bar{\beta}_\tau\right) - \left(\frac{\tau}{\sigma}\right)^{1/2}\left(\bar{\alpha} - F_{\widehat{\eta}}G + FG_{\widehat{\eta}} - (1+\Delta)\bar{\beta}\right).\end{aligned} \tag{4.29}$$

In section 4.2.1, when solving solving the primary initial profile for $\tau \ll 1$, the asymptotic expansion $F(\widehat{\eta},\tau) = F_0(\widehat{\eta}) + \tau F_1(\widehat{\eta}) + O(\tau^2)$ was posed, where the leading order solution $F_0(\widehat{\eta})$ is given in (4.22). We adopt a similar method to solve the oblique problem and let $G(\widehat{\eta},\tau) = G_0(\widehat{\eta}) + \tau G_1(\widehat{\eta}) + O(\tau^2)$. Substituting this expansion into (4.30) gives

$$\begin{aligned}\left(\frac{\sigma}{\tau}\right)^{1/2}\left(G_0'' + \frac{\widehat{\eta}}{2}G_0' - \frac{1}{2}G_0 - \frac{1}{2}\bar{\beta}\right) = \\ - (\sigma\tau)^{1/2}\left(G_1'' + \frac{\widehat{\eta}}{2}G_1' - \frac{3}{2}G_1 - \bar{\beta}_\tau\right) \\ - \left(\frac{\tau}{\sigma}\right)^{1/2}\left(\bar{\alpha} - F_0'G_0 + F_0G_0' - (1+\Delta)\bar{\beta}\right) + O\left(\tau^{3/2}\right).\end{aligned} \tag{4.30}$$

At leading order, we find

$$G_0'' + \frac{\widehat{\eta}}{2}G_0' - \frac{1}{2}G_0 = \frac{1}{2}\bar{\beta}, \tag{4.31}$$

with boundary conditions $G_0(0) = 0$ and $G_0(\widehat{\eta}) \to \widehat{\eta} - \bar{\beta}(\tau)$ as $\widehat{\eta} \to \infty$, where the prime denotes differentiation with respect to $\widehat{\eta}$. The particular solution of (4.31) is given by $G_0(\widehat{\eta},\tau) = -\bar{\beta}$. Combining this with the solution to the homogeneous equation, gives the leading order solution

$$G_0 = A\widehat{\eta} + B\left[2\sqrt{\pi}e^{-\widehat{\eta}^2/4} + \pi\widehat{\eta}\,\mathrm{erf}\left(\frac{\widehat{\eta}}{2}\right)\right] - \bar{\beta}. \tag{4.32}$$

After applying the leading order boundary conditions, we find

$$G_0 = \left[1 - \frac{\bar{\beta}\sqrt{\pi}}{2}\right]\widehat{\eta} + \frac{\bar{\beta}}{2\sqrt{\pi}}\left[2\sqrt{\pi}e^{-\widehat{\eta}^2/4} + \pi\widehat{\eta}\mathrm{erf}\left(\frac{\widehat{\eta}}{2}\right)\right] - \bar{\beta}. \tag{4.33}$$

Therefore, the oblique velocity profile, in terms of the original the variable η, is given by

$$\begin{aligned}\psi_O(\eta,\tau) &= \left[1-\left(\frac{\sigma}{\tau}\right)^{1/2}\frac{\widehat{\beta}\sqrt{\pi}}{2}\right]\eta+\frac{\widehat{\beta}}{2\sqrt{\pi}}\left[2\sqrt{\pi}e^{-\sigma\eta^2/4\tau}\right. \\ &\quad \left.+\pi\left(\frac{\sigma}{\tau}\right)^{1/2}\eta\,\mathrm{erf}\left(\left(\frac{\sigma}{\tau}\right)^{1/2}\frac{\eta}{2}\right)\right]-\widehat{\beta}+O(\tau).\end{aligned} \tag{4.34}$$

In the next section, the leading order velocity profiles (4.25) and (4.34) for $\tau \ll 1$ are used to solve the primary and oblique equations (4.6) and (4.7), for selected values of the frequency σ and amplitude Δ.

4.3 Numerics

In sections 4.2.1 and 4.2.2, the asymptotic solutions for the primary and oblique problems for $\tau \ll 1$ were found and are given in (4.25) and (4.34). In this section, we use these solutions as initial velocity profiles to solve the primary and oblique equations, which were initially stated in equations (4.6) and (4.7) and are given by

$$\sigma\psi_{P\eta\tau}+\left(\psi_{P\eta}\right)^2-\psi_P\psi_{P\eta\eta} = \sigma a_\tau+a^2+\psi_{P\eta\eta\eta}, \tag{4.35}$$

$$\sigma\psi_{O\tau}+\psi_{P\eta}\psi_O-\psi_P\psi_{O\eta} = -\sigma\widehat{\beta}_\tau+\widehat{\alpha}-a\widehat{\beta}+\psi_{O\eta\eta}, \tag{4.36}$$

with boundary conditions

$$\psi_P(0,\tau)=0,\quad \psi_{P\eta}(0,\tau)=0,\quad \psi_O(0,\tau)=0, \tag{4.37}$$

$$\psi_P(\eta,\tau)\to a(\tau)\eta-\widehat{\alpha},\quad \psi_O(\eta,\tau)\to\eta-\widehat{\beta}\quad\text{as}\quad\eta\to\infty, \tag{4.38}$$

where $a(\tau)=1+\Delta\cos\tau$, $\widehat{\beta}(\tau)=b_M+b_O\cos\tau$ and $\widehat{\alpha}(\tau)$ is obtained from the primary solution. To solve equations (4.35) and (4.36), a finite-difference technique is used with a second order accurate Crank-Nicolson method, which can be found in most numerical methods books, for example Gerald and Wheatley (1989). This method averages the centrally discretised functions at two time steps n and $n+1$. One benefit of using the Crank-Nicolson method over other finite-difference schemes is the stability, as there is no

restriction on the relation between the temporal and spatial step sizes. As the oblique equation (4.36) is dependent upon the primary equation, we begin by solving (4.35). Due to the nonlinear terms in equation (4.35), we write $\psi_q = \psi_{P\eta}$ and rewrite the primary equation as

$$\sigma\psi_{q_\tau} + \psi_q\psi_{P\eta} - \psi_P\psi_{q_\eta} \;=\; \sigma a_\tau + a^2 + \psi_{q_{\eta\eta}}, \tag{4.39}$$

giving a system which is linear in the two variables ψ_{P_η} and ψ_q. To begin, we give an example of the Crank-Nicolson method by discretising the convection terms in equation (4.39). We use the notation $\psi^n_{q_i} = \psi_q(\eta_i, t_n)$ and $\psi^n_{P_i} = \psi_P(\eta_i, t_n)$ and write

$$\begin{aligned}
\psi_q\psi_{P\eta} &\approx \frac{1}{2}\left[\psi^{n+1}_{q_i}\frac{\left(\psi^{n+1}_{P_{i+1}} - \psi^{n+1}_{P_{i-1}}\right)}{2h} + \psi^n_{q_i}\frac{\left(\psi^n_{P_{i+1}} - \psi^n_{P_{i-1}}\right)}{2h}\right], \\
\psi_P\psi_{q_\eta} &\approx \frac{1}{2}\left[\psi^{n+1}_{P_i}\frac{\left(\psi^{n+1}_{q_{i+1}} - \psi^{n+1}_{q_{i-1}}\right)}{2h} + \psi^n_{P_i}\frac{\left(\psi^n_{q_{i+1}} - \psi^n_{q_{i-1}}\right)}{2h}\right],
\end{aligned} \tag{4.40}$$

where h corresponds to the grid spacing $\eta_i = ih$ with $i = 1...N$ and dt represents the time interval $t_n = ndt$ with $n = 1...M$. Discretising the primary problem and using the expansions given in (4.40), we obtain

$$\begin{aligned}
&\sigma\frac{\left(\psi^{n+1}_{q_i} - \psi^n_{q_i}\right)}{dt} + \frac{\psi^{n+1}_{q_i}(\psi^{n+1}_{P_{i+1}} - \psi^{n+1}_{P_{i-1}}) - \psi^{n+1}_{P_i}(\psi^{n+1}_{q_{i+1}} - \psi^{n+1}_{q_{i-1}})}{4h} \\
&\qquad + \frac{\psi^n_{q_i}(\psi^n_{P_{i+1}} - \psi^n_{P_{i-1}}) - \psi^n_{P_i}(\psi^n_{q_{i+1}} - \psi^n_{q_{i-1}})}{4h} \\
&\qquad\qquad = \\
&\qquad \frac{1}{2}\Big(\sigma a_\tau + a^2\Big)^n_i + \frac{1}{2}\Big(\sigma a_\tau + a^2\Big)^{n+1}_i \\
&\qquad + \frac{\left(\psi^{n+1}_{q_{i+1}} - 2\psi^{n+1}_{q_i} + \psi^{n+1}_{q_{i-1}} + \psi^n_{q_{i+1}} - 2\psi^n_{q_i} + \psi^n_{q_{i-1}}\right)}{2h^2},
\end{aligned} \tag{4.41}$$

with boundary conditions

$$\psi^n_{q_1} = 0, \qquad \psi^n_{q_N} = 1 + \Delta\cos(Mdt). \tag{4.42}$$

The first term in equation (4.41) corresponds to the unsteady term in equation (4.35) and the second and third terms are a combination of the convective terms given in (4.40). The unsteady time-dependent components a and a_τ

have been averaged over two time steps and finally the last term represents the viscous term in (4.35). We rewrite (4.41) in terms of the tridiagonal system

$$A_i\psi^{n+1}_{q_{i+1}} + B_i\psi^{n+1}_{q_i} + C_i\psi^{n+1}_{q_{i-1}} = D_i, \tag{4.43}$$

with coefficients $A_i ... D_i$ given by

$$\begin{aligned}
A_i &= -1 - \frac{h}{2}\psi^{n+1}_{P_i}, && (4.44)\\
B_i &= \frac{2h^2\sigma}{dt} + 2 + \frac{h}{2}\left(\psi^{n+1}_{P_{i+1}} - \psi^{n+1}_{P_{i-1}}\right), && (4.45)\\
C_i &= -1 + \frac{h}{2}\psi^{n+1}_{P_i}, && (4.46)\\
D_i &= \psi^n_{q_{i+1}}\left(1 + \frac{h}{2}\psi^n_{P_i}\right) + \psi^n_{q_i}\left[\frac{2h^2\sigma}{dt} - 2 - \frac{h}{2}\left(\psi^n_{P_{i+1}} - \psi^n_{P_{i-1}}\right)\right] && (4.47)\\
&\quad + \psi^n_{q_{i-1}}\left(1 - \frac{h}{2}\psi^n_{P_i}\right) + \frac{h^2}{2}\left[\left(\sigma a_\tau + a^2\right)^n_i + \left(\sigma a_\tau + a^2\right)^{n+1}_i\right].
\end{aligned}$$

Within the coefficient D_i, everything is known at the n^{th} time step, whereas the coefficients A_i, B_i and C_i all have unknown functions at the $n+1^{th}$ time step.

To solve the tridiagonal system (4.43), we use the using the leading order asymptotic approximation found in section 4.2.1 as a starting profile. This profile could be written in terms of the scaled variable $\widehat{\eta} = (\sigma/\tau)^{1/2}\eta$, which was used in obtaining the small τ approximation. However, this would require the primary equation and boundary conditions to be rescaled in terms of $\widehat{\eta}$ and the numerics beginning at $\tau = 0$. Instead, it is easier to consider the initial profile in terms of η, given by

$$\begin{aligned}
\psi^n_{q_i} &= (1+\Delta)\mathrm{erf}\left[\left(\frac{\sigma}{\tau}\right)^{1/2}\frac{\eta^n_i}{2}\right], && (4.48)\\
\psi^n_{P_i} &= (1+\Delta)\left[\left(\frac{\sigma}{\tau}\right)^{1/2}\eta^n_i\mathrm{erf}\left(\left(\frac{\sigma}{\tau}\right)^{1/2}\frac{\eta^n_i}{2}\right) + \frac{2}{\sqrt{\pi}}\left(e^{-\frac{\eta^{2n}_i\sigma}{4\tau}} - 1\right)\right], && (4.49)
\end{aligned}$$

and begin the numerics at small τ. Figure 4.5 illustrates the starting profile $\psi_q(\eta, \tau_{initial})$ for different start times, denoted $\tau_{initial}$. Numerical trials have suggested that the starting profile does not affect the solution $\psi_q(\eta, \tau)$ as long as $\tau_{initial}$ is small and only the leading order initial profile is required to give accurate solutions.

At the first time step, $\psi_P^{n+1} = \psi_P^n$, where ψ_P^n is the initial profile (4.49). The tridiagonal system (4.43) is solved using the Thomas algorithm, which can be found, for example in Hoffman (2001), to give ψ_q^{n+1}. Integrating this function with respect to η via the trapezium rule, we obtain ψ_P^{n+1}. An iterative procedure is performed, where $\psi_{P_i}^{n+1}$ is compared with the previous iterate. When these iterates are within a small tolerance of each other, the value of ψ_P^{n+1} is then used as the initial profile at the next time step.

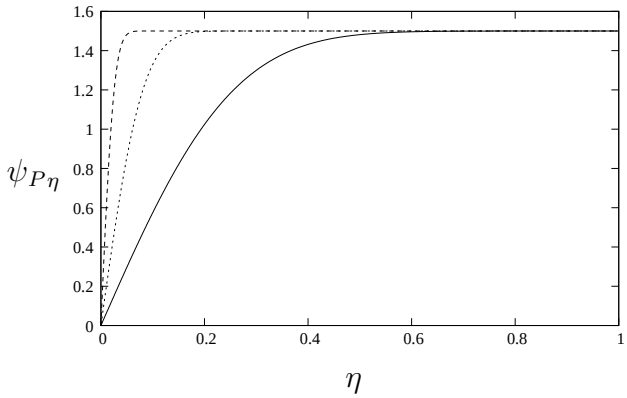

Figure 4.5: The initial velocity profile $\psi_{P\eta}(\eta, \tau)$, given in (4.48), for $\sigma = 0.5$ and $\Delta = 0.5$, initiated at different starting times, from left to right, $\tau = 0.0001$, $\tau = 0.001$ and $\tau = 0.01$.

Having described the method used to solve the primary equation, a similar method is used to solve the oblique equation (4.36). As this equation is linear in $\psi_{O_i}^n = \psi_O(\eta_i, t_n)$, the solution $\psi_{P_i}^n = \psi_P(\eta_i, t_n)$ at each time step is used. The oblique equation (4.36) is discretised as

$$\begin{aligned}
\sigma\frac{\left(\psi_{O_i}^{n+1}-\psi_{O_i}^{n}\right)}{dt} + \frac{\psi_{O_i}^{n+1}(\psi_{P_{i+1}}^{n+1}-\psi_{P_{i-1}}^{n+1}) - \psi_{P_i}^{n+1}(\psi_{O_{i+1}}^{n+1}-\psi_{O_{i-1}}^{n+1})}{4h} \\
+\frac{\psi_{O_i}^{n}(\psi_{P_{i+1}}^{n}-\psi_{P_{i-1}}^{n}) - \psi_{P_i}^{n}(\psi_{O_{i+1}}^{n}-\psi_{O_{i-1}}^{n})}{4h} \\
= \\
-\frac{\sigma}{2}\left(\widehat{\beta}_{\tau i}^{n}+\widehat{\beta}_{\tau i}^{n+1}\right)+\frac{1}{2}\left(\widehat{\alpha}_i^{n}+\widehat{\alpha}_i^{n+1}\right)-\frac{1}{4}\left(\left(a_i^n+a_i^{n+1}\right)\left(\widehat{\beta}_i^{n}+\widehat{\beta}_i^{n+1}\right)\right) \\
+\frac{\left(\psi_{O_{i+1}}^{n+1}-2\psi_{O_i}^{n+1}+\psi_{O_{i-1}}^{n+1}+\psi_{O_{i+1}}^{n}-2\psi_{O_i}^{n}+\psi_{O_{i-1}}^{n}\right)}{2h^2},
\end{aligned} \tag{4.50}$$

with boundary conditions

$$\psi_{O_1}^n = 0, \qquad \psi_{O_N}^n = hN - \widehat{\beta}_N^n. \tag{4.51}$$

The terms in (4.50) have been discretised similar to that of the primary equation (4.41). Additionally, the time-dependent function $\widehat{\alpha} = \lim_{\eta\to\infty}(a\eta - \psi_P)$ is obtained from solving the primary problem and is discretised over the current and next time step, with the function $\widehat{\beta}(\tau)$ discretised similarly over two time steps. Expressing equation (4.50) in terms of a tridiagonal system, we obtain

$$a_i\psi^{n+1}_{O_{i+1}} + b_i\psi^{n+1}_{O_i} + c_i\psi^{n+1}_{O_{i-1}} = d_i, \tag{4.52}$$

with coefficients $a_i ... d_i$ given by

$$a_i = -1 - \frac{h}{2}\psi^{n+1}_{P_i}, \tag{4.53}$$

$$b_i = \frac{2h^2\sigma}{dt} + 2 + \frac{h}{2}\left(\psi^{n+1}_{P_{i+1}} - \psi^{n}_{P_{i-1}}\right), \tag{4.54}$$

$$c_i = -1 + \frac{h}{2}\psi^{n+1}_{P_i}, \tag{4.55}$$

$$\begin{aligned} d_i = {} & \psi^n_{O_{i+1}}\left(1 + \frac{h}{2}\psi^n_{P_i}\right) + \psi^n_{O_i}\left[\frac{2h^2\sigma}{dt} - 2 - \frac{h}{2}\left(\psi^n_{P_{i+1}} - \psi^n_{P_{i-1}}\right)\right] \\ & + \psi^n_{O_{i-1}}\left(1 - \frac{h}{2}\psi^n_{P_i}\right) - \frac{\sigma}{2}\left(\widehat{\beta}^n_{\tau i} + \widehat{\beta}^{n+1}_{\tau i}\right) \\ & + \frac{1}{2}\left(\widehat{\alpha}^n_i + \widehat{\alpha}^{n+1}_i\right) - \frac{1}{4}\left[\left(a^n_i + a^{n+1}_i\right)\left(\widehat{\beta}^n_i + \widehat{\beta}^{n+1}_i\right)\right]. \end{aligned} \tag{4.56}$$

We note that the form of the oblique equation (4.36) is similar to that of the equation for ψ_q, given by (4.39). Consequently, the coefficients a_i, b_i and c_i are identical to the coefficients A_i, B_i and C_i from the primary discretisation and the only difference between d_i and D_i are the contributions from the time-dependent functions a, $\widehat{\alpha}$ and $\widehat{\beta}$. However, as the primary problem is now known at each time step the coefficients $a_i ... d_i$ are already known.

To solve the tridiagonal system (4.52), we use the leading order asymptotic approximation for small τ found in section 4.2.2. Similar to the primary problem, the starting profile could be written in terms of the scaled variable $\widehat{\eta}$, but that would require a rescaling of equation (4.36). Instead, we choose to write the initial profile in terms of η, which is given by

$$\begin{aligned} \psi^n_{O_i} = {} & \left[1 - \left(\frac{\sigma}{\tau}\right)^{1/2}\frac{\widehat{\beta}\sqrt{\pi}}{2}\right]\eta^n_i + \frac{\widehat{\beta}}{2\sqrt{\pi}}\left[2\sqrt{\pi}e^{-\sigma\eta_i^{2n}/4\tau}\right. \\ & \left. + \pi\left(\frac{\sigma}{\tau}\right)^{1/2}\eta^n_i \mathrm{erf}\left(\left(\frac{\sigma}{\tau}\right)^{1/2}\frac{\eta^n_i}{2}\right) - 2\sqrt{\pi}\right], \end{aligned} \tag{4.57}$$

and begin the numerics for small τ. We note when $\widehat{\beta} = 0$, the starting profile is independent of time and is simply given by $\psi_{O_i}^n = \eta_i^n$. As an example, we plot the initial oblique profile (4.57) in figure 4.6 when $\widehat{\beta} = 1$, for different starting times. Similar to the primary problem, numerical trials have shown that the oblique starting profile (4.57) does not affect the oblique solutions, as long as the starting time is small.

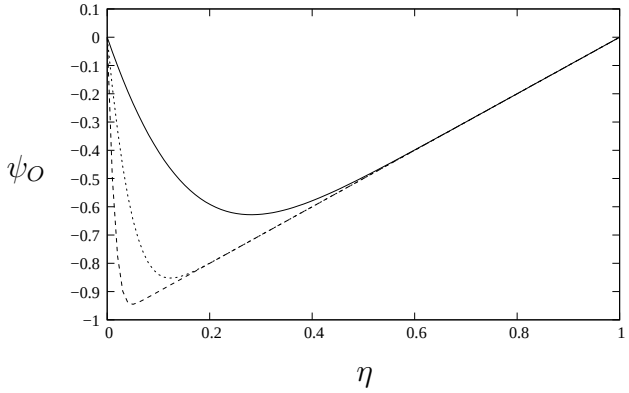

Figure 4.6: The initial velocity profile for $\psi_O(\eta, \tau)$ for $\widehat{\beta} = 1$ and $\sigma = 0.5$, initiated at different starting times, from top to bottom, $\tau = 0.01$, $\tau = 0.001$ and $\tau = 0.0001$.

Having described the theory used in solving the primary and oblique equations, by means of a Crank-Nicolson finite difference technique, we proceed by presenting a sample of results for selected values of the amplitude Δ and the frequency σ for different times, τ.

Figure 4.7 illustrates the velocity profiles $\psi_{P_\eta}(\eta, \tau)$ and $\psi_O(\eta, \tau)$ where $\widehat{\beta} = 0$ for $\sigma = 0.5$ and $\Delta = 0.1, 0.5, 0.8$ at $\tau = 1$. It can be seen in figure 4.7(b) that $\psi_O(\eta, \tau)$ is virtually independent of Δ over the whole range of η. This is due to the amplitude Δ not appearing in equation (4.50) or the boundary conditions (4.51) and the only contribution comes from the primary solution $\psi_P(\eta, \tau)$. Therefore, there is very little difference between the velocity profiles for differing values of the amplitude. For the parameter values chosen, the largest difference occurs in the region $0.5 < \eta < 2$ and this is illustrated in 4.7(c).

In figure 4.8(a), the oblique velocity profile is plotted for $\sigma = 0.5$ and $\Delta = 0.5$ at $\tau = 1$, where $b_O = 0$ and $b_M = 0, 1.02, 1.5$, i.e. $\widehat{\beta}$ only contains a mean

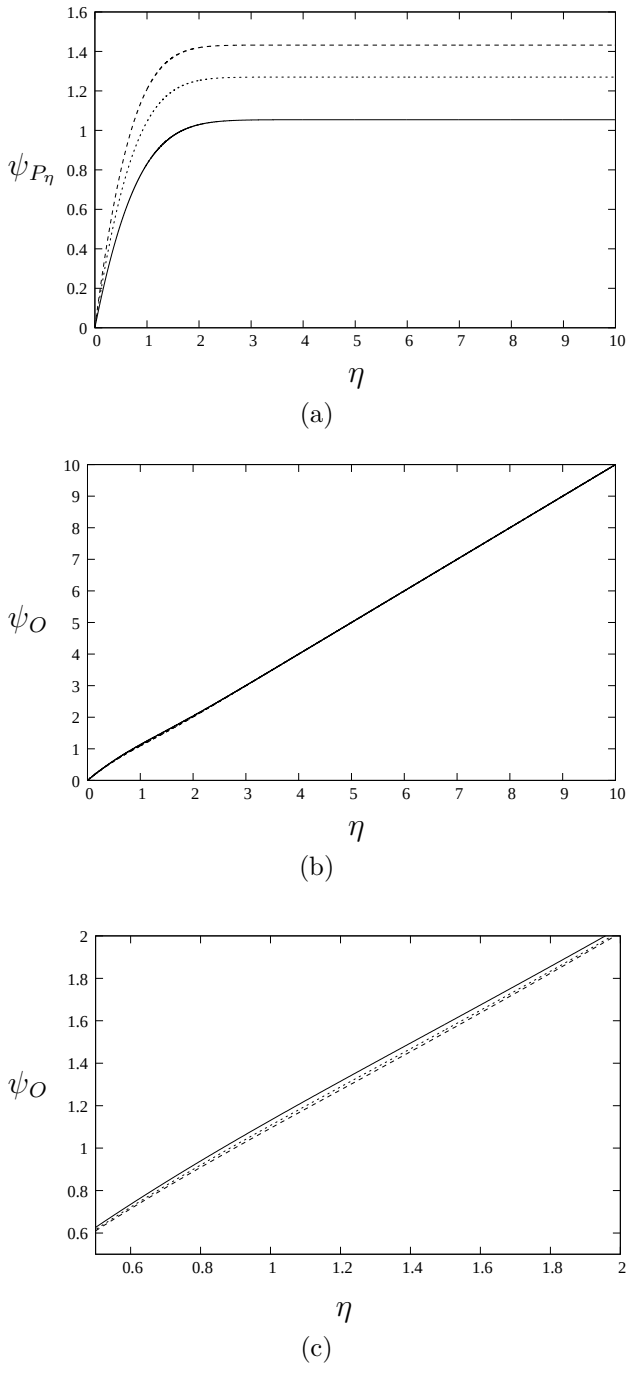

Figure 4.7: (a) The primary velocity profile for $\sigma = 0.5$ and $\Delta = 0.1, 0.5, 0.8$ at $\tau = 1$. (b) The oblique velocity profile for $\widehat{\beta} = 0$, $\sigma = 0.5$ and $\Delta = 0.1, 0.5, 0.8$ at $\tau = 1$. (c) A close up of the oblique velocity profile for the same parameters at $\tau = 1$. In each case $\Delta = 0.1$ is represented by the solid line, $\Delta = 0.5$, the dotted lines and $\Delta = 0.1$, the dashed lines.

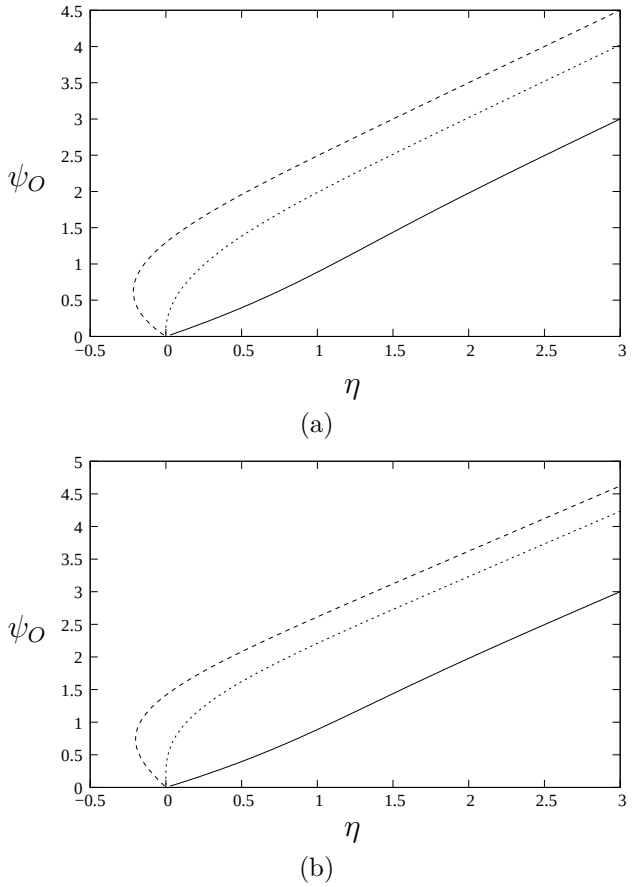

Figure 4.8: (a) The oblique velocity profile for $\sigma = 0.5$, $\Delta = 0.5$ at $\tau = 1$, where $b_O = 0$ and, from left to right, $b_M = 1.5, 1.02, 0$. (b) The oblique velocity profile for $\sigma = 0.5$, $\Delta = 0.5$ at $\tau = 1$, where $b_M = 0$ and, from left to right, $b_O = 3, 2.28, 0$.

component. When $b_M > 1.02$, a region of flow reversal occurs close to the wall. Increasing the mean component b_M, increases this region. Numerical trials have shown that as σ increases, the value of b_M at which flow reversal occurs decreases. Figure 4.8(b) illustrates the oblique velocity profile when $b_M = 0$ and $b_O = 0, 2.28, 3$, i.e. $\widehat{\beta}(\tau)$ is purely oscillatory. Similarly, we notice that when $b_O > 2.28$, a region of flow reversal is present close to the wall. Therefore, for a fixed value of the frequency and amplitude there exists a value of $\widehat{\beta}$, above which there is a region of flow reversal.

In performing these numerics, we have taken the spatial step size $h = 0.001$ and the temporal step size $dt = 0.001$. In the standard way, the values of h and dt are decreased as a way of validating our numerical calculations,

which do not affect our solutions. For the selected values of Δ chosen, solutions are found for $\tau < 1$. However, Blyth and Hall (2003) found that for a fixed frequency, if the amplitude is increased beyond a critical value, $\psi_P(\eta, \tau)$ breaks down at a finite-time singularity. Therefore, we proceed by considering the long term behaviour of $\psi_P(\eta, \tau)$ and $\psi_O(\eta, \tau)$ for values of Δ, both above and below the critical amplitude, which we denote $\Delta_c(\sigma)$.

For $\Delta < \Delta_c$, the primary wall shear component $\psi_{P_{\eta\eta}}(0, \tau)$ is obtained for all τ and is illustrated in figure 4.9(a) over a period of 2π for $\sigma = 0.5$ and $\Delta = 0.5, 0.8, 1$. However, for $\Delta > \Delta_c$, a time is reached at which the numerical scheme fails and the solutions break down at a finite-time singularity. This can be seen in figure 4.9(b), where the $\psi_{P_{\eta\eta}}(0, \tau)$ is plotted for $\sigma = 0.5$ and $\Delta = 2, 4, 6$.

Similarly, the oblique wall shear component $\psi_{O_\eta}(0, \tau)$ is computed for $\Delta < \Delta_c$ and $\Delta > \Delta_c$ respectively. For $\Delta < \Delta_c$, the oblique wall shear component is obtained for all τ and is plotted over a period of 2π in figure 4.10(a) for $\sigma = 0.5$ and $\Delta = 0.5, 0.8, 1$. Like that of the primary problem, for $\Delta > \Delta_c$, the oblique problem breaks down at a finite-time singularity, which is illustrated in figure 4.10(b) for $\sigma = 0.5$ and $\Delta = 2, 4, 6$. We note that the finite-time singularity is the same for both the primary and the oblique problems and the singular behaviour is more noticeable in the oblique case. We note that figures 4.9(b) and 4.10(b) show that for a fixed value of σ, the time at which the solutions break down decreases as Δ increases. An estimate of the finite-time singularity can be obtained numerically for each value of the amplitude for a fixed frequency. However, in the next section, the behaviour of the solutions close to the finite-time singularity are discussed and a more accurate value of the finite-time singularity is obtained.

4.3.1 The behaviour of the velocity profiles close to the finite-time singularity

For a given σ and Δ, the methods described in the previous section give a good estimate to the finite-time singularity, which occurs in the primary

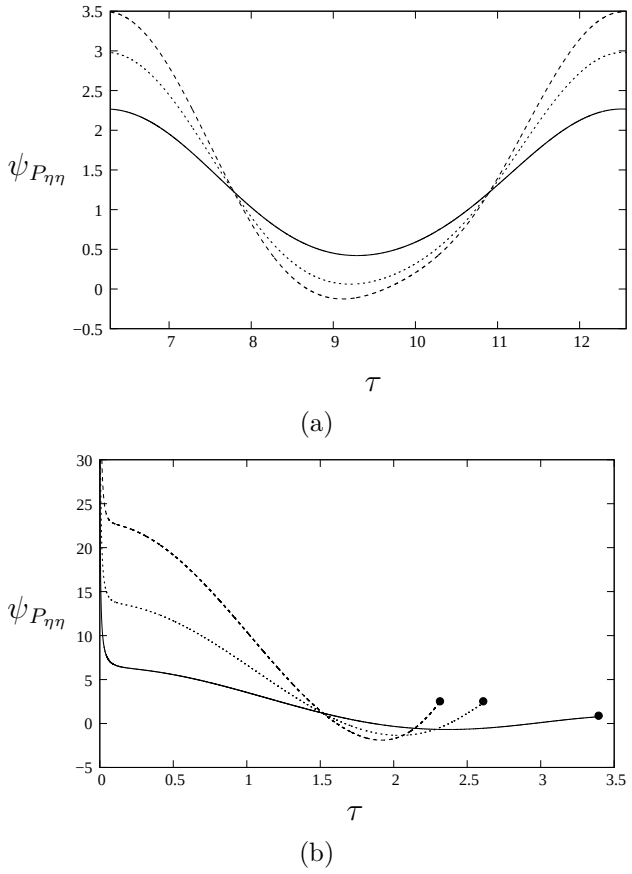

Figure 4.9: (a) The primary wall shear component $\psi_{P_{\eta\eta}}(0,\tau)$ for $\sigma = 0.5$ and $\Delta < \Delta_c$ over a single time period, for $\Delta = 0.5$ (solid line), $\Delta = 0.8$ (dotted lines) and $\Delta = 1$ (dashed lines). (b) The primary wall shear component $\psi_{P_{\eta\eta}}(0,\tau)$ for $\sigma = 0.5$ and $\Delta > \Delta_c$, where $\Delta = 2$ (solid line), $\Delta = 4$ (dotted lines) and $\Delta = 6$ (dashed lines). The dots represent where the numerics break down.

and oblique problems when, for a fixed frequency, the amplitude exceeds a critical amplitude. Similar time singularities appear in the flow around an impulsively rotated sphere considered by Banks and Zaturska (1979). In this case, a local asymptotic analysis in the region close to the finite-time singularity was presented. A similar technique was used by Blyth and Hall (2003) for the primary problem. We extend this analysis, to include the oblique problem. Blyth and Hall discovered that as $\tau \to \tau_s^-$, where τ_s denotes the finite-time singularity, the velocity profile $\psi_q(\eta,\tau)$ develops a minimum $\psi_{q_{min}}$ at η_{min}. Close to the finite-time singularity, η_{min} scales like $(\tau_s - \tau)^{-1}$, and $\psi_{q_{min}}$ scales like $(\tau_s - \tau)^{-1}$ as $\tau \to \tau_s^-$. Using these, we obtain $\psi_{q_{min}}$ at each time step and a linear relationship is obtained between

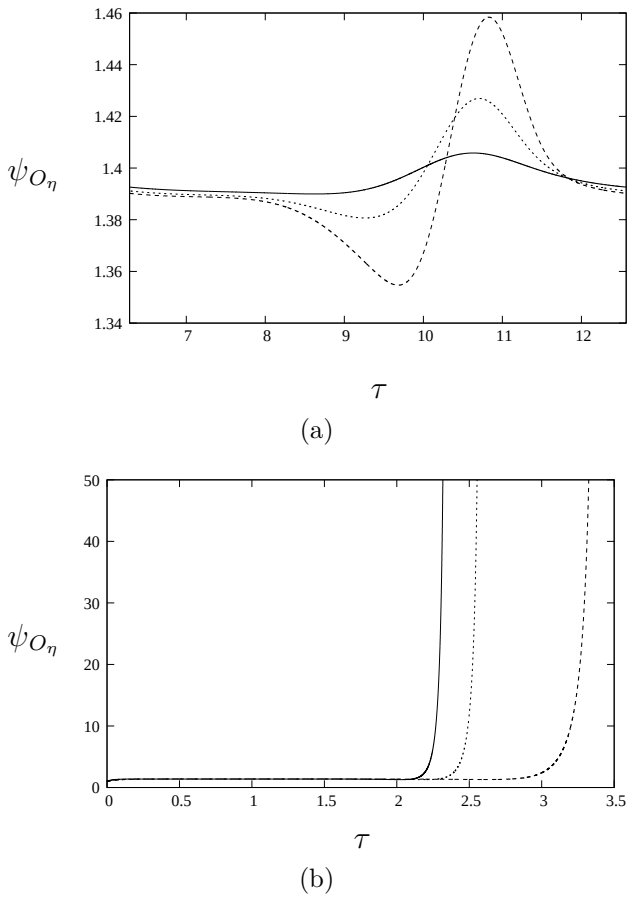

Figure 4.10: (a) The oblique wall shear component $\psi_{O_\eta}(0,\tau)$ illustrated for $\widehat{\beta} = 0$, $\sigma = 0.5$ and $\Delta < \Delta_c$ over a single time period, for $\Delta = 0.5$ (solid line), $\Delta = 0.8$ (dotted lines) and $\Delta = 1$ (dashed lines). (b) The oblique wall shear component $\psi_{O_\eta}(0,\tau)$ for $\widehat{\beta} = 0$, $\sigma = 0.5$ and $\Delta > \Delta_c$, where $\Delta = 2$ (the solid line), $\Delta = 4$ (dotted lines) and $\Delta = 6$ (dashed lines).

$\psi^{-1}_{q_{min}}(\eta_{min},\tau)$ and τ, for a fixed value of σ and $\Delta > \Delta_c$ as $\tau \to \tau_s^-$. We illustrate this relationship by considering the case for $\sigma = 0.5$ and $\Delta = 2$, which was previously discussed by Blyth and Hall (2003). Additionally, we confirm the finite-time singularity τ_s, calculated by Blyth and Hall for this choice of parameters and use this result and method to discuss the behaviour of the primary and oblique velocity profiles as the finite-time singularity is approached.

Using the numerical results obtained in section 4.3, for $\sigma = 0.5$ and $\Delta = 2$, $\psi_{q_{min}}(\eta_{min},\tau)$ is obtained at each time step. Figure 4.11(a) illustrates this minimum for $\tau = 3.37$, which is close to the finite-time singularity τ_s. We

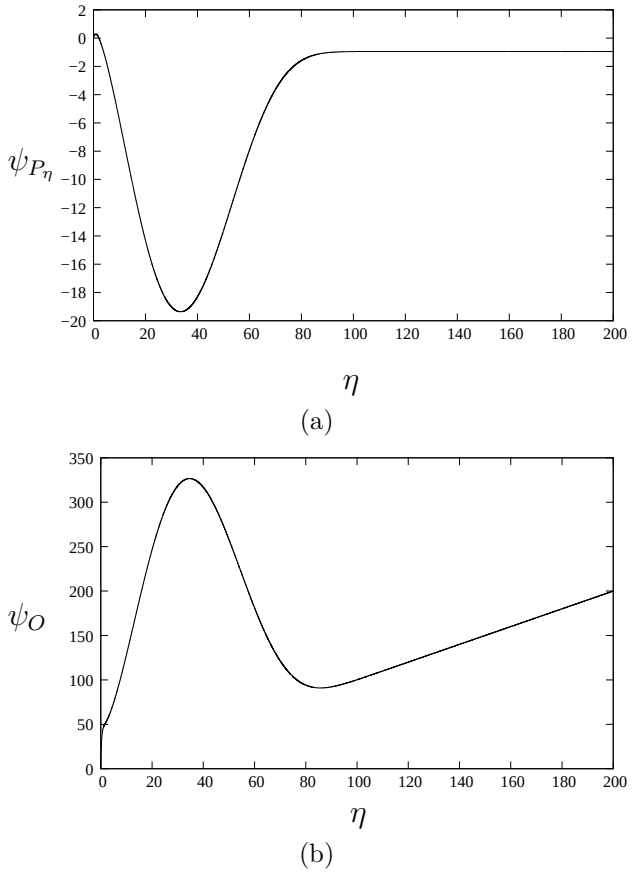

Figure 4.11: (a) The primary velocity profile, illustrating a minimum as $\tau \to \tau_s$ for $\sigma = 0.5$ and $\Delta = 2$ at $\tau = 3.37$. (b) The oblique velocity profile showing a maximum as $\tau \to \tau_s$, where $\sigma = 0.5$ and $\Delta = 2$ at $\tau = 3.37$. For these given parameters, the finite-time singularity is numerically calculated and given by $\tau_s = 3.396$.

improve $\psi_{q_{min}}(\eta_{min}, \tau)$ at each time step by using quadratic interpolation. Three points around the minimum, denoted $(\eta_1, \psi_{q_1}), (\eta_2, \psi_{q_2})$ and (η_3, ψ_{q_3}) are taken. A quadratic polynomial is sought through these points and we solve the system

$$\psi_{q_i} = b\eta_i^2 + c\eta_i + d, \tag{4.58}$$

for $i = 1, 2, 3$. Having obtained the values for b, c and d at each minimum, we obtain the interpolating polynomial $\psi_q^* = b\eta^2 + c\eta + d$. The minimum occurs when $\frac{d\psi_q^*}{d\eta} = 0$, at $\eta_{min} = -\frac{c}{2b}$. From the improved value of η_{min}, we can obtain the improved minimum, $\psi_{q_{min}} = b\eta_{min}^2 + c\eta_{min} + d$. The improved minimum is calculated for each value of τ as $\tau \to \tau_s^-$.

In figures 4.12(a) and 4.12(b), $\psi^{-1}_{q_{min}}(\eta_{min}, \tau)$ is plotted against τ, illustrating the linear relationship between $\psi^{-1}_{q_{min}}$ and τ as $\tau \to \tau_s^-$. By linear extrapolation, this line can be extended to meet the intercept of τ axis, which corresponds to the finite-time singularity, τ_s. To obtain the line through these points, the least squares method is used (Mathews (1986)). For ease of notation, we let $\psi^{-1}_{q_{min}} = q_n^{-1}$ at each time τ_n, where $n = 1...N$. Using the results obtained from the interpolation method, the least squares line through the points $(\tau_1, q_1^{-1}) - (\tau_N, q_N^{-1})$ is found. We write the least squares line as $q(\tau_n) = C\tau_n + D$, where C and D are to be found. The error between $q(\tau_n)$ and q_n^{-1} is defined by $e_n = q(\tau_n) - q_n^{-1}$ and we express the root-mean-square error as

$$E(q) = \left[\frac{1}{N}\sum_{n=1}^{N}\left|q(\tau_n) - q_n^{-1}\right|^2\right]^{1/2}. \tag{4.59}$$

It follows that

$$E(C, D) = \sum_{n=1}^{N}\left(C\tau_n + D - q_n^{-1}\right)^2 = N\left[E(q)\right]^2. \tag{4.60}$$

To calculate the minimal value of (4.60), we find the partial derivatives of $E(C, D)$ with respect to C and D and set these equal to zero. Therefore, we obtain the system

$$C\sum_{n=1}^{N}\tau_n^2 + D\sum_{n=1}^{N}\tau_n = \sum_{n=1}^{N}\tau_n q_n^{-1}, \tag{4.61}$$

$$C\sum_{n=1}^{N}\tau_n + ND = \sum_{n=1}^{N}q_n^{-1}, \tag{4.62}$$

where q_n^{-1} and τ_n are known at each time step n. Solving the system of equations (4.61) and (4.62), we obtain C and D, which correspond to the gradient and the intercept of the least squares line respectively. We are most interested in the intercept D, as this corresponds to the finite-time singularity, τ_s. The results of the linear extrapolation can be seen in table 4.3.1, where C and D have been calculated for different spatial step sizes and different time ranges. However, it can be seen that C and D are independent of these changes and we find $C = 0.50$ and $D = 3.396$. Therefore, for $\sigma = 0.5$ and

$\Delta = 2.0$, we obtain $\tau_s = 3.396$ correct to 3.d.p, which is in good agreement to Blyth and Hall (2003), who found $\tau_s = 3.39$.

Turning our attention to the oblique problem, a maximum, denoted $\psi_{O_{max}}(\eta_{max}, \tau)$, develops in the oblique velocity profile as $\tau \to \tau_s$, which can be seen in figure 4.11(b). Close to the finite-time singularity, we choose η_{max} to scale like $(\tau_s - \tau)^{-1}$, which follows from the primary problem and $\psi_{O_{max}}$ to scale like $(\tau_s - \tau)^{-1}$ as $\tau \to \tau_s^-$. From these scalings, a linear relationship can be seen between $\psi_{O_{max}}^{-1}(\eta_{max}, \tau)$ and τ as $\tau \to \tau_s^-$, which is illustrated in figure 4.12(c). Upon repeating the above analysis for the oblique problem, the finite-time singularity agrees with that calculated for the primary problem and is independent of the value of $\widehat{\beta}$. We note that the primary velocity profile develops a minimum as $\tau \to \tau_s^-$, however, the oblique velocity profile develops a maximum as $\tau \to \tau_s^-$.

Having obtained the finite-time singularity for $\sigma = 0.5$ and $\Delta = 2$ in figure 4.13, we present the time singularities for other selected values of σ and Δ, where lines of constant Δ are plotted. These time singularities were obtained using the method described above. As an example, for $\sigma = 2.5$ an $\Delta = 3$, the finite-time singularity is given by $\tau_s = 5.179$. We note that as σ tends to the critical value for a fixed Δ, the time at which the solutions break down increases.

Having solved the primary and oblique equations numerically, in the next section, we consider solutions in the small frequency limit. In addition to this, the small frequency approximation to the finite-time singularity is obtained.

4.4 Small frequency

In section 4.3, the primary and oblique equations, (4.6) and (4.7) respectively, were solved numerically. In this section, solutions to the primary and oblique equations are obtained in the small frequency limit. Also, an asymptotic expansion to the finite-time singularity for small σ is obtained, with comparisons being made with the time singularities calculated in section 4.3.

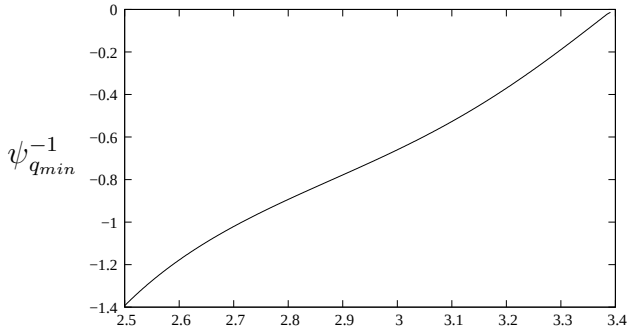

(a)

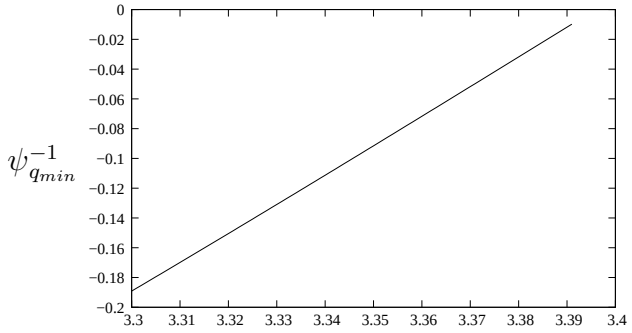

(b)

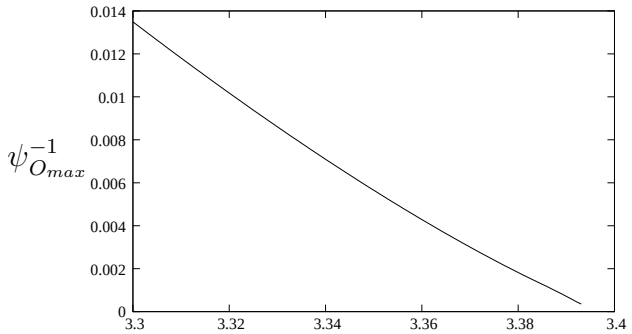

(c)

Figure 4.12: (a) The primary function, $\psi^{-1}_{q_{min}}(\eta_{min}, \tau)$ plotted against τ as $\tau \to \tau_s^-$ for $\Delta = 2$ and $\sigma = 0.5$. (b) A close-up of the primary function, $\psi^{-1}_{q_{min}}(\eta_{min}, \tau)$ plotted against τ as $\tau \to \tau_s^-$ for $\Delta = 2$ and $\sigma = 0.5$. (c) The oblique function, $\psi^{-1}_{O_{max}}(\eta_{max}, \tau)$ plotted against τ as $\tau \to \tau_s^-$ for $\widehat{\beta} = 0$, $\Delta = 2$ and $\sigma = 0.5$.

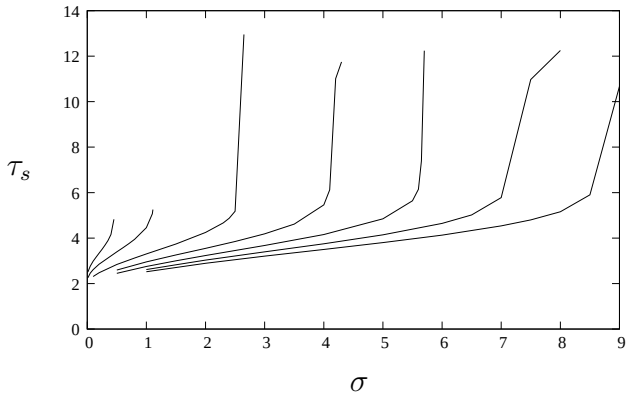

Figure 4.13: The time singularities calculated for fixed values of Δ. Lines of constant Δ are plotted, from left to right, $\Delta = 1.5, 2, 3, 4, 5, 6, 7$.

Riley and Vasantha (1989), who considered a flow with only an oscillatory component in the far-field, obtained the finite-time singularity expressed as an asymptotic series as $\sigma \to 0$. Blyth and Hall (2003) paralleled their work by considering the primary problem for $\sigma \to 0$. They found, for a fixed value of the amplitude above the threshold limit, a similar small frequency asymptotic approximation to the finite-time singularity. We follow Blyth and Hall (2003) by duplicating their work for the primary problem to validate their analysis and to enable us to solve the oblique problem.

When the frequency $\sigma = 0$, the primary equation reduces to the steady Hiemenz equation and the oblique equation reduces to that of the steady oblique equation discussed in chapter 3. Therefore, we expect as $\sigma \to 0$, the primary and oblique equations to be quasi-steady. To seek the primary solution, we pose the asymptotic expansion $\psi_P(\eta, \tau) = f_0(\eta, \tau) + \sigma f_1(\eta, \tau) + O(\sigma^2)$, as $\sigma \to 0$. Substituting this expansion into the primary equation (4.6), gives at leading order

$$f_{0\eta} f_{0\eta\eta} - f_{0\eta}^2 + f_{0\eta\eta\eta} + a^2 = 0, \tag{4.63}$$

with boundary conditions $f_0(0, \tau) = 0$, $f_0'(0, \tau) = 0$ and $f_0'(\eta, \tau) \to a(\tau)$ as $\eta \to \infty$, where $a(\tau) = 1 + \Delta \cos \tau$. To remove the time dependence from equation (4.63), we write $f_0 = a^{1/2} \widetilde{f}_0$ and $\widetilde{\eta} = a^{1/2} \eta$, where $a(\tau) > 0$, to give the leading order equation

$$\widetilde{f}_{0\widetilde{\eta}\widetilde{\eta}\widetilde{\eta}} - \widetilde{f}_{0\widetilde{\eta}}^2 + \widetilde{f}_0 \widetilde{f}_{0\widetilde{\eta}\widetilde{\eta}} + 1 = 0, \tag{4.64}$$

τ_R	A	B	h
3.30-3.39	0.50689	3.39624	0.001
3.31-3.39	0.55571	3.3961	0.001
3.32-3.39	0.504385	3.39608	0.001
3.33-3.39	0.503332037	3.39602	0.001
3.34-3.39	0.502411456	3.3959	0.001
3.35-3.39	0.5016214	3.39595	0.001
3.36-3.39	0.500955	3.39593	0.001
3.37-3.39	0.5003979	3.39591	0.001
3.38-3.39	0.49988	3.395906	0.001
3.33-3.39	0.50345	3.39603	0.005
3.34-3.39	0.502512	3.39598	0.005
3.35-3.39	0.501704479	3.39595	0.005
3.36-3.39	0.50102189	3.39593	0.005
3.37-3.39	0.50045	3.395917	0.005
3.38-3.39	0.4999444	3.39590	0.005

Table 4.1: Computing the gradient and the intercept of $\psi^{-1}_{q_{min}}$, where τ_R is the range over which the least squares analysis is conducted.

with boundary conditions $\widetilde{f}_0(0) = 0$, $\widetilde{f}_0'(0) = 0$ and $\widetilde{f}_0'(\widetilde{\eta}) \to 1$ as $\widetilde{\eta} \to \infty$. Therefore, the leading order equation in scaled variables for $0 < \Delta < 1$, as $\sigma \to 0$, is the same as the Hiemenz equation (3.3).

Having obtained the quasi-steady leading order approximation for the primary equation, we seek a similar approximation for the oblique equation. To do so, we write $\psi_O(\eta, \tau) = g_0(\eta, \tau) + \sigma g_1(\eta, \tau) + O(\sigma^2)$, as $\sigma \to 0$. Also, the primary scalings above are used with $\widehat{\alpha} = a^{1/2}\alpha$. This scaling follows from the far-field boundary condition (4.9), where α is a constant known from the steady problem in chapter 3. Upon substituting these scalings into the oblique equation, we obtain the leading order equation

$$\sigma g_{0\tau} + a\left(\widetilde{f}_{0\widetilde{\eta}} g_0 - \widetilde{f}_0 g_{0\widetilde{\eta}}\right) = -\sigma\widehat{\beta}_\tau + a^{1/2}\alpha - a\widehat{\beta} + a g_{0\widetilde{\eta}\widetilde{\eta}\widetilde{\eta}}. \tag{4.65}$$

The far-field boundary condition $\psi_O(\eta, \tau) \to \eta - \widehat{\beta}$ suggests the scalings $g_0 = a^{-1/2}\widetilde{g}_0$ and $\widehat{\beta} = a^{-1/2}\beta$, where $a(\tau) > 0$. The constant β is known from the steady problem in chapter 3 and is the strength of the uniform stream.

Using these scalings, equation (4.65) becomes

$$\sigma a^{-1/2}\widetilde{g}_{0\tau} + a^{1/2}\left(\widetilde{f}_{0\widetilde{\eta}}\widetilde{g}_0 - \widetilde{f}_0\widetilde{g}_{0\widetilde{\eta}}\right) = \\ -\sigma a^{-1/2}\beta_\tau + a^{1/2}(\alpha-\beta) + a^{1/2}\widetilde{g}_{0\widetilde{\eta}\widetilde{\eta}\widetilde{\eta}}. \tag{4.66}$$

Thus, as $\sigma \to 0$, the leading order equation in scaled variables for $0 < \Delta < 1$ is given by

$$\widetilde{g}_{0\widetilde{\eta}\widetilde{\eta}\widetilde{\eta}} + \widetilde{f}_0\widetilde{g}_{0\widetilde{\eta}} - \widetilde{g}_0\widetilde{f}_{0\widetilde{\eta}} = \beta - \alpha, \tag{4.67}$$

with boundary conditions $\widetilde{g}_0(0) = 0$ and $\widetilde{g}_0(\widetilde{\eta}) \to \widetilde{\eta} - \beta$ as $\widetilde{\eta} \to \infty$, which is the same as the steady oblique equation (3.5).

When $\Delta > 1$, the approximations (4.64) and (4.67) are no longer valid for all τ as there is a region in which $a(\tau) < 0$. This is illustrated in figure 4.14, where the leading order asymptotic approximation $\psi_{P_{\eta\eta}}(0,\tau) = (1 + \Delta\cos\tau)^{3/2}\widetilde{f}_0''(0)$ is plotted for $\Delta = 0.5, 1, 2$, where $\widetilde{f}_0''(0) = 1.233$. Therefore, we proceed by looking for solutions to the primary and oblique equations (4.6) and (4.7), when $\Delta > 1$ for small σ.

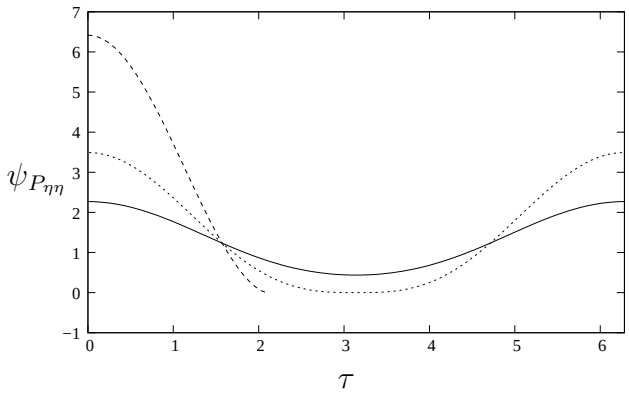

Figure 4.14: The leading order asymptotic primary wall shear component $\psi_{P_{\eta\eta}}(0,\tau)$ plotted against τ for $\Delta = 0.5$ (solid line), $\Delta = 1$ (dotted lines) and $\Delta = 2$ (dashed lines). When $\Delta > 1$, it is observed that the primary wall shear component breaks down.

When $\Delta > 1$, $a(\tau) = 1 + \Delta\cos\tau$ develops a zero at $\tau_0 = \pi - \cos^{-1}(\frac{1}{\Delta})$. The quasi-steady approximations break down when $\tau \to \tau_0$, i.e. when the time-dependent terms become comparable to the steady terms in equations (4.6) and (4.7). Comparing the magnitudes of the terms in the primary

equation, $\sigma\psi_{P\eta\tau} \sim \left(\psi_{P\eta}\right)^2$ leads to the approximation $a \sim \sigma^{1/2}$. Using this scaling, we rescale the primary and oblique variables as

$$\psi_P(\eta,\tau) = \sigma^{1/4}\widehat{P}(Y,T), \quad \psi_O(\eta,\tau) = \sigma^{-1/4}\widehat{O}(Y,T), \quad \eta = \sigma^{-1/4}Y, \quad (4.68)$$
$$(\tau_0 - \tau) = \sigma^{1/2}T, \quad \widehat{\alpha} = \sigma^{1/4}\widetilde{\alpha}, \quad \widehat{\beta} = \sigma^{-1/4}\widetilde{\beta}.$$

As $a(\tau)$ appears explicitly in the primary equation (4.6), we take a Taylor expansion of $a(\tau)$ about τ_0, to obtain

$$a = a_\tau(\tau_0)(\tau - \tau_0) + O\left((\tau - \tau_0)^2\right), \quad (4.69)$$

since $a(\tau_0) = 0$. Using the property $\sin\tau_0 = (1 - \cos^2\tau_0)^{1/2}$, we find $\sin\tau_0 = \frac{1}{\Delta}\left(\Delta^2 - 1\right)^{1/2}$ and (4.69) becomes

$$a = (\Delta^2 - 1)^{1/2}(\tau_0 - \tau) + O\left((\tau - \tau_0)^2\right). \quad (4.70)$$

Using the scalings (4.68) and the expansion (4.70), the primary and oblique equations become

$$-\widehat{P}_{YT} + \widehat{P}_Y^2 - \widehat{P}\widehat{P}_{YY} = -\mu + \mu^2 T^2 + \widehat{P}_{YYY}, \quad (4.71)$$
$$-\widehat{O}_T + \widehat{O}\widehat{P}_Y - \widehat{P}\widehat{O}_Y = \widetilde{\beta}_T + \widetilde{\alpha} - \mu T\widetilde{\beta} + \widehat{O}_{YY}, \quad (4.72)$$

with boundary conditions

$$\widehat{P}(0,T) = 0, \quad \widehat{P}'(0,T) = 0, \quad \widehat{O}(0,T) = 0, \quad (4.73)$$
$$\widehat{P}'(Y,T) \to \mu T, \quad \widehat{O}(Y,T) \to Y - \widehat{\beta} \quad \text{as} \quad Y \to \infty, \quad (4.74)$$

where $\mu = (\Delta^2 - 1)^{1/2}$ with $\Delta^2 - 1 > 0$.

We begin by solving equations (4.71) and (4.72) using a Crank-Nicolson finite-difference technique described previously in section 4.3. However, equations (4.71) and (4.72) are integrated backwards in T, which is equivalent to integrating forwards in τ. The computations are initiated at $T = T_\infty = 5$. At T_∞, the functions $\widehat{P}(Y,T)$ and $\widehat{O}(Y,T)$ need to match to the quasi-steady approximations (4.64) and (4.67). Hence, we write $\widehat{P} = \left(\frac{\mu T}{T_\infty}\right)^{1/2}\widetilde{P}$, $\widehat{O} = \left(\frac{\mu T}{T_\infty}\right)^{-1/2}\widetilde{O}$, $\widetilde{\alpha} = \left(\frac{\mu T}{T_\infty}\right)^{1/2}\bar{\alpha}$, $\widetilde{\beta} = \left(\frac{\mu T}{T_\infty}\right)^{-1/2}\bar{\beta}$ with variable $Z = \left(\frac{\mu T}{T_\infty}\right)^{1/2}Y$.

Substituting these scalings into equations (4.71) and (4.72), we obtain the leading order profiles

$$\widetilde{P}''' + \widetilde{P}\widetilde{P}'' - \widetilde{P}'^2 + T_\infty^2 = 0, \tag{4.75}$$

$$\widetilde{O}'' + \widetilde{P}\widetilde{O}' - \widetilde{O}\widetilde{P}' = \bar{\alpha} - T_\infty\bar{\beta}, \tag{4.76}$$

with boundary conditions

$$\widetilde{P}(0,T) = 0, \quad \widetilde{P}'(0,T) = 0, \quad \widetilde{O}(0,T) = 0, \tag{4.77}$$

$$\widetilde{P}'(Z,T) \to T_\infty, \quad \widetilde{O}(Z,T) \to Z - \widetilde{\beta} \quad \text{as} \quad Z \to \infty, \tag{4.78}$$

where the prime denotes differentiation with respect to Z. We note the equations (4.75) and (4.76) are scaled versions of the leading order quasi-steady approximations (4.64) and (4.67).

To solve the primary equation (4.71), we use the starting profile (4.75), which is a scaled version of the Hiemenz equation, to initiate the numerics. The solutions $\widehat{P}(Y,T)$ are used at each time step T to solve the oblique equation (4.72) with the starting profile (4.76). As the primary equation (4.71) is nonlinear, we write $Q = \widehat{P}_Y$ and rewrite the equation (4.71) as

$$-Q_T + Q\widehat{P}_Y - \widehat{P}Q_Y = -\mu + \mu^2 T^2 + Q_{YY}, \tag{4.79}$$

with boundary conditions $Q(0,T) = 0$ and $Q(Y,T) \to \mu T$ as $Y \to \infty$. Equation (4.79) is discretised similarly to that in section 4.3 and integrated backwards in T using the Thomas algorithm until the computations fail to converge at some T, denoted T_s.

We solve (4.79) for the example case of $\Delta = 2$, which was the case considered by Blyth and Hall (2003). Similarly to that of the primary problem discussed in section 4.3.1, $Q(Y,T)$ develops a minimum $Q_{min}(Y_{min},T)$, as $T \to T_s^+$. We choose the scalings $Q_{min} \sim (T_s - T)^{-1}$ with $Y_{min} \sim (T_s - T)^{-1}$ as $T \to T_s^+$ and a linear relationship is found between $Q_{min}^{-1}(Y_{min},T)$ and T. To improve the minimum $Q_{min}(Y_{min},T)$, which was obtained numerically at each time step, we seek a quadratic polynomial through the three points around the minimum. Figure 4.15(a) illustrates the linear relationship between the improved minimum $Q_{min}^{-1}(Y_{min},T)$ and T for $\Delta = 2$. Using linear

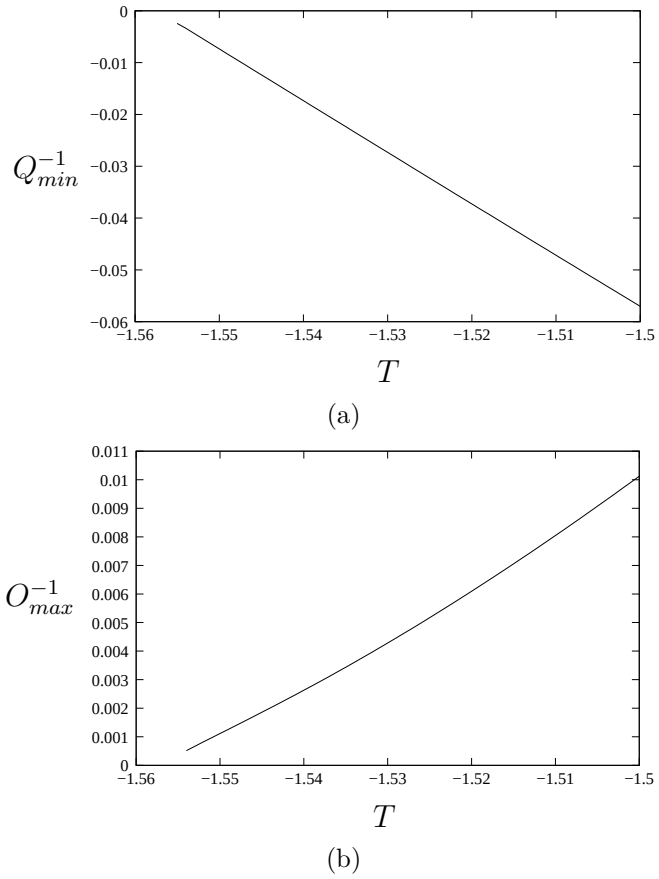

Figure 4.15: (a) The primary function $Q_{min}^{-1}(Y_{min}, T)$ plotted against T as $T \to T_s^+$ for $\Delta = 2$. (b) The oblique function $O_{max}^{-1}(Y_{max}, T)$ plotted against T as $T \to T_s^+$, for $\widehat{\beta} = 0$. Both of these figures illustrate a linear relationship as $T \to T_s^+$.

extrapolation, this line is extended to intersect the T-axis, where the intercept corresponds to the finite-time singularity T_s. These methods were previously discussed in section 4.3.1. In the case of $\Delta = 2$, we find $T_s = -1.557$.

This finite-time singularity T_s differs slightly from the work of Blyth and Hall (2003), who calculate the finite-time singularity $T_s = -1.51$. Therefore, to confirm the accuracy of our numerics and T_s, figure 4.16 illustrates $Q_{min}^{-1}(Y_{min}, T)$ plotted against T for different values of the spacial and temporal step sizes. It can be seen when both the spacial and the temporal step sizes are decreased, there is no change to the linear relationship or the finite-time singularity T_s. We also note that the value of the intercept T_s is independent of the starting time T_∞, as long as T_∞ is large. As an outcome, we believe that the finite-time singularity calculated is correct.

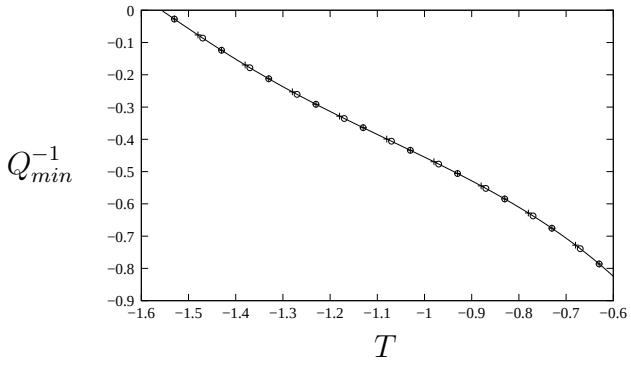

Figure 4.16: The primary function $Q_{min}^{-1}(Y_{min}, T)$ plotted against T as $T \to T_s^+$, confirming the accuracy of the finite-time singularity $T_s = -1.557$. The solid line represents a spacial and temporal step size of 0.001. The crosses represent a spacial step size of $h = 0.001$ and a temporal step size of $dt = 0.0005$. The circles represent a spacial step size of $h = 0.0005$ and a temporal step size of $dt = 0.001$.

The oblique equation (4.72) is solved using the same method as that for the primary equation (4.71). Similar to that of the oblique equation discussed in section 4.3.1, $\widehat{O}(Y, T)$ develops a maximum $\widehat{O}_{max}(Y_{max}, T)$, as $T \to T_s^+$ and we scale $\widehat{O}_{max} \sim (T_s - T)^{-1}$ with $Y_{max} \sim (T_s - T)^{-1}$ as $T \to T_s^+$. Using these scalings, a linear relationship between $\widehat{O}_{max}^{-1}(Y_{max}, T)$ and T occurs as $T \to T_s^+$. The maximum $\widehat{O}_{max}$, which was obtained numerically, is improved using a quadratic polynomial through three points around the maximum. We illustrate the linear relationship between the improved maximum $\widehat{O}_{max}^{-1}(Y_{max}, T)$ and T in figure 4.15(b) for $\Delta = 2$ and we find $T_s = -1.557$, which agrees with the finite-time singularity calculated in the primary problem.

To obtain the general relation for the finite-time singularity T_s and τ_s, we use the scaling given in (4.68) and find

$$\frac{\tau_s(\sigma, \Delta)}{\sigma} = \frac{\pi - \cos^{-1}\left(\frac{1}{\Delta}\right)}{\sigma} - \frac{T_s(\Delta)}{\sigma^{1/2}} + O(\sigma) \quad \text{as} \quad \sigma \to 0. \tag{4.80}$$

For the sample case of $\Delta = 2$, we find τ_s is given by

$$\frac{\tau_s}{\sigma} = \frac{2\pi}{3\sigma} + \frac{1.557}{\sigma^{1/2}} + \cdots \quad \text{as} \quad \sigma \to 0. \tag{4.81}$$

In figure 4.17, the finite-time singularity (4.81) is considered alongside the numerical results obtained in section 4.3 for $\Delta = 2$, showing good agreement as $\sigma \to 0$.

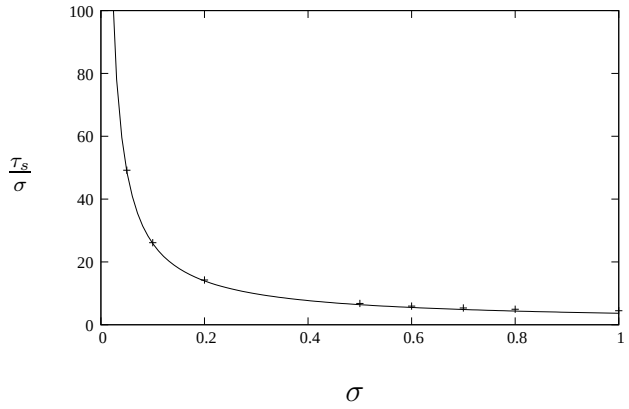

Figure 4.17: The finite-time singularity approximation (4.81), represented by the solid line, plotted alongside some numerical results from section 4.3 for $\Delta = 2$, represented by the crosses. Good agreement can be seen between the numerical results and the asymptotic solution for $\sigma \sim 1$.

Having considered the solutions to the primary and oblique equations, both numerically for selected values of the amplitude Δ and frequency σ and in the small frequency limit, in the next section we discuss the streamlines for different values of σ and Δ. Predominantly, in this section, the numerics have been obtained for $\widehat{\beta} = 0$, whereas in the next section the effect of the time-dependent horizontal component $\widehat{\beta} \neq 0$ is discussed.

4.5 The structure of the near-wall flow

In section 4.3, the primary and oblique equations have been solved numerically using a finite-difference method for selected values of Δ and σ. In this section, we discuss the flow structure near the wall. To do so, we consider the dividing streamline and the attachment point with the wall for a range of values of Δ and σ.

We recall that the streamfunction, initially stated in (4.5), is given by

$$\psi(x, \eta, \tau) = (\nu k)^{1/2} x \psi_P(\eta, \tau) + \widehat{\zeta}\Big(\frac{\nu}{k}\Big) \int_0^\eta \psi_O(z, \tau) \mathrm{d}z, \tag{4.82}$$

where $\eta = (k/\nu)^{1/2} y$, $\widehat{\zeta}$ is the constant vorticity, k is the strength of the orthogonal component and ν is the viscosity. To find the dividing streamline,

we set (4.82) equal to zero, to obtain

$$x_d = -\widehat{\zeta}\left(\frac{\nu}{k^3}\right)^{1/2} \frac{\int_0^\eta \psi_O(z,\tau)\mathrm{d}z}{\psi_P(\eta,\tau)}. \tag{4.83}$$

Due to the wall boundary conditions $\psi_P(0,\tau) = \psi_{P_\eta}(0,\tau) = 0$, the denominator of (4.83) equals zero at $\eta = 0$. Therefore, the primary and oblique components are expressed in the small η limit as $\psi_O(0,\tau) = \psi_{O_\eta}(0,\tau)\eta + \psi_{O_{\eta\eta}}(0,\tau)\eta^2/2 + O(\eta^3)$ and $\psi_P(0,\tau) = \psi_{P_{\eta\eta}}(0,\tau)\eta^2/2 + \psi_{P_{\eta\eta\eta}}(0,\tau)\eta^3/6 + O(\eta^4)$. Substituting these expansions into (4.83), we obtain $x_d = x_0 + G\eta$, where x_0 is given by

$$x_0 \;=\; -\widehat{\zeta}\left(\frac{\nu}{k^3}\right)^{1/2} \frac{\psi_{O_\eta}(0,\tau)}{\psi_{P_{\eta\eta}}(0,\tau)}, \tag{4.84}$$

which is the point at which the dividing streamline meets the wall. Additionally, the gradient of the dividing streamline at the wall is given by $1/G$, where

$$G \;=\; -\widehat{\zeta}\left(\frac{\nu}{k^3}\right)^{1/2} \frac{1}{3\psi_{P_{\eta\eta}}(0,\tau)}\left[\psi_{O_{\eta\eta}}(0,\tau) - \frac{\psi_{O_\eta}(0,\tau)\psi_{P_{\eta\eta\eta}}(0,\tau)}{\psi_{P_{\eta\eta}}(0,\tau)}\right]. \tag{4.85}$$

We recall that only the oblique function $\psi_O(\eta,\tau)$ is dependent upon the time-dependent function $\widehat{\beta}(\tau) = b_M + b_O\cos\tau$, where the oscillatory component oscillates with the same frequency as $a(\tau) = 1 + \Delta\cos\tau$. For the most part, in this section, the dividing streamline is considered for $\widehat{\beta}(\tau) = 0$, but the effect of $\widehat{\beta}(\tau) \neq 0$ is also discussed.

In order to analyse x_0, we illustrate the primary and oblique wall shear components $\psi_{P_{\eta\eta}}(0,\tau)$ and $\psi_{O_\eta}(0,\tau)$ in figure 4.18 for $\sigma = 1$ and $\Delta = 0.5, 0.85$ and $\Delta = 1.2$ over a single time period. Figure 4.18(a) shows that as Δ increases, $\psi_{P_{\eta\eta}}(0,\tau)$ develops zeros and becomes negative at some point during the time period. Numerical trials indicate that when $\Delta < 0.785$ there are no zeros in $\psi_{P_{\eta\eta}}(0,\tau)$. The zeros in $\psi_{P_{\eta\eta}}(0,\tau)$, which occur in the case when $\Delta = 0.85$, are surprising as $a(\tau)$, illustrated in figure 4.3 for $\Delta = 0.85$ does not have any zeros and the primary flow does not reverse. Therefore, the zeros occurring in the primary wall shear component and $a(\tau)$ are independent. We note that the oblique wall shear component, illustrated in figure 4.18(b), is positive everywhere for the selected values of Δ above.

When $\Delta = 0.5$, both $\psi_{P_{\eta\eta}}(0,\tau) > 0$ and $\psi_{O_\eta}(0,\tau) > 0$, implying that as τ increases, the attachment point x_0, given in (4.84), is negative and oscillates between two bounding values. This is illustrated in figure 4.19(a) for $\sigma = 1$ and $\Delta = 0.5$ over one time period.

We now consider the behaviour of the dividing streamline x_d, which is given in (4.83), far from the wall. We note that for $\widehat{\beta} = 0$, the oblique function $\int_0^\eta \psi_O(z,\tau)\mathrm{d}z \to \eta^2/2$ as $\eta \to \infty$ over the time period. Additionally, as $\psi_{P_{\eta\eta}}(0,\tau) > 0$, a local minimum in ψ_P occurs at $\eta = 0$ and as $\eta \to \infty$, $\psi_P(\eta,\tau) \to a\eta - \widehat{\alpha}$. Since $a(\tau) > 0$ for $\Delta = 0.5$, $\psi_P(\eta,\tau)$ is positive as $\eta \to \infty$. Hence, the dividing streamline is negative and oscillates between two bounding values. This behaviour is illustrated in figure 4.20, where the dividing streamline is plotted for $\sigma = 1$, $\Delta = 0.5$ and $\widehat{\beta} = 0$ over a single time period.

The gradient of the dividing streamline at the wall $1/G$, where G is given in (4.85) is also considered. In figure 4.19(c), we illustrate the gradient $1/G$ for $\sigma = 1$ and $\Delta = 0.5$. We note that the gradient over a period of 2π sweeps between two bounding values.

Due to the zeros that occur in the primary wall shear component for $\Delta = 0.85$ and $\Delta = 1.2$, which can be seen in figure 4.18, the attachment point x_0 and the dividing streamline x_d behave differently to those described above for $\Delta = 0.5$. We note in each case, $\psi_{O_\eta}(0,\tau) > 0$ over the cycle. When $\psi_{P_{\eta\eta}}(0,\tau) > 0$, x_0 is negative. As we progress through the time period and the zero in $\psi_{P_{\eta\eta}}(0,\tau)$ is approached, x_0 tends to negative infinity before reappearing at positive infinity. Similarly, when $\psi_{P_{\eta\eta}}(0,\tau) < 0$, the attachment point x_0 is positive and tends to positive infinity before reappearing at negative infinity. The attachment point x_0 is illustrated for $\sigma = 1$ and $\Delta = 1.2$ in figure 4.19(b). The gradient with the wall for the same parameters is shown in figure 4.19(d).

The dividing streamline x_d, given in (4.83), is now discussed at a fixed time τ for both $\psi_{P_{\eta\eta}}(0,\tau) < 0$ and $\psi_{P_{\eta\eta}}(0,\tau) > 0$. When $\psi_{P_{\eta\eta}}(0,\tau) < 0$, $\psi_P(\eta,\tau)$ has a local maximum at $\eta = 0$ and as $\eta \to \infty$, $\psi_P(\eta,\tau) \to a\eta - \widehat{\alpha}$.

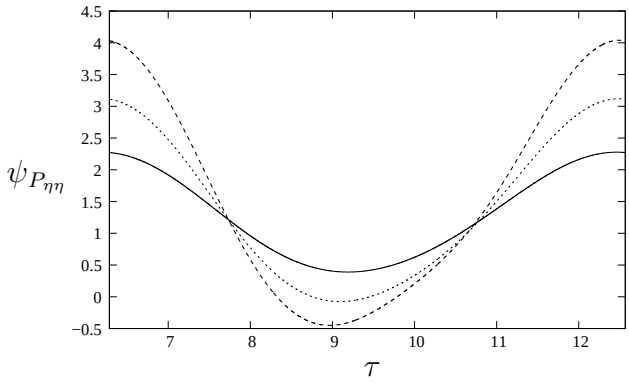

(a)

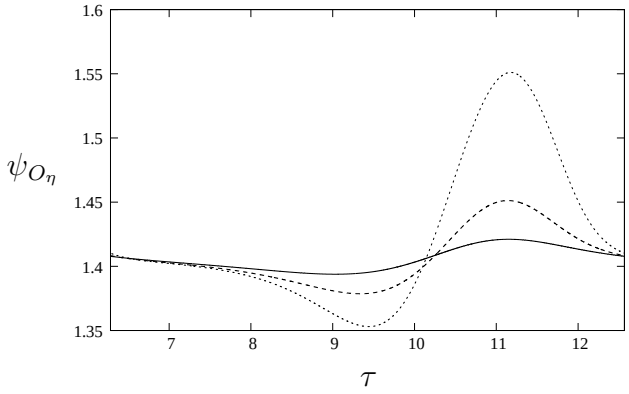

(b)

Figure 4.18: (a) The primary wall shear component $\psi_{P_{\eta\eta}}(0,\tau)$ and (b) the oblique wall shear component $\psi_{O_\eta}(0,\tau)$, both for $\widehat{\beta}(\tau) = 0$, $\sigma = 1$ and $\Delta = 0.5$ (solid line), $\Delta = 0.85$ (dashed lines) and $\Delta = 1.2$ (dotted lines).

If $a(\tau) < 0$, $\psi_P(\eta,\tau)$ is negative and the dividing streamline x_d is to the right of x_0, similar to the dividing streamline discussed above for $\sigma = 1$ and $\Delta = 0.5$. If $a(\tau) > 0$, $\psi_P(\eta_1^*,\tau) = 0$ at $\eta = \eta_1^*$, as illustrated in figure 4.21(a) for $\sigma = 1$ and $\Delta = 1.2$. To consider how the dividing streamline behaves close to $\eta = \eta_1^*$, we perform a local analysis about $\eta = \eta_1^*$. Differentiating the streamfunction (4.82), we obtain the velocity components $u = (\nu k)^{1/2}u^*$ and $v = (\nu k)^{1/2}v^*$, where u^* and v^* are given by

$$u^* = X\psi_{P_\eta}(\eta,\tau) + \frac{\widehat{\zeta}}{k}\psi_O(\eta,\tau), \tag{4.86}$$

$$v^* = -\psi_P(\eta,\tau), \tag{4.87}$$

where $X = \left(\frac{k}{\nu}\right)^{1/2} x$. The vertical velocity component (4.87) suggests that the stagnation points occur when $\psi_P(\eta,\tau) = 0$, i.e. when $\eta = 0$ and $\eta = \eta_1^*$. At

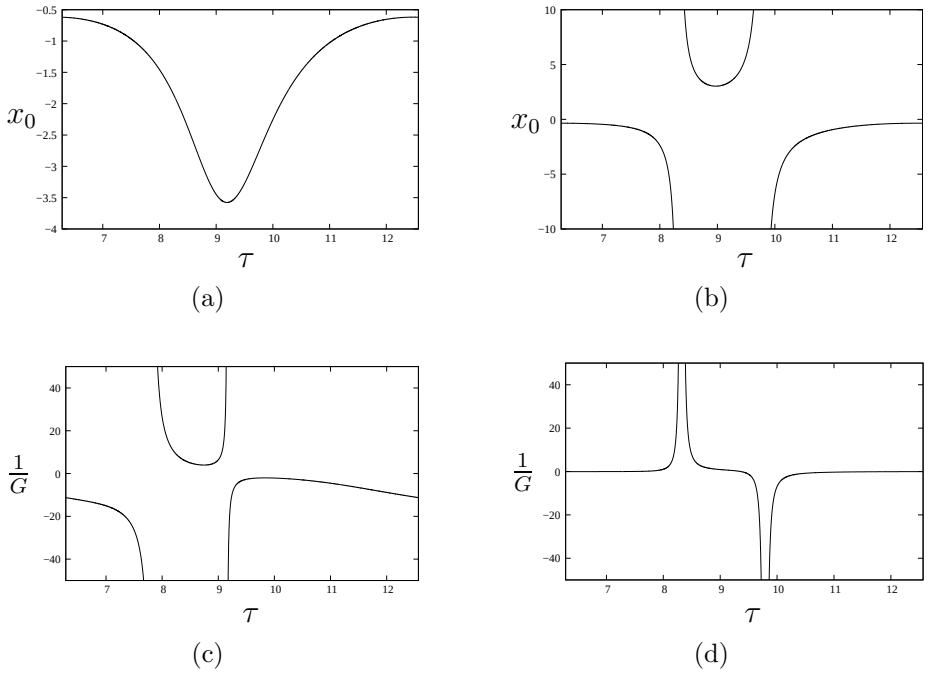

Figure 4.19: (a) The attachment point x_0 over a single time period for $\sigma = 1$ and $\Delta = 0.5$. (b) The attachment point x_0 for $\sigma = 1$ and $\Delta = 1.2$. (c) The gradient of the dividing streamline at the wall over a single time period for $\sigma = 1$ and $\Delta = 0.5$. (d) The gradient of the dividing streamline at the wall for $\sigma = 1$ and $\Delta = 1.2$. In each case, $\widehat{\zeta} = \nu = k = 1$.

$\eta = 0$, $\psi_{P_{\eta\eta}}(0,\tau) < 0$ and as η increases, $\psi_P(\eta,\tau)$ decreases, so the dividing streamline x_d, given in (4.83), increases. The second stagnation point, $\eta = \eta_1^*$ corresponds to the point located at (X_1, η_1^*), for example. To determine this nature of the stagnation point, we write $N = \eta - \eta_1^*$ and $\widehat{X} = X - X_1$ and the velocity components (4.86) and (4.87) are rewritten as

$$u^* = (\widehat{X} + X_1)\psi_{P_\eta}(N + \eta_1^*, \tau) + \frac{\widehat{\zeta}}{k}\psi_O(N + \eta_1^*, \tau), \tag{4.88}$$

$$v^* = -\psi_P(N + \eta_1^*, \tau). \tag{4.89}$$

Expanding (4.88) and (4.89) using a Taylor's series, we find

$$u^* = \left[(\widehat{X} + X_1)\left(\psi_{P_\eta}(\eta_1^*, \tau) + N\psi_{P_{\eta\eta}}(\eta_1^*, \tau)\right)\right] + \frac{\widehat{\zeta}}{k}\left[\psi_O(\eta_1^*, \tau) + N\psi_{O_\eta}(\eta_1^*, \tau)\right] + O(N^2), \tag{4.90}$$

$$v^* = -\left[\psi_P(\eta_1^*, \tau) + N\psi_{P_\eta}(\eta_1^*, \tau)\right] + O(N^2). \tag{4.91}$$

Upon linearising and using the properties $X_1\psi_{P_\eta}(\eta_1^*, \tau) + \frac{\widehat{\zeta}}{k}\psi_O(\eta_1^*, \tau) = 0$ and

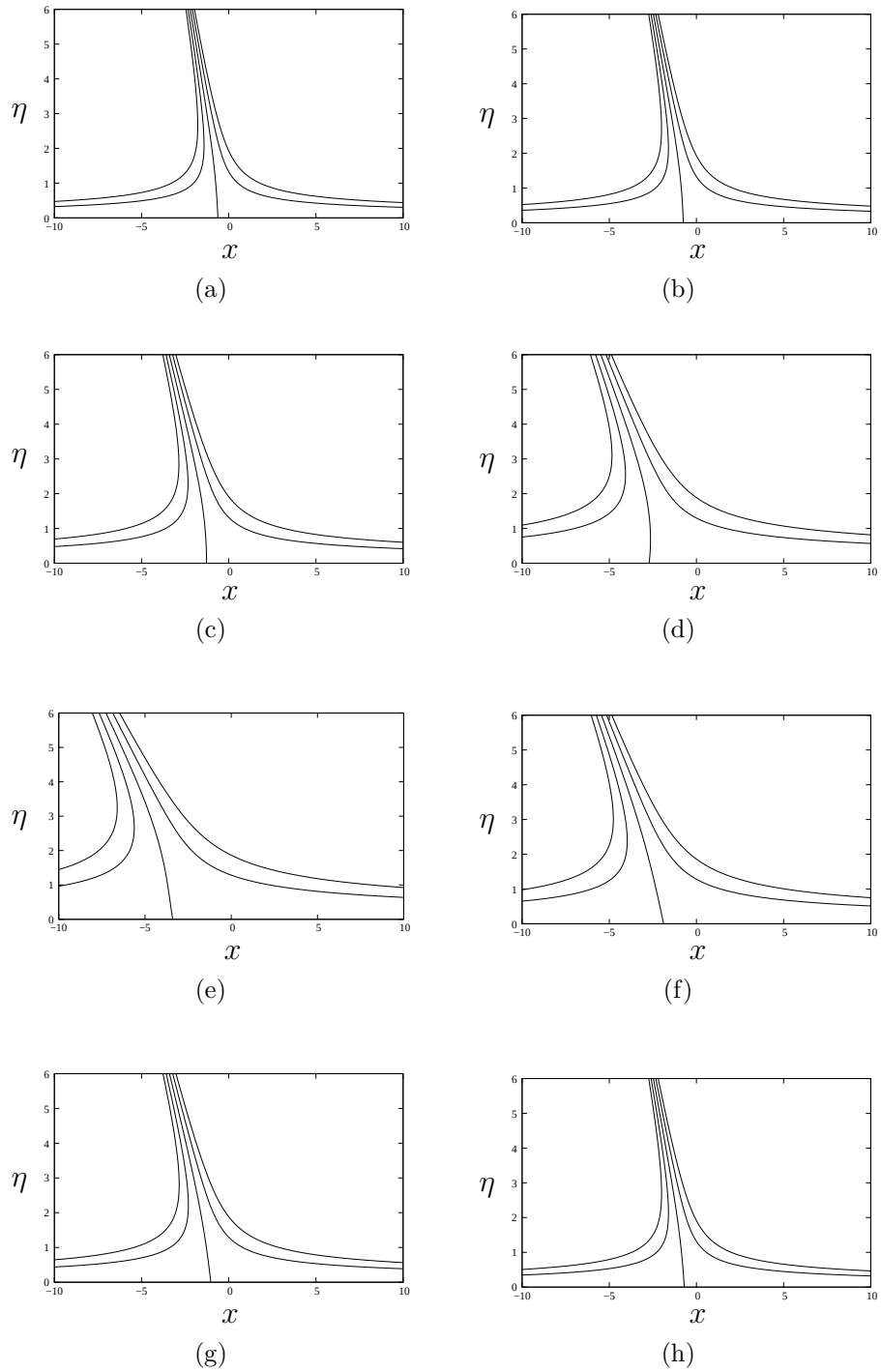

Figure 4.20: The instantaneous streamlines for $\widehat{\zeta} = \nu = k = 1$, $\widehat{\beta} = 0$, $\sigma = 1$ and $\Delta = 0.5$ over a period of 2π in equally spaced intervals of $\pi/4$, beginning at 2π.

$\psi_P(\eta_1^*, \tau) = 0$, we obtain

$$u^* = \widehat{X}\psi_{P_\eta}(\eta_1^*, \tau) + N\left[X_1\psi_{P_{\eta\eta}}(\eta_1^*, \tau) + \frac{\widehat{\zeta}}{k}\psi_{O_\eta}(\eta_1^*, \tau)\right], \quad (4.92)$$

$$v^* = -N\psi_{P_\eta}(\eta_1^*, \tau). \quad (4.93)$$

We express the velocity components as $u^* = \frac{dX}{ds}$ and $v^* = \frac{d\eta}{ds}$, where s represents a parameter along the streamline. Therefore, (4.92) and (4.93) become

$$\frac{\mathrm{d}\widehat{X}}{\mathrm{d}s} = A\widehat{X} + BN, \quad \frac{\mathrm{d}N}{\mathrm{d}s} = -AN, \quad (4.94)$$

where $A = \psi_{P_\eta}(\eta_1^*, \tau)$ and $B = X_1\psi_{P_{\eta\eta}}(\eta_1^*, \tau) + \frac{\widehat{\zeta}}{k}\psi_{O_\eta}(\eta_1^*, \tau)$. Using standard techniques for analysing equilibrium points, we express the system (4.94) in matrix form, to find

$$\frac{\mathrm{d}}{\mathrm{d}s}\begin{pmatrix}\widehat{X}\\ N\end{pmatrix} = \begin{pmatrix}A & B\\ 0 & -A\end{pmatrix}\begin{pmatrix}\widehat{X}\\ N\end{pmatrix}, \quad (4.95)$$

where the eigenvalues of the system are given by $-A$ and A. As the determinant of the matrix is negative, this suggests that η_1^* is a saddle point. The first eigenvector represents the horizontal streamline through η_1^* and the second eigenvector represents the streamline

$$\eta = \frac{-2A}{B}(X - X_1) + \eta_1^*, \quad (4.96)$$

which is the dividing streamline through η_1^*, with gradient $-2A/B$. The horizontal position of this stagnation point can be calculated numerically by setting the horizontal velocity component (4.86) equal to zero and evaluating at (X_1, η_1^*), to give $X_1 = -\frac{\widehat{\zeta}}{k}\psi_O(\eta_1^*, \tau)/\psi_{P_\eta}(\eta_1^*, \tau)$. An example of this flow structure can be seen in figure 4.21(b), for $\sigma = 1$, $\Delta = 1.2$ and $\widehat{\beta} = 0$ at $\tau = 11\pi/4$, where $x_0 = 4.043$, $X_1 = -21.776$ and $\eta_1^* = 2.475$ for $\widehat{\zeta} = k = 1$.

Having discussed the dividing streamline x_d, when $\psi_{P_{\eta\eta}}(0, \tau) < 0$, we now consider the streamline pattern when x_d at a fixed time τ when $\psi_{P_{\eta\eta}}(0, \tau) > 0$. As mentioned above, when $\psi_{P_{\eta\eta}}(0, \tau) > 0$, the attachment point x_0, given in (4.84) is negative, as $\psi_{O_\eta}(0, \tau) > 0$ over the time period. There exists a minimum at $\eta = 0$ and as $\eta \to \infty$, $\psi_P(\eta, \tau) \to a\eta - \widehat{\alpha}$. Similar to the case

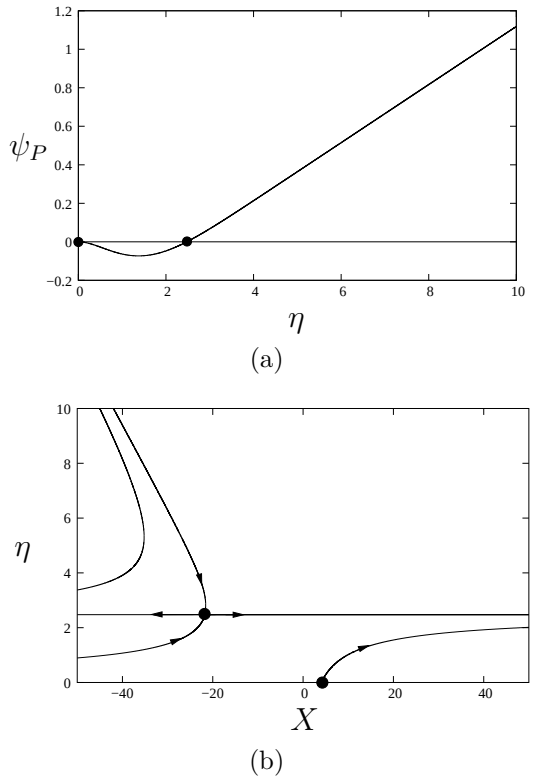

Figure 4.21: (a) The primary function $\psi_P(\eta, \tau)$ for $\sigma = 1$, $\Delta = 1.2$ at $\tau = 11\pi/4$, illustrating the two stagnation points at $\eta = 0$ and $\eta = \eta_1^*$, which are represented by the solid dots. (b) The corresponding dividing streamline x_d. At $\tau = 11\pi/4$, the vertical distance of the horizontal streamline from the wall is $\eta_1^* = 2.475$, the horizontal position of the stagnation point is $X_1 = -21.776$ and the attachment point is $x_0 = 4.04$ where $\widehat{\zeta} = k = 1$.

when $\psi_{P_{\eta\eta}}(0, \tau) < 0$, $a(\tau)$ can either be positive or negative. If $a(\tau) > 0$, the dividing streamline has one stagnation point at $\eta = 0$ and as η increases, $\psi_P(\eta, \tau)$ is positive. So, the dividing streamline is negative and oscillates between two limits. If $a(\tau) < 0$, there will be two stagnation points, one at $\eta = 0$ and another at $\eta = \eta_2^*$. The stagnation point $\eta = \eta_2^*$ behaves similarly to η_1^*, which was discussed for the case when $\psi_{P_{\eta\eta}}(0, \tau) < 0$. Therefore, $\eta = \eta_2^*$ is a saddle point with a horizontal streamline and a streamline with gradient $-2A/B$, through the stagnation point.

In figure 4.22, the instantaneous streamlines for $\sigma = 1$ and $\Delta = 1.2$ are illustrated over a period of 2π, in equally spaced intervals. It can be seen that over one time period the horizontal streamline appears and then disappears. To consider the behaviour of the horizontal streamline over one

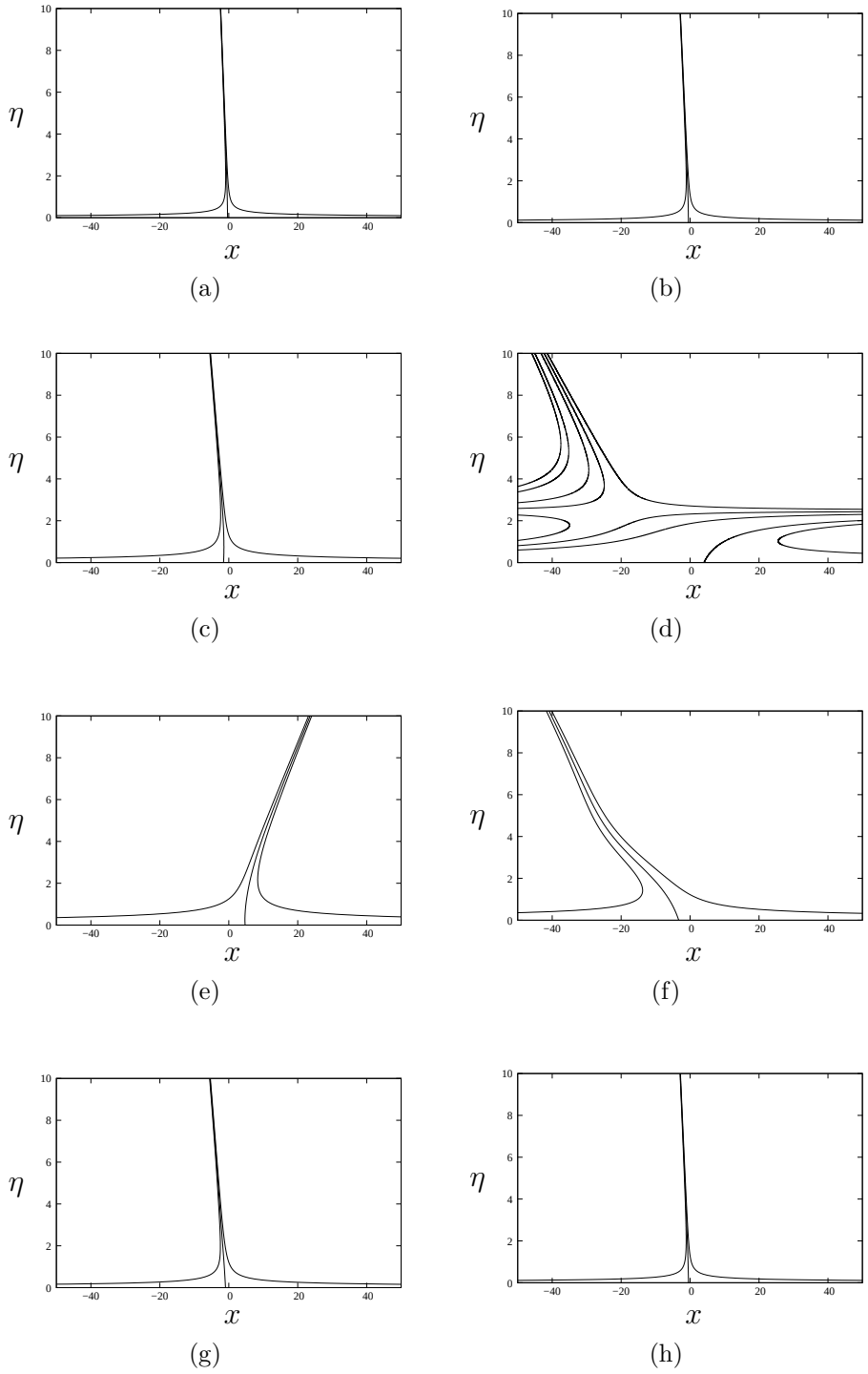

Figure 4.22: The instantaneous streamlines for $\widehat{\zeta} = \nu = k = 1$, $\widehat{\beta} = 0$, $\sigma = 1$ and $\Delta = 1.2$ over a period of 2π in equally spaced intervals of $\pi/4$, beginning at 2π.

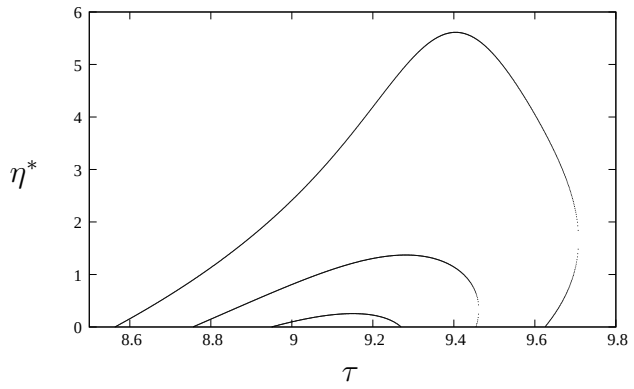

(a)

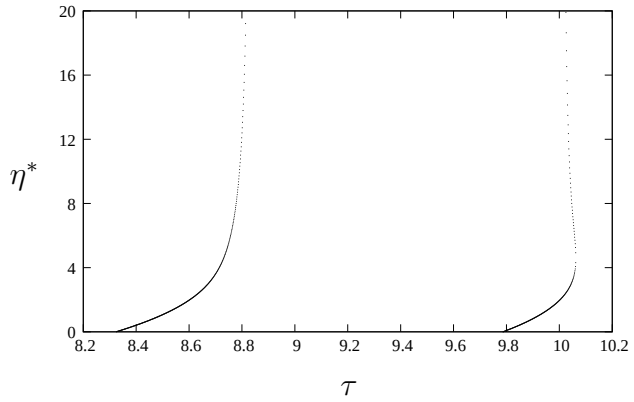

(b)

Figure 4.23: (a) The vertical location of the horizontal streamline for $\sigma = 1$ and $\Delta = 0.8$ (bottom curve), $\Delta = 0.85$ (middle curve) and $\Delta = 0.95$ (top curve). (b) The vertical location of the horizontal streamline for $\sigma = 1$ and $\Delta = 1.2$

time period, we illustrate the zero of ψ_P, which we denote η^*, for $\sigma = 1$ and $\Delta = 0.8, 0.85, 0.95$ in figure 4.23(a). We observe that for $\Delta = 0.8$, the zero appears at $\tau = 8.95$ and then disappears at $\tau = 9.27$. For $\Delta = 0.85$, it can be seen that one zero appears at $\tau = 8.76$, with a second zero appearing at $\tau = 9.455$ before both disappear at $\tau = 9.46$. This behaviour is illustrated more clearly for $\Delta = 0.95$, where the first zero appears at $\tau = 8.56$, the second appears at $\tau = 9.63$ and then both disappear at $\tau = 9.71$.

In figure 4.23(b), the zeros are illustrated for $\sigma = 1$ and $\Delta = 1.2$. We notice in this case there are two distinct time intervals over the period when a zero is present. At $\tau = 8.33$, the zero appears from the wall before moving up to infinity. This time corresponds to the zero of $a(\tau) = 1 + \Delta \cos \tau$, which

occurs at $\tau = \cos^{-1}(1/\Delta) = 8.84$. However, in the second time interval, the first zero appears from the wall at $\tau = 9.79$ and the second zero descends from infinity at $\tau = \cos^{-1}(1/\Delta) = 10.01$. The two zeros collide and disappear at $\tau = 10.06$.

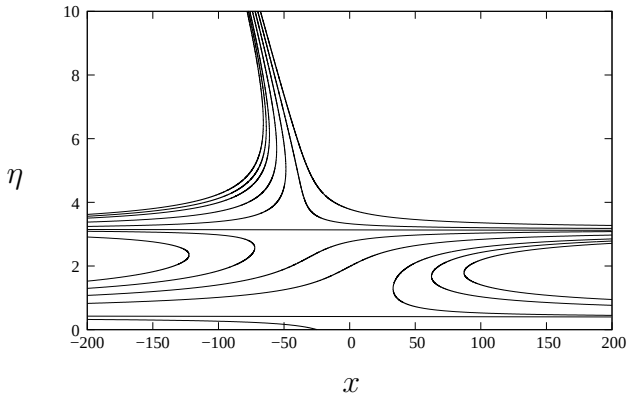

Figure 4.24: The instantaneous streamlines for $\Delta = 0.95$ and $\sigma = 1$ at $\tau = 9.66$, illustrating a triple-layered structure, where $\nu = k = \widehat{\zeta} = 1$.

Having given some numerical examples of the behaviour of the horizontal streamlines, we now discuss the flow structure over one time period for $\sigma = 1$. When $\Delta < 0.785$, the structure of the instantaneous streamlines are single-layered with the dividing streamline approaching from infinity and meeting the wall at an angle. When $0.785 < \Delta < 0.835$, a horizontal streamline appears once over the cycle. This causes the flow to develop a double-layered structure, where the layer near the wall is separated from the upper region by the horizontal streamline. The horizontal streamline then moves back to the wall and the flow returns to a single-layered flow. For $0.835 < \Delta < 1$, a similar structure to the previous case occurs, with a horizontal streamline moving up from the wall. However, as the first horizontal streamline moves down towards the wall, a second horizontal streamline appears from the wall, causing the flow to develop triple-layered structure. Figure 4.24, illustrates the instantaneous streamlines for $\sigma = 1$ and $\Delta = 0.95$ at $\tau = 9.66$, where the triple-layered structure is present. When these two horizontal streamlines meet, the structure again returns to a single-layered flow.

When $\Delta > 1$, there are two distinct regions within the time period where

the flow becomes multi-layered. In the first instance, one horizontal streamline emerges from the wall, creating a double-layered structure. This case is unlike those described above, as the horizontal streamline moves up to infinity instead of returning to the wall. At the second time interval, a horizontal streamline appears from the wall, creating a double-layered structure. As this horizontal streamline moves away from the wall, a horizontal streamline moves down from infinity creating a triple-layered structure, similar to the one illustrated in figure 4.24. When these horizontal streamlines collide, the flow returns to a single-layered flow.

We now consider the instantaneous streamlines for an amplitude above the critical value Δ_c. In figures 4.25, 4.26 and 4.27, we illustrate the instantaneous streamlines for $\sigma = 40$ and choose $\Delta = 20$, which corresponds to a value above the critical amplitude $\Delta_c(\sigma)$, given in section 4.1. Using the method presented in section 4.3.1, the finite-time singularity is given by $\tau_s = 18.443$. Figure 4.28 illustrates the zeros of $\psi_{P_{\eta\eta}}(0,\tau)$ for $\sigma = 40$ and $\Delta = 20$. It can be seen that as $\tau \to \tau_s^-$, the zero, which descends from infinity, does not meet the zero that appears from the wall and instead moves up to infinity. We also illustrate the orthogonal velocity profile as $\tau \to \tau_s^-$ in figure 4.29(a) and we can see that as $\tau \to \tau_s^-$, the minimum which develops in the orthogonal velocity component decreases, i.e. the region of flow reversal gets bigger and the distance required to satisfy the far-field boundary condition increases.

The above analysis has been presented for $\widehat{\beta} = 0$. We now discuss the streamline pattern when $\widehat{\beta} \neq 0$. We recall that the time-dependent function $\widehat{\beta}(\tau) = b_M + b_O \cos\tau$. We note that the vertical location of the horizontal streamline is solely dependent upon the primary problem. However, the horizontal position of the stagnation point on the horizontal streamline is affected.

For the parameters $\sigma = 1$ and $\Delta = 0.5$, we illustrate the oblique wall shear component $\psi_{O_\eta}(0,\tau)$ in figure 4.30 for $b_O = 0$ and $b_M = 0, 0.94, 1.54$. When $b_M > 0.94$, the oblique wall shear component becomes negative over

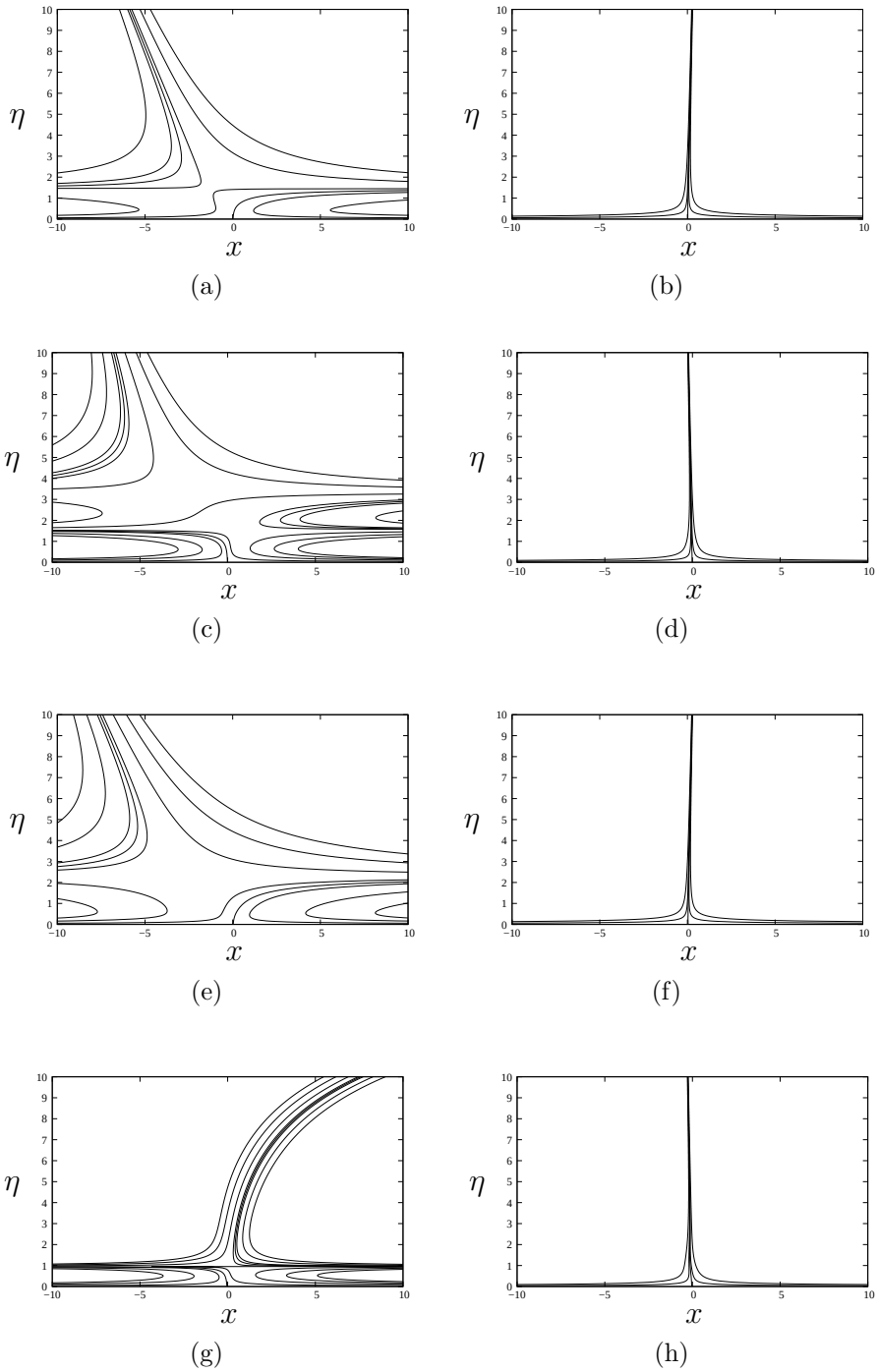

Figure 4.25: The instantaneous streamlines as $\tau \to \tau_s$ at intervals of $\tau = \pi/2$, for $\widehat{\beta} = 0$, $\Delta = 20$ and $\sigma = 40$, beginning at $\tau = \pi/2$, where $\widehat{\zeta} = \nu = k = 1$.

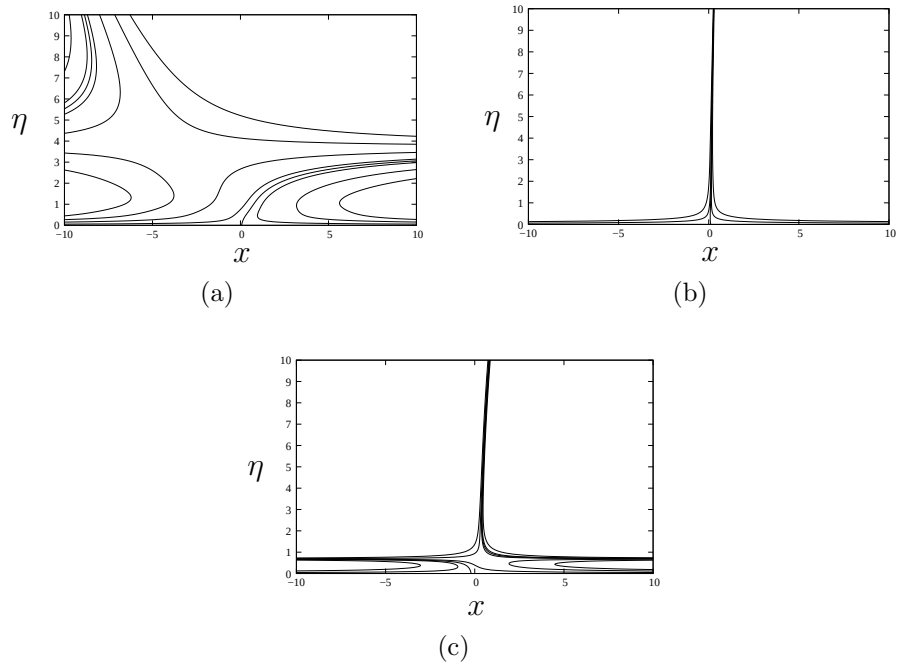

Figure 4.26: The streamlines as $\tau \to \tau_s$ at intervals of $\tau = \pi/2$ beginning at $\tau = 9\pi/2$ for $\widehat{\beta} = 0$, $\Delta = 20$ and $\sigma = 40$, where $\widehat{\zeta} = \nu = k = 1$. This figure is a continuation of figure 4.25.

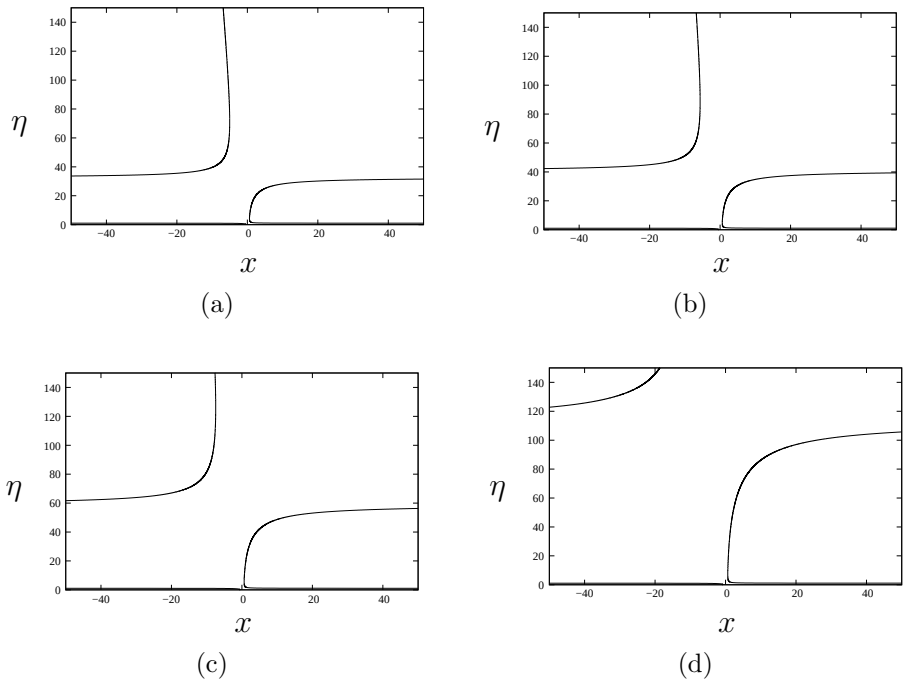

Figure 4.27: The streamlines as $\tau \to \tau_s^-$, for $\sigma = 40$ and $\Delta = 20$ at (a) $\tau = 18.0$, (b) $\tau = 18.1$, (c) $\tau = 18.2$, (d) $\tau = 18.3$, where $\tau_s = 18.443$ and $\widehat{\zeta} = \nu = k = 1$. This figure is a continuation of figure 4.26.

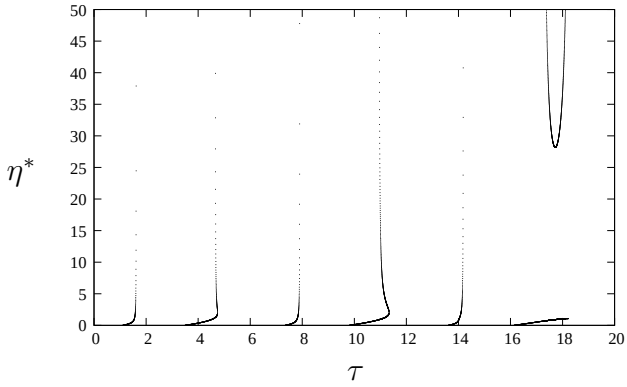

Figure 4.28: The vertical location of the horizontal streamlines for $\sigma = 40$ and $\Delta = 20$.

a certain period of the cycle. As $\psi_{P_{\eta\eta}}(0,\tau) > 0$ over the whole period, when $\psi_{O_\eta}(0,\tau) < 0$, the attachment point x_0, given in (4.84), becomes positive. Additionally, when $b_M > 1.54$, $\psi_{O_\eta}(0,\tau) < 0$ everywhere over the time period. Therefore, the attachment point x_0, is positive over the entire time period. These results are illustrated in figure 4.32(a), where x_0 is plotted as a function of τ for $b_O = 0$ and $b_M = 0, 0.94, 1.54$. Similarly, figure 4.30 shows the oblique wall shear component for $b_M = 0$ and $b_O = 0, 0.9, 1.5$. When $b_O > 0.9$, $\psi_{O_\eta}(0,\tau)$ is negative for some portion of the time period. So as with the case described above, when $\psi_{O_\eta}(0,\tau) < 0$, the attachment point becomes positive and can be seen in figure 4.32(b), where x_0 is illustrated over a single time period. We note that there exist two values over the time period that give the same value of x_0, irrespective of b_O.

A similar analysis can be applied when $\sigma = 1$ and $\Delta = 1.2$. In figure 4.31(a), the oblique wall shear component is illustrated for $\sigma = 1$, $\Delta = 1.2$, $b_O = 0$ and $b_M = 0, 0.78, 1.5$. When $b_M > 0.78$, $\psi_{O_\eta}(0,\tau)$ is negative over a short interval of the time period. As $\psi_{P_{\eta\eta}}(0,\tau) > 0$ in this time interval, the attachment point x_0, becomes positive. When $b_M > 4.5$, the oblique wall shear component is negative everywhere over the time period. Therefore, the attachment point x_0 behaves similarly to that in figure 4.19(b) for $\Delta = 1.2$, but is reflected in the y-axis, i.e. the sign of x_0 changes. In figure 4.31(b), the oblique wall shear component is plotted for $\sigma = 1$, $\Delta = 1.2$, $b_M = 0$ and for $b_O = 0, 0.77, 1.5$. Similar to the discussion above, when $b_O > 0.77$,

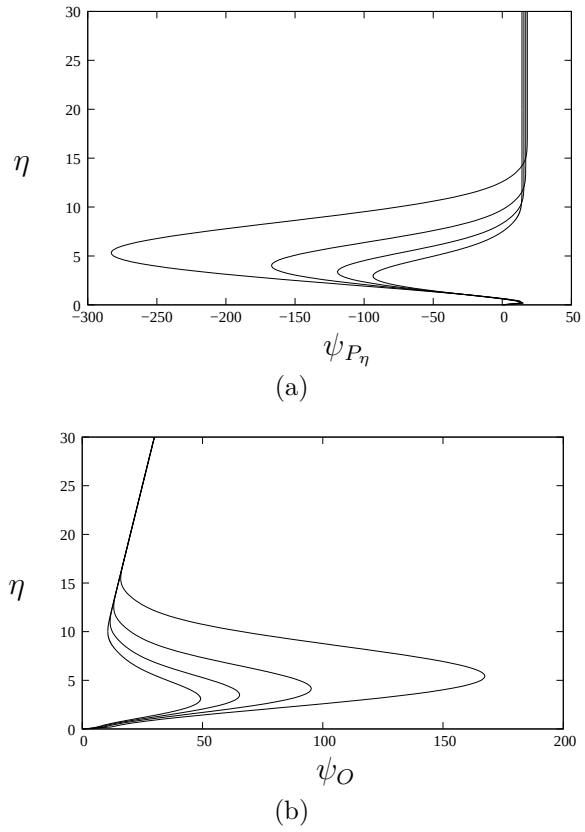

Figure 4.29: (a) The primary velocity profile as $\tau \to \tau_s$ for $\sigma = 40$ and $\Delta = 20$, working from right to left at $\tau = 18.0, 18.1, 18.2, 18.3$. (b) The oblique velocity profile for $\widehat{\beta} = 0$ at the same times approaching the finite-time singularity $\tau_s = 18.443$.

the oblique wall shear component becomes negative for some time during the time period. During this time interval, $\psi_{P_{\eta\eta}}(0,\tau) > 0$ and the attachment point x_0 is positive. Therefore, as Δ increases, the values of b_M and b_O, which cause $\psi_{O_\eta}(0,\tau) < 0$, decrease.

Finally, we consider how the far-field dividing streamline changes as $\widehat{\beta}$ changes, when the flow is single-layered. To do so, we choose a point in the far-field $\eta_N = 50$ and the corresponding point on the dividing streamline x_N is given by

$$x_N = -\widehat{\zeta}\left(\frac{\nu}{k^3}\right)^{1/2} \frac{\int_0^{\eta_N} \psi_O(z,\tau)\mathrm{d}z}{\psi_P(\eta_N,\tau)}. \tag{4.97}$$

In figure 4.32(c) we plot x_N for $\sigma = 1$, $\Delta = 0.5$, $b_O = 0$ and $b_M = 0, 0.94, 1.54$, which are the same values of b_M that were chosen when considering the attachment point x_0 above. Upon increasing b_M, x_N is shifted in the positive

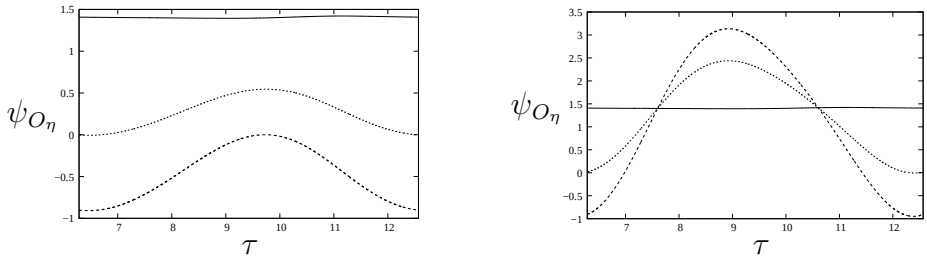

Figure 4.30: (a) The oblique wall shear stress component $\psi_{O_\eta}(0,\tau)$ for $\sigma = 1$, $\Delta = 0.5$, $b_O = 0$ and $b_M = 0$ (solid line), $b_M = 0.94$ (dotted lines) and $b_M = 1.54$ (dashed lines). (b) The oblique wall shear stress component $\psi_{O_\eta}(0,\tau)$ for $\sigma = 1$, $\Delta = 0.5$, $b_M = 0$ and $b_O = 0$ (solid line), $b_O = 0.9$ (dotted lines) and $b_O = 1.5$ (dashed lines).

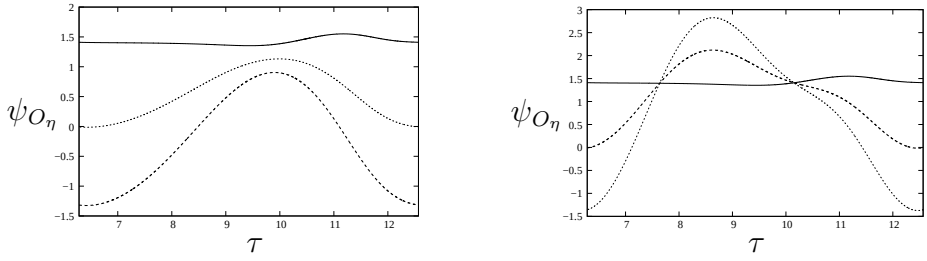

Figure 4.31: (a) The oblique wall shear stress component $\psi_{O_\eta}(0,\tau)$ for $\sigma = 1$, $\Delta = 1.2$, $b_O = 0$ and $b_M = 0$ (solid line), $b_M = 0.78$, (dotted lines) and $b_M = 1.5$ (dashed lines). (b) The oblique wall shear stress component $\psi_{O_\eta}(0,\tau)$ for $\sigma = 1$, $\Delta = 1.2$, $b_M = 0$ and $b_O = 0$ (solid line), $b_O = 0.77$ (dotted lines) and $b_O = 1.5$ (dashed lines).

direction and behaves similarly to that of the steady case discussed in chapter 3, where b_M acts as a horizontal shift. Similarly, we consider $\widehat{\beta}$ as a purely oscillatory function, i.e. $b_M = 0$ and figure 4.32(d) illustrates x_N for $b_O = 0, 0.9.1.5$. As b_O is increased, the dividing streamline simply oscillates about its mean position. We note that in both the cases, when $b_M \neq 0$ and $b_O \neq 0$ that the horizontal velocity component $\widehat{\beta}$ affects the dividing streamline in the far-field and close to the wall differently.

When the flow structure is multi-layered, the time-dependent horizontal velocity component $\widehat{\beta}$ affects the horizontal position of the stagnation point on the horizontal streamline. In chapter 5, a large frequency asymptotic analysis is performed and the effect of $\widehat{\beta}$ on the streamlines when the flow is

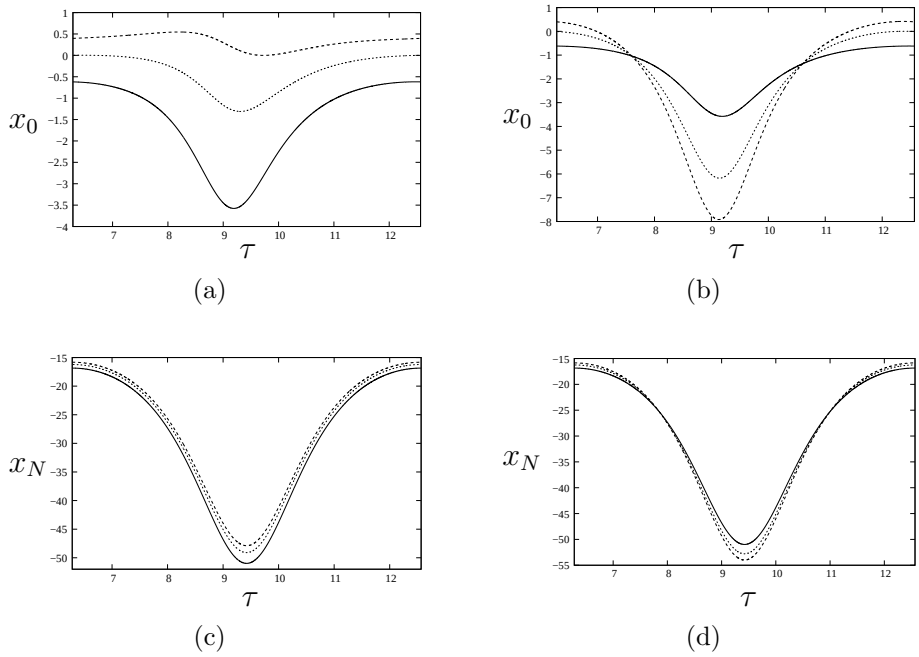

Figure 4.32: (a) The attachment point x_0 for $\sigma = 1$, $\Delta = 0.5$, $b_O = 0$ and, from bottom to top, $b_M = 0, 0.94, 1.54$, where $\widehat{\zeta} = \nu = k = 1$. (b) The attachment point for $\sigma = 1$, $\Delta = 0.5$, $b_M = 0$ and $b_O = 0$ (solid line), $b_O = 0.9$ (dotted line) and $b_O = 1.5$ (dashed lines). (c) A point in the far-field x_N for $\sigma = 1$, $\Delta = 0.5$, $b_O = 0$ and from bottom to top $b_M = 0, 0.94, 1.54$. (d) A point in the far-field x_N for $\sigma = 1$, $\Delta = 0.5$, $b_M = 0$ and $b_O = 0$ (solid line), $b_O = 0.9$ (dotted line) and $b_O = 1.5$ (dashed lines).

multi-layered is discussed.

4.6 Summary

In this chapter, a two-dimensional unsteady oblique stagnation-point flow travelling towards a fixed wall has been considered. In the far-field, the flow is the sum of three separate flows. The first is an unsteady orthogonal stagnation-point flow with a mean component and an oscillatory component, dependent upon a relative amplitude parameter Δ and a dimensionless frequency parameter σ. Superimposed onto this is a shear flow with constant vorticity and a time-dependent horizontal velocity component.

At the wall, a similarity solution, which is an exact solution of the Navier-Stokes equations, is introduced consisting of two components, the first representing the orthogonal stagnation-point flow and the second representing the shear and horizontal velocity components. Two partial differential equations are obtained and solved numerically for a range of parameters Δ and σ using a Crank-Nicolson finite-difference method, whose numerical calculations are initiated with asymptotic solutions for small time.

The flow has been investigated for different values of the relative amplitude parameter Δ. When $\Delta < \Delta_1$, where $\Delta_1 < \Delta_2 < 1$, the flow structure is at its simplest. The far-field dividing streamline approaches the wall obliquely and near the wall, due to the viscosity, it bends towards the wall at an angle closer to the normal and meets the wall at a stagnation point. Over a single time period, the dividing streamline, the attachment point and the angle with the wall oscillate between two bounding values. As Δ increases, the structure of the flow becomes more complex. When $\Delta_1 < \Delta < \Delta_2$, a horizontal streamline appears from the wall, creating a double-layered structure in the flow. There is one layer at the wall, which is separated from the upper region by a horizontal streamline. This horizontal streamline returns to the wall after a short time and the flow returns to a single-layered structure. When $\Delta_2 < \Delta < 1$, again a horizontal streamline appears from the wall. As this horizontal streamline returns to the wall, a second horizontal streamline appears, causing the flow to develop a triple-layered structure. When these

two horizontal streamlines collide, the flow again returns to a simple single-layered flow. When $\Delta > 1$, in each time period, there are two time intervals in which the horizontal streamlines are present. The first of these intervals exhibits single and double-layered structures. However, different to the cases described above, the horizontal streamline that appears from the wall moves up to infinity. The second time interval exhibits all three structures. The first horizontal streamline moves up from wall, creating a double-layered structure. When the second horizontal streamline moves down from infinity, a triple-layered structure develops before the two horizontal streamlines collide, returning the flow to a single-layered structure.

Streamline patterns were plotted for various parameter values. For the simplest case when $\Delta < \Delta_1$, it was observed that the time-dependent horizontal velocity component affects the instantaneous streamlines far from the wall and close to the wall differently. Far from the wall, over a single period, the horizontal velocity component simply shifted the streamline pattern about its mean position. In contrast, close to the wall, over a one time period, increasing the horizontal velocity component affects the attachment point and the gradient of the dividing streamline differently, depending on the time interval chosen. For other values of the amplitude, due to the whole range of different behaviour close to the wall, the streamline pattern is much more complicated.

When the relative amplitude Δ becomes large, the existence of time periodic solutions must be considered. For the orthogonal problem, Merchant and Davis (1989) showed that for a fixed dimensionless frequency, there exists a critical relative amplitude, above this, the orthogonal solution breaks down at a finite-time singularity. In this chapter, this analysis was extended to include the other components of the far-field flow. We found that the oblique solution, as it has a coupling with the orthogonal equation, also breaks down at the same finite-time singularity.

The next chapter follows on from the work in this chapter but the orthogonal and oblique equations are considered in the limit $\sigma \to \infty$, where the

relative amplitude is close to the critical value. The double and triple-layered structures described above are still present within this limit and are considered further using the asymptotic method which was previously discussed in chapter 2.

We note that a concise study of the work within this chapter can be found in Tooke et al. (2010).

Chapter 5

Unsteady oblique stagnation-point flow in the large frequency limit

5.1 Introduction

This chapter follows on immediately from chapter 4, where an unsteady two-dimensional oblique stagnation-point flow travelling towards a fixed wall was discussed. The flow in the far-field comprises of a two-dimensional stagnation-point flow, dependent on the relative amplitude parameter Δ and the dimensionless frequency parameter σ, a shear flow with constant vorticity and a time-dependent horizontal velocity component. A similarity solution was found close to the wall, from which two equations were derived. The first describes an orthogonal stagnation-point flow and is denoted the primary equation. The second represents the shear flow and the horizontal velocity component, which we denote the oblique equation.

In chapter 4, the primary and oblique equations were solved numerically for a range of values of the parameters σ and Δ. For certain values of the relative amplitude and the dimensionless frequency parameter, the flow structure becomes double or triple-layered. This is due to interior stagnation points appearing in the flow, each with a horizontal streamline passing through it.

In chapter 2, when only the primary problem was analysed, it was found that as $\sigma \to \infty$, a critical amplitude Δ_c arises, such that for $\Delta > \Delta_c$, solutions break down at a finite-time singularity. In this limit, the flow structure exhibits a Stokes layer at the wall and a steady streaming layer matching the Stokes layer to that of the far-field flow. In the present chapter, we solve the oblique equation close to the critical amplitude and obtain solutions in the Stokes and the steady streaming layers.

We conclude with a discussion on the instantaneous streamlines in the Stokes and the steady streaming layers, confirming the multi-layered structure which was present in chapter 4. Additionally, a particle path analysis in the steady streaming layer is performed.

5.2 Problem formulation

In chapter 4, the streamfunction in the far-field, describing the unsteady oblique stagnation-point flow, initially stated in (4.3), is given by

$$\psi = a(t)kxy + \frac{1}{2}\widehat{\zeta}y^2 - \widehat{\beta}(t)\widehat{\zeta}\left(\frac{\nu}{k}\right)^{1/2} y, \tag{5.1}$$

as $y \to \infty$. The first term is an unsteady orthogonal stagnation-point flow with strength k and $a(t) = 1 + \Delta\cos\omega t$. The second term is a shear flow with constant vorticity with constant vorticity $-\widehat{\zeta} < 0$ and the third is a time-dependent horizontal velocity, dependent upon an arbitrary function $\widehat{\beta}(t)$. A sketch of the dividing streamline, $\psi = 0$, is illustrated in figure 4.1. As the far-field solution (5.1) does not satisfy the no-slip condition, close to the wall we write

$$\psi(x,\eta,\tau) = (\nu k)^{1/2} x\psi_P(\eta,\tau) + \widehat{\zeta}\Big(\frac{\nu}{k}\Big)\int_0^\eta \psi_O(z,\tau)\mathrm{d}z, \tag{5.2}$$

where $\eta = (k/\nu)^{1/2}y$ and $\tau = \omega t$. The first component represents the orthogonal stagnation-point flow and is denoted $\psi_P(\eta,\tau)$, the primary component. The second term in (5.2) represents the shear flow and the time-dependent horizontal velocity component and is denoted $\psi_O(\eta,\tau)$, the oblique component. The equations for $\psi_P(\eta,\tau)$ and $\psi_O(\eta,\tau)$ have previously been derived

in section 4.2 and are given by

$$\sigma\psi_{P\eta\tau} + \left(\psi_{P\eta}\right)^2 - \psi_P\psi_{P\eta\eta} = \sigma\Delta\sin\tau + (1+\Delta\cos\tau)^2 + \psi_{P\eta\eta\eta}, \quad (5.3)$$

$$\sigma\psi_{O\tau} + \psi_{P\eta}\psi_O - \psi_P\psi_{O\eta} = -\sigma\widehat{\beta}_\tau + \widehat{\alpha} - (1+\Delta\cos\tau)\widehat{\beta} + \psi_{O\eta\eta}, \quad (5.4)$$

with primary boundary conditions

$$\psi_P(0,\tau) = 0, \quad \psi_{P\eta}(0,\tau) = 0 \quad \text{on} \quad \eta = 0, \quad (5.5)$$

$$\psi_P(\eta,\tau) \to (1+\Delta\cos\tau)\eta - \widehat{\alpha} \quad \text{as} \quad \eta \to \infty, \quad (5.6)$$

and subsidiary boundary conditions

$$\psi_O(0,\tau) = 0, \quad \text{on} \quad \eta = 0, \quad (5.7)$$

$$\psi_O(\eta,\tau) \to \eta - \widehat{\beta} \quad \text{as} \quad \eta \to \infty, \quad (5.8)$$

where $\widehat{\alpha} = \lim_{\eta\to\infty}(a\eta - \psi_P)$ and $\sigma = \omega/k$ is the Strouhal number. For convenience, we choose the scalings $\psi_P = \Delta^{1/2}\widehat{\psi_P}$, $\psi_O = \Delta^{-1/2}\widehat{\psi_O}$ and $\widehat{\alpha} = \Delta^{1/2}\widetilde{\alpha}$, with $\eta = \Delta^{-1/2}\widehat{\eta}$ and $\widehat{\beta} = \Delta^{-1/2}\widetilde{\beta}$. Additionally, the parameters $\widehat{\epsilon} = 1/\Delta$ and $\Omega = \sigma/\Delta$ are introduced, where $\widehat{\epsilon}$ is a small parameter. The equations (5.3) and (5.4) in terms of the new variables become

$$\Omega\widehat{\psi}_{P\widehat{\eta}\tau} + \left(\widehat{\psi}_{P\widehat{\eta}}\right)^2 - \widehat{\psi}_P\widehat{\psi}_{P\widehat{\eta}\widehat{\eta}} = -\Omega\sin\tau + (\widehat{\epsilon}+\cos\tau)^2 + \widehat{\psi}_{P\widehat{\eta}\widehat{\eta}\widehat{\eta}}, \quad (5.9)$$

$$\Omega\widehat{\psi}_{O\tau} + \widehat{\psi}_{P\widehat{\eta}}\widehat{\psi}_O - \widehat{\psi}_P\widehat{\psi}_{O\widehat{\eta}} = -\Omega\widetilde{\beta}_\tau + \widetilde{\alpha} - (\widehat{\epsilon}+\cos\tau)\widetilde{\beta} + \widehat{\psi}_{O\widehat{\eta}\widehat{\eta}}, \quad (5.10)$$

with the primary flow boundary conditions

$$\widehat{\psi}_P(0,\tau) = 0, \quad \widehat{\psi}_{P\widehat{\eta}}(0,\tau) = 0 \quad \text{on} \quad \widehat{\eta} = 0, \quad (5.11)$$

$$\widehat{\psi}_P(\widehat{\eta},\tau) \to (\cos\tau + \widehat{\epsilon})\widehat{\eta} - \widetilde{\alpha} \quad \text{as} \quad \widehat{\eta} \to \infty, \quad (5.12)$$

and the subsidiary flow boundary conditions

$$\widehat{\psi}_O(0,\tau) = 0 \quad \text{on} \quad \widehat{\eta} = 0, \quad (5.13)$$

$$\widehat{\psi}_O(\widehat{\eta},\tau) \to \widehat{\eta} - \widetilde{\beta} \quad \text{as} \quad \widehat{\eta} \to \infty. \quad (5.14)$$

As we wish to solve equations (5.9) and (5.10) asymptotically, an expansion for $\widehat{\epsilon}$ is required in terms of Ω, which has previously been found in chapter 2 and is given by $\widehat{\epsilon} = a_0\Omega^{-1} + a_1\Omega^{-2}$. The constant a_0 can be thought

of as the boundary between the solutions existing and breaking down at a finite-time singularity and a_1 is the correction term. The time-dependent function $\widetilde{\alpha}(\tau)$ is found from solving the primary equation (5.9), which is discussed in section 5.3 and is written $\widetilde{\alpha} = \Omega^{-1/2}\alpha_0 + O(\Omega^{-3/2})$. Additionally, we choose the magnitude of the horizontal velocity component $\widehat{\beta}$ to be the same size as the mean component in the far-field orthogonal flow $a(\tau)$, i.e. $\widehat{\beta} \sim O(1)$. Therefore, it follows that $\widetilde{\beta} = \Omega^{1/2}\beta_0(\tau) + \Omega^{-1/2}\beta_1(\tau) + O\left(\Omega^{-3/2}\right)$. In section 5.5, we comment on other possible magnitudes of $\widehat{\beta}$.

Due to the coupling of $\widehat{\psi}_P$ and $\widehat{\psi}_O$ in equation (5.10), we begin by summarising the primary solution, which was previously solved in chapter 2, before seeking a solution to the oblique equation (5.10).

5.3 Summary of primary flow

In this section, the primary flow is summarised by describing the necessary methods and results that are required to solve the oblique equation (5.10), with a more detailed account found in section 2.4.

At the wall, there exists a Stokes layer of thickness $O(\Omega^{-1/2})$ with variable $\xi = \Omega^{1/2}\widehat{\eta}$, where $\xi = O(1)$. Solving equation (5.9) in the Stokes layer, we find

$$\begin{aligned} \widehat{\psi}_P \;\sim\; & \Omega^{-1/2}\left[\xi\cos\tau - \cos\left(\tau - \frac{\pi}{4}\right)\right] \\ & + \Omega^{-3/2}\left[\frac{13}{4\sqrt{2}} - \frac{3}{4}\xi - \frac{1}{2\sqrt{2}}\cos\left(2\tau + \frac{\pi}{4}\right)\right] + O(\Omega^{-5/2}), \end{aligned} \tag{5.15}$$

as $\xi \to \infty$. As equation (5.15) does not, at first order, satisfy the far-field boundary condition $\widehat{\psi}_{P_\xi}(\xi,\tau) \to \Omega^{-1/2}\cos\tau + \Omega^{-3/2}a_0 + O\left(\Omega^{-5/2}\right)$ as $\xi \to \infty$, a steady streaming layer is introduced to match the Stokes layer solution to that of the far-field. To allow for correct matching, we introduce the variable $\zeta = \Omega^{-1/2}\widehat{\eta}$, where $\zeta = O(1)$. After solving (5.9) in the steady streaming layer, we find

$$\widehat{\psi}_P \;=\; \Omega^{1/2}\zeta\cos\tau + \Omega^{-1/2}\left[f_0(\zeta) - \cos\left(\tau - \frac{\pi}{4}\right)\right] + O(\Omega^{-3/2}), \tag{5.16}$$

where $f_0(\zeta)$ is the numerical solution to

$$f_0''' - f_0'^2 + f_0 f_0'' + a_0^2 \;=\; 0, \tag{5.17}$$

with boundary conditions

$$f_0(0) = 0, \qquad f_0'(0) = -\frac{3}{4}, \qquad f_0(\zeta) \to a_0\zeta - C \quad \text{as} \quad \zeta \to \infty, \tag{5.18}$$

where the constant C is found numerically by solving equation (5.17) using a fourth-order Runge-Kutta technique and a finite-difference technique.

To solve the oblique equation (5.10), the asymptotic expansion for $\widetilde{\alpha}$ is required. By matching the steady streaming layer solution (5.16) with the primary far-field boundary condition $\widehat{\psi}_P(\widehat{\eta},\tau) \to (\widehat{\epsilon}+\cos\tau)\widehat{\eta} - \widetilde{\alpha}$ as $\widehat{\eta} \to \infty$, we find $\widetilde{\alpha}(\tau) = \Omega^{-1/2}\alpha_0 + O(\Omega^{-3/2})$, where $\alpha_0 = \cos\left(\tau - \frac{\pi}{4}\right) + C$.

Having summarised the main results of the primary equation (5.9), in the subsequent section we solve the oblique equation (5.10).

5.4 The oblique equation

In this section, we solve the oblique equation (5.10) in the limit $\Omega \to \infty$, with $\widehat{\epsilon} \sim O(\Omega^{-1})$. The structure of the solution is similar to that of the primary solution, with a Stokes layer closest to the wall. Due to this solution not satisfying the far-field boundary condition, a steady streaming layer is introduced, matching the Stokes layer and the far-field flow.

5.4.1 Stokes layer

Similar to the primary equation (5.9), the dominating terms in (5.10) are the unsteady and the viscous terms, $\Omega\widehat{\psi}_{O_\tau} \sim \widehat{\psi}_{O_{\widehat{\eta}\widehat{\eta}}}$ implying the scaling $\widehat{\eta} \sim \Omega^{-1/2}$. Therefore, we have a Stokes layer of thickness $O(\Omega^{-1/2})$ with variable $\xi = \Omega^{1/2}\widehat{\eta}$, where $\xi = O(1)$. We rescale the oblique equation (5.10) in terms of the Stokes layer variable ξ with $\widetilde{\beta}(\tau) = \Omega^{1/2}\beta_0(\tau) + \Omega^{-1/2}\beta_1(\tau) + O(\Omega^{-3/2})$ and $\widetilde{\alpha} = \Omega^{-1/2}\alpha_0 + O(\Omega^{-3/2})$, which were initially stated in section 5.2, to

give

$$\begin{aligned}\Omega\widehat{\psi}_{O\tau} + \Omega^{1/2}\left(\widehat{\psi}_O\widehat{\psi}_{P\xi} - \widehat{\psi}_P\widehat{\psi}_{O\xi}\right) &= -\Omega^{3/2}\left(\beta_{0\tau} + \Omega^{-1}\beta_{1\tau} + \Omega^{-2}\beta_{2\tau}\right) \\ &+ \Omega^{-1/2}\alpha_0 - \Omega^{1/2}(\cos\tau + a_0\Omega^{-1} + a_1\Omega^{-2})(\beta_0 + \Omega^{-1}\beta_1) \\ &+ \Omega\widehat{\psi}_{O\xi\xi} + O(\Omega^{-3/2}),\end{aligned} \tag{5.19}$$

with the wall boundary condition

$$\widehat{\psi}_O(0,\tau) = 0, \quad \text{on} \quad \xi = 0. \tag{5.20}$$

We pose the asymptotic expansion

$$\widehat{\psi}_O = \Omega^{1/2}\Psi_{O_0}(\xi,\tau) + \Omega^{-1/2}\Psi_{O_1}(\xi,\tau)) + O(\Omega^{-3/2}), \tag{5.21}$$

and recall the primary expansion

$$\widehat{\psi}_P = \Omega^{-1/2}\Psi_{P_0}(\xi,\tau) + \Omega^{-3/2}\Psi_{P_1}(\xi,\tau) + O(\Omega^{-5/2}). \tag{5.22}$$

Substituting these expansions into (5.19), the leading, first and second order equations are given by

$$\Psi_{O_0\tau} - \Psi_{O_0\xi\xi} = -\beta_{0\tau}, \tag{5.23}$$

$$\Psi_{O_1\tau} - \Psi_{O_1\xi\xi} = \Psi_{P_0}\Psi_{O_0\xi} - \Psi_{P_0\xi}\Psi_{O_0} - \beta_{1\tau} - \beta_0\cos\tau, \tag{5.24}$$

$$\begin{aligned}\Psi_{O_2\tau} - \Psi_{O_2\xi\xi} &= \Psi_{P_0}\Psi_{O_1\xi} + \Psi_{P_1}\Psi_{O_0\xi} - \Psi_{P_0\xi}\Psi_{O_1} - \Psi_{P_1\xi}\Psi_{O_0} \\ &\quad -\beta_{2\tau} + \alpha_0 - a_0\beta_0 - \beta_1\cos\tau,\end{aligned} \tag{5.25}$$

with boundary conditions on the wall

$$\Psi_{O_0}(0,\tau) = 0, \quad \Psi_{O_1}(0,\tau) = 0, \quad \Psi_{O_2}(0,\tau) = 0. \tag{5.26}$$

We express $\beta_i = \beta_i^M + \beta_i^O\cos(\tau+\phi)$ for $i \geq 0$, where β_i^M is the mean component and β_i^O is the oscillatory component with an arbitrary phase difference ϕ. To solve equations (5.23) - (5.25), we use the boundary condition on the wall (5.26) and note that $\Psi_{O_i}(\xi,\tau)$ are periodic and bounded, i.e. $\Psi_{O_i}(\xi,\tau)$ does not have exponentially large solutions. Therefore, the leading

and first order solutions are given by

$$\Psi_{O_0}(\xi,\tau) = b\xi + \beta_0^O\left[e^{-\xi/\sqrt{2}}\cos\left(\tau+\phi-\frac{\xi}{\sqrt{2}}\right)-\cos\left(\tau+\phi\right)\right], \tag{5.27}$$

$$\begin{aligned}\Psi_{O_1}(\xi,\tau) &= c\xi + \frac{3\sqrt{2}\beta_0^O}{4}\cos\left(\phi+\frac{\pi}{4}\right) - \frac{1}{4}\beta_0^O\sqrt{2}e^{-\xi\sqrt{2}}\sin\left(\phi+\frac{\pi}{4}\right) \\ &\quad -\frac{1}{2}\beta_0^O e^{-\xi/\sqrt{2}}\left[\sin\left(\frac{\xi}{\sqrt{2}}+\phi\right)+3\sin\left(\frac{\xi}{\sqrt{2}}-\phi\right)\right. \\ &\quad \left.+\cos\left(\frac{\xi}{\sqrt{2}}-\phi\right)\right]+\frac{1}{2}\beta_0^O\xi e^{-\xi/\sqrt{2}}\left[\sin\left(\phi-\frac{\xi}{\sqrt{2}}+\frac{\pi}{4}\right)\right. \\ &\quad \left.-\sin\left(2\tau-\frac{\xi}{\sqrt{2}}+\phi+\frac{\pi}{4}\right)\right] \\ &\quad +\frac{1}{2}\beta_0^O e^{-\xi}\sin\left(\xi-2\tau-\phi\right)-\frac{1}{2}\beta_0^O e^{-\xi/\sqrt{2}}\sin\left(\frac{\xi}{\sqrt{2}}-2\tau-\phi\right) \\ &\quad -\frac{1}{2}\beta_0^O\xi e^{\xi/\sqrt{2}}\sin\left(2\tau-\frac{\xi}{\sqrt{2}}+\phi+\frac{\pi}{4}\right) \\ &\quad +\beta_1^O\left[e^{-\xi/\sqrt{2}}\cos\left(\frac{\xi}{\sqrt{2}}-\tau-\phi\right)-\cos\left(\tau+\phi\right)\right] \\ &\quad -\beta_0^M\left[e^{-\xi/\sqrt{2}}\sin\left(\frac{\xi}{\sqrt{2}}-\tau\right)+\sin\tau\right] \\ &\quad +b\left[\frac{3\xi}{4}e^{-\xi/\sqrt{2}}\sin\left(\frac{\xi}{\sqrt{2}}-\tau\right)-e^{-\xi/\sqrt{2}}\cos\left(\tau-\xi/\sqrt{2}+\frac{\pi}{4}\right)\right. \\ &\quad \left.+\cos\left(\tau+\frac{\pi}{4}\right)+\frac{1}{4}\xi^2 e^{-\xi/\sqrt{2}}\sin\left(\tau-\xi/\sqrt{2}+\frac{\pi}{4}\right)\right],\end{aligned} \tag{5.28}$$

$$\Psi_{O_2}(\xi,\tau) = \left(a_0\beta_0^M - C\right)\frac{\xi^2}{2}+\frac{11\sqrt{2}b}{16}\xi^2+d\xi+T(\xi,\tau), \tag{5.29}$$

where b, c and d are constants and $T(\xi,\tau)$ is a function containing time-dependent and exponentially decaying terms.

At the top of the Stokes layer, we find

$$\begin{aligned}\widehat{\psi}_O &\sim \Omega^{1/2}\Big[b\xi-\beta_0^O\cos\left(\tau+\phi\right)\Big] \\ &\quad +\Omega^{-1/2}\left[c\xi+\frac{3\sqrt{2}\beta_0^O}{4}\cos\left(\phi+\frac{\pi}{4}\right)\right. \\ &\quad \left.-\beta_0^M\sin\tau-\beta_1^O\cos\left(\tau+\phi\right)+b\cos\left(\tau+\frac{\pi}{4}\right)\right] \\ &\quad +\Omega^{-3/2}\left[\left(a_0\beta_0^M-C\right)\frac{\xi^2}{2}+\frac{11\sqrt{2}b}{16}\xi^2+d\xi+T(\xi,\tau)\right]+O(\Omega^{-5/2}),\end{aligned} \tag{5.30}$$

as $\xi \to \infty$. As equation (5.30) does not satisfy the far-field boundary condition $\widehat{\psi}_O \to \left(\beta_0^M - \beta_0^O \cos(\tau+\phi)\right) + \Omega^{-1/2}\left(\xi - \beta_1^M - \beta_1^O \cos(\tau+\phi)\right)$, a steady streaming layer solution is introduced to match to the far-field flow. When matching the Stokes layer to the steady streaming layer the constants b, c and d are found.

5.4.2 Steady streaming layer

In this section, we seek a solution to (5.10) in the steady streaming layer, which matches the solution in the Stokes layer to the far-field flow. From the primary problem, the steady streaming layer has thickness $O(\Omega^{1/2})$ with steady streaming layer variable $\zeta = \Omega^{-1/2}\widehat{\eta}$, where $\zeta = O(1)$. Also, as before, $\widetilde{\beta}(\tau) = \Omega^{1/2}\beta_0 + \Omega^{-1/2}\beta_1 + O(\Omega^{-3/2})$ and $\widetilde{\alpha}(\tau) = \Omega^{-1/2}\alpha_0 + O(\Omega^{-3/2})$. Rewriting the oblique equation (5.10) in terms of the steady streaming layer variable ζ, we obtain

$$\begin{aligned}\Omega\widehat{\psi}_{O\tau} + \Omega^{-1/2}\left(\widehat{\psi}_O\widehat{\psi}_{P\zeta} - \widehat{\psi}_P\widehat{\psi}_{O\zeta}\right) &= -\Omega^{3/2}(\beta_{0\tau} + \Omega^{-1}\beta_{1\tau} + \Omega^{-2}\beta_{2\tau}) \\ &+ \Omega^{-1/2}\alpha_0 - \Omega^{1/2}(\cos\tau + a_0\Omega^{-1} + a_1\Omega^{-2})(\beta_0 + \Omega^{-1}\beta_1) \\ &+ \Omega^{-1}\widehat{\psi}_{O\zeta\zeta} + O(\Omega^{-3/2}),\end{aligned} \tag{5.31}$$

with the matching condition to the far-field flow given by

$$\widehat{\psi}_O \to \Omega^{1/2}(\zeta - \beta_0) - \Omega^{-1/2}\beta_1 + O(\Omega^{-3/2}) \quad \text{as} \quad \zeta \to \infty, \tag{5.32}$$

where $\beta_i = \beta_i^M + \beta_i^O \cos(\tau+\phi)$ for $i \geq 0$.

Rewriting the dominant terms in the Stokes layer, which are given in (5.30), in terms of ζ suggests we write

$$\begin{aligned}\widehat{\psi}_O &= \Omega^{3/2}\Big(H_0(\zeta,\tau) + h_0(\zeta)\Big) + \Omega^{1/2}\Big(H_1(\zeta,\tau) + h_1(\zeta)\Big) \\ &\quad + \Omega^{-1/2}\Big(H_2(\zeta,\tau) + h_2(\zeta)\Big),\end{aligned} \tag{5.33}$$

where the functions $H_i(\zeta,\tau)$ have a zero time-average and $h_i(\zeta)$ are the mean components, where $i \geq 0$. Upon substituting oblique expansion (5.33) and the primary steady streaming layer solution (5.16) into equation (5.31), we

obtain

$$
\begin{aligned}
H_{0\tau} &= 0, && (5.34)\\
H_{1\tau} &= \zeta(H_{0\zeta}+h_{0\zeta})\cos\tau-(H_0+h_0)\cos\tau+\beta_0^O\sin(\tau+\phi), && (5.35)\\
H_{2\tau} &= \zeta(H_{1\zeta}+h_{1\zeta})\cos\tau+\left[f_0-\cos\left(\tau-\frac{\pi}{4}\right)\right](H_{0\zeta}+h_{0\zeta}) && (5.36)\\
&\quad -(H_1+h_1)\cos\tau-f_{0\zeta}(H_0+h_0)+\beta_1^O\sin(\tau+\phi)\\
&\quad -\beta_0^M\cos\tau-\beta_0^O\cos\tau\cos(\tau+\phi)+H_{0\zeta\zeta}+h_{0\zeta\zeta}.
\end{aligned}
$$

Upon integrating (5.34) and (5.35) with respect to τ and taking a time-average to obtain the function of integration, we find

$$
\begin{aligned}
H_0(\zeta,\tau) &= 0, && (5.37)\\
H_1(\zeta,\tau) &= -\beta_0^O\cos(\tau+\phi)+(\zeta h_0'-h_0)\sin\tau, && (5.38)
\end{aligned}
$$

where the prime denotes differentiation with respect to ζ. Taking a time-average of equation (5.36), we obtain

$$h_0''+f_0h_0-h_0f_0''=0. \tag{5.39}$$

To find the boundary conditions on $\zeta=0$, we match the steady streaming layer expansion (5.33) to the Stokes layer. The Stokes layer solution in terms of ζ, is given by

$$
\begin{aligned}
\widehat{\psi}_O &= \Omega^{3/2}b\zeta+\Omega^{1/2}\Bigg[c\zeta+(a_0\beta_0^M-C)\frac{\zeta^2}{2}-\frac{11\sqrt{2}b}{16}\zeta^2 && (5.40)\\
&\quad -\beta_0^O\cos(\tau+\phi)\Bigg]+\Omega^{-1/2}\Bigg[\frac{3\sqrt{2}\beta_0^O}{4}\cos\left(\phi+\frac{\pi}{4}\right)+d\zeta-\beta_0^M\sin\tau\\
&\quad -\beta_1^O\cos(\tau+\phi)+b\cos\left(\tau+\frac{\pi}{4}\right)\Bigg]+O(\Omega^{-3/2}).
\end{aligned}
$$

Therefore, matching (5.40) with the steady streaming layer expansion (5.33), we find $h_0(\zeta)\to b\zeta$ as $\zeta\to 0$. Similarly, matching the steady streaming layer to the far-field boundary condition (5.32), we find $h_0(\zeta)\to 0$ as $\zeta\to\infty$. Hence, the boundary conditions for equation (5.39) are given by

$$h_0(0)=0,\quad h_0(\zeta)\to 0\quad\text{as}\quad\zeta\to\infty. \tag{5.41}$$

Numerical solutions of equation (5.39) along with the boundary conditions (5.41) suggest $h_0(\zeta)=0$. To illustrate that there are no eigensolutions to equation (5.39), an analytic solution is obtained.

One solution to equation (5.39) is given by $h_0(\zeta) = f_0''(\zeta)$, where $f_0(\zeta)$ is given in equation (5.17). To seek the second solution we use the method of reduction of order and write $h_0(\zeta) = f_0''(\zeta)U(\zeta)$, to obtain

$$h_0(\zeta) = AF(\zeta) + Bf_0''(\zeta). \tag{5.42}$$

where

$$F(\zeta) = f_0''(\zeta)\int_0^{\zeta} \left[f_0''(\bar{\zeta})\right]^{-2} e^{-\int_0^{\bar{\zeta}} f_0(s)ds} \mathrm{d}\bar{\zeta}. \tag{5.43}$$

Applying the boundary conditions $h_0(0) = 0$ and $h_0'(0) = b$, we find $A = bf_0''(0)$ and $B = 0$. Therefore, we obtain the solution $h_0 = bf_0''(0)F(\zeta)$. Following Glauert (1956), it can be shown that $F(\zeta) \to \kappa_1\zeta + \kappa_2$ as $\zeta \to \infty$, where κ_1 and κ_2 are dependent upon a_0 and are obtained numerically. Thus, to satisfy the far-field boundary condition $h_0(\zeta) \to 0$ as $\zeta \to \infty$, the only possibility is $b = 0$ as $f_0''(0) \neq 0$ and it follows that the only solution to equation (5.39) is $h_0(\zeta) = 0$.

The steady streaming layer solution can now be expressed as

$$\begin{aligned} \widehat{\psi}_O &= \Omega^{1/2}\left[(h_1(\zeta) - \beta_0^O\cos(\tau+\phi)\right] + \Omega^{-1/2}\big[-\beta_1^O\cos(\tau+\phi) \\ &\quad -\beta_0^M\sin\tau + (\zeta h_1'(\zeta) - h_1(\zeta))\sin\tau + h_2(\zeta)\big] + O(\Omega^{-3/2}). \end{aligned} \tag{5.44}$$

To obtain the equation for $h_1(\zeta)$, we collect terms of $O(\Omega^{-1/2})$ in equation (5.31), to find

$$\begin{aligned} H_{3\tau} &= -(H_1+h_1)f_0' - (H_2+h_2)\cos\tau + \zeta\cos\tau(H_2'+h_2') \\ &\quad + \left[f_0 - \cos\left(\tau - \frac{\pi}{4}\right)\right](H_1'+h_1') + \beta_2^O\sin(\tau+\phi) + \alpha_0 \\ &\quad -a_0\Big(\beta_0^M + \beta_0^O\cos(\tau+\phi)\Big) \\ &\quad -\cos\tau\Big(\beta_1^M + \beta_1^O\cos(\tau+\phi)\Big) + H_1'' + h_1''. \end{aligned} \tag{5.45}$$

We substitute $\alpha_0 = \cos\left(\tau - \frac{\pi}{4}\right) + C$, $H_1(\zeta,\tau)$ which is given in (5.38) and $H_2(\zeta,\tau) = (\zeta h_1' - h_1)\sin\tau - \beta_1^O\cos(\tau+\phi) - \beta_0^M\sin\tau$ into (5.45). After taking a time-average over one time period, we obtain

$$h_1'' + f_0h_1' - h_1f_0' = a_0\beta_0^M - C. \tag{5.46}$$

The constant $C = \lim_{\zeta\to\infty}(a_0\zeta - f_0)$ and is found by solving the equation for $f_0(\zeta)$, given in (5.17). Similarly, to obtain the equation for $h_2(\zeta)$, we collect terms of size $O(\Omega^{-3/2})$ in equation (5.31) and take a time-average, to find

$$h_2'' + f_0 h_2' - f_0' h_2 = f_1' h_1 - f_1 h_1' + a_0\beta_1^M + a_1\beta_0^M - D. \tag{5.47}$$

The constant $D = \lim_{\zeta\to\infty}(a_1\zeta - f_1)$, which is calculated by solving equation (2.54).

We proceed by solving the numerical equations (5.46) and (5.47), but first, the boundary conditions on $\zeta = 0$ and as $\zeta \to \infty$ are needed. To find the boundary conditions at $\zeta = 0$, we match the Stokes layer (5.40) to the steady streaming layer expansion (5.33), to obtain $h_1 \to c\zeta + (a_0\beta_0^M - C)\frac{\zeta^2}{2}$ and $h_2 \to \frac{3\beta_0^O}{4}\cos\left(\phi + \frac{\pi}{4}\right) + d\zeta + O(\zeta^2)$ as $\zeta \to 0$. To obtain the constants c and d, it is necessary to find the small ζ expansions for $h_1(\zeta)$ and $h_2(\zeta)$. As these are dependent upon the primary functions $f_0(\zeta)$ and $f_1(\zeta)$, we initially find the small ζ expansion for $f_0(\zeta)$. We express $f_0(\zeta) = -\frac{3}{4}\zeta + \frac{C_1\zeta^2}{2} + O(\zeta^3)$, having used the boundary conditions $f_0(0) = 0$ and $f_0'(0) = -\frac{3}{4}$. The constant C_1 is obtained by substituting this expansion into the equation for $f_0(\zeta)$, given by (5.17) and equating coefficients. Hence, we find

$$f_0(\zeta) \;=\; -\frac{3}{4}\zeta + \frac{f_0''(0)\zeta^2}{2} + O(\zeta^3). \tag{5.48}$$

By repeating this process, we find

$$f_1(\zeta) \;=\; \frac{13}{4\sqrt{2}} + \frac{f_1''(0)\zeta^2}{2} + O(\zeta^3), \tag{5.49}$$

$$h_1(\zeta) \;=\; h_1'(0)\zeta + (a_0\beta_0 - C)\frac{\zeta^2}{2} + O(\zeta^3), \tag{5.50}$$

$$h_2(\zeta) \;=\; \frac{3\beta_0^O}{4}\cos\left(\phi + \frac{\pi}{4}\right) + h_2'(0)\zeta + (a_0\beta_0 - C)\frac{\zeta^2}{2} + O(\zeta^3). \tag{5.51}$$

Therefore, we find $c = h_1'(0)$ and $d = h_2'(0)$ and the boundary conditions at $\zeta = 0$ are given by

$$h_1(0) = 0, \quad h_1'(0) = c, \quad h_2(0) = \frac{3\beta_0^O}{4}\cos\left(\phi + \frac{\pi}{4}\right), \quad h_2'(0) = d. \tag{5.52}$$

The far-field boundary conditions are given by

$$h_1(\zeta) \to \zeta - \beta_0^M, \quad h_2(\zeta) \to -\beta_1^M \quad \text{as} \quad \zeta \to \infty, \tag{5.53}$$

which are obtained by matching to the steady streaming layer solution to the far-field boundary condition (5.32).

To find the analytic solution for $h_1(\zeta)$, whose equation is given by (5.46), we note that the homogenous solution satisfying the new boundary conditions at $\zeta = 0$, $h_1(0) = 0$ and $h_1'(0) = \delta$, is given by $h_1 = \lambda F$, where $F(\zeta)$ is given by (5.43). At $\zeta = 0$, we find $\delta = \lambda F'(0) = \lambda / f_0''(0)$. As discussed above, $F(\zeta) \to \kappa_1 \zeta + \kappa_2$ as $\zeta \to \infty$, so to satisfy the far-field boundary condition $h_1'(\zeta) \to 1$ as $\zeta \to \infty$, we find $\kappa_1 = 1/(\delta f_0''(0))$.

Combining the homogeneous solution with the particular solution, we obtain

$$h_1 = \frac{F(\zeta)}{\kappa_1} + \left(\frac{C - a_0 \beta_0^M}{a_0^2} \right) \left(f_0'(\zeta) + \frac{3 f_0''(\zeta)}{4 f_0''(0)} \right), \tag{5.54}$$

where $F(\zeta)$ is given by (5.43) and from $h_1(\zeta)$,

$$c = \frac{1}{\kappa_1 f_0''(0)} + \left(\frac{C - a_0 \beta_0^M}{a_0^2} \right) \left(f_0''(0) + \frac{27}{64 f_0''(0)} - \frac{3 a_0^2}{4 f_0''(0)} \right). \tag{5.55}$$

For the example case of $a_0 = 1$ and $\beta_0^M = 1$, we compute $\kappa_1 = 2.257$ and using the relation given in (5.55), we find $c = 0.893$.

Having obtained the analytic solution for $h_1(\zeta)$, we now solve $h_1(\zeta)$ numerically. To do so, we use a fourth order Runge-Kutta method with a shooting technique. We begin by converting equation (5.46) into two first order ones by writing $h_1 = z_1$ with $f_0 = y_1$ and $f_0' = y_2$. It follows that

$$z_1' = z_2, \tag{5.56}$$

$$z_2' = z_1 y_2 - z_2 y_1 + a_0 \beta_0^M - C, \tag{5.57}$$

with boundary conditions

$$z_1(0) = 0, \quad z_1(\infty) = \zeta - \beta_0^M, \tag{5.58}$$

where $z_2(0)$ is chosen, such that the condition $z_1(\infty)$ is satisfied. The primary functions y_1, y_2 and C have previously been found in chapter 2, for all values of $a_0 > 0.6017$. As the system (5.56) - (5.58) is reliant upon the primary function $f_0(\zeta)$, we find two solutions when $0.6017 < a_0 < 0.75$ and one

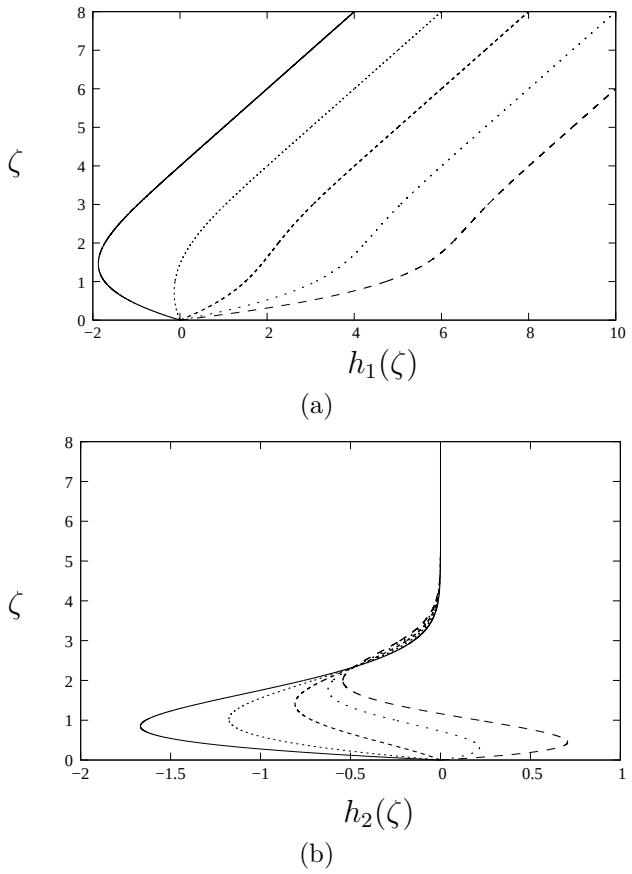

Figure 5.1: (a) The oblique function $h_1(\zeta)$ for, working from left to right, $\beta_0^M = 4, 2, 0, -2, -4$ and $a_0 = 1$. (b) The oblique function $h_2(\zeta)$ for, working from left to right, $\beta_0^M = 4, 2, 0, -2, -4$, $a_0 = 1$ and $a_1 = -0.5$.

solution when $a_0 > 0.75$. Figure 5.1(a) illustrates the solutions to $h_1(\zeta)$ for $a_0 = 1$ and $\beta_0^M = -4, -2, 0, 2, 4$. It can be seen that as β_0^M increases, a region of flow reversal develops close to $\zeta = 0$. Numerical trials have suggested that as a_0 decreases, the value of β_0^M at which flow reversal occurs increases. Since the results plotted in figure 5.1(a) are for equally spaced values of β_0^M, the behaviour of $h_1(\zeta)$ for $\zeta \gg 1$ suggests that in the far-field, $h_1(\zeta)$ and β_0^M have a linear relationship. This is confirmed by the analytic solution (5.54).

For completeness, the equation for $h_2(\zeta)$, given by (5.47), is solved numerically using a similar method, although $h_2(\zeta)$ has very little effect on the steady streaming layer solution (5.44). Figure 5.1(b) illustrates the velocity profiles for selected values of β_0^M for $a_0 = 1$, $a_1 = -0.5$ and $\beta_0^M = -4, -2, 0, 2, 4$.

In this section, the solution of the oblique equation (5.10) has been found

in the Stokes layer and a steady streaming layer. In the steady streaming layer solution (5.44), the leading order steady component $h_1(\zeta)$ has been solved. It can be seen clearly in figure 5.1(a) that the value of β_0^M, which is the leading order mean horizontal velocity component, determines whether flow reversal occurs and its extent.

Having found solutions in both the Stokes layer and the steady streaming layer, in the next section we discuss the flow structure in both these layers over one time period. Additionally, a particle path analysis is performed in the steady streaming layer.

5.5 The structure of the near-wall flow

In chapter 4, where the primary and oblique equations were solved numerically, it was found that for certain parameters and over some time intervals of the cycle, horizontal streamlines appear in the flow, creating a multi-layered flow. In the present chapter, we have investigated the primary and oblique problems for large frequency with $\Delta \sim O(\sigma^{1/2})$ and have found the problem is described in terms of a Stokes layer and a steady streaming layer. In this section, the flow structure in both of these layers is discussed, with comparisons being drawn to the numerical results in chapter 4.

The streamfunction, which is previously defined in equation (5.2), is written in terms of the scalings $\psi_P = \Delta^{1/2}\widehat{\psi_P}$, $\psi_O = \Delta^{-1/2}\widehat{\psi_O}$ with $\eta = \Delta^{-1/2}\widehat{\eta}$, which were introduced in section 5.2, to give

$$\psi = (\nu k)^{1/2} x \Delta^{1/2} \widehat{\psi}_P(\widehat{\eta}, \tau) + \widehat{\zeta}\Big(\frac{\nu}{k}\Big)\Delta^{-1} \int_0^{\widehat{\eta}} \widehat{\psi}_O(z, \tau)\mathrm{d}z. \tag{5.59}$$

To consider the flow structure in the Stokes layer, we differentiate the streamfunction (5.59), to obtain the horizontal and vertical velocity components

$$u = kx\Delta\widehat{\psi}_{P_{\widehat{\eta}}} + \widehat{\zeta}\left(\frac{\nu}{k}\right)^{1/2}\Delta^{-1/2}\widehat{\psi}_O, \tag{5.60}$$

$$v = -(\nu k)^{1/2}\Delta^{1/2}\widehat{\psi}_P. \tag{5.61}$$

Upon writing the velocity components (5.60) and (5.61) in terms of the Stokes layer variable, $\xi = \Omega^{1/2}\widehat{\eta}$ and using the expansion

$$\Delta = \frac{\Omega}{a_0} - \frac{a_1}{a_0^2} + O(\Omega^{-1}), \tag{5.62}$$

we obtain

$$\begin{aligned} u &= \frac{kx}{a_0}\left[\Omega\Psi_{P_0\xi} + \Psi_{P_1\xi} - \frac{a_1}{a_0}\Psi_{P_0\xi} + O\left(\Omega^{-1}\right)\right] + \\ &\quad \widehat{\zeta}\left(\frac{\nu a_0}{k}\right)^{1/2}\left[\Psi_{O_0} + \Omega^{-1}\left(\frac{a_1}{2a_0}\Psi_{O_0} + \Psi_{O_1}\right) + O\left(\Omega^{-2}\right)\right], \end{aligned} \tag{5.63}$$

$$v = -\left(\frac{\nu k}{a_0}\right)^{1/2}\Psi_{P_0} + O\left(\Omega^{-1}\right). \tag{5.64}$$

Stagnation points occur when the velocity components u and v, given in (5.63) and (5.64) are equal to zero. Considering the vertical velocity component, $\Psi_{P_0}(\xi,\tau) = 0$ when $\xi = 0$ and $\xi = \xi_0$. To examine what effect these zeros have on the flow structure, we begin by obtaining the dividing streamline. To do so, we set (5.59) equal to zero and rewrite it in terms of the Stokes layer variables, to give

$$x_d = -\widehat{\zeta}\left(\frac{\nu a_0^3}{k^3}\right)^{1/2}\frac{1}{\Omega}\frac{\int_0^\xi \Psi_{O_0}(z,\tau)\mathrm{d}z}{\Psi_{P_0}(\xi,\tau)} + O\left(\Omega^{-2}\right). \tag{5.65}$$

As $\Psi_{P_0}(0,\tau) = 0$, $\Psi_{P_0\xi}(0,\tau) = 0$ and $\Psi_{O_0}(0,\tau) = 0$, at the wall the denominator is equal to zero. So, we take small ξ expansions of the primary and oblique functions, $\Psi_{P_0}(0,\tau) = \Psi_{P_0\xi\xi}(0,\tau)\xi^2/2 + O\left(\xi^3\right)$ and $\Psi_{O_0}(0,\tau) = \Psi_{O_0\xi}(0,\tau)\xi + O\left(\xi^2\right)$, to obtain the attachment point of the dividing streamline with the wall. We recall the primary leading order solution is given by

$$\Psi_{P_0}(\xi,\tau) = \xi\cos\tau - \cos\left(\tau - \frac{\pi}{4}\right) + e^{-\xi/\sqrt{2}}\cos\left(\tau - \frac{\xi}{\sqrt{2}} - \frac{\pi}{4}\right) \tag{5.66}$$

and the oblique leading order solution is given in (5.27). Therefore, the attachment point of the dividing streamline with the wall, is given by

$$x_0 = \widehat{\zeta}\left(\frac{\nu a_0^3}{k^3}\right)^{1/2}\frac{\beta_0^O}{\Omega}\frac{\cos\left(\tau + \phi + \frac{\pi}{4}\right)}{\cos\left(\tau + \frac{\pi}{4}\right)} + O\left(\Omega^{-2}\right). \tag{5.67}$$

If the phase difference ϕ is an integer multiple of π, the time-dependent horizontal velocity component $\widehat{\beta}$ is either exactly in phase or exactly out of

phase with the primary function $a(\tau)$. When $\beta_0^O \neq 0$, if ϕ is an even multiple of π, the attachment point is positive and is fixed over the time period. Similarly, if ϕ is an odd multiple, the attachment point is negative and fixed over the time period. For any other value of ϕ, the attachment point tends to either positive or negative infinity as $\tau \to \pi/4$ and $\tau \to 5\pi/4$.

Having discussed the zero at $\xi = 0$, we now consider the zero at $\xi = \xi_0$. We find this zero only occurs when $\pi/4 \leq \tau \leq \pi/2$ and $5\pi/4 \leq \tau \leq 3\pi/2$. In figure 5.2, the first of these non-trivial zeros, ξ_0 is illustrated. This zero causes a horizontal streamline to appear in the flow, creating a double-layered flow. As τ increases within these time intervals, the horizontal streamline moves up through the Stokes layer and approaches infinity as $\tau \to \frac{\pi}{2}^-$ and as $\tau \to \frac{3\pi}{2}^-$.

We now investigate the behaviour of the non-trivial zero ξ_0 in the time interval $\pi/4 \leq \tau \leq \pi/2$. As stated above, a non-trivial zero $\xi = \xi_0$, develops within the Stokes layer solution at $\tau = \pi/4$. To consider the flow structure around this time, we expand the primary and oblique leading order solutions in the Stokes layer, by writing $\tau = \frac{\pi}{4} + \widehat{T}$ where $|\widehat{T}| \ll 1$. Initially considering the primary solution, we find

$$\begin{aligned} \Psi_{P_0} &= \left[\frac{\xi}{\sqrt{2}} - 1 + e^{-\xi/\sqrt{2}} \cos\left(\frac{\xi}{\sqrt{2}}\right)\right] \\ &\quad + \widehat{T}\left[-\frac{\xi}{\sqrt{2}} + e^{-\xi/\sqrt{2}} \sin\left(\frac{\xi}{\sqrt{2}}\right)\right] + O(\widehat{T}^2). \end{aligned} \tag{5.68}$$

The first squared bracketed term only has a zero at $\xi = 0$. Balancing the leading and first order terms in (5.68), we find the zero $\xi = \xi_0$ appears when

$$\xi_0 = 3\sqrt{2}\widehat{T}, \tag{5.69}$$

for small $\widehat{T} > 0$. Similarly, for small $\widehat{T}$, the oblique Stokes layer solution becomes

$$\begin{aligned} \Psi_{O_0} &= \beta_0^O \left[e^{-\xi/\sqrt{2}} \cos\left(\frac{\pi}{4} + \phi - \frac{\xi}{\sqrt{2}}\right) - \cos\left(\frac{\pi}{4} + \phi\right)\right] \\ &\quad + \widehat{T}\left[\sin\left(\frac{\pi}{4} + \phi\right) - e^{-\xi/\sqrt{2}} \sin\left(\frac{\pi}{4} + \phi - \frac{\xi}{\sqrt{2}}\right)\right] + O(\widehat{T}^2). \end{aligned} \tag{5.70}$$

On the horizontal streamline, a stagnation point is present. To consider the horizontal position of this stagnation point, we set the horizontal velocity

component (5.63) equal to zero and obtain

$$x|_{\xi=\xi_0} = -\widehat{\zeta}\left(\frac{\nu a_0^3}{k^3}\right)^{1/2}\frac{1}{\Omega}\frac{\Psi_{O_0}(\xi_0,\tau)}{\Psi_{P_0\xi}(\xi_0,\tau)} + O\left(\Omega^{-2}\right). \tag{5.71}$$

Evaluating the primary and oblique leading order solutions about (5.69), we find

$$\Psi_{P_0\xi}\Big|_{\xi=\xi_0} \sim \frac{3}{\sqrt{2}}\widehat{T}^2, \quad \Psi_{O_0}\Big|_{\xi=\xi_0} \sim 3\sqrt{2}\widehat{T}\beta_0^O\sin\phi. \tag{5.72}$$

Substituting the leading order expansions (5.72) into (5.71), we obtain

$$x|_{\xi=\xi_0} \sim -\widehat{\zeta}\left(\frac{\nu a_0^3}{k^3}\right)^{1/2} 2\beta_0^O\sin\phi\Omega^{-1}\widehat{T}^{-1}, \tag{5.73}$$

for small $\widehat{T}$. Therefore, the horizontal streamline emerges from the wall at $\tau = \pi/4$ and moves up through the Stokes layer, with the stagnation point on the horizontal streamline moving in from either positive or negative infinity, depending on the parameters, β_0^O and ϕ.

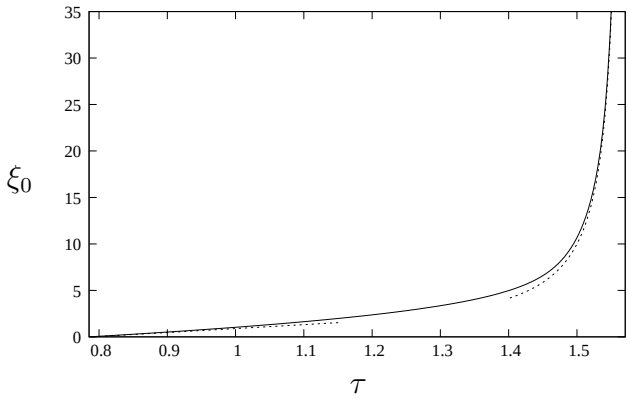

Figure 5.2: The numerically calculated non-trivial zero ξ_0, in the Stokes layer, which is represented by the solid line, alongside the asymptotic predictions of the behaviour of the zeros ξ_0, close to $\pi/4$ and $\pi/2$, which are represented by the dotted lines.

To investigate the behaviour of the zero ξ_0 close to $\tau = \pi/2$, we let $\tau = \frac{\pi}{2} + \widetilde{T}$, where $|\widetilde{T}| \ll 1$. Hence, the primary leading order equation (5.66), becomes

$$\Psi_{P_0} = -\xi\sin\widetilde{T} - \cos\left(\frac{\pi}{4} + \widetilde{T}\right) + e^{-\xi/\sqrt{2}}\cos\left(\frac{\pi}{4} + \widetilde{T} - \frac{\xi}{\sqrt{2}}\right). \tag{5.74}$$

Expanding for small $\widetilde{T}$, we obtain

$$\begin{aligned}\Psi_{P_0} &= -\frac{1}{\sqrt{2}}\left[1+e^{-\xi/\sqrt{2}}\left(\cos\left(\frac{\xi}{\sqrt{2}}\right)+\sin\left(\frac{\xi}{\sqrt{2}}\right)\right)\right] \\ &\quad +\widetilde{T}\left[-\xi+\frac{1}{\sqrt{2}}\left(1+e^{-\xi/\sqrt{2}}\left(\sin\left(\frac{\xi}{\sqrt{2}}\right)-\cos\left(\frac{\xi}{\sqrt{2}}\right)\right)\right)\right]+O(\widetilde{T}^2).\end{aligned} \tag{5.75}$$

For a zero to occur in (5.75), we need $\xi \sim O(\widetilde{T}^{-1})$. Therefore, we set $\xi = \widetilde{\xi}/\widetilde{T}$, to give

$$\Psi_{P_0} \sim -\frac{1}{\sqrt{2}} - \widetilde{\xi}. \tag{5.76}$$

Therefore, as $\tau \to \frac{\pi}{2}^-$, the zero of Ψ_{P_0} occurs when

$$\xi_0 = -\frac{1}{\sqrt{2}}\widetilde{T}^{-1}, \tag{5.77}$$

as $\widetilde{T} \to 0^-$. This estimate is illustrated alongside the numerically computed zero as $\tau \to \frac{\pi}{2}^-$ in figure 5.2. As $\widetilde{T} \to 0^-$, the horizontal streamline moves up through the Stokes layer and enters the steady streaming layer.

To consider the behaviour of the stagnation point on the horizontal streamline close to $\tau = \frac{\pi}{2}$ in the Stokes layer, we evaluate the leading order primary and oblique solutions in the present time zone and find

$$\Psi_{P_0\xi}\Big|_{\xi=\xi_0} \sim -\widetilde{T}, \quad \Psi_{O_0}\Big|_{\xi=\xi_0} \sim \beta_0^O \sin\phi. \tag{5.78}$$

Substituting (5.78) into (5.71), we obtain

$$x|_{\xi=\xi_0} \sim \widehat{\zeta}\left(\frac{\nu a_0^3}{k^3}\right)^{1/2} \beta_0^O \sin\phi \Omega^{-1}\widetilde{T}^{-1}. \tag{5.79}$$

Therefore, as the horizontal streamline moves up through the Stokes layer, the stagnation point on the horizontal streamline moves towards either positive or negative infinity, depending upon β_0^O and ϕ.

We now discuss how the horizontal streamline behaves as it enters the steady streaming layer. We write the primary steady streaming solution (5.16) in terms of the present time variable and find

$$\widehat{\psi}_P = -\Omega^{1/2}\zeta\sin\widetilde{T} - \frac{\Omega^{-1/2}}{\sqrt{2}}\left(\cos\widetilde{T}-\sin\widetilde{T}\right)+\Omega^{-1/2}f_0+O\left(\Omega^{-3/2}\right). \tag{5.80}$$

Taking small $\widetilde{T}$ expansions of (5.80), we find

$$\widehat{\psi}_P = -\Omega^{1/2}\zeta\widetilde{T} + \Omega^{-1/2}\left(f_0 - \frac{1}{\sqrt{2}}\right) + o\left(\Omega^{-1/2}\right). \tag{5.81}$$

To balance the first two terms, we choose $\widetilde{T} = \mu\Omega^{-1}$, where $\mu = O(1)$. Therefore, (5.81) becomes

$$\widehat{\psi}_P = -\Omega^{-1/2}\left(f_0 - \mu\zeta - \frac{1}{\sqrt{2}}\right) + O\left(\Omega^{-3/2}\right). \tag{5.82}$$

The bracketed term in (5.82), for large negative values of μ has a zero ζ_0, which is small in magnitude. Expanding (5.82) for small ζ, we obtain the approximation

$$\zeta_0 \sim -\frac{1}{\sqrt{2}\left(\mu + \frac{3}{4}\right)}. \tag{5.83}$$

As μ increases, the zero ζ_0 increases and the horizontal streamline moves upwards through the steady streaming layer. The numerical results suggest that $\zeta_0 \to \infty$ as $\mu \to a_0^-$. We estimate ζ_0 asymptotically, by seeking a large ζ approximation of (5.82), where $f_0' \to a_0$ as $\zeta \to \infty$ and we find that

$$\zeta_0 \sim \frac{d}{a_0 - \mu}, \quad \text{where} \quad d = \frac{1}{\sqrt{2}} + \lim_{\zeta\to\infty}\left(a_0\zeta - f_0\right). \tag{5.84}$$

Therefore, as $\mu \to a_0^-$, ζ_0 increases and the horizontal streamline moves up to infinity. This occurs at $\tau \sim \widehat{\tau} = \frac{\pi}{2} + a_0\Omega^{-1}$. The critical time $\widehat{\tau}$, corresponds to a zero developing in the primary function $a(\tau) = 1 + \Delta\cos\tau$, which arises at $\tau = \pi - \cos^{-1}\left(\frac{1}{\Delta}\right)$. Expanding for large Δ, we obtain $\tau = \frac{\pi}{2} + \frac{1}{\Delta} \sim \widehat{\tau}$, where $\Delta \sim \Omega/a_0$. In figure 5.3, we plot on a log-log graph the asymptotic prediction of the zeros ζ_0, given in (5.84), with the numerically computed zeros for a range of values of μ, showing excellent agreement.

To find the location of the stagnation point as the horizontal streamline enters the steady streaming layer, we set the horizontal velocity component (5.60) equal to zero and rewrite in terms of the steady streaming layer variables, to give

$$x|_{\zeta=\zeta_0} = -\frac{\widehat{\zeta}}{\Omega}\left(\frac{\nu a_0^3}{k^3}\right)^{1/2}\frac{h_1(\zeta_0) - \beta_0^O\cos(\tau+\phi)}{\cos\tau + \Omega^{-1}f_0'(\zeta_0)}. \tag{5.85}$$

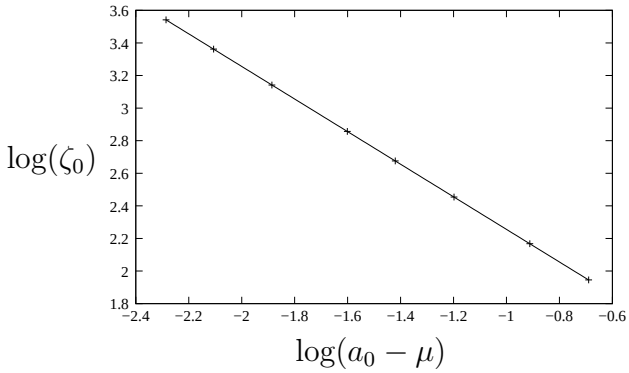

Figure 5.3: The asymptotic prediction of the behaviour of the zeros ζ_0, alongside the numerically calculated zeros, which are represented by the crosses, showing excellent agreement.

Close to $\tau = \frac{\pi}{2}$, (5.85) is rewritten as

$$x|_{\zeta=\zeta_0} \sim \frac{\widehat{\zeta}}{\Omega}\left(\frac{\nu a_0^3}{k^3}\right)^{1/2} \frac{h_1(\zeta_0) + \beta_0^O \sin\phi}{T - \Omega^{-1} f_0'(\zeta_0)}. \tag{5.86}$$

This matches directly to the Stokes layer expansion (5.79) when $\widetilde{T} \to -\infty$, where the small ζ_0 approximation, given in (5.83), is used. To consider how the stagnation point on the horizontal streamline behaves as the horizontal streamline moves up to infinity, we recall that $h_1(\zeta) \to \zeta - \beta_0^M$ and $f_0'(\zeta) \to a_0$ as $\zeta \to \infty$. Using the scaling $\widetilde{T} = \mu\Omega^{-1}$ and the large ζ_0 approximation, given in (5.84), we find

$$x|_{\zeta=\zeta_0} \sim -\widehat{\zeta}\left(\frac{\nu a_0^3}{k^3}\right)^{1/2} \frac{d}{(a_0 - \mu)^2}. \tag{5.87}$$

The constant d, given in (5.84), is plotted in figure 5.4. This figure illustrates that for all possible values of a_0, d is positive. Therefore, as $\mu \to a_0^-$, which corresponds to point when the horizontal streamline moves up to infinity, the stagnation point on this streamline tends to negative infinity, irrespective of the choice of $\widehat{\beta}$. This result agrees with the numerical results in chapter 4.

Extending the above analysis over a period of 2π, the streamline pattern changes between a single and a double-layered structure. In the interval $0 \leq \tau \leq \frac{\pi}{4}$, the streamline pattern is single-layered, with the dividing streamline approaching the wall at an angle. When $\frac{\pi}{4} \leq \tau \leq \widehat{\tau}$, the flow structure is double-layered, with a horizontal streamline present within the fluid, which moves upwards to infinity and vanishes at $\widehat{\tau}$. For $\widehat{\tau} \leq \tau \leq \frac{5\pi}{4}$, the flow returns

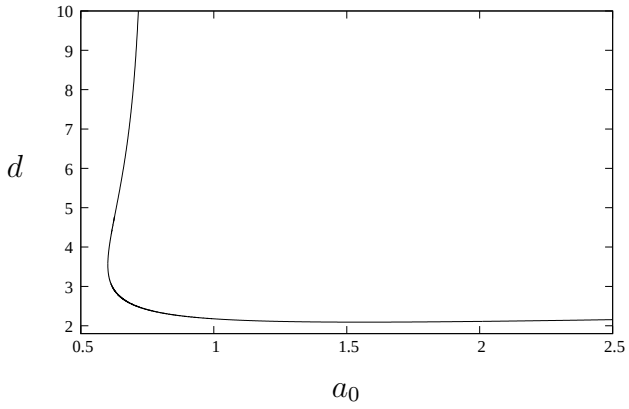

Figure 5.4: The constant d given in (5.84) plotted against a_0, illustrating for all values of a_0, d is positive. The upper branch of the curve asymptotes to $a_0 = 0.75$.

to a single-layered structure. At $\tau = \frac{5\pi}{4}$, a horizontal streamline develops in the Stokes layer and behaves similarly to the case described above when $\tau = \frac{\pi}{4}$. To observe how the horizontal streamline moves through the steady streaming layer, we write $\tau = \frac{3\pi}{2} + \bar{T}$ for $|\bar{T}| \ll 1$ and the steady streaming layer solution becomes

$$\widehat{\psi}_P = \Omega^{1/2}\zeta\bar{T} + \Omega^{-1/2}\left(f_0 - \frac{\bar{T}}{\sqrt{2}} + \frac{1}{\sqrt{2}}\right) + O(\Omega^{-3/2}). \tag{5.88}$$

To gain a balance between the first and second terms, we write $\bar{T} = \bar{\mu}\Omega^{-1}$, where $\bar{\mu} = O(1)$ is a constant. Therefore, we obtain

$$\widehat{\psi}_P = \Omega^{-1/2}\left(f_0 + \bar{\mu}\zeta + \frac{1}{\sqrt{2}}\right) + o\left(\Omega^{-1/2}\right). \tag{5.89}$$

For a large positive $\bar{\mu}$, the bracketed term in (5.89) has no zeros and for large negative values of $\bar{\mu}$ there is one zero. This zero corresponds to a horizontal streamline entering the steady streaming layer from the Stokes layer. When $\bar{\mu} = -a_0^+$, a second zero occurs in the bracketed term in (5.89). This corresponds to a second horizontal streamline entering the flow from infinity when $\bar{\mu} = -a_0^+$, i.e. when $\tau = \frac{3\pi}{2} - a_0\Omega^{-1}$, where $\Delta = \Omega/a_0$. Therefore, the flow develops a triple-layered structure. As $\bar{\mu}$ increases, the second horizontal streamline moves down from infinity. At some point, the two streamlines collide and the flow returns to a single-layered structure for the remainder of the period. These observations agree with the numerical results obtained in section 4.5.

Having considered the instantaneous streamlines in both the Stokes and steady streaming layers, we now discuss the particle paths in the steady streaming layer, as this layer occupies the larger part of the region at the wall. To begin, we rewrite the velocity components (5.60) and (5.61), in terms of the steady streaming layer variables, to give

$$u = kx\Omega^{-1/2}\left(\frac{\Omega}{a_0}-\frac{a_1}{a_0^2}\right)\widehat{\psi}_{P_\zeta}+\widehat{\zeta}\left(\frac{\nu a_0}{k}\right)^{1/2}\Omega^{-1/2}\left(1+\frac{a_1}{2\Omega a_0}\right)\widehat{\psi}_O, \quad (5.90)$$

$$v = -\left(\frac{\nu k}{a_0}\right)^{1/2}\Omega^{1/2}\left(1-\frac{a_1}{2\Omega a_0}\right)\widehat{\psi}_P. \quad (5.91)$$

Substituting the primary and oblique solutions (5.16) and (5.44) into (5.90) and (5.91), we obtain

$$u = kx\left(\frac{\Omega}{a_0}-\frac{a_1}{a_0^2}\right)\left[\cos\tau+\Omega^{-1}f_0'+O\left(\Omega^{-2}\right)\right] \quad (5.92)$$
$$+\widehat{\zeta}\left(\frac{\nu a_0}{k}\right)^{1/2}\left(1+\frac{a_1}{2\Omega a_0}\right)\left[h_1-\beta_0^O\cos\left(\tau+\phi\right)+O\left(\Omega^{-1}\right)\right],$$

$$v = -\left(\frac{\nu k}{a_0}\right)^{1/2}\Omega\left(1-\frac{a_1}{2\Omega a_0}\right)\left[\zeta\cos\tau+\Omega^{-1}\Big(f_0 \quad (5.93)\right.$$
$$\left.-\cos\left(\tau-\frac{\pi}{4}\right)\Big)+O\left(\Omega^{-2}\right)\right].$$

Initially we discuss the steady terms in the steady streaming layer. Later, the time-dependent terms are included and the particle paths are sought to consider what effect the time-dependence has on the steady streamlines.

To consider the flow structure of the steady components, we note that the vertical velocity (5.93) is equal to zero when $f_0(\zeta)=0$. This occurs when $\zeta=0$, which corresponds to a stagnation point at the bottom of the steady streaming layer. In addition to this, we find a second zero at $\zeta=\zeta^*$, which corresponds to an interior stagnation point in the steady streaming layer, through which a horizontal streamline exists, causing the flow to have a double-layered structure. The steady streamline pattern is illustrated in figure 5.5 for $a_0=0.6017$ and $a_0=1$, when the vorticity $\widehat{\zeta}=0$, i.e. solely the primary flow is considered.

When $\widehat{\zeta}\neq 0$, the flow is made up of both primary and oblique components. The dividing streamline is no longer orthogonal and the streamlines now approach the wall at an oblique gradient of $-2a(\tau)k/\widehat{\zeta}$, where

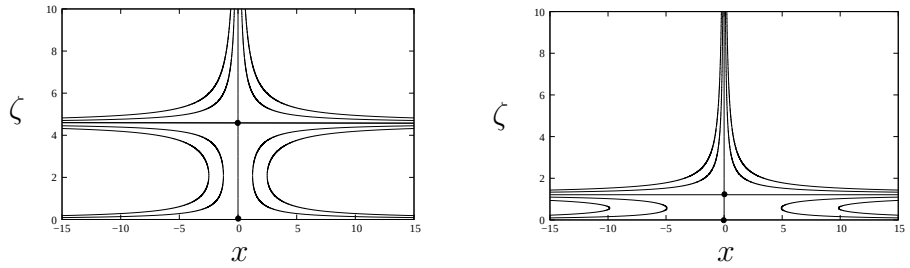

(a) (b)

Figure 5.5: The orthogonal steady streamlines in the steady streaming layer for (a) $a_0 = 0.6017$ and (b) $a_0 = 1$. In both cases $\nu = k = 1$ and the solid dots represent the stagnation points.

$a(\tau) = 1 + \Delta \cos \tau$. Figure 5.6 illustrates the streamlines for $a_0 = 1$ and $\beta_0^M = 1.2, 1.4442, 1.5, 1.582, 1.8$. We note that there are two dividing streamlines, the first is the dividing streamline in the far-field, which divides the streamlines either travelling to the right or the left and the second is the dividing streamline which intersects with the bottom of the steady streaming layer. In figure 5.6, it can be seen that upon increasing β_0^M causes the streamlines in the far-field shift to the right and below the horizontal streamline at $\zeta = \zeta^*$, the direction of the flow along the streamlines changes. Also, it can be seen that the gradient of the dividing streamline changes as β_0^M increases. We note there are two critical values of β_0^M. The first, where the dividing streamline goes through both stagnation points, $\zeta = 0$ and $\zeta = \zeta^*$, when $\beta_0^M = 1.4442$, is illustrated in figure 5.6(b). The second is where both of the stagnation points are at $x = 0$, which occurs when $\beta_0^M = 1.582$ and can be seen in figure 5.6(d).

To consider the behaviour of the stagnation point along the horizontal streamline, we set the horizontal velocity component (5.92) equal to zero and find

$$x^* = -\widehat{\zeta} \left(\frac{\nu a_0^3}{k^3} \right)^{1/2} \frac{h_1(\zeta^*)}{f_0'(\zeta^*)} + O\left(\Omega^{-1}\right), \tag{5.94}$$

where x^* is the location of the stagnation point and $\widehat{\zeta}$, k and ν are constants. The horizontal location x^* is obtained numerically for different values of β_0^M. A linear relationship between x^* and β_0^M is observed and as β_0^M is increased x^* moves to the right, which is illustrated in figure 5.7 for $a_0 = 1$. This is

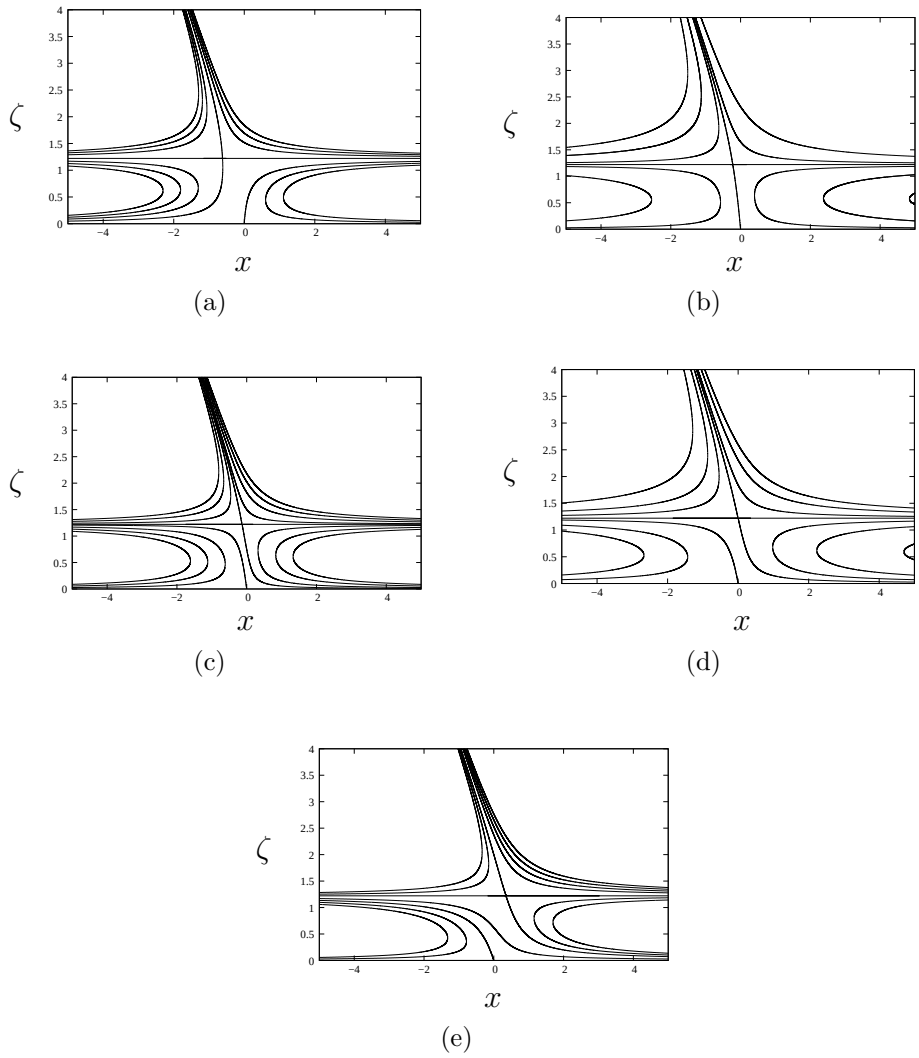

Figure 5.6: The mean components of the steady streaming layer illustrated for $a_0 = 1$ and (a) $\beta_0^M = 1.2$, (b) $\beta_0^M = 1.4442$, (c) $\beta_0^M = 1.5$, (d) $\beta_0^M = 1.582$, (e) $\beta_0^M = 1.8$. In each case $\widehat{\zeta} = \nu = k = 1$.

confirmed by the analytic solution found for $h_1(\zeta)$, given in (5.54), where $h_1(\zeta)$ has a linear dependence upon β_0^M.

We now consider the time-dependent terms as well as the steady terms in velocity components (5.92) and (5.93). The particle paths are computed as the solution of the differential system

$$u = \frac{\mathrm{d}x}{\mathrm{d}t}, \qquad v = \frac{\mathrm{d}y}{\mathrm{d}t}, \tag{5.95}$$

where u and v are given in (5.92) and (5.93). We recall that $\tau = \sigma k t$ and using the relation for σ in terms of Ω, which was initially given in (2.144),

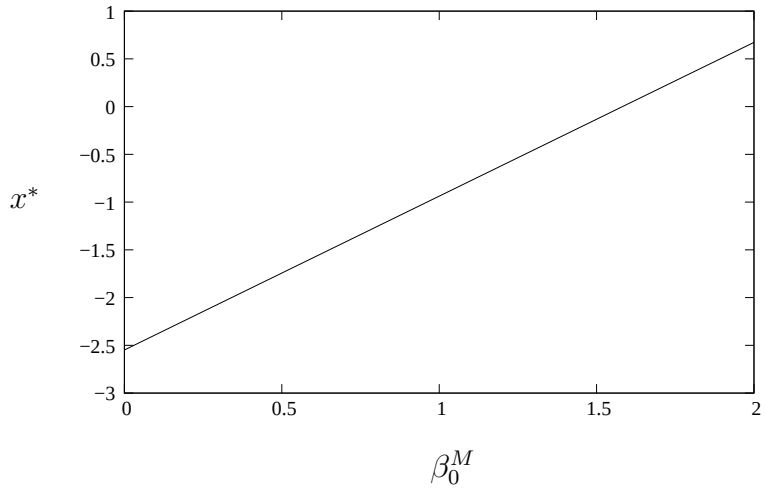

Figure 5.7: The leading order mean component of the time-dependent function, β_0^M plotted against x^*, the horizontal position of the stagnation-point for $\widehat{\zeta} = \nu = k = a_0 = 1$.

we find

$$\tau = \left(\frac{\Omega^2}{a_0} - \frac{\Omega a_1}{a_0^2}\right) kt + O(1). \tag{5.96}$$

We rewrite the velocity components (5.92) and (5.93) in terms of the dimensional variables x, y and t and upon introducing the small parameter $\delta = \Omega^{-1}$, we obtain

$$\begin{aligned} \frac{\mathrm{d}x}{\mathrm{d}t} &= kx\left(\frac{1}{a_0\delta} - \frac{a_1}{a_0^2}\right)\cos\left[\left(\frac{1}{a_0\delta^2} - \frac{a_1}{a_0^2\delta}\right)kt\right] + \frac{kx}{a_0}f_0' \\ &\quad + \widehat{\zeta}\left(\frac{\nu a_0}{k}\right)^{1/2}\left[h_1 - \beta_0^O\cos\left(\left(\frac{1}{a_0\delta^2} - \frac{a_1}{a_0^2\delta}\right)kt + \phi\right)\right] + O(\delta), \end{aligned} \tag{5.97}$$

$$\begin{aligned} \frac{\mathrm{d}y}{\mathrm{d}t} &= -ky\left(\frac{1}{a_0\delta} - \frac{a_1}{a_0^2}\right)\cos\left[\left(\frac{1}{\delta^2 a_0} - \frac{a_1}{\delta a_0^2}\right)kt\right] \\ &\quad - \left(\frac{\nu k}{a_0}\right)^{1/2}\left[f_0 - \cos\left(\left(\frac{1}{a_0\delta^2} - \frac{a_1}{a_0^2\delta}\right)kt - \frac{\pi}{4}\right)\right] + O(\delta). \end{aligned} \tag{5.98}$$

As the right hand sides of (5.97) and (5.98) involve both steady terms and unsteady terms with high frequency oscillations, the particle paths are expected to operate on two distinct time scales. Therefore, we introduce the new slow and fast time variables $\bar{t}$ and T, which are given by

$$\bar{t} = \frac{kt}{a_0} \quad \text{and} \quad T = \left(\frac{1}{\delta^2 a_0} - \frac{a_1}{\delta a_0}\right)kt. \tag{5.99}$$

Since the right hand side of (5.98) is independent of x, we begin by solving this equation. As the variables $x(\bar{t}, T)$ and $y(\bar{t}, T)$ are dependent upon both

the time scales, it follows that

$$\frac{\mathrm{d}}{\mathrm{d}t} = \frac{k}{a_0}\frac{\partial}{\partial \bar{t}} + k\left(\frac{1}{\delta^2 a_0} - \frac{a_1}{\delta a_0^2}\right)\frac{\partial}{\partial T}. \tag{5.100}$$

By rewriting (5.98) in terms of the new time scales, we obtain

$$\begin{aligned}\frac{k}{a_0}\delta^2 y_{\bar{t}} + k\left(\frac{1}{a_0} - \frac{\delta a_1}{a_0^2}\right) y_T = -ky\delta\left(\frac{1}{a_0} - \frac{\delta a_1}{a_0^2}\right)\cos T \\ - \delta^2\left(\frac{\nu k}{a_0}\right)^{1/2}\left[f_0 - \cos\left(T - \frac{\pi}{4}\right)\right] + O\left(\delta^3\right).\end{aligned} \tag{5.101}$$

The dominant balance in equation (5.101) is $y_T = -\delta y \cos T$, which gives the solution

$$y(\bar{t}, T) = \widehat{Y}E, \quad \text{where} \quad E = e^{-\delta \sin T}. \tag{5.102}$$

Substituting (5.102) into equation (5.101), gives

$$\begin{aligned}\delta^2 E\frac{k}{a_0}\widehat{Y}_{\bar{t}} + E\left(\frac{1}{a_0} - \frac{\delta a_1}{a_0^2}\right)\widehat{Y}_T = \\ - \delta^2\left(\frac{\nu k}{a_0}\right)^{1/2}\left[f_0(E\widehat{Y}) - \cos\left(T - \frac{\pi}{4}\right)\right] + O\left(\delta^3\right).\end{aligned} \tag{5.103}$$

We pose the asymptotic expansion $\widehat{Y}(\bar{t}, T) = Y_0(\bar{t}, T) + \delta Y_1(\bar{t}, T) + \delta^2 Y_2(\bar{t}, T) + O(\delta^3)$, giving at leading and first order, $Y_0 = \widetilde{Y}_0(\bar{t})$ and $Y_1 = \widetilde{Y}_1(\bar{t})$. At second order, we find

$$Y_{2T} = -\widetilde{Y}_{0\bar{t}} - \left(\frac{\nu a_0}{k}\right)^{1/2}\left[f_0(\widetilde{Y}_0) - \cos\left(T - \frac{\pi}{4}\right)\right]. \tag{5.104}$$

Integrating this with respect to T, we obtain

$$Y_2 = -\left[\widetilde{Y}_{0\bar{t}} + \left(\frac{\nu a_0}{k}\right)^{1/2} f_0(\widetilde{Y}_0)\right] T + \left(\frac{\nu a_0}{k}\right)^{1/2}\sin\left(T - \frac{\pi}{4}\right) + \widetilde{Y}_2\left(\bar{t}\right), \tag{5.105}$$

where $\widetilde{Y}_2\left(\bar{t}\right)$ is a function of integration. Following the standard method for multiple scales, to avoid the growth of the secular term in (5.105), we require

$$\widetilde{Y}_{0\bar{t}} = -\left(\frac{\nu a_0}{k}\right)^{1/2} f_0(\widetilde{Y}_0). \tag{5.106}$$

We now consider the particle path for x, whose equation is given by (5.97). Rewriting (5.97) in terms of the two time scales given in (5.100), we find

$$\begin{aligned}\frac{k}{a_0}\delta^2 x_{\bar{t}} + \left(\frac{1}{a_0} - \frac{\delta a_1}{a_0^2}\right) x_T = kx\delta\left(\frac{1}{a_0} - \frac{\delta a_1}{a_0^2}\right)\cos T + \delta^2\frac{k}{a_0}x f_0' \\ + \delta^2\widehat{\zeta}\left(\frac{\nu a_0}{k}\right)^{1/2}\left[h_1 - \beta_0^O\cos\left(T + \phi\right)\right] + O(\delta^3).\end{aligned} \tag{5.107}$$

Similar to equation (5.101), the dominant balance in equation (5.107) is $x_T = -\delta x \cos T$, giving

$$x(\bar{t}, T) = \widehat{X}\widehat{E}, \quad \text{where} \quad \widehat{E} = e^{\delta \sin T}. \tag{5.108}$$

Upon substituting (5.108) into (5.107), we find

$$\begin{aligned} \delta^2 \widehat{E}\frac{k}{a_0}\widehat{X}_{\bar{t}} + \widehat{E}\left(\frac{1}{a_0} - \frac{\delta a_1}{a_0^2}\right)\widehat{X}_T = \delta^2\Bigg[\widehat{E}\frac{k}{a_0}\widehat{X}f_0'(E\widehat{Y}) \\ + \widehat{\zeta}\left(\frac{\nu a_0}{k}\right)^{1/2}\left(h_1(E\widehat{Y}) - \beta_0^O\cos\left(T+\phi\right)\right)\Bigg] + O\left(\delta^3\right). \end{aligned} \tag{5.109}$$

Equation (5.109) suggests the asymptotic expansion $\widehat{X}(\bar{t}, T) = X_0(\bar{t}, T) + \delta X_1(\bar{t}, T) + \delta^2 X_2(\bar{t}, T) + O(\delta^3)$. It follows that at leading and first order, $X_0 = \widetilde{X}_0(\bar{t})$ and $X_1 = \widetilde{X}_1(\bar{t})$ and at second order

$$X_{2T} = -\widetilde{X}_{0\bar{t}} + \widetilde{X}_0 f_0'(\widetilde{Y}_0) + \widehat{\zeta}\left(\frac{\nu a_0^3}{k^3}\right)^{1/2}\left(h_1(\widetilde{Y}_0) - \beta_0^O\cos\left(T+\phi\right)\right). \tag{5.110}$$

Upon integrating (5.110) with respect to T, we obtain

$$\begin{aligned} X_2 \;=\; &\left[-\widetilde{X}_{0\bar{t}} + \widetilde{X}_0 f_0'(\widetilde{Y}_0) + \widehat{\zeta}\left(\frac{\nu a_0^3}{k^3}\right)^{1/2} h_1(\widetilde{Y}_0)\right]T \\ &-\widehat{\zeta}\left(\frac{\nu a_0^3}{k^3}\right)^{1/2}\beta_0^O\sin\left(T+\phi\right) + \widetilde{X}_2(\bar{t}), \end{aligned} \tag{5.111}$$

where $\widetilde{X}_2(\bar{t})$ is a function of integration. To avoid the secular term in (5.111) growing, we let

$$\widetilde{X}_{0\bar{t}} = \widetilde{X}_0 f_0'(\widetilde{Y}_0) + \widehat{\zeta}\left(\frac{\nu a_0^3}{k^3}\right)^{1/2} h_1(\widetilde{Y}_0). \tag{5.112}$$

Equations (5.106) and (5.112) are solved numerically, using a second order Runge-Kutta method. Different particle paths are found, by choosing different initial conditions, $\widetilde{X}_0(\bar{t}=0)$ and $\widetilde{Y}_0(\bar{t}=0)$. The functions f_0 and h_1 have been solved numerically earlier in this chapter for each value of $a_0 > 0.6017$. To obtain values for $f_0(\widetilde{Y}_0)$ and $h_1(\widetilde{Y}_0)$ at a given value of $\widetilde{Y}_0$, a linear interpolation is performed. Once the solutions $\widetilde{X}_0(\bar{t})$ and $\widetilde{Y}_0(\bar{t})$ have been computed, they are combined with the oscillatory component $E = e^{-\delta \sin T}$ to give the leading order particle paths $x = E^{-1}\widetilde{X}_0$ and $y = E\widetilde{Y}_0$. In figure 5.8(a), we illustrate $\widetilde{X}_0(\bar{t})$ and $\widetilde{Y}_0(\bar{t})$ for $a_0 = 1$ and $\beta_0^M = 1.2$. We notice that the

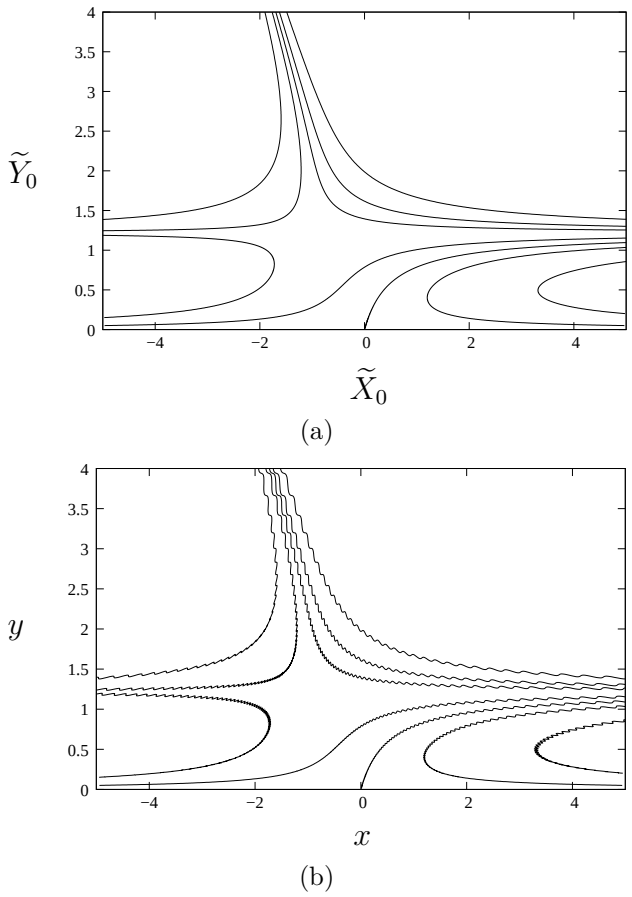

Figure 5.8: (a) The streamlines that correspond to the streamlines of steady components in the steady streaming layer for $a_0 = 1$ and $\beta_0^M = 1.2$ with $\widehat{\zeta} = \nu = k = 1$. (b) The particle paths for the same parameters where the oscillation amplitude is $\Omega = 100$.

streamlines in this figure correspond to the streamlines of steady components in the steady streaming layer seen in figure 5.6(a). Figure 5.8(b) illustrates the particle paths for the same parameters with $\delta = 0.01$, which corresponds to an oscillation amplitude of $\Omega = 100$. Therefore, the small oscillations simply cause the particle paths to oscillate about their mean position.

To conclude this section, we consider the effect of the oblique components on the wall shear stress, which is defined as $S = \mu u_y|_{y=0} = \mu\psi_{yy}|_{y=0}$. Using the streamfunction (5.59), which is written in terms of the scaled variables introduced in section 5.2, we find the wall shear stress is given by

$$S = \mu \left(\frac{k^3}{\nu}\right)^{1/2} \Delta^{3/2}\widehat{\psi}_{P\widehat{\eta}\widehat{\eta}} + \mu\widehat{\zeta}\widehat{\psi}_{O\widehat{\eta}}\Big|_{\widehat{\eta}=0}. \tag{5.113}$$

Expressing (5.113) in terms of the Stokes layer variables, we obtain

$$\begin{aligned} S &= \mu\left(\frac{k^3}{\nu a_0^3}\right)^{1/2} x\left[\Omega^2\Psi_{P_0\xi\xi}+\Omega\left(\Psi_{P_1\xi\xi}-\frac{a_1}{2a_0}\Psi_{P_0\xi\xi}\right)+O\left(1\right)\right] \\ &\quad +\widehat{\zeta}\Big[\Omega\Psi_{O_0\xi}+\Psi_{O_1\xi}+O\left(\Omega^{-1}\right)\Big]\Big|_{\xi=0}. \end{aligned} \tag{5.114}$$

Upon substituting the Stokes layer components in (5.114) and evaluating at $\xi = 0$, we find the wall shear stress is given by

$$\begin{aligned} S &= \mu\left(\frac{k^3}{\nu a_0^3}\right)^{1/2} x\Bigg[\Omega^2\cos\left(\tau+\frac{\pi}{4}\right) \\ &\quad +\Omega\left(\frac{1}{2\sqrt{2}}+\sin\left(2\tau+\frac{\pi}{4}\right)\left(1-\frac{1}{\sqrt{2}}\right)\right)+O\left(1\right)\Bigg] \\ &\quad +\mu\widehat{\zeta}\Bigg[\Omega\beta_0^O\sin\left(\tau+\phi-\frac{\pi}{4}\right)+c-\frac{1}{2}\beta_0^O\sin\left(\phi+\frac{\pi}{4}\right) \\ &\quad -\left(1-\frac{1}{\sqrt{2}}\right)\sin\left(2\tau+\frac{\pi}{4}+\phi\right)-\beta_0^M\sin\left(\tau+\frac{\pi}{4}\right) \\ &\quad -\beta_1^O\cos\left(\tau+\frac{\pi}{4}+\phi\right)+O(\Omega^{-1})\Bigg]. \end{aligned} \tag{5.115}$$

Taking a time-average over one time period, we obtain the mean wall shear stress

$$\begin{aligned} \bar{S} &= \mu\left(\frac{k^3}{\nu a_0^3}\right)^{1/2} x\left[\frac{\Omega}{2\sqrt{2}}+O\left(1\right)\right] \\ &\quad +\mu\widehat{\zeta}\left[c-\frac{1}{2}\beta_0^O\sin\left(\phi+\frac{\pi}{4}\right)+O\left(\Omega^{-1}\right)\right], \end{aligned} \tag{5.116}$$

where $\bar{S}$ is the average value and c is a constant which is given in (5.55). In both the wall shear stress and the mean wall shear stress, the dominant contribution comes from the orthogonal component of the flow. We note that although the component proportional to β_0^O in (5.116) is only dependent upon the time-dependent horizontal velocity component, this term arises due to the coupling of the orthogonal and oblique components. Additionally, the mean wall shear stress term $c\widehat{\zeta}$ describes the interaction between the orthogonal stagnation-point flow and the shear flow, as c is dependent upon orthogonal parameters. In the absence of an orthogonal flow, i.e. $\widehat{\psi}_P = 0$, equation (5.10) becomes

$$\Omega\widehat{\psi}_{O\tau}-\widehat{\psi}_{O\widehat{\eta}\widehat{\eta}}=-\Omega\widetilde{\beta}_\tau, \tag{5.117}$$

with the boundary conditions $\widehat{\psi}_O(0,\tau) = 0$ and $\widehat{\psi}_O(\widehat{\eta},\tau) \to \widehat{\eta} - \beta_0^O \cos(\tau+\phi)$ as $\widehat{\eta} \to \infty$, where $\beta_0^M = 0$. Upon solving equation (5.117), we find

$$\widehat{\psi}_O = \widehat{\eta} + \Omega^{1/2}\beta_0^O \left[e^{-\Omega^{1/2}\widehat{\eta}/\sqrt{2}} \cos\left(\tau - \frac{\Omega^{1/2}\widehat{\eta}}{\sqrt{2}} + \phi \right) - \cos\left(\tau+\phi\right) \right]. \quad (5.118)$$

The wall shear stress in this case is given by $S = \mu\widehat{\zeta}$, which is the wall shear stress imposed by the shear flow.

In the current analysis, we have assumed that the horizontal velocity component $\widehat{\beta} \sim O(1)$, which corresponds to $\widehat{\beta}$ being of the same order of magnitude as the mean component in $a(\tau) = 1 + \Delta\cos\tau$. However, other magnitudes of $\widehat{\beta}$ could have been chosen. A weaker time-dependent horizontal velocity could be considered by setting β_0^M and β_0^O equal to zero. Also, we could have chosen a stronger horizontal velocity and considered the problem where $\widehat{\beta}$ is of the same order of magnitude as the oscillatory component in $a(\tau)$, i.e. $\widehat{\beta} \sim O(\Delta)$. This corresponds to choosing

$$\begin{aligned} \widetilde{\beta} \;\; = \;\; & \Omega^{3/2}\left(\beta_0^M + \beta_0^O\cos(\tau+\phi)\right) \\ & + \Omega^{1/2}\left(\beta_1^M + \beta_1^O\cos(\tau+\phi)\right) + O(\Omega^{-1/2}). \end{aligned} \quad (5.119)$$

Using this new expansion for $\widetilde{\beta}$, an asymptotic analysis similar to the one used previously is performed. We find the Stokes layer expansion is now given by $\psi_O \sim O(\Omega^{3/2})$, where the leading and first order equations are the same as those given in (5.23) and (5.24). Additionally, the steady streaming layer $\psi_O \sim O(\Omega^{5/2})$. We note that both of these layers are Ω times that of those discussed above. In solving the oblique equation in the steady streaming layer, the equation for h_1 is given by

$$h_1'' + f_0 h_1' - f_0' h_1 = a_0\beta_0^M, \quad (5.120)$$

with boundary conditions

$$h_1(0) = 0, \quad h_1'(0) = c, \quad h_1 \to -\beta_0^M \quad \text{as} \quad \zeta \to \infty. \quad (5.121)$$

We note this is not the same as the equation for h_1 given in (5.46), as the primary constant $C = \lim_{\zeta\to\infty}(a_0\zeta - f_0)$ is unaffected by the choice of $\widetilde{\beta}$

and appears at higher order. The analytic solution to equation (5.120) is obtained in a similar way to that in section 5.4.2 and has the solution

$$h_1 = -\frac{\beta_0^M}{a_0}\left(f_0'(\zeta) + \frac{3f_0''(\zeta)}{4f_0''(0)}\right), \tag{5.122}$$

where

$$c = -\frac{\beta_0^M}{a_0}\left(f_0''(0) + \frac{27}{64f_0''(0)} - \frac{3a_0^2}{4f_0''(0)}\right). \tag{5.123}$$

This solution is of interest as the constant c appears in the mean wall shear stress.

To obtain the wall shear stress, we substitute the new oblique Stokes layer expansion into (5.113) and find

$$\begin{aligned} S = \mu\left(\frac{k^3}{\nu a_0^3}\right)^{1/2} x\left[\Omega^2\Psi_{P_0\xi\xi} + \Omega\left(\Psi_{P_1\xi\xi} - \frac{a_1}{2a_0}\Psi_{P_0\xi\xi}\right) + O(1)\right] \\ +\widehat{\zeta}\Big[\Omega^2\Psi_{O_0\xi} + \Omega\Psi_{O_1\xi} + O(1)\Big]\Big|_{\xi=0}. \end{aligned} \tag{5.124}$$

Substituting the Stokes layer solutions into (5.124) and upon taking a time-average over one time period, we obtain the mean wall shear stress

$$\bar{S} = \mu\left(\frac{k^3}{\nu a_0^3}\right)^{1/2} x\frac{\Omega}{2\sqrt{2}} + \mu\widehat{\zeta}\Omega\left[c - \frac{1}{2}\beta_0^O\sin\left(\phi + \frac{\pi}{4}\right)\right] + O(1). \tag{5.125}$$

Therefore, we find that increasing the magnitude of the horizontal velocity component $\widehat{\beta}$, causes the oblique component to appear at the same order as the primary component in both the wall shear stress and the mean wall shear stress, unlike that when $\widehat{\beta} \sim O(1)$.

The point at which the mean shear stress is equal to zero, is given by

$$x_s = -2\sqrt{2}\widehat{\zeta}\left[c - \frac{1}{2}\beta_0^O\sin\left(\phi + \frac{\pi}{4}\right)\right]. \tag{5.126}$$

The point of zero mean wall shear stress x_s, can be shifted either upstream or downstream depending on the values of a_0, β_0^M, β_0^O and ϕ. In figure 5.9, we illustrate the constant c/β_0^M against a_0. For all values of a_0, c/β_0^M is always negative. Therefore, in the case when $\beta_0^O = 0$, the point of zero mean wall shear stress is positive and as β_0^M increases, x_s is shifted in a positive direction.

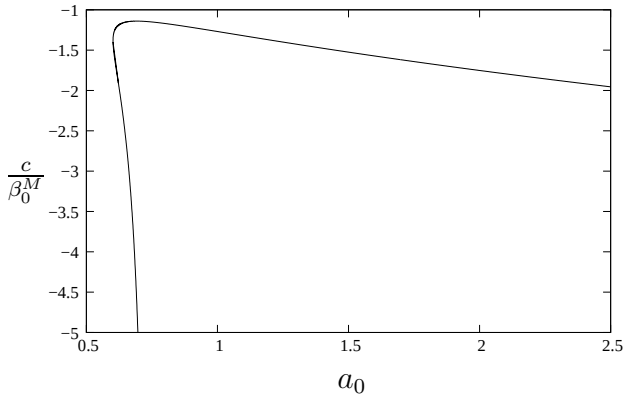

Figure 5.9: The constant $\frac{c}{\beta_0^M}$, given in (5.123), plotted against a_0. The lower branch of the curve asymptotes to $a_0 = 0.75$.

5.6 Summary

This chapter is a continuation of chapter 4, but now focuses on a large frequency asymptotic analysis of a two-dimensional unsteady stagnation-point flow, travelling obliquely towards a fixed wall. As in chapter 4, the flow in the far-field is made up of an unsteady orthogonal stagnation-point flow, including both a mean component and an oscillatory component, which is dependent upon a relative amplitude parameter Δ, and a dimensionless frequency parameter σ. Added to this is a shear flow with constant vorticity and a time-dependent horizontal velocity component.

As initially discussed in chapter 2, for a given dimensionless frequency, a critical relative amplitude occurs, above which the orthogonal and oblique solutions break down at a finite-time singularity. We have performed an asymptotic analysis for large parameters close to the critical value, through which we found that the problem exhibits a double-layer structure. At the wall, a Stokes layer is present and due to a mean velocity persisting to the top of the Stokes layer, a steady streaming layer is introduced to match between the Stokes layer and the far-field flow.

Over a single time period, the flow structure is particularly complicated as a multi-layered structure appears twice. In the first time interval, a horizontal streamline appears at the Stokes layer, creating a double-layered structure. This streamline then moves up through the steady streaming layer, until it

disappears to infinity and the flow returns to a single-layered structure. At the second time interval, like that of the first, a horizontal streamline emerges from the Stokes layer and moves upwards into the steady streaming layer. A second horizontal streamline moves down from infinity, creating a triple-layered structure. At some time in the interval, the two horizontal streamlines collide and the streamline pattern returns to a single-layered structure.

When the structure of the streamlines is single-layered, the horizontal velocity component simply shifts the instantaneous streamlines in the far-field and the attachment point with the wall to the right. When the flow has a double or triple-layered structure, the location of the stagnation point on the horizontal streamline emerges from either positive or negative infinity. As the streamline moves up to infinity, the stagnation point tends to negative infinity regardless of the horizontal velocity.

When considering the mean wall shear stress, for which we have chosen a horizontal velocity of the same order of magnitude as that of the mean component of the unsteady orthogonal stagnation-point flow, the contribution for the oblique components appear at a higher order than the orthogonal components. However, choosing the horizontal velocity component to be the same order of magnitude as the large oscillatory component of the orthogonal flow, we find that the oblique component appears at the same order as the orthogonal component in the mean wall shear stress. In this case, the location of zero mean wall shear stress can be moved upstream or downstream by altering the parameters.

The particle paths within the steady streaming layer were considered using the method of multiple scales. It was observed that the particle paths have small amplitude rapid oscillations, which simply cause the particles to oscillate about their mean position.

A brief summary of the work within this chapter can be found in Tooke et al. (2010).

Chapter 6

Conclusion

6.1 Concluding remarks

This thesis has focused on orthogonal and oblique stagnation-point flows. In each case, the problem comprised an orthogonal equation with a secondary equation, which is coupled with the orthogonal equation and describes the additional components of the problem.

In chapter 2, an unsteady orthogonal stagnation-point flow travelling towards an oscillating wall was considered. This problem was previously addressed by Hazel and Pedley (1998) in reference to a simplified model of an arterial end-to-side anastomosis, which is illustrated in figure 1.1. Hazel and Pedley considered the problem for a large dimensionless frequency parameter, but chose a relative amplitude parameter to prevent flow reversal occurring. The orthogonal problem was addressed by many authors, including Merchant and Davis (1989). They showed that for a large dimensionless frequency, there exists a critical relative amplitude, above which solutions do not exist. Blyth and Hall (2003) extended this analysis and found that solutions above the critical amplitude break down at a finite-time singularity. Therefore, we performed an asymptotic analysis for a large dimensionless frequency close to the critical amplitude, which allows for flow reversal. The solutions exhibit a double layer structure, where the thickness of the layers is dependent upon the relative sizes of the mean and oscillatory components

of the far-field orthogonal flow. In the case where the oscillatory component is dominant in the far-field, the solution exhibits a Stokes layer at the wall with a steady streaming layer matching between the Stokes layer and the far-field flow. The wall shear stress was calculated and we found that for a large dimensionless frequency parameter, the oscillatory components of the flow do not effect the mean wall shear stress. This agreed with the results obtained by Hazel and Pedley (1998). Therefore, even though the asymptotic structure has changed, the effect of the oscillatory components on the mean wall shear stress has not.

In chapter 2, we followed Hazel and Pedley (1998) by considering an oscillating stagnation-point flow travelling towards an oscillating wall. However, in the subsequent chapters, stagnation-point flows were discussed travelling towards fixed walls. By a simple change of frame of reference, it is easy to switch between frames, with only the pressure term being affected.

Chapter 3 considered a two-dimensional stagnation-point flow where the streamlines approach a fixed wall obliquely. The problem is comprised of three separate flows, a Hiemenz stagnation-point flow, a shear flow with constant vorticity and a uniform stream. As the streamlines approach the wall, the viscosity caused the dividing streamline to turn in towards the wall and meet the wall at an angle closer to the normal. We ascertained that increasing the uniform stream in the far-field, simply shifted the streamlines and the attachment point of the dividing streamline with the wall to the right, without affecting the structure of the streamlines.

As an extension to chapter 3, chapter 4 considered an oblique unsteady two-dimensional stagnation-point flow. Like that in chapter 2, in the far-field, there is a orthogonal stagnation-point flow, which is dependent upon a dimensionless frequency and a relative amplitude parameter. Superimposed onto this is a shear flow with constant vorticity and a time-dependent horizontal velocity component. The problem can be described as two coupled equations and solved numerically using a Crank-Nicolson finite-difference technique.

Over a single time period, the flow structure is dependent upon the

relative amplitude parameter. For a fixed dimensionless frequency, when $\Delta < \Delta_1$, where $\Delta_1 < \Delta_2 < 1$, the streamline pattern is at its simplest. The dividing streamline approaches the wall obliquely and its gradient oscillates between two bounding values. When $\Delta_1 < \Delta < \Delta_2$, a horizontal streamline appears from the wall, creating a double-layered structure in the flow for a short time interval. The layer at the wall is separated from the remaining flow by a horizontal streamline through a stagnation point. As the horizontal streamline returns to the wall, the flow returns to a single-layered flow. When $\Delta_2 < \Delta < 1$, a horizontal streamline appears at the wall and moves into the fluid. As the first horizontal streamline is moving back towards the wall, a second horizontal streamline appears from the wall. This creates a triple-layered structure in the flow for a short time, before the two streamlines meet and the flow returns to a single-layered structure. When $\Delta > 1$, there are two time intervals over the period in which the horizontal streamline appear within the flow. At the first time interval, a horizontal streamline appears in the flow before moving up and disappearing at infinity. In the second case, the horizontal streamline appears from the wall and after a short time, a second horizontal streamline moves down from infinity creating a triple-layered structure. When these two horizontal streamlines collide, the flow returns to a single-layered flow.

When $\Delta > 1$, there exists a critical relative amplitude parameter $\Delta_s(\sigma)$, such that when $\Delta > \Delta_s$, the orthogonal and oblique solutions breakdown at a finite-time singularity. In the large frequency limit, which was discussed in chapter 5, an exact expression was found for the relationship between Δ_s and σ.

The particle paths within the steady streaming layer were obtained using the method of multiple scales. It was found that the particle paths follow the streamlines that correspond to the steady components of the steady streaming layer solution, with the particles performing small rapid oscillations about their mean position.

If the magnitude of the horizontal velocity component is the same order

as the oscillatory component of the unsteady orthogonal stagnation-point flow, the location of the zero mean wall shear stress can be shifted upstream or downstream dependent upon the parameters chosen.

6.2 Further work

As discussed in the introduction, the stagnation-point flows considered in this thesis can have applications to blood flow, specifically as simplified models of an end-to-side anastomosis, which is a surgical graft performed to bypass a blocked artery, for example. To allow for more accurate models to be calculated, we discuss some of those simplifications.

Hazel and Pedley (1998), who considered this application provide physiological values for all the required parameters. In particular, they calculate the dimensionless amplitude parameter to be $\Delta = 0.6$, which does not allow for any flow reversal to occur. Due to the pulsatile nature of the heart, there are two alternating cycles called systole and diastole. During systole, the blood is pumped from the heart, whereas during diastole, the period when the heart is resting, the flow is either stationary or reversed in some arteries, such as the external carotid or the femoral artery (Ku (1997)). Hazel and Pedley (1998) have previously discussed the three-dimensional orthogonal stagnation-point flow, but like that of the two-dimensional case, as discussed above, they chose a relative amplitude parameter that does not allow for flow reversal. Hence, an obvious extension is to consider the orthogonal problem in the three dimensional case, for a relative amplitude parameter, which will allow flow reversal to occur.

Hazel and Pedley (1998) found the frequency parameter $\sigma \approx 0.62$. Heil and Hazel (2003) investigated an oscillating two-dimensional stagnation-point flow similar to that of Hazel and Pedley. Their application was to consider how the flow close to a stagnation point in an end-to-side anastomosis behaves and they focussed on the parameter range $0.04 < \sigma < 0.4$. Therefore, the analysis performed in chapter 4, where an unsteady oblique

stagnation-point flow was considered, can be applied to an end-to-side anastomosis for these parameters. Also, if physiological parameters can be obtained for the oblique problem, the optimum angle at which the streamlines approach the wall, which may improve the graft's longevity could be investigated.

Ojha et al. (1990), are among many who have found that there is a link between low wall shear stress and intimal hyperplasia, which is the thickening of the inner layer of an artery. This thickening of the arterial wall causes changes in the geometry of the vessel wall, which can no longer be considered flat. Therefore, a more physical assumption would be to consider the wall with either a bump or dip on its surface. In addition, the effect of surface curvature could take be taken into account like that of Sanchez-Sanz and Blyth (2007) who considered an unsteady axisymmetric orthogonal stagnation-point flow approaching a cylinder.

In this thesis, only two-dimensional problems have been considered. Both Riley (1993) and Weidman and Putkaradze (2003) investigated axisymmetric problems. Riley considered the flow travelling towards a cylinder orthogonally, while Weidman and Putkaradze considered a steady axisymmetric flow travelling obliquely towards a cylinder. Therefore, the oblique analysis performed in chapters 4 and 5 can be extended to consider an axisymmetric oblique unsteady stagnation-point flow travelling towards an cylinder.

Even though blood is non-Newtonian, Perktold et al. (1991) stated that in large arteries there was very little difference in the flow characteristics between non-Newtonian and Newtonian fluids. However, Gijsen et al. (1999) later suggested that the effect of shear thinning and the viscoelasticity of the blood is important in the carotid artery. Therefore, as an extension, the orthogonal and oblique problems could be considered in a non-Newtonian fluid, where comparisons could be drawn with the analysis and results within this thesis.

Appendix A

Asymptotic solution of $F_0(\zeta)$ about $a_0 \approx 0.75$

In this appendix, we obtain the asymptotic solution of $\widehat{F}_0(\widehat{\zeta})$ close to $a_0 \approx 0.75$. This equation was initially derived in chapter 2 and from the numerical results obtained in section 2.6.3, it can be seen that the velocity profiles exhibit a region of flow reversal close to $\widehat{\zeta} = 0$ as $a_0 \to 0.75$. By seeking the asymptotic solution close to $a_0 \approx 0.75$, we confirm this behaviour.

The equation for $\widehat{F}_0$, which was previously derived in equation (2.132), is given by

$$\widehat{F}_0''' - \widehat{f}_0'\widehat{F}_0' + \widehat{f}_0\widehat{F}_0'' = \frac{1 - \widehat{f}_0'}{2}, \tag{A.1}$$

with boundary conditions

$$\widehat{F}_0(0) = 0, \quad \widehat{F}_0'(0) = \frac{1}{2}, \quad \widehat{F}_0'(\widehat{\zeta}) \to 0 \quad \text{as} \quad \widehat{\zeta} \to \infty. \tag{A.2}$$

Similar to the analysis used when obtaining the primary asymptotic solution in section 2.4.4, we introduce the parameter $\lambda = \frac{3}{4a_0}$ and write $\lambda = 1 + \epsilon$ where $0 < \epsilon \ll 1$. We note that $\lambda = 1$ is equivalent to $a_0 = 0.75$.

We begin by considering the solution close to $\widehat{\zeta} = 0$. Unlike the primary problem, where $\widehat{f}_0''(0) \sim \epsilon^{1/2}$ as $\epsilon \to 0$, the numerical results for the subsidiary problem, obtained in section 2.6.3, show that $\widehat{F}_0''(0) \sim \epsilon^{-1}$ as $\epsilon \to 0$. This relationship is illustrated in figure A.1. This relation, along with the

boundary conditions at $\widehat{\zeta} = 0$, suggests the scaling $\widehat{F}_0 = \delta^2 G$ with variable $Y = \widehat{\zeta}/\delta^2$. The parameter $\delta = (2\epsilon)^{1/2}$ was found when obtaining the primary asymptotic solution in section 2.4.4.

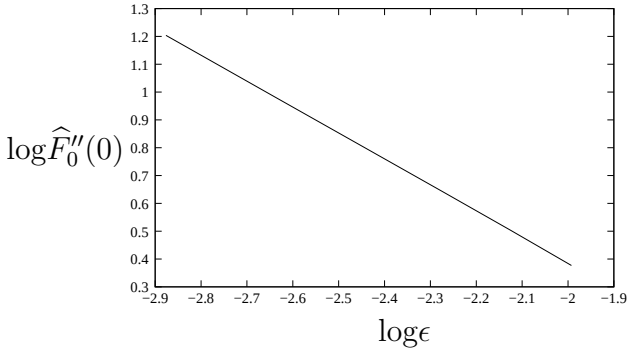

Figure A.1: The numerical results for the subsidiary problem illustrating a linear relationship between $\widehat{F}_0''(0)$ and ϵ.

We recall the primary asymptotic solution close to $\widehat{\zeta} = 0$, which as previously stated in equation (2.75), is given by

$$\begin{aligned} \widehat{f}_0 &= -\frac{\sin(\chi)}{\delta} + \frac{\delta}{2}\Big[B(\sin(\chi) - \chi\cos(\chi)) \\ &+ \cos(\chi)\int_0^{\chi} \ln(\tan(\bar{\chi}/2))\mathrm{d}\bar{\chi} - \sin(\chi)\ln(\tan(\chi/2))\Big] + \cdots, \end{aligned} \tag{A.3}$$

where $\chi = \delta\widehat{\zeta}$. In the limit $Y \to 0$, we can approximate equation (A.3) as

$$\widehat{f}_0 = -\delta^2 Y - \frac{\delta^4 Y}{2} + \cdots. \tag{A.4}$$

Upon substituting (A.4) and the subsidiary scalings into equation (A.1), we obtain

$$G_{YYY} + \delta^4\Big(G_Y - YG_{YY} - 1\Big) + O(\delta^6) = 0. \tag{A.5}$$

Equation (A.5) suggests we expand $G = G_0 + O(\delta^4)$ and at leading order, we find $G_{0_{YYY}} = 0$. Integrating this three times and applying the boundary conditions at $Y = 0$, we find $G_0(Y) = \frac{AY^2}{2} + \frac{Y}{2}$, where A is an arbitrary constant. Therefore,

$$\widehat{F}_0 = \frac{\delta^2}{2}\left(AY^2 + Y\right). \tag{A.6}$$

We shall denote this the region $1a$ solution, which is within region 1 of the primary solution. Figure A.3 illustrates the structure of the layers in both the primary and subsidiary problems.

As (A.6) does not satisfy the boundary condition at infinity, $\widehat{F}' \to 0$ as $\widehat{\zeta} \to \infty$, we introduce another region, within the region 1 primary solution. Similar to the results found in figure A.1, it appears that $\widehat{F}_0(\widehat{\zeta}) \sim \epsilon^{-2}$ as $\widehat{\zeta} \to \infty$. Therefore, we let $\widehat{F}_0 = \frac{1}{\delta^4} H(\chi)$ with $\chi = \delta\widehat{\zeta}$, where this variable was initially introduced when obtaining the primary asymptotic solution in region 1. Upon substituting the primary solution (A.3) and the subsidiary scalings into the subsidiary equation (A.1), we find

$$\delta^2 H_{\chi\chi\chi} + \cos(\chi) H_\chi - \sin(\chi) H_{\chi\chi} = \delta^3 \left(\frac{1 + \cos\chi}{2} \right). \tag{A.7}$$

This expansion suggests we write $H = H_0 + O(\delta^2)$ and we solve the leading order equation, $\cos(\chi) H_{0_\chi} - \sin(\chi) H_{0_{\chi\chi}} = 0$, to obtain

$$H_0(\chi) = C\cos(\chi) + D. \tag{A.8}$$

This is denoted the region $1b$ solution. Therefore, the primary region 1 solution spans the subsidiary regions $1a$ and $1b$. The constants C and D are found via matching to the region $1a$ solution. We let $\chi \to 0$ and approximate (A.8) as the power series, $H_0(\chi) \sim C + D - \frac{C\chi^2}{2} + O(\chi^4)$. In the matching region, the region $1a$ and $1b$ leading order solutions are given by

$$\widehat{F}_0 = \frac{A\chi^2}{2\delta^4} + \frac{\chi}{2\delta}, \tag{A.9}$$

$$\widehat{F}_0 = \frac{1}{\delta^4} \left(C + D - \frac{C\chi^2}{2} \right). \tag{A.10}$$

From these, we can see that $A = -C$ and $C + D = 0$. Therefore, the region $1b$ solution is given by

$$\widehat{F}_0 = \frac{A}{\delta^4} \Big(1 - \cos(\chi) \Big). \tag{A.11}$$

In section 2.4.4, it was found that the leading order primary solution in region 1, $\widehat{f}_0' = -\cos\chi$, is unable to satisfy the far-field boundary condition $\widehat{f}_0' \to 1$ as $\chi \to \infty$. Due to the subsidiary equation being dependent upon the primary equation, the solution (A.11) also breaks down when $\chi = \pi$, i.e. $\widehat{\zeta} = \pi/\delta$. As with the primary problem, to allow for matching with the far-field boundary condition $\widehat{F}_0' \to 0$ as $\chi \to \infty$, another region is introduced,

centred on $\widehat{\zeta} = \pi/\delta$, which we denote region 2. We recall, for the primary problem, we write $\widehat{f_0} = Z + N(Z)$ with $|N'(Z)| \ll 1$ and $Z = \widehat{\zeta} - \frac{\pi}{\delta}$. Similarly, the far-field boundary condition $\widehat{F}_0' \to 0$ as $\widehat{\zeta} \to \infty$, along with the region $1b$ expansion $\widehat{F}_0 = H_0/\delta^4$, suggests we write

$$\widehat{F}_0 = \frac{1}{\delta^4}\left(B + a(Z)\right), \tag{A.12}$$

where $|a'(Z)| \ll 1$ and B is an arbitrary constant, which is found through matching to the region $1b$ solution. Substituting these scalings into the subsidiary equation (A.1), gives

$$a''' - (1 + N')a' + (Z + N)a'' = -\frac{N'}{2}. \tag{A.13}$$

After neglecting the quadratic terms in a and N, we obtain

$$a''' - a' + Za'' = -\frac{N'}{2}. \tag{A.14}$$

Upon choosing $a(Z) = -\frac{N(Z)}{2}$, we retrieve equation (2.77), where the function $N(Z)$ has a solution in the form of a parabolic cylinder function, $N'(Z) = -\frac{\Gamma(3)\delta^2}{2\sqrt{2\pi}} e^{-Z^2/4} D_{-3}(Z)$. To find the constant B, we match this solution to the region $1b$ solution (A.11) about $\chi = \pi$. We find $B = 2A$ and the region 2 solution is given by

$$\widehat{F}_0 = \frac{2A}{\delta^4} + \frac{\Gamma(3)}{4\delta^2\sqrt{2\pi}} \int^{\widehat{\zeta} - \frac{\pi}{\delta}} e^{-\widehat{Z}^2/4} D_{-3}(\widehat{Z}) d\widehat{Z}. \tag{A.15}$$

The constant A is obtained numerically using the relation $\delta^2 \widehat{F}_0''(0) = A$. As $\delta \to 0$, $A \to -0.4$. In figure A.2 the region $1a, 1b$ and 2 leading order asymptotic solutions are plotted for $\epsilon = 0.001$ alongside the numerical solution for the same parameter showing excellent agreement. Therefore, we have obtained the analytic solution for $F_0(\zeta)$ close to $a_0 = 0.75$ and confirmed the numerical results and the behaviour of the velocity profiles as $a_0 \to 0.75$ in section 2.6.3.

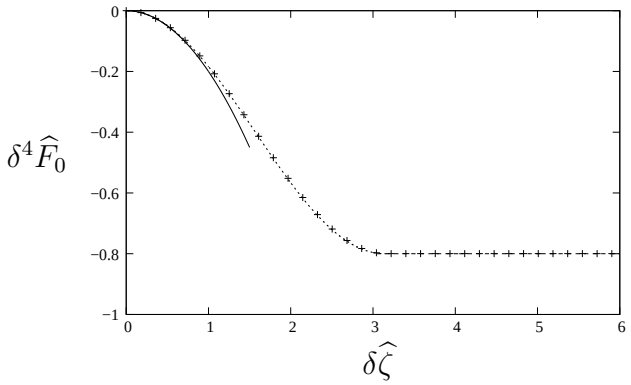

Figure A.2: The region 1, 2 and 3 asymptotic solutions, represented by the solid line, the dotted lines and the dashed lines for $\epsilon = 0.001$, where $\delta = (2\epsilon)^{1/2}$, alongside the numerical solution for the same parameter, represented by the crosses.

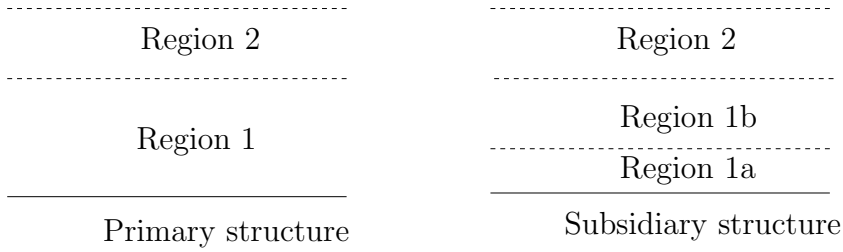

Figure A.3: An illustration of the primary and subsidiary regions.

Appendix B

Change of frame of reference

The problem discussed in chapter 4, described a two-dimensional unsteady stagnation-point flow travelling obliquely towards a fixed wall. In this appendix, we show by a simple change of frame of reference that this problem is equivalent to a two-dimensional unsteady stagnation-point flow, travelling towards an oscillating wall.

The streamfunction in the far-field, initially stated in equation (5.1), is given by

$$\psi = a(t)kxy + \frac{1}{2}\widehat{\zeta}y^2 - \widehat{\beta}(t)\widehat{\zeta}\left(\frac{\nu}{k}\right)^{1/2} y. \tag{B.1}$$

Using the properties $u = \psi_y$ and $v = -\psi_x$, the velocity components are expressed as

$$u = a(t)kx + \widehat{\zeta}y - \widehat{\beta}(t)\widehat{\zeta}\left(\frac{\nu}{k}\right)^{1/2}, \tag{B.2}$$

$$v = -a(t)ky, \tag{B.3}$$

with boundary conditions at the wall given by

$$u = 0, \quad v = 0 \quad \text{on} \quad y = 0, \tag{B.4}$$

where the stagnation point is located at $x = \widehat{\beta}\widehat{\zeta}(\nu/k)^{1/2}/(ak)$.

To consider this problem approaching an oscillating wall, similar to the change of frame of reference in chapter 2, we write

$$\widehat{x} = x - \frac{\widehat{\beta}(t)\widehat{\zeta}\left(\frac{\nu}{k}\right)^{1/2}}{ak} \quad \text{and} \quad \widehat{u} = u - \frac{d}{dt}\left(\frac{\widehat{\beta}(t)\widehat{\zeta}\left(\frac{\nu}{k}\right)^{1/2}}{ak}\right), \tag{B.5}$$

with no change to the vertical length and velocity scale $\widehat{y}$ and $\widehat{v} = v$. Therefore, the far-field velocity boundary conditions can be rewritten as

$$\widehat{u} = a(t)k\widehat{x} + \widehat{\zeta}\widehat{y} - B, \tag{B.6}$$

$$\widehat{v} = -a(t)k\widehat{y}, \tag{B.7}$$

with boundary conditions on the wall

$$\widehat{u} = -B, \quad \widehat{v} = 0 \quad \text{on} \quad \widehat{y} = 0, \tag{B.8}$$

where

$$B = \widehat{\zeta}\left(\frac{\nu}{k}\right)^{1/2} \frac{d}{dt}\left(\widehat{\beta}(t)\right). \tag{B.9}$$

Having performed this change of frame of reference, the problem given by (B.6) - (B.8) now describes a two-dimensional stagnation-point flow, travelling obliquely towards an oscillating wall. Therefore, problems of this nature can either be solved approaching an oscillating or a fixed wall.

Bibliography

M. Abramowitz and I. A. Stegun. *Handbook of mathematical functions with formulas, graphs, and mathematical tables*. Dover publications, 1964.

W. H. H. Banks and M. B. Zaturska. The collision of unsteady laminar boundary layers. *Journal of Engineering Mathematics*, 13(3):193–212, 1979.

G. K. Batchelor. *An introduction to fluid dynamics*. Cambridge University Press, 2000.

M. G. Blyth and P. Hall. Oscillatory Flow near a Stagnation Point. *Siam Journal on Applied Mathematics*, 63(5):1604–1614, 2003.

W. W. Cheney and D. Kincaid. *Numerical mathematics and computing*. Brooks/Cole Publishing Co. Pacific Grove, CA, USA, 1994.

J. M. Dorrepaal. An exact solution of the Navier-Stokes equation which describes non-orthogonal stagnation-point flow in two dimensions. *Journal of Fluid Mechanics*, 163:141–147, 1986.

P. G. Drazin and N. Riley. *The Navier-Stokes equations: a classification of flows and exact solutions*. Cambridge University Press, 2006.

C. F. Gerald and P. O. Wheatley. *Applied numerical analysis*. Addison-Wesley Longman, 1989.

F. J. H. Gijsen, F. N. Van de Vosse, and J. D. Janssen. The influence of the non-Newtonian properties of blood on the flow in large arteries: steady flow

in a carotid bifurcation model. *Journal of Biomechanics*, 32(6):601–608, 1999.

M. B. Glauert. The laminar boundary layer on oscillating plates and cylinders. *Journal of fluid mechanics*, pages 97–110, 1956.

C. E. Grosch and H. Salwen. Oscillating stagnation point flow. *Proceedings of the Royal Society of London. Series A, Mathematical and Physical Sciences*, 384:175–190, 1982.

A. L. Hazel and T. J. Pedley. Alteration of Mean Wall Shear Stress Near an Oscillating Stagnation Point. *Journal of Biomechanical Engineering*, 120: 227, 1998.

M. Heil and A. L. Hazel. Mass transfer from a finite strip near an oscillating stagnation point–implications for atherogenesis. *Journal of Engineering Mathematics*, 47(3):315–334, 2003.

K. Hiemenz. Die Grenzschicht an einem in den gleichformigen Flussigkeitsstrom eingetauchten geraden Kreiszylinder. *Dinglers Polytech. J*, 326:321–410, 1911.

J. D. Hoffman. *Numerical methods for engineers and scientists*. CRC, 2001.

D. N. Ku. Blood flow in arteries. *Annual Review of Fluid Mechanics*, 29(1): 399–434, 1997.

F. Loth, P. F. Fischer, and H. S. Bassiouny. Blood Flow in End-to-Side Anastomoses. *Annual Review of Fluid Mechanics*, 40:367–393, 2008.

J. H. Mathews. *Numerical methods for computer science, engineering, and mathematics*. Prentice-Hall, Inc. Upper Saddle River, NJ, USA, 1986.

G. J. Merchant and S. H. Davis. Modulated stagnation-point flow and steady streaming. *Journal of Fluid Mechanics*, 198:543–555, 1989.

M. Ojha, C. R. Ethier, K. W. Johnston, and R. S. C. Cobbold. Steady and pulsatile flow fields in an end-to-side arterial anastomosis model. *Journal of vascular surgery*, 12(6):747–753, 1990.

T. J. Pedley. Two-dimensional boundary layers in a free stream which oscillates without reversing. *Journal of Fluid Mechanics*, 55:359–383, 1972.

K. Perktold, M. Resch, and H. Florian. Pulsatile non-Newtonian flow characteristics in a three-dimensional human carotid bifurcation model. *Journal of biomechanical engineering*, 113:464, 1991.

N. Riley. Oscillating Viscous Flows. *Mathematika*, 12:165–175, 1965.

N. Riley. Unsteady flow at a stagnation point. *Journal of Fluid Mechanics*, 256:487–498, 1993.

N. Riley and R. Vasantha. An unsteady stagnation-point flow. *Quarterly Journal of Mechanics and Applied Mathematics*, 42:511–521, 1989.

N. Riley and P. D. Weidman. Multiple solutions of the Falkner-Skan equation for flow past a stretching boundary. *SIAM Journal on Applied Mathematics*, pages 1350–1358, 1989.

N. Rott. Unsteady viscous flow in the vicinity of a stagnation point. *Quarterly of Applied Mathematics*, 13(4):444–451, 1956.

M. Sanchez-Sanz and M. G. Blyth. Unsteady axisymmetric stagnation flow on a circular cylinder. *The Quarterly Journal of Mechanics and Applied Mathematics*, 2007.

J. T. Stuart. The viscous flow near a stagnation point when the external flow has uniform vorticity. *Journal of Aerospace Science*, 26:124–125, 1959.

J. T. Stuart. Double boundary layers in oscillatory viscous flow. *Journal of Fluid Mechanics*, 24(4):673–687, 1966.

K. Tamada. Two-dimensional stagnation point flow impinging obliquely on a plane wall. *Journal of the Physical Society of Japan*, 46(2):310–311, 1979.

R. M. Tooke and M. G. Blyth. A note on oblique stagnation-point flow. *Physics of Fluids*, 20:033101, 2008.

R. M. Tooke, M. G. Blyth, and P. W. Hammerton. Oscillatory oblique stagnation-point flow toward a plane wall. *To be submitted.* 2010.

J. Watson. The two-dimensional laminar flow near the stagnation point of a cylinder which has an arbitrary transverse motion. *The Quarterly Journal of Mechanics and Applied Mathematics*, 12(2):175, 1959.

P. D. Weidman and V. Putkaradze. Axisymmetric stagnation flow obliquely impinging on a circular cylinder. *European Journal of Mechanics-B/Fluids*, 22(2):123–131, 2003.

E. T. Whittaker and G. N. Watson. *A course of modern analysis*. Cambridge University Press, 1963.